STRUCTURAL ENZYMOLOGY OF SOLUBLE METHANE MONOOXYGENASE PROTEIN INTERACTIONS

A DISSERTATION

SUBMITTED TO THE FACULTY OF

UNIVERSITY OF MINNESOTA

BY

JASON CHRISTOPHER JONES

IN PARTIAL FULLFILLMENT OF THE REQUIREMENTS

FOR THE DEGREE OF

DOCTOR OF PHILOSOPHY

ADVISOR: JOHN D. LIPSCOMB

MAY 2021

Acknowledgements

I'd like to thank:

Dr. John D. Lipscomb for accepting me as a student in his laboratory when others wouldn't.

Dr. Rahul Banerjee for being a great lab mentor

Dr Ke Shi for being an awesome crystallographer

Dr. William Pomerantz for letting me pick his brain and ask questions about ^{19}F-NMR

Dr Ian Armitage for his expertise in NMR

Manny Semonis for all of his hard work and dedication.

Jason Jones Jr. for being the best son in the world

Abstract

Soluble methane monooxygenase (sMMO) is a multicomponent metalloenzyme that activates molecular oxygen, breaks the 105 kcal/mol C-H bond of CH_4, and inserts one atom of O to create methanol at ambient temperature and pressure. This feat of catalytic prowess requires all three protein components of sMMO for efficient multiple turnover catalysis: the hydroxylase (sMMOH), the reductase (MMOR), and the regulatory protein (MMOB). The structural mechanism of how these sMMO components interact to regulate the formation and decay of the chemical intermediates of the reaction cycle is not well understood. Our recent advances in sMMOH expression and purification have allowed us to obtain protein crystals of the sMMOH:MMOB complex. Using X-rays generated by either an X-ray free electron laser at room temperature or a synchrotron at 100 K, we obtained high resolution structures of the *Methylosinus trichosporium* OB3b sMMOH:MMOB complex for the first time. Analysis of the data shows in great detail how MMOB modulates the structure of sMMOH during the steps leading up to O_2 binding. New insight is gained about the path O_2 and methane take into the sMMOH active site, and how the selectivity and timing of this entry is controlled by MMOB in the sMMOH:MMOB complex. Additionally, biosynthetic incorporation of 5-fluorotryptophan into MMOB and MMOR, as well as post-translational modification of an MMOB variant with a trifluoroacetone probe, allowed us to use 1D-^{19}F-NMR to investigate the complex series of sMMO protein interactions that regulate the beginning of the sMMO catalytic cycle. A new model emerges describing how sMMO protein component affinities and exchange from protein-protein complexes control the dynamics of reaction cycle intermediates to drive catalysis.

Table of Contents

List of Figures

List of Tables

Table of Schemes

Abbreviations

BADAN, 6-bromoacetyl-2-dimethylaminoaphthalene

BMM, bacterial multicomponent monooxygenase

CD, circular dichroism

DFT, density functional theory

FAD, flavin adenine dinucleotide

IPTG, isopropylthio-β-galactoside

KIE, kinetic isotope effect

MCD, magnetic circular dichroism

MMO, methane monooxygenase

MMOB, regulatory protein

MMOR, reductase

MOPS, 3-(N-morpholino)propanesulfonic acid

NADH, nicotinamide adenine dinucleotide

NMR, nuclear magnetic resonance

pMMO, particulate methane monooxygenase

RFQ, rapid freeze quench

RT-SFX, room temperature serial femtosecond X-ray crystallography

sMMO, soluble methane monooxygenase

sMMOH, methane monooxygenase hydroxylase

$sMMOH^{ox}$:MMOB, diferric sMMOH in complex with MMOB

$sMMOH^{red}$:MMOB, chemically reduced sMMOH in complex with MMOB.

VTVH, variable-temperature variable field

XAS, X-ray absorption spectroscopy

XFEL, X-ray free electron laser

EPR, electron paramagnetic resonance

5FW, 5-fluorotryptophan

BTFA, 3-bromo-1,1,1-trifluoroacetone

Chapter 1 Introduction

1.1 Biological Oxygen Activation

Molecular oxygen (O_2) is the second most abundant gas in Earth's atmosphere today (~21%), but this was not always the case. Earth's earliest atmosphere was nearly devoid of O_2 and anaerobic organisms ruled the planet. About 2.5-2.2 billion years ago, the "Great Oxidation Event" occurred causing the Earth's atmosphere to shift from anoxic to oxygenic.[1-5] This shift resulted in the demise of anaerobic organisms living on Earth's surface, because they were unable to cope with the toxic waste product (O_2) produced by photosynthesis.[4] On the other hand, organisms capable of tolerating O_2 flourished, because they had the biochemical toolkit needed to transport and activate O_2 as well as protect themselves from the harmful effects of reactive oxygen species.[6] Most of the O_2 consumed by aerobic organisms is used to fuel their cellular respiration, the biochemical process of aerobically converting glucose into energy.[7] The remainder of consumed O_2 is used in making biomolecules that are important in various biological processes such as cell growth, development, and reproduction.[8] In order to perform this aerobic biochemistry, enzymes evolved that catalyze the activation of O_2 and subsequent reaction with organic substrates.

In the absence of a catalyst, reaction of O_2 with organic substrates is thermodynamically favored, yet kinetically sluggish. This phenomenon arises because O_2 has a triplet electronic ground state (two unpaired electrons; S = 1) and most organic substrates have a singlet electronic ground state (no unpaired electrons; S = 0). The difference in spin state between triplet O_2 and singlet organic substrates results in a large activation energy barrier which restricts the reaction from occurring under normal conditions (i.e. it is spin forbidden), hence the kinetic sluggishness. Uncatalyzed reactions between triplet O_2 and singlet organic substrates are possible *via* a free radical autooxidation process. In this process an initiator is required to generate a radical organic substrate which can then react with triplet O_2. This particular pathway of O_2 activation is not ideal for a biological system to rely on because there is no control over substrate specificity and product yield. Unsurprisingly, Nature evolved a way catalyze the spin forbidden reaction between triplet O_2 and singlet organic substrates by employing metalloenzymes.

Metalloenzymes contain transition metals such as copper, manganese, or iron in the active site. The transition metals, depending on their oxidation state, can bind O_2 and then reductively activate O_2 through a series of electron transfer steps which results in the formation and stabilization of the following biological oxidants: i.) a superoxo (O_2^-) radical species capable of reacting directly with a radical organic substrate as seen in *myo*-inositol oxygenase,[9] ii) a (hydro)peroxo (O_2^{2-}/HO_2^-) species with a singlet electronic state which can react with singlet organic substrates as seen in deoxyhypusine hydroxylase,[10, 11] or iii) a high valent-oxo, highly reactive species capable of oxidizing strong C-H bonds as seen in soluble methane monooxygenase.[5] The family metalloenzymes that catalyze the insertion of either one or two atoms of O from O_2 into an organic substrate are called monooxygenases or dioxygenases, respectively.[12, 13] The studies described in this dissertation deal with the metalloenzyme soluble methane monooxygenase (sMMO), which utilizes a dinuclear iron cluster in the active site to reductively activate O_2 and generate a high valent Fe_2^{4+} chemical intermediate.[5, 14, 15] Stabilization of this powerful, highly oxidizing, highly electrophilic, high valent metal-oxo species requires precise regulatory strategies needed to prevent non-specific reactions. Understanding the means by which sMMO controls the reactivity of oxygen once it is activated is a major goal of the research described here.

1.2 Methane, a Powerful Greenhouse Gas.

Methane (CH_4) is a potent greenhouse gas that it is 28 - 36 times more effective than CO_2, another greenhouse gas, at warming the Earth's lower atmosphere over a 100-year period.[16] The small percentage of CH_4 along with other greenhouse gases in the atmosphere make up the "blanket" which warms our planet. Over the last few decades, atmospheric levels of CH_4 have increased at an alarming rate and continue to accelerate, causing the average global temperature to rise.[17] This increase in atmospheric CH_4 is largely attributed to the following anthropogenic activities: agriculture, landfills, and natural gas flaring.[16, 18]Although agriculture and landfill sources are small producers of CH_4 individually, the combined total of global agriculture- and landfill-generated CH_4 is considered to be the main cause of rising CH_4 concentrations in Earth's atmosphere.[16, 17]

Currently, no economically viable way to capture, transport, and store gaseous CH_4 from remote sources exists.[18, 19] Until this problem is solved, anthropogenic CH_4 emissions will continue to present environmental issues. One way to deal with this problem is to develop a rapidly deployable mobile platform that is capable of biologically converting methane gas into liquid methanol, which is easier to store and transport.[18] The bioconversion of methane to methanol is accomplished in Nature by bacteria that express the metalloenzymes called methane monooxygenases (MMOs). It is a long-term goal of the research described in this dissertation to learn how to harness the catalytic power of MMOs to address the environmental toxicity of methane.

1.3 Methanotrophic Bacteria

Natural sources of atmospheric CH_4 include: methanogens, termites, lakes, rivers, wildfires, wild animals, geological sources (e.g. gas seepage, hydrates), and wetlands. Amongst all of the different natural sources, wetlands are the largest source of natural CH_4, producing between 177 and 284 million tons of CH_4 a year.[16] Microbes called methanogens, which live in the O_2 depleted zones of wetlands as well as other ecological niches, are the main biological source of CH_4 in wetlands. As CH_4 transitions from the anoxic zone into the oxic zone of wetlands, microbes called methanotrophs metabolize the CH_4 rising from below, preventing a large amount of CH_4 created in wetlands from entering the atmosphere. Most known aerobic methanotrophic bacteria use CH_4 as their sole source of carbon and energy.[20-22] There are three known types of methanotrophs; *Gammaproteobacterial* (Type I) and *Alphaproteobacterial* (Type II), which both belong to the *Proteobacterial* phylum, and methanotrophs that belong to the *Verrucomicrobia* phylum.[23, 24] Regardless of the type of methanotroph, the first step in an aerobic obligate methanotrophs metabolic pathway (**Scheme 1-1**) is the oxidation of CH_4 to methanol (CH_3OH). This remarkable ability of methanotrophs to break the strong 105 kcal/mol C-H bond of CH_4 as well as activate O_2 at ambient temperature and pressure is due to MMOs. Two types of MMOs are expressed in methanotrophs: i.) a copper dependent, membrane-bound form, called particulate methane monooxygenase (pMMO),[25] and ii.) an iron dependent, soluble form, called soluble methane monooxygenase (sMMO). Due to the inherent

technical difficulties associated with studying membrane bound proteins, characterization of the active site of pMMO and its mechanism has been challenging. In contrast, sMMO has proven to be much more approachable and a great deal of chemical, spectroscopic, and structural data have been obtained over the past 4 decades.[5]

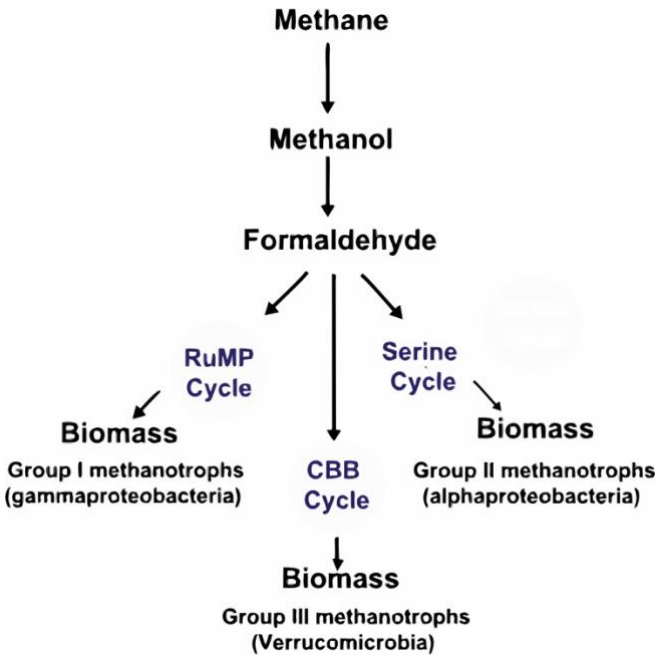

Scheme 1-1 The Different Methanotrophic Metabolic Pathways.
RuMP = Ribulose monophosphate cycle.
CBB = Calvin-Benson-Bassham cycle

1.4 Particulate Methane Monooxygenase (pMMO)

Particulate methane monooxygenase is a 300 kDa copper-dependent integral membrane metalloenzyme. The quaternary structure of pMMO is homotrimeric and each protomer is composed of an alpha (PmoA, 24 kDa), beta (PmoB, 42 kDa), and gamma (PmoC, 22 kDa) subunit (**Figure 1-1**).[26-30] The pmoA and pmoC subunits are predominantly embedded in the lipid bilayer (7 and 5 transmembrane helices respectively), whereas PmoB has two transmembrane helices linked to a large periplasmic domain. Three copper binding sites have been identified in pMMO: i.) the putative bis-His copper binding site is located in the soluble domain of PmoB, ii.) the CuB site is also located in the soluble domain of PmoB is considered to be a mononuclear Cu(II) site

with square pyramidal geometry coordinated by three conserved histidines, and iii.) the CuC site is located in the transmembrane domain of PmoC and contains a mononuclear copper coordinated by two histidines and an aspartic acid.[30-32]

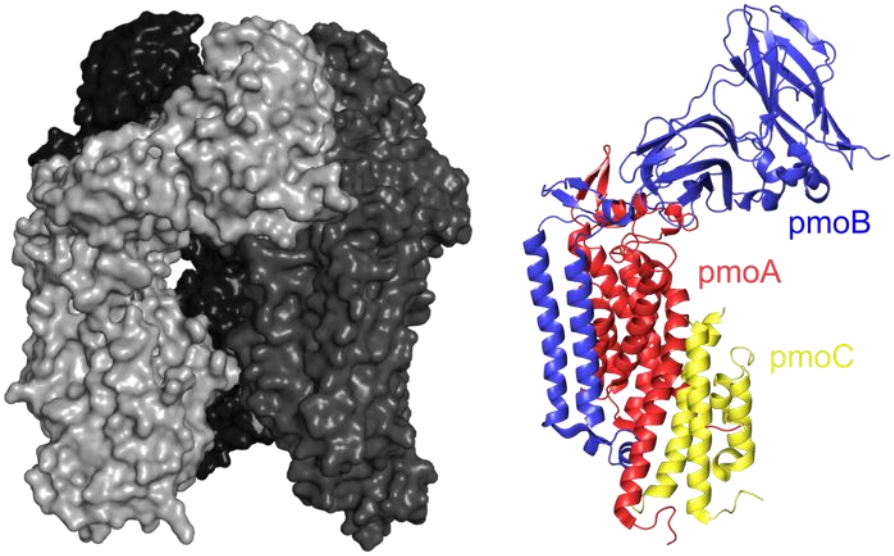

Figure 1-1 Overall structure of particulate methane monooxygenase. The left image is a van der Waals surface representation of homotrimeric pMMO, each protomer is colored a different shade of gray. The right image is a cartoon representation of one pMMO protomer and the subunits are colored red (pmoA), blue (pmoB), and yellow (pmoC). The PDB code: 6CXH was used to make this figure.

Since the first x-ray crystal structure of pMMO was obtained in 2005, a general consensus on which copper binding site catalyzes methane oxidation has not been reached (**Table 1-1**). Recent experimental evidence has been obtained using native top-down mass spectrometry (nTDMS) on nanodisc-reconstituted pMMO to elucidate which copper binding site is the site of CH_4 oxidation.[31] In this study, the effects of exogenous copper ($CuSO_4$) on nanodisc reconstituted pMMO was found to increase methane oxidation activity 6-fold compared to samples having no exogenous copper added. Inductively coupled plasma-mass spectrometry (ICP-MS) of nanodisc reconstituted pMMO provided evidence that the $CuSO_4$ supplemented samples contained two coppers per protomer, compared to non-supplemented samples which contained one copper per protomer. nTDMS was then used to determine which pMMO subunits have copper bound. It was determined that pmoB

and pmoC are the copper binding sites. A correlation between the increased methane activity and occupancy of copper in the pmoC subunit, indicated that the site is important for methane oxidation.

Table 1-1 Particulate Methane Monooxygenase X-ray Crystal Structures

PDB code	Methanotroph	Resolution (Å)	Year
1YW	*Methylococcus capsulatus* (Bath)	2.8	2005
3CHX	*Methylosinus trichosporium* (OB3b)	3.9	2008
3RGB	*Methylococcus capsulatus* (Bath) Reprocessed 2005 data	2.8	2011
3RFR	*Methylocystis* sp. strain M	2.68	2011
4PHZ	*Methylocystis* sp. ATCC49242 Rockwell	2.59	2014
4PI0	*Methylocystis* sp. ATCC49242 Rockwell (soaked in copper)	3.15	2014
4PI2	*Methylocystis* sp. ATCC49242 Rockwell (soaked in zinc)	3.33	2014
6CXH	*Methylomicrobium alcaliphilum* 20Z	2.70	2018

1.5 Soluble Methane Monooxygenase (sMMO)

The studies of soluble methane monooxygenase (sMMO) have been principally focused on enzymes from two bacterial sources over the last four decades, *Methylosinus trichosporium* OB3b (*Mt* OB3b)[15, 33, 34] and *Methylococcus capsulatus* Bath (*Mc* Bath).[14, 35, 36] These bacteria represent two major genera that differ in internal membrane structure and pathway for carbon assimilation, but their sMMOs have proven to be similar in structure and function. As stated above, sMMO is a multicomponent metalloenzyme and requires three proteins for biologically relevant multiple turnover catalysis of CH_4 to CH_3OH at ambient temperature and pressure: i.) a 245 kDa hydroxylase (sMMOH), ii) a 38 kDa electron transfer reductase (MMOR), and iii.) a 15 kDa regulatory protein (MMOB) (**Scheme 1-2**). [33, 35, 37-50]

Scheme 1-2 Soluble Methane Monooxygenase

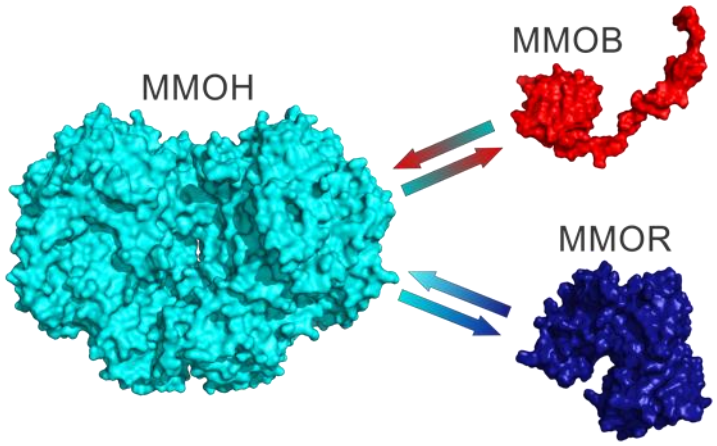

The sMMO gene cluster includes six genes: *mmoX, mmoY, mmoB, mmoZ, mmoD,* and *mmoC*.[51] The *mmoX, mmoY,* and *mmoZ* genes express the protein subunits required for the catalytically active sMMOH. The *mmoB* and *mmoC* genes express MMOB and MMOR, respectfully. The *mmoD* gene expresses a protein of unknown function called MMOD.[52] MMOB and MMOR interact with sMMOH in an intricate way that precisely regulates the transport of substrates (two electrons, molecular oxygen, two protons, and methane) to achieve the desired products (methanol and water).

$$CH_4 + O_2 + 2e^- + 2H^+ \xrightarrow{sMMO} CH_3OH + H_2O$$

1.6 Methane Monooxygenase Hydroxylase (sMMOH)

The overall quaternary structure of the hydroxylase (sMMOH) is homodimeric and each protomer is composed of an alpha, beta, and gamma protein subunit (**Figure 1-2**).[37, 40] A dinuclear iron cluster is present in the active site. The cluster is buried in the alpha subunit and supported by ligands from a 4-helix bundle. In the diferric state, the cluster is coordinated by 4 glutamates, 2 histidines, and 3 hydroxo/aquo ligands (**Figure 1-3**).

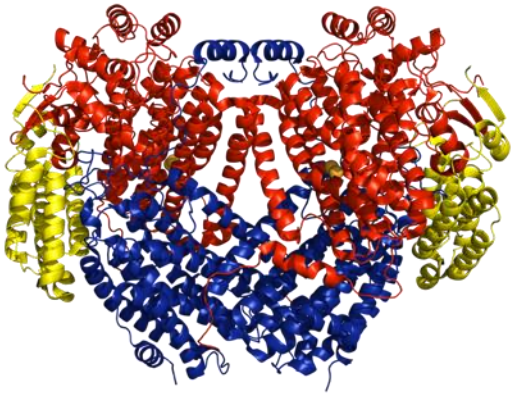

Figure 1-2 The quaternary structure of sMMOH
sMMOH is represented as a cartoon and the alpha subunit is red, the beta subunit is blue, and the gamma subunit is yellow.

Upon the addition of two electrons, either from MMOR or chemical reductants, the diiron cluster is reduced to the diferrous state. Reduction of the diiron cluster causes a rotomeric conformational change in the side chain of active site residue Glutamate 243 (E243) and simultaneous displacement of a hydroxo ligand from the diiron cluster (**Figure 1-3**). In the diferrous state, the nonheme diiron active site has the chemical potential to activate molecular oxygen. Although diferrous sMMOH can react with O_2 alone, the catalytic ability of sMMOH is truly unlocked upon formation of a protein complex with MMOB.

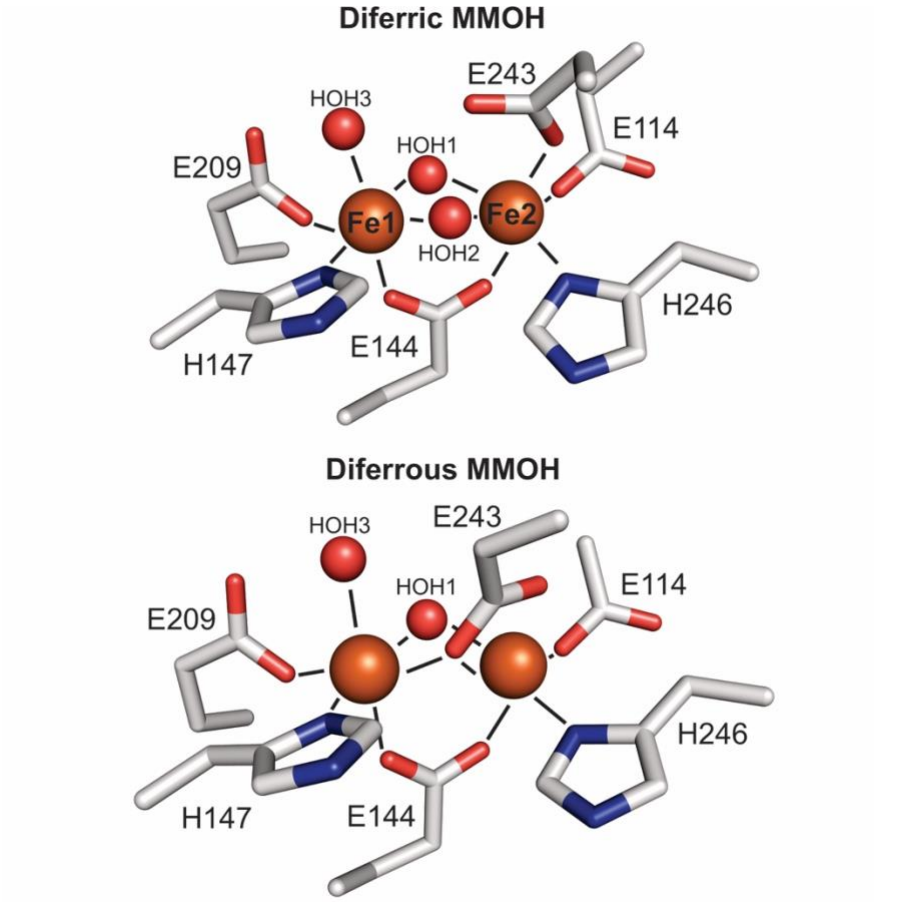

Figure 1-3 Diferric and diferrous sMMOH active site structures.
The top image is of the diferric cluster active site environment and the bottom image is of the diferrous active site environment. Amino acid side chains are represented as sticks where red is oxygen, blue is nitrogen, and white is carbon. The diiron cluster is shown as bright orange spheres and the hydroxo/aquo ligands are represented as red spheres. Black lines represent the bonds from the coordinating ligands. The major difference between the two oxidation states is the rotomeric conformation of E243 and the displacement of HOH2 from the active site. PDB codes 1MHY and 1FYZ were used to make this figure.

1.7 Proposed Substrate Transport Routes to the Active Site

In the initial crystal structures of sMMOH, the diiron cluster appeared to be completely inaccessible to substrates.[37, 40] However, subsequent studies and comparison with other members of the large bacterial multicomponent monooxygenase (BMM) family have revealed potential access routes. One route is via a conserved BMM structural feature known as the pore region (**Figure 1-4**).[53-55] The 12 Å long pore in sMMOH extends from the active site pocket directly to the protein surface through two of the α-helices housing the diiron cluster and is the shortest path from bulk solvent to the active site. The sMMOH pore region, like those of BMM family counter parts; phenylalanine hydroxylase (PHH), toluene/o-xylene monooxygenase (ToMO), and toluene 4 monooxygenase (T4MO), is lined with conserved threonine (sMMOH T213), asparagine (sMMOH N214), and glutamate/glutamine (sMMOH E240) residues. In diferric sMMOH, E240 and N214 side chains are solvent exposed, whereas T213 side chain faces the active site. On the basis of mutagenesis studies of ToMO and structural comparisons in T4MO, it has been proposed that one role for the pore residues is to mediate the transfer of protons from bulk solvent to the diiron center.

A second type of potential access route in the hydroxylase components of many BMM enzymes is a series of three cavities that trace a long 35–40 Å path from the active site to bulk solvent. In sMMOH, the three cavities are located in the α-subunit, and cavity 1 contains the diiron cluster and active site (**Figure 1-4**).[37, 39, 53-56] It differs from the other BMM enzymes in that the path between cavities 1 and 2 is blocked by residue phenylalanine 188 (F188). The sMMOH cavities were characterized by soaking oxidized sMMOH crystals with very high concentrations of various halogenated substrate and product analogs and by xenon pressurization experiments. [43, 50] Under these conditions, the product analogs were found bound in all three cavities, whereas Xe atoms and substrate analogs were found bound to cavities 2 and 3. Accordingly, the cavities were proposed to serve the dual functions of substrate ingress (CH_4 and O_2) and product egress.

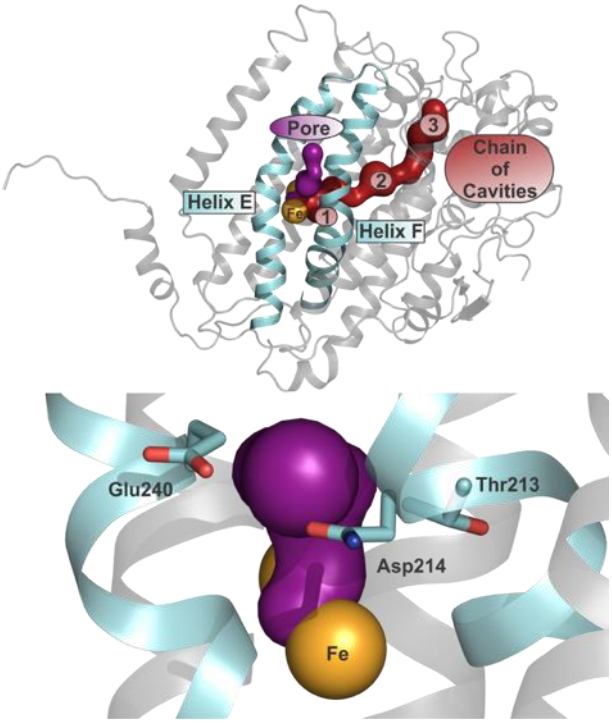

Figure 1-4 Proposed substrate access route in the sMMOH alpha subunit. In both the top and bottom a cartoon representation of the sMMOH alpha subunit (cyan and gray) is shown. The diiron cluster is represented as orange spheres, the pore is colored purple and, the chain of cavities is colored red. The bottom image is a zoomed in view of the pore region and pore residues (Thr213, Asp214, and Glu240) are shown as sticks; carbon is cyan, oxygen is red, and nitrogen is blue.

1.8 Methane Monooxygenase Reductase (MMOR)

The reductase (MMOR) is a 38 kDa protein that contains two cofactors, a flavin adenine dinucleotide (FAD) molecule in the N-terminal domain and a [2Fe-2S] cluster in the C-terminal domain.[57-60] In the resting state, each of the irons in the [2Fe-2S] cluster is ferric, and they are antiferromagnetically coupled.[61] The first step in the electron transfer process is the binding of NADH to MMOR (K_d = 3.8 µM) followed by the transfer of two electrons in the form of a hydride ion to FAD.[57, 62] Redox potentials for transfer of electrons out of the FAD are; E_1°'= -176 ± 7 mV and E_2°'= -266 ± 15 mV.[62] One electron from reduced FAD is transferred to the diferric [2Fe-2S] cluster, which has a redox potential of -209 ± 14 mV, at a rate of 130 ± 17 s^{-1}.[62] At this point of the

electron transfer process, if MMOR is bound to sMMOH, then two electrons total will transfer one at a time from the [2Fe-2S] cluster to the sMMOH diferric cluster. The FAD semiquinone transfers the second electron to the [2Fe-2S] cluster as an intermediate step. Neither an X-ray crystal or cryo-EM structure of the sMMOH:MMOR complex has been obtained to date, but chemical crosslinking, NMR, hydrogen−deuterium exchange coupled to mass spectrometry (HDX-MS), and molecular docking studies have provided some details about the interaction. Chemical cross-linking studies using full-length MMOR determined that the reductase binds to the beta subunit of sMMOH.[63] NMR studies using a truncated form of *Mc* Bath MMOR containing the [2Fe-2S] cluster (MMOR-Fd, Residues 99-348), provided information about MMOR residues involved in the molecular interactions of the sMMOH:MMOR complex.[59] Additionally, hydrogen−deuterium exchange coupled to mass spectrometry (HDX-MS) and molecular docking studies of MMOR-Fd provided evidence that the [2Fe-2S] domain of MMOR binds to the alpha subunit of sMMOH.[64]

1.9 Methane Monooxygenase Regulatory Protein (MMOB)

Nuclear magnetic resonance (NMR) solution structures of heterologously expressed MMOB using protein sequences of two different types of methanotrophs, *Mt* OB3b and *Mc* Bath have been obtained.[44, 45] Both NMR structures show that the 15 kDa regulatory protein has a dynamic N-terminal tail, a folded core region, and a dynamic C-terminal tail in solution (**Figure 1-5**). Additional NMR studies aimed at characterizing the *Mt* OB3b sMMOH:MMOB protein complex provided details about which MMOB amino acids are involved in the electrostatic interactions stabilizing the sMMOH:MMOB complex.[46] MMOB variants were created to determine if changes to the amino acids identified by NMR had a regulatory role in sMMO catalysis.[46, 65-67] Kinetic studies showed that mutations in both the core region and N-terminal tail of MMOB effect the formation and decay rate constants of various sMMO chemical intermediates. A 2.9 Å X-ray crystal structure of the *Mc* Bath sMMOH:MMOB complex showed that both the core region and N-terminal tail of MMOB form polar contacts with sMMOH. As noted above, the N-terminal tail is dynamic in solution, yet in the X-ray crystal structure of the *Mc* Bath sMMOH:MMOB complex

the tail adopts a ring-like structure on the surface of sMMOH. Additionally, sections of the N-terminal tail transform from having a loop secondary structure to a helical secondary structure.

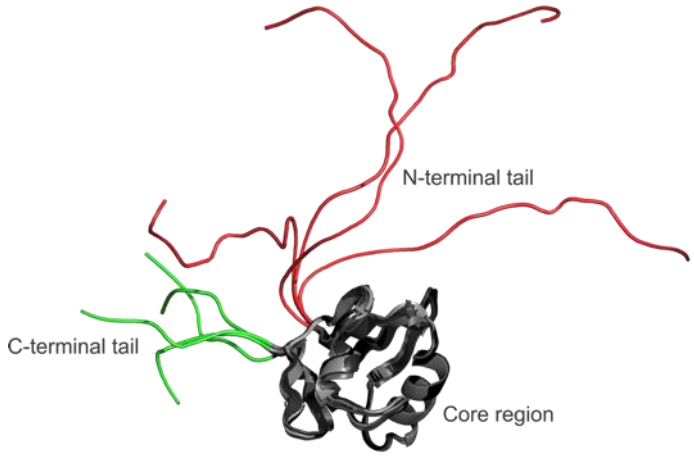

Figure 1-5 Nuclear magnetic resonance solution structure of MMOB. Four of the fourteen ensemble structures of *Mc* Bath MMOB (PDB: 1CKV) are shown superimposed on one another. The N-terminal tail is colored red, the C-terminal tail is colored green, and the core region is colored gray. The N- and C-terminal tails are more dynamic in solution compared to the core region.

1.10 Conformational Changes in sMMOH when MMOB is Bound

While sMMOH is capable of oxidizing methane slowly in isolation,[33] the catalytic ability of sMMOH is truly unlocked upon formation of a protein complex with MMOB. Kinetic studies have shown that the turnover number increases by 150 fold, the rate constant for reaction with O_2 increases 1000-fold, and the product yield doubles.[33, 68, 69] The 2.9 Å crystal structure of the protein complex of sMMOH with MMOB has provided many insights into how MMOB regulates the catalytic cycle.[70] Many structural changes in the α-subunit of sMMOH occur, including large-scale movement of secondary structures and rotation of amino acid side chains. Fifteen out of nineteen α-helices and eight out of twenty-four loop regions undergo conformational changes while the beta and gamma subunits remain rigid. The diiron coordinating ligands shift and rotate, but the distance between the irons and the coordinating ligands is conserved. One exception is E243 where the side-chain carboxylate rotates to coordinate with one iron in a bidentate manner and bridges to bind in

a monodentate manner to the other iron. The latter change also occurs in sMMOH alone upon reduction (**Figure 1-3**),[38, 39] so the observation in the complex may be due to reduction of sMMOH in the synchrotron beam rather than a direct effect of MMOB binding. The carboxylate shift is important because it is accompanied by the dissociation of one or both solvent bridges between the irons, creating a binding site for O_2 between the irons.

1.11 Overview of Catalytic Cycle

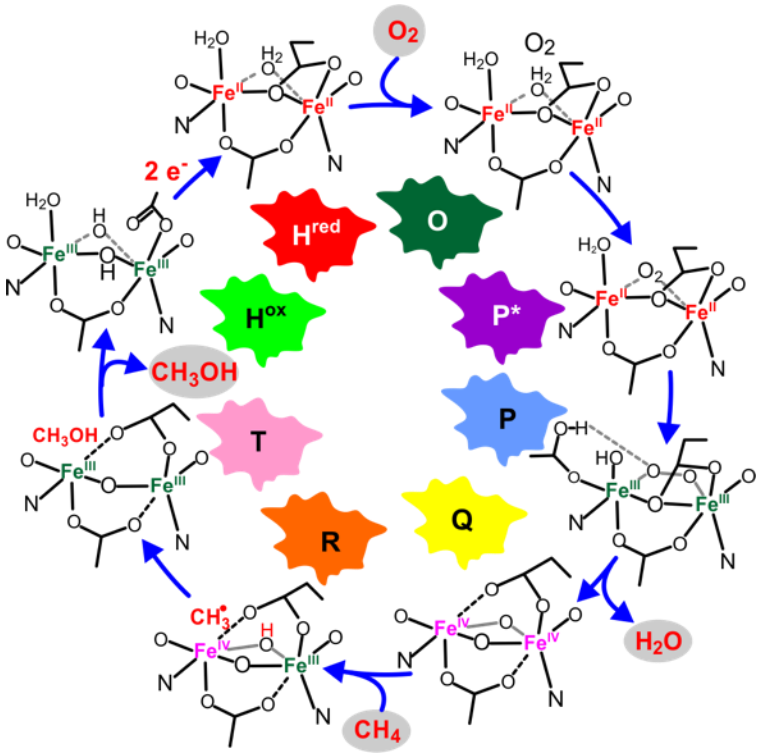

Figure 1-6 Single turnover catalytic cycle of soluble methane monooxygenase. Only the diiron cluster of sMMOH is illustrated. MMOB must be present in equal concentration to the diiron cluster to detect the intermediates in full yield. All of the lettered intermediates except R have been directly detected. Abbreviations: MMOB, regulatory component of sMMO; sMMOH, hydroxylase component of sMMO; sMMO, soluble methane monooxygenase. H^{red}, H^{ox}, P, P*, Q, R, and T are intermediates of the sMMO reaction cycle in which the sMMOH diiron clusters are proposed to have the structures indicated in the figure.

The single turnover catalytic cycle of sMMO illustrated in **Figure 1-6** has been studied in detail for the case in which MMOB and sMMOH are present and reduction of the diferric sMMOH diiron

cluster (**H^{ox}**) is carried out using chemical reductants rather than MMOR and NADH.[14, 68, 71-76] The resulting MMOH^{red}:MMOB complex reacts rapidly with O_2 to form intermediate **O**.[69] The diiron clusters of **H^{red}** and **O** exhibit identical optical and EPR spectra. The EPR spectra are characterized by a signal at g = 16 arising from ferromagnetic coupling of the two high spin S = 2 irons to yield an S = 4 species. [33, 77] This unique signal proved useful in tracking the kinetics of intermediate **O** conversion through the application of rapid freeze quench (RFQ) techniques.[68, 72] The occurrence of **O** was established by the finding that the formation rate constants for all subsequent intermediates in the catalytic cycle are independent of O_2 concentration,[69] thereby requiring the irreversible formation of an intermediate between **H^{red}** and the downstream intermediates. The lack of spectroscopic change suggests that **O** has O_2 bound in the active site but not to the diiron cluster. In general, the binding and activation of O_2 by the iron atoms occurs through a metal-to-ligand transfer of electrons. Two chromophorically and electronically distinct intermediates (**P*** and **P**) have been characterized in this process that culminates in the cleavage of the O-O bond to generate the reactive intermediate termed **Q**.[68, 73, 75, 76] **Q** can react directly with methane to insert an oxygen atom into one of the C-H bonds. Our proposal for the mechanism envisioned a hydrogen atom abstraction reaction to yield a cluster-bound hydroxyl radical and a methyl radical species termed **R**.[68, 78-80] Subsequent recombination of the radicals would yield the bound methanol product complex **T**.[68] Finally, release of methanol from **T** would reform **H^{ox}** in the rate-limiting step of the overall reaction [68]. It is interesting to note that in the absence of MMOB, the reaction with O_2 to form either **O** or **P*** becomes the rate-limiting step.[69] Thus, the dramatic influence of MMOB on the progress of the reaction was immediately clear from early experiments.

It is important to mention at this point that, unlike most enzyme systems, the rate constants for the steps in the sMMO catalytic cycle decrease as the cycle progresses such that **Q** decays over several seconds in the absence of methane.[68] This favorable kinetic scenario enabled the RFQ trapping of the intermediates as they occurred in the single turnover cycle for detailed spectroscopic characterization. Also, even though methane is the only metabolically relevant substrate for sMMO,

the enzyme is promiscuous in nature and will oxidize a large range of alternative non-polar aliphatic and aromatic compounds.[15, 35, 74] This catalytic versatility allowed many types of studies to probe the mechanism. The following sections describe the current understanding of the nature of the key reaction cycle intermediates.

1.12 Intermediate P*

Intermediates **O** and **P*** have similar broad, weak absorption spectra in the visible region, with that of **P*** being very slightly more intense between 325 and 700 nm.[76] The discovery of **P*** was based on two indirect observations: (i) The rate constant for **O** decay monitored at 350 nm or via the decay of its g = 16 EPR spectrum[68] is significantly faster than the formation rate constant for intermediate **P** followed at 700 nm, and (ii) The rate constant for **O** decay is pH independent while that for **P** formation is strongly pH dependent.[73, 76] The direct spectroscopic characterization of intermediate **P*** was facilitated by the use of the MMOB mutant H33A (see below) that enhanced the yield of **P*** by decreasing its decay rate constant while leaving its formation rate constant unaffected.[71] The observed loss of the g = 16 EPR signal during **P*** formation led to the assumption that **P*** would have one or both irons in the ferric state.[73, 75] However, RFQ EPR and Mössbauer studies of **P*** showed that it is a diferrous species that does not possess the g = 16 signal.[76] We proposed that subtle electronic changes in **P*** as O_2 begins the metal binding process cause the loss of the g = 16 signal without net oxidation of the diiron cluster. An intermediate between **O** and **P** is also observed in the *Mc* Bath sMMOH catalytic cycle,[75] but it appears to be a diferric peroxo species similar to **P**.

1.13 Intermediate P

Intermediate **P** ($\mathbf{H_{peroxo}}$ in *Mc* Bath sMMOH) has a broad electronic absorption spectrum with a band at 700 nm (ε_{700} = 2500 M^{-1} cm^{-1}) that is characteristic of a peroxo species.[73, 75, 76] The Mössbauer spectrum of **P** (δ = 0.66 mm/s, ΔE_Q = 1.53 mm/s) indicates that the iron atoms are present in the ferric oxidation state. Thus, **P** is designated as a diiron (III)-peroxo species. In the

absence of a resonance Raman characterization of **P**, the binding mode of the peroxo moiety is an open question. However, a comparison with vibrationally characterized peroxo intermediates in related diiron systems and synthetic model compounds possessing similar spectroscopic features suggests either a *cis*- or *trans*-μ-1,2 binding mode.[14, 81] A comparison of the Mössbauer isomer shift with those of protonated and deprotonated peroxo intermediates in synthetic model compounds of mononuclear Fe^{III}-peroxo complexes suggests that a deprotonated peroxo ligand is present in **P**.[76] However, no model complexes for protonated diiron complexes have yet been synthesized. There is no observed reaction of **P** with hydrocarbon substrates,[68] although reaction with easily oxidized substrates has been described.[82, 83]

The rate constants for both formation and decay of **P** were found to increase with a decrease in pH from 8.5 to 6.5.[73, 75] Proton inventory studies in which H_2O is progressively replaced with D_2O in the buffer showed that a single proton is involved in each step in a "one-hop" process from a donor group with a fractionation factor near 1 and a pK_a value of 7.6.[73] A water molecule bound to one of the iron atoms, as seen consistently in crystal structures, is believed to be the most likely source of the proton.[73] If the peroxo-bridge in **P** is unprotonated, it is possible that the proton transfer is to the carboxylate function of one of the Glu ligands to the diiron cluster. Such a transfer is supported by studies with synthetic diiron model compound mimics of **P**.[84]

1.14 Intermediates Q and T

The rate constant for formation of **Q** is independent of substrate concentration, but the decay rate constant exhibits a linear dependence for most substrates.[68] In contrast to the preceding intermediates in the reaction cycle, **Q** possesses an intense electronic absorption spectrum with bands at 330 and 430 nm (ε_{330} = 9800 M^{-1} cm^{-1}, ε_{430} = 7500 M^{-1} cm^{-1}) (**Figure 1-7**A).[68, 85] The Mössbauer spectrum of **Q** in *Mt* OB3b sMMOH indicates the presence of two anti-ferromagnetically coupled high-spin Fe^{IV} atoms in similar electronic environments (δ = 0.17 mm/s, ΔE_Q = 0.53 mm/s) (**Figure 1-7**B).[86] To date, this is the only characterized biological example of a

dinuclear Fe^{IV} cluster. The irons in *Mc* Bath sMMO **Q** are also both Fe^{IV}, but Mössbauer shows they reside in slightly dissimilar electronic environments.[72, 87]

The time-resolved resonance Raman spectrum of **Q** (**Figure 1-7**C) exhibits an Fe-O vibrational mode at 690 cm^{-1} when generated with $^{16}O_2$ that downshifts to 654 cm^{-1} when made with $^{18}O_2$.[85] Upon the formation of **Q** with the mixed-label O_2 isotope $^{16}O^{18}O$, an intermediate vibrational mode is observed at 673 cm^{-1}. Based upon a comparison with the vibrational spectra of model complexes, the frequencies and isotopic shifts for **Q** match those of the tetra-atomic vibration of a Fe_2-(μ-O)$_2$ 'diamond core' structure (illustrated in **Figure 1-7**).[88] The $^{16}O^{18}O$ labeling pattern also indicates that both oxygen atoms from O_2 are retained in the diamond core upon conversion from intermediate **P** to **Q**, an observation that lends support to a homolytic cleavage model of the O-O bond. Upon reaction of **Q** with methane, one of the oxygen atoms is transferred to the methanol product.[89] A new vibrational mode at 556 cm^{-1} that down shifts to 533 cm^{-1} for samples prepared with $^{18}O_2$ was observed,[85] showing that the second atom of oxygen from O_2 is retained in the mono-μ-oxo bridged diferric cluster of the product complex **T**.

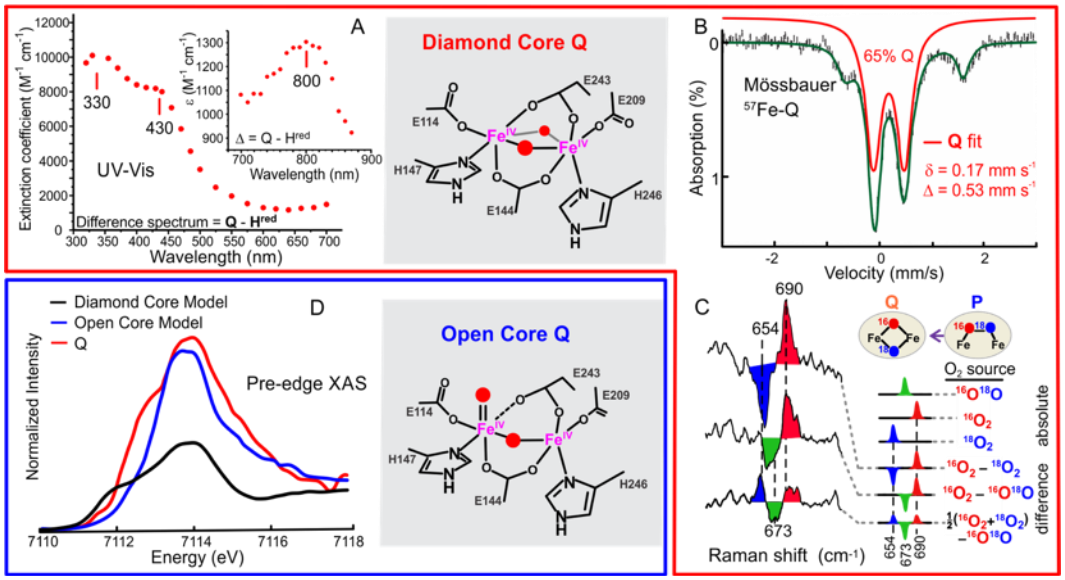

Figure 1-7 Experimental evidence favoring a diamond core Q over an open core Q. (a) UV-Vis features at 330, 430, and 800 nm with high-extinction coefficients characteristic of diamond core model complexes; (b) a single Mössbauer quadrupole double showing that the irons are in similar environments, which is inconsistent with the single Fe^{IV} = O of the open core structure; and (c) a resonance Raman feature at 690 cm^{-1} with the isotopic shifts characteristic of diamond core tetra-atomic vibration. Experimental evidence favoring an open core **Q** includes *(d)* pre-edge XAS intensity and EXAFS spectra similar to those of an open core model.

An early Mössbauer and EXAFS investigation of **Q** provided the first indication that it might have a diamond core structure. The two Fe^{IV} atoms were found to be 2.46 Å apart and each iron was found to have Fe-O bonds of 1.77 Å and 2.05 Å that could not be assigned to protein ligands.[90] The Fe-O bonds are too long to be assigned as an Fe^{IV}=O moiety based on model compounds.[91] The most reasonable structure to account for these characteristics is the diamond core. In the last two decades since the EXAFS study of **Q**, a large range of synthetic model compound mimics of **Q** have been generated.[81] Improvements to the XAS technique, such as Fe Kα high-energy-resolution fluorescence-detected XAS (HERFD XAS) have also enhanced the resolution of the pre-edge XAS features. A recent study employed both of these advances along with time-dependent density functional theory calculations to study the pre-edge XAS spectrum of **Q** (**Figure 1-7**).[92] The pre-edge intensity of **Q** was observed to be three times higher than those of

a diamond core model complex, but comparable to that of an open-core model complex containing a terminal Fe^{IV}=O and a mono-μ-oxo bridging moiety (illustrated in **Figure 1-7**).

The open core model for **Q** finds support from the observation that open-core and diamond core model compounds with the same ligand environment exhibit vastly different oxidizing reactivity.[93] The open-core species with a terminal oxo moiety was found to be 1000 times more reactive than the diamond core model (after spin state compensation). It is important to add a caveat that a diamond core model complex with high-spin iron (S = 2) atoms like those of **Q** has not yet been generated.[81] Nonetheless, both the XAS and model studies suggest a role for a terminal Fe^{IV}=O moiety in the reaction with methane. One possibility is that **Q** may exist in an equilibrium between open-core and diamond core structures in which the more potent open-core structure can react with methane.

1.15 Chemical Mechanism of sMMO

The remarkable ability of sMMO to catalyze one of the most difficult oxidation reactions in organic chemistry at room temperature and halt after a single oxygen transfer has encouraged many experimental and computational attempts to understand the mechanism. The computational studies have all been based on the same X-ray crystal structures of $\mathbf{H^{ox}}$ and $\mathbf{H^{red}}$ but differences in the size of the adopted active site model and the specific method employed (e.g. choice of density function theory (DFT) functional, QM/MM approaches) have resulted in significantly different proposed mechanisms. Generally, the mechanisms for the C-H bond breaking and oxygen insertion reactions fall into the traditional concerted or non-concerted classes.[94-99] The experimental results are readily accounted for by the non-concerted models. However, it has been shown that the concerted mechanisms can also account for the experimental observations under special conditions (e.g. formation of an Fe-C bond that causes distortion of the tetrahedral symmetry of the substrate carbon,[100, 101] asynchrony of vibrational modes in the bond breaking and bond forming reactions in the transition state,[102] or coordinated electrophilic and nucleophilic attack by two Fe^{IV}=O moieties

leading to the formation of a pentavalent carbon species).[103] It is unclear whether these special conditions are possible in a biological system. The most recent computations have utilized a large model and employed molecular mechanic methods to assess the role of the protein beyond the first sphere of the metals.[104] These models favor a hydrogen atom abstraction reaction.

1.16 Key Insights into Mechanism from Chiral Substrate Reactions

The chemical mechanism of cytochrome P450 oxygenase was proposed by our group and others as a model for sMMO catalysis.[33, 35, 105] This mechanism involves abstraction of a hydrogen atom from the substrate by the heme Fe^{IV}=O π cation radical reactive species to give a substrate radical and heme Fe^{IV}-OH.[106, 107] Rebound of the hydroxyl radical to the substrate radical completes the hydroxylation reaction. The **Q** intermediate of sMMO is electronically equivalent to the heme Fe^{IV}=O π cation radical and might be expected to carry out similar chemistry. The direct detection of a transient substrate radical intermediate is almost impossible considering the ultrashort lifetimes expected for such species when the reactive hydroxyl radical associated with the diiron cluster is nearby in the active site. One type of indirect detection employed the use of chiral hydrocarbon substrates (**Figure 1-8**A). The *Mt* OB3b sMMO catalyzed oxidation of chiral, carrier free (*R*) and (*S*) 1-[$^2H_1$,$^3H_1$] ethane to ethanol proceeded with 34% inversion of stereochemistry.[78] Likewise, the chiral ethane and chiral butane hydroxylation reactions with *Mc* Bath sMMO displayed a 28% and 23% inversion of stereochemistry, respectively.[108] These results are consistent with formation of a radical or cation intermediate, but the lack of complete racemization suggests a very short lifetime on the order of a C-C bond rotation ($k = 10^{12}$ to 10^{13} s^{-1}). This rate constant is too fast for a physical motion of the hydroxyl group as it rebounds onto the substrate radical, indicating that hydroxylation in sMMO is subtly different from a classical two-step radical mechanism attributed to P450. A computational model assuming a "caged" structure that locks the radical species in close proximity provides a reasonable explanation for these observations.[104, 109, 110]

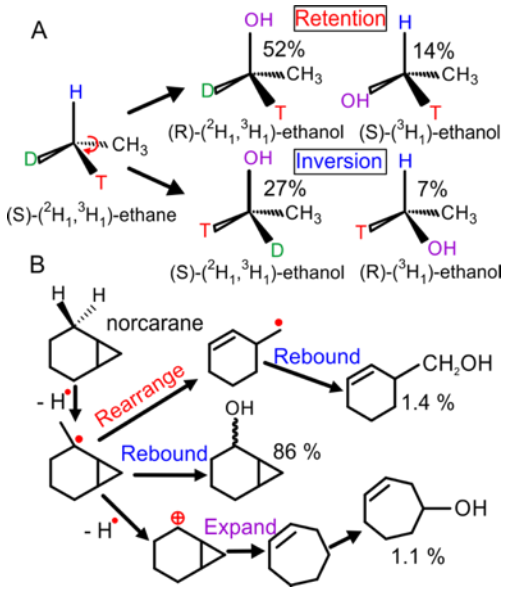

Figure 1-8 Examples of experimental evidence for radical or cation intermediates. *(a)* Chiral ethane is converted to chiral ethanol with 34% inversion of stereochemistry by soluble methane monooxygenase (sMMO), implying an intermediate with a lifetime <1 ps. *(b)* Products from the norcarane reaction with sMMO show primarily radical (lifetime <20 ps) but also cation intermediates.

1.17 Radical Clock Reactions

A large variety of radical clock compounds have been used as sMMO substrates to assess the presence of transient radical intermediates (one example in **Figure 1-8**B).[79, 80, 111-113] In summary, rearranged products derived from both radical and cation substrate intermediates have been observed for several radical clock compounds. However, the lack of correlation between rearranged product yield and rearrangement rates for the radical clocks suggests that steric factors in the active site alter how radical clock substrates are presented to **Q**. The role of steric factors in the oxidation reaction agrees with earlier experiments probing the stereochemistry of isopentane oxidation, where it was observed that the least sterically hindered carbon atom of isopentane was preferentially hydroxylated despite its stronger C-H bonds.[114] While radical clock sMMO substrates can only be used qualitatively, they do indicate in all cases that the radical lifetimes are very short ($k_{rebound} > 10^{10}$ s^{-1}), consistent with the results of the chiral substrate experiments.

1.18 Isotope Effect Studies

The chromophore of **Q** allows the reaction with substrates to be directly observed. We are aware of no other case in which the specific oxygen transfer step can be studied independently of other steps in the reaction cycle. One application of this experimental advantage was the direct determination of the intermolecular deuterium kinetic isotope effect (KIE) on the rate constant of the **Q** reaction with methane (**Figure 1-9**). The KIE value of 50 for this reaction is one of the largest for any biological system.[66, 89, 115] A KIE value of this order unequivocally indicates the C-H bond-breaking step is the primary determinant in the reaction coordinate of methane oxidation by **Q**. Remarkably, hydrocarbon substrates with a molecular size larger than methane failed to display a KIE.[66] As in the case of the chiral substrate and radical clock experiments, the observation of a large KIE is clearly supportive of a non-concerted mechanism.

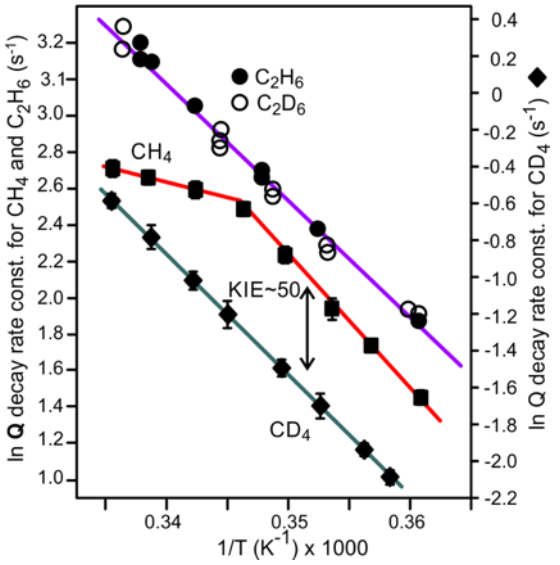

Figure 1-9 Arrhenius plots for intermediate Q reaction with substrates.
The large KIE for methane reaction with **Q** and the lack of a KIE for the reaction with ethane are illustrated. Only the Arrhenius plot for the methane reaction exhibits a break due to a change in the rate-limiting step in the accessible temperature range. Substrate concentration = 400 μM

1.19 Quantum Tunneling in the sMMO Reaction

The much larger than classical limiting value (< 7) for the primary intermolecular deuterium KIE for methane reaction with **Q** suggests the presence of a hydrogen atom tunneling contribution in the C-H bond breaking reaction of methane by **Q.** A definitive proof of hydrogen tunneling requires kinetic studies over a much larger temperature range than is possible with sMMO.[116] However, a plot of ln KIE versus 1/T in the temperature range where C-H bond breaking is rate-limiting shows a positive slope of 3.4, which is larger than an expected value of 1.25 based upon a difference in the zero point bond-dissociation energy for the isotopes.[67] This value is similar to those obtained from other enzymes demonstrated to exhibit tunneling,[117] supporting a role for tunneling in the reaction of **Q** with methane.[118]

1.20 Regulation of sMMO

Oxygenases in general, and sMMO in particular, must employ mechanisms to ensure that the powerful reactive species they generate react with substrates with high specificity. A second regulatory consideration for monooxygenases is the requirement to couple reducing equivalents

utilized to initiate O_2 activation with substrate oxygenation. The most common form of regulation in oxygenases involves the initiation of the catalytic cycle solely in the presence of substrate, but many other strategies have been described.[119-126] Regulation in sMMO plays out at many different stages during the catalytic cycle. However, it does not appear that regulation by substrate triggering of oxygen activation is utilized, because none of the rate constants through **Q** formation are affected by the presence of hydrocarbon substrates.[68] sMMO must be capable of overcoming two major regulatory hurdles. First, all of the alternative substrates of sMMO are easier to oxidize than methane but metabolically useless to a methanotroph, so a mechanism to favor methane oxidation must be present. Second, the enzyme must have a mechanism to prevent MMOR from reducing **Q** before it can react with methane. The effector protein MMOB appears to play a pivotal role in overcoming these hurdles.

1.21 Role of MMOB in Controlling O_2 Binding to the Diiron Cluster

MMOB greatly accelerates the first steps of the reaction cycle leading ultimately to **Q** formation. Some insight into the mechanism by which this change occurs has been provided by CD, MCD and VTVH MCD spectroscopies and ligand field (LF) and DFT calculations.[127, 128] These studies showed that the binding of MMOB caused two types of structural changes in $\mathbf{H^{red}}$. CD indicated that there is a global change in the diiron cluster environment, while MCD and VTVH MCD showed that there is also a local change at one of the irons. In contrast, MMOB variants that did not accelerate the O_2 binding steps caused only the MCD and VTVH MCD changes, showing that global change in sMMOH structure detected by CD is also required for full activity. The possible significance of this global structural change is discussed in section 1.22.

1.22 Role of MMOB in Gating Methane Substrate into sMMOH

The unexpected linear change in the rate constant of **Q** decay with substrate concentration has at least two reasonable explanations.[68, 115] Either the reaction is truly second order in which collision of activated sMMOH with the substrate results in immediate oxygen transfer, or the collision results

in slow complex formation followed by very rapid reaction with **Q**. Experimental evidence has been collected favoring the second option. One approach was to determine the rate constant of **Q** decay as a function of temperature. Typically, the Arrhenius plots from such an experiment are linear, and this is what is observed for fully deuterated methane and all substrates other than methane (**Figure 1-9**). In contrast, the use of methane as the substrate causes the plot to display a discrete breakpoint.[74] It was proposed that the non-linear Arrhenius plots indicated the presence of two chemical steps in the decay of **Q** with methane, nominally substrate binding followed by reaction with **Q**. If the activation parameters for these two steps are different, then the rate-limiting step might change in the temperature range of the experiment. Fully deuterated methane has a much slower reaction with **Q**,[89] so its reaction might be rate-limiting throughout the observable temperature range. On the other hand, if substrates larger than methane bind slowly, binding might be rate-limiting at all accessible temperatures. In support of this scenario, the absence of a substrate KIE in the **Q** decay reaction with ethane and other larger substrates indicated that the substrate-binding step is rate-limiting for all substrates larger in size than methane. The combination of size-restricted binding and very fast reaction with **Q** due to weaker C-H bonds means that the observed rate constants for all substrates other than methane do not reflect the BDE of the bond. Thus, the comparatively fast rate constant for methane reaction is reflective of its size rather than its stability. We termed this the "molecular sieve" effect of sMMOH to suggest that something in its structure is size selective for molecules the size of methane.[71]

The molecular sieve effect was investigated further using MMOB variants. The interface between MMOB and sMMOH was first identified by cross-linking and spectroscopic studies [44-46, 63, 129-132] and then confirmed by the X-ray crystal structure of the sMMOH:MMOB complex.[70] The biophysical studies allowed the selection of four key MMOB residues in the center of the interface. These residues were changed to smaller residues in MMOB from *Mt* OB3b to form the 'Quad' variant (N107G/S109A/S110A/T111A). Analysis of the reaction cycle kinetics in the presence of this variant showed the following perturbations: (i) a substantial increase in the rate constant of

reaction of **Q** with large substrates like nitrobenzene and furan, (ii) faster release of products from large substrates from the active site, and (iii) a decrease in the rate constant of **Q** reaction with methane (**Figure 1-10**A).[65, 71] The enhancement in the decay rate constant of **Q** and accelerated product release observed for large substrates was interpreted to suggest that the smaller residues in the sMMOH:MMOB interface effectively increase the pore size of the molecular sieve. Another method to validate the molecular sieve hypothesis was to show that increasing access to larger substrates using the Quad variant would make C-H bond cleavage rate limiting and allow a KIE to be detected. Accordingly, a KIE of 2.0 was observed for ethane.[66] The location of the putative molecular sieve pore is unknown. However, the well characterized sMMOH pore region immediately over the active site where the Quad variant binds would be a possible candidate. In the studies described in this thesis, we show that there is a better candidate for the molecular sieve.

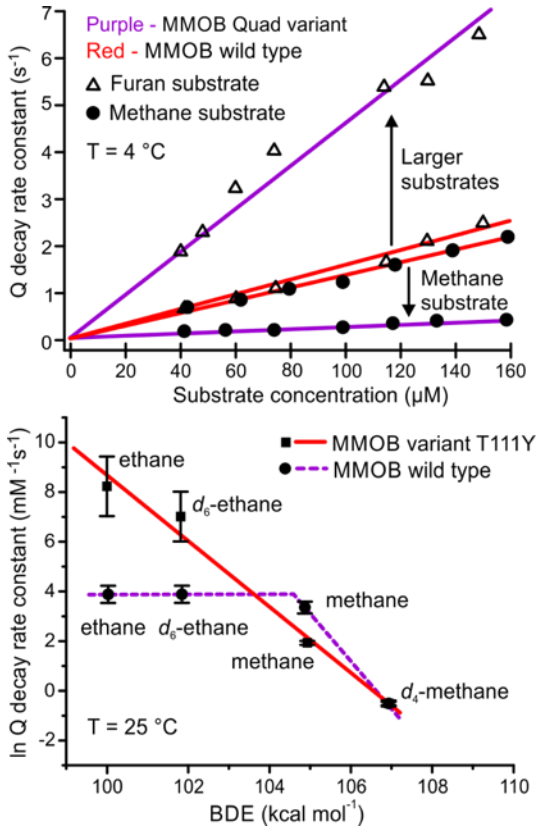

Figure 1-10 Regulatory effects of MMOB revealed by variants.
(a) Linear substrate concentration dependence of the **Q** decay rate constant. The quad variant of *Mt* OB3b MMOB increases the second-order rate constant for larger substrates by opening the molecular sieve and decreases that for the methane reaction owing to loss of tunneling. *(b)* The T111Y variant of *Mt* OB3b appears to open the active site, removing the molecular sieve effect and tunneling. Accordingly, the rate constants for methane and ethane reaction with **Q** reflect the C-H BDE of the molecules.

A competing proposal for a route of methane (and perhaps O_2) entry into the sMMOH active site invokes the series of interconnected hydrophobic cavities in sMMOH described above (**Figure 1-4**).[133] In support of this proposal, mutagenesis and kinetic studies with the related ToMO enzyme suggested that O_2 enters the active site using an analogous route.[134] However, the series of cavities in sMMOH is 35 – 40 Å long and would likely fill with methane as it does with halogenated alkanes and xenon in the crystallographic experiments that were used to demonstrate its existence. If this is the case, methane would be delivered to **Q** from a bound state in the channel rather than from solution, so the rate constant for the reaction would not appear to be linear with methane

concentration. The reaction would also not be likely to become rate-limited by methane binding at low temperature as seen in the Arrhenius plots.

The linear substrate concentration dependence suggests that no matter how substrate binding is regulated, a structural change must occur as **Q** is formed to permit substrate entry from bulk solvent. In this context, the observation that the pore is closed in the oxidized (and likely reduced) sMMOH:MMOB complex is in accord with the kinetic data. The competing models for regulation of substrate binding could, in principle, be tested by making sMMOH variants. Unfortunately, heterologous expression of sMMOH has not been successful despite the sustained efforts of many research groups. Promising approaches using homologous expression have been reported.[135-137]

1.23 Role of MMOB in Regulating Quantum Tunneling in Methane Oxidation

Quantum tunneling plays a major role in methane but possibly not ethane oxygenation, as evidenced by the ethane KIE in the classical range even when the molecular sieve is opened using the Quad variant. Importantly, the KIE for methane is decreased from the tunneling range of 50 to the classical range of 6 when this variant is used, suggesting that tunneling has been compromised. Thus, the conformational changes caused by MMOB in the sMMOH:MMOB complex not only open the active site for methane, but they also direct the approach of methane to the diiron cluster to optimize orbital overlap required for tunneling.[138] The same precise sMMOH active site structural changes apparently do not occur when the sMMOH:MMOB interface is perturbed by the use of MMOB variants as indicated by the lack of CD spectral change noted above. When wild type MMOB is used, ethane is not granted easy access and once in the active site, its oxygenation does not occur preferentially by tunneling. Together these effects account for the ~4000-fold rate advantage given to methane over ethane based on their roughly equal rate constants of reaction with **Q** despite a 5 kcal/mole difference in BDE. One way to test this proposal arose from the finding that the T111Y variant of MMOB appeared to interact with sMMOH in a way that opened the active site completely, thereby removing both the sizing and tunneling advantages given to methane.[65] The ln k_{obs} vs BDE plot shown in **Figure 1-10**B for normal and deuterated methane and

ethane was found to be linear and also demonstrated the expected differences in rate constant due purely to the strength of the hydrocarbon bonds.

1.24 Regulation by the N-terminal and C-terminal Regions of MMOB

There are regions other than the well-folded core of MMOB where mutations alter the rate constants of chemical steps at the sMMOH diiron cluster. For example, deletion of the first 29-35 residues of the N-terminal region of MMOB abolishes steady state activity.[46, 70, 139] Among the substitution mutants, the H33A and H5A MMOB variants decrease the rate constant of conversion of **P*** to **P** and **P** to **Q**, respectively.[71] This effect might be attributed to a role for histidine in providing the protons required for these steps. However, the proton inventory plots for these steps are not compatible with multistep transfer of the protons, which would be required from surface histidines. Alternatively, a loss of ability to effect a structural change at the diiron cluster by the H33A and H5A variants could be responsible for the slow formation of **P** and **Q**.

The C-terminal region of MMOB is also implicated in the regulation of kinetic steps in the catalytic cycle. Deletion mutants decreased the rate constant of formation of intermediate **P** and lowered the steady-state turnover number associated with **T** decay.[140] Moreover, these variants resulted in a large uncoupling of the reaction owing to a dissociation of peroxide from **P**. Thus, the regulatory role of MMOB extends to ensuring a properly coupled turnover system to maximize product yield and prevent the generation of toxic reactive oxygen species.

1.25 Continuous Binding of MMOB During Catalysis

When all of the MMOB variants tested to date are considered together, at least one can be found that alters the rate constant for each step in the catalytic cycle.[65, 71] One application of these variants has been to test whether MMOB dissociates from sMMOH during the reaction cycle. When the reaction was initiated in the presence of two MMOB variants that affect the rate constants of different steps, the time course of the reaction could only be simulated under the assumption that no MMOB dissociation of either variant occurred between O_2 binding and product release.[71]

1.26 Role of MMOB in the Regulation of Electron Transfer to the Diiron Cluster

The presence of reduced MMOR during single turnover reactions significantly lowers product yield unless MMOB is also present.[141] This observation suggests that MMOB plays a role in preventing the transfer of electrons to **Q** from MMOR. One way in which this might be implemented is if the sMMOH:MMOB complex at the **Q** stage of the reaction cycle blocks formation of the sMMOH:MMOR^{red} complex. Conflicting results remain over whether MMOB and MMOR compete with each other for binding sMMOH at any stage of the cycle.[64, 142] However, early chemical cross-linking studies showed that a MMOR cross-links to the beta subunit of sMMOH.[63] Recent hydrogen-deuterium exchange coupled to mass-spectrometry experiments showed that sMMOH:MMOR interface in the *Mc* Bath sMMO system overlaps with the sMMOH:MMOB binding surface.[64] Taking all of these findings into account, a model has emerged where reduced MMOR binds diferric sMMOH and reduces the diiron cluster. MMOB then displaces MMOR from the pore region of sMMOH, whereupon the catalytic cycle starts with O_2 binding.[64] The finding described above that MMOB remains bound throughout the remainder of the cycle explains why MMOR does not rebind to quench **Q** by electron transfer. One potential problem with this scenario is that the affinity of MMOB for *Mt* OB3b sMMOH in the diferric state is very high (68 nM) and decreases at least 3 orders of magnitude when sMMOH is reduced.[129] These values were directly measured by fluorescence titration of MMOB labeled with a fluorophore, but they are also in accord with the 132 mV decrease in the redox potential of sMMOH when the complex with MMOB is formed.[143] The high affinity of MMOB for *Mc* Bath sMMOH was not observed,[144] but a similar shift in redox potential was reported,[145] which requires a large decrease in affinity. Consequently, for regulation by component displacement proposal to be correct, the affinity of MMOR^{red} to MMOH^{ox} must be even higher than that of MMOB, and the opposite must be true for MMOR^{ox} binding to MMOH^{red}. The observed shift in redox potential coupled to binding for formation of the sMMOH:MMOR complex does not support this model for MMOR binding.[141] However, the

hysteretic effects of MMOR on sMMOH make the shift difficult to measure.[141, 146] Many of the questions raised in these past studies are directly addressed in this dissertation.

1.27 Scope of Present Work

Four decades of soluble methane monooxygenase (sMMO) research have provided much detail about how Nature catalyzes the activation of molecular oxygen and subsequent hydroxylation of methane to methanol at ambient temperature and pressure. Although much has been discovered, the most difficult questions regarding the molecular details of sMMO regulation remain unanswered. As explained above, the exact structure of the active site when intermediate **Q** is formed remains unknown, the structural mechanisms that regulate the transport of substrates are not well understood, and the precise timing of protein interactions during the catalytic cycle is still a mystery. This dissertation provides experimental evidence furthering our understanding in the three areas just mentioned. Chapter 2 describes how high-resolution X-ray crystal structures of the sMMOH:MMOB complex were obtained using a methodology termed serial femtosecond X-ray crystallography. Subsequent analysis of the structural data provides molecular details of the effects MMOB has on sMMOH structure. Chapter 3 further explores how the molecular structure of the sMMOH:MMOB complex regulates the transport of substrates. Structural data coupled with transient kinetics of MMOB variants provides evidence of a transient molecular tunnel sized uniquely to transport molecular oxygen and methane into the active site. Chapter four investigates the protein interactions between sMMOH, MMOB, and MMOR in solution using ^{19}F-NMR. Based on these studies, a new model is proposed describing how MMOR and MMOB interact with sMMOH so that catalysis is driven forward.

Chapter 2 High-Resolution XFEL Structure of the Soluble Methane Monooxygenase Hydroxylase Complex with its Regulatory Component at Ambient Temperature in Two Oxidation States

Portions of this chapter are reprinted and adapted with permission from: Vivek Srinivas, Rahul Banerjee, Hugo Lebrette, Jason C. Jones, Oskar Aurelius, In-Sik Kim, Cindy C. Pham, Sheraz Gul,Kyle D. Sutherlin, Asmit Bhowmick, Juliane John, Esra Bozkurt, Thomas Fransson, Pierre Aller, Agata Butryn, Isabel Bogacz, Philipp Simon, Stephen Keable, Alexander Britz, Kensuke Tono, Kyung Sook Kim, Sang-Youn Park, Sang Jae Lee, Jaehyun Park, Roberto Alonso-Mori,¶ Franklin D. Fuller, Alexander Batyuk, Aaron S. Brewster, Uwe Bergmann, Nicholas K. Sauter, Allen M. Orville, Vittal K. Yachandra, Junko Yano,* John D. Lipscomb,* Jan Kern,* and Martin Högbom* *J. Am. Chem. Soc.,* ***2020,*** *142, 14249-14266.* © 2020 American Chemical Society

My contributions to this project were: conceiving and planning the experiments, sample preparation, participate in onsite experiments at LCLS (California) and SACLA (Japan) XFEL facilities, trouble shoot the experimental setup, analyzed the results, draft manuscript preparation, and review/approve the final manuscript.

2.1 Synopsis

Soluble methane monooxygenase (sMMO) is a multicomponent metalloenzyme that catalyzes the conversion of methane to methanol at ambient temperature using a nonheme, oxygen-bridged dinuclear iron cluster in the active site. Structural changes in the hydroxylase component (sMMOH) containing the diiron cluster caused by complex formation with a regulatory component (MMOB) and by iron reduction are important for the regulation of O_2 activation and substrate hydroxylation. Structural studies of metalloenzymes using traditional synchrotron-based X-ray crystallography are often complicated by partial X-ray-induced photoreduction of the metal center, thereby obviating determination of the structure of the enzyme in pure oxidation states. Here microcrystals of the sMMOH:MMOB complex from *Methylosinus trichosporium* OB3b were serially exposed to X-ray free electron laser (XFEL) pulses, where the [35 fs duration of exposure of an individual crystal yields diffraction data before photoreduction-induced structural changes can manifest. Merging diffraction patterns obtained from thousands of crystals generates radiation damage free, 1.95 Å resolution crystal structures for the fully oxidized and fully reduced states of the sMMOH:MMOB complex for the first time. The results provide new insight into the manner by which the diiron cluster and the active site environment are reorganized by the regulatory protein component in order to enhance the steps of oxygen activation and methane oxidation. This study also emphasizes the value of XFEL and serial femtosecond crystallography (SFX) methods for investigating the structures of metalloenzymes with radiation sensitive metal active sites.

2.2 Introduction

The soluble form of methane monooxygenase (sMMO) isolated from methanotrophic bacteria catalyzes the oxygenation of methane to methanol at room temperature without over oxidation.[5]

$$CH_4 + O_2 + NADH + H^+ \rightarrow CH_3OH + H_2O + NAD^+$$

This enzyme, and a structurally unrelated membrane-bound methane monooxygenase (pMMO) produced by methanotrophs when the solution copper to biomass ratio exceeds ~ 5.7 μmol/g protein, prevent the atmospheric egress of a large fraction of the global production of biogenic methane.[147, 148] The significant contribution of methane in the atmosphere to global warming is a cause of current concern, highlighting the importance of sMMO and pMMO to economic, health, and societal policies.[16, 17] The remarkable catalytic prowess of these enzymes also stimulates research into the generation of biomimetic synthetic catalysts for gas-to-liquid conversion, as well as the bioengineering of novel pathways into organisms to make value-added products from methane.[18, 149]

The sMMO enzyme consists of three protein components: a 245 kDa $(\alpha\beta\gamma)_2$ hydroxylase (sMMOH), a 37 kDa FAD and Fe_2S_2 cluster-containing reductase (MMOR), and a 15 kDa regulatory protein (MMOB).[5, 14, 33, 35, 71] The active site is buried deep within sMMOH and contains an oxygen-bridged dinuclear Fe^{III} cluster in which the irons are bridged by two hydroxo moieties and a carboxylate from Glu144.[37, 38, 40, 150] After reduction, the diiron cluster functions to activate O_2 and insert an oxygen atom into a highly stable (105 kcal/mol bond dissociation energy) C-H bond of methane.[33, 151]

Although chemically reduced sMMOH can carry out the oxygenation chemistry alone,[114] the reaction only proceeds at a physiologically relevant rate when sMMOH is complexed with MMOB. [33, 63, 69] Many regulatory functions of MMOB have been discovered (**Scheme 2-1**),[15] but its most important effects are to decrease the redox potential of the diiron cluster by 132 mV, accelerate O_2 binding by 1000-fold, increase the turnover number 150-fold, and tune sMMOH to

selectively bind and oxygenate methane over other more easily oxidized hydrocarbons. [5, 69, 71, 143] Indeed, the interaction of sMMOH with MMOB is so central to sMMO catalysis that the chemistry catalyzed by this remarkable enzyme cannot be fully appreciated without also elucidating all of the regulatory functions of MMOB.

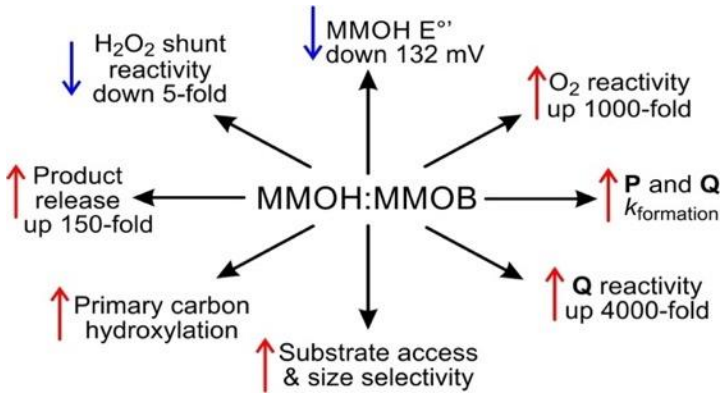

Scheme 2-1 The regulatory functions of MMOB on sMMO catalysis

The complex between MMOB and sMMOH has been structurally characterized by both spectroscopic and crystallographic approaches in order to understand the mechanism of regulation by MMOB.[33, 44-46, 70, 77, 131, 144] The core structural region of MMOB binds to the surface of sMMOH approximately 12 Å above the diiron cluster. An extended 30-residue N-terminal tail region of MMOB is disordered in solution, but it was observed to bind to the sMMOH surface in the structure of the oxidized sMMOH:MMOB complex of sMMO isolated from *Methylococcus capsulatus* Bath (*Mc* Bath).[44, 45, 70] These structural observations have been supported by transient kinetic and mutagenic studies, which have shown that the core region and both the N- and C-terminal regions of MMOB affect the rate constants of steps throughout the reaction cycle.[65, 67, 71, 140]

Despite the clues provided by the structural and biochemical studies, the mechanisms by which MMOB exerts its many effects on oxygen activation and other aspects of the reaction are largely unknown. The absence of a structure of reduced sMMOH in complex with MMOB has held back our understanding of this regulation, as this is the key enzymatic state that is primed to react

with O_2. Structural studies of uncomplexed sMMOH have shown that reduction of the diiron cluster causes a shift in the position of Glu243, a monodentate ligand to Fe2 in the diferric cluster as illustrated in **Scheme 2-2**. [38]

Scheme 2-2 Carboxylate Shift in the Diiron Cluster of sMMOH Upon Reduction

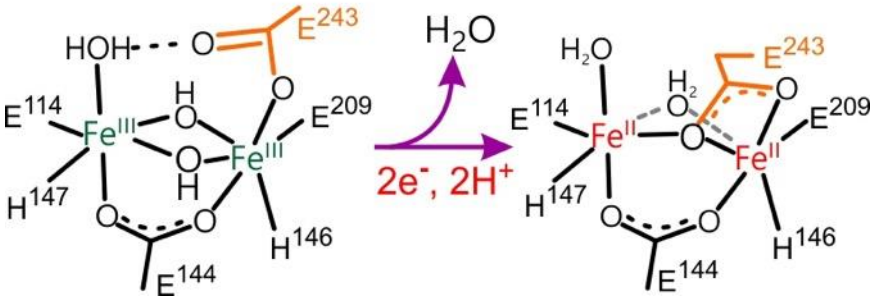

In the shifted position, Glu243 bridges Fe1 and Fe2 via one of its carboxylate oxygens, thereby directly displacing one of the bridging solvents. The second bridging solvent bond is weakened, which presumably allows facile displacement by O_2 to begin the oxygen activation process. Surprisingly, in the 2.9 Å resolution X-ray crystal structure of the diferric state of the *Mc* Bath sMMOH:MMOB complex, the position of Glu243 relative to Fe2 was also found to be shifted to the bridging position.[70] The observation of a carboxylate shift in the diferric state of the sMMOH:MMOB complex led to the proposal that one mechanism by which MMOB acts is to cause this critical change in the cluster structure.[70] However, a significant problem often encountered in determining the X-ray crystal structure of metalloenzymes is the ease with which the metal is reduced by hydrated electrons generated by the synchrotron X-ray beam.[152-157] Partial reduction of the clusters might explain the observed shift in Glu243 without invoking a role for MMOB.

Recently, it has become possible to solve protein crystal structures by injecting a slurry of microcrystals into the beam of an X-ray free electron laser (XFEL).[158-165] The instrumentation records a zero-rotation ("still") diffraction pattern for each micro-crystal exposed to the beam, on

the femtosecond time scale (between 10 and 35 fs in this study). The approach has three significant advantages: (a) the diffraction data are generated faster than the rate of reaction with beam-generated solvated electrons, (b) the diffraction data are obtained at physiologically relevant temperature rather than at 100 K as in typical synchrotron protein crystallography experiments, and (c) the potential exists to observe structures of reaction cycle intermediates if the enzyme reaction can be initiated *in-crystallo* at room temperature.[166-171] In addition, concomitant collection of transition metal X-ray emission spectra (XES) has been recently demonstrated for different metalloenzymes at XFELs, enabling a parallel measurement of the metal oxidation state during the crystallographic experiment.[161, 172, 173]

Here, we report new sMMOH:MMOB crystal structures of the highly active sMMO components isolated from *Methylosinus trichosporium* OB3b (*Mt* OB3b). Using XFEL data, room temperature structures of the homogeneous diferric and diferrous states of sMMOH:MMOB are reported at 1.95 Å resolution. The structures are used to define the changes effected in sMMOH upon binding of MMOB and to characterize the geometric state of the diiron cluster prepared to bind and activate O_2.

2.3 Experimental Procedures

2.3.1 Protein Isolation, Crystallization, and Crystal Reduction.

The sMMOH protein was isolated from frozen cell pellets of the native *Mt* OB3b cultured using methane as the sole carbon source as previously described.[174] The MMOB protein was heterologously expressed in *E. coli* BL21(DE3) cells as previously described.[44] sMMOH and MMOB were purified as previously described.[34, 76] A protein solution of 53 μM sMMOH and 106 μM MMOB in 25 mM MOPS pH 7 was used to screen for suitable crystallization conditions. Swissci MRC-2-drop plates (Molecular Dimensions) were used to setup crystallization experiments using the TTP mosquito® nanoliter pipetting robot. The plates were setup with a reservoir volume of 50 μl and drop volume of 400 nl. Rhombohedral crystals were observed in B7 condition of the

Morpheus crystal screen (Molecular Dimensions). The microcrystals were further optimized using the additive screen (Hampton Research), with condition A11 producing 20-30 μm long bipyramidal shaped crystals within 3 days of incubation at room temperature. Larger volume sMMOH:MMOB complex crystals were aerobically grown in Cryschem M sitting drop vapor diffusion plates (Hampton Research), with a 30 μl drop volume (22.5 μl protein solution plus 7.5 μl reservoir solution) against a reservoir volume of 500 μl. The final crystallization condition is as follows: 100 mM HEPES/MOPS pH 7.5, 30 mM NaI, 30 mM NaBr, 30 mM NaF, 20 % (v/v) glycerol, 10 % (w/v) PEG 4000, and 10 mM $FeCl_3$. The crystals were harvested by individually pooling the drops with bipyramidal crystals into a microfuge tube. Chemical reduction of the sMMOH:MMOB crystal slurry was carried out in an anaerobic glove box. The crystal slurry was incubated in reservoir solution containing 46 mM dithionite, 15 mM methyl viologen, and 1 mM phenosafranine for 12 h at room temperature. The crystal slurry primed for *in-crystallo* re-oxidation experiments was reduced as above before clearing the crystal slurry of any chemical reductants. This was accomplished by pelleting the chemically reduced crystal slurry in a benchtop centrifuge followed by removal of the chemical reductant-containing supernatant solution. The loosely packed crystal pellet was subsequently resuspended in fresh, anaerobic, $FeCl_3$-free reservoir solution. This step was repeated 5 times to dilute the resulting concentration of chemical reductants in the crystal slurry solution used for re-oxidation experiments.

2.3.2 Data Collection and Model Refinement.

The crystals of oxidized sMMOH:MMOB were first tested for XFEL compatibility at SACLA, Japan, using the grease matrix extruder setup.[175, 176] Crystals of sMMOH:MMOB were mixed with synthetic grease and injected using a 150 μm diameter nozzle and a flow rate of 20-80 μl/min using an HPLC pump. X-ray diffraction was generated by <10 fs long X-ray pulses at 10.9 keV with a pulse energy of around 0.32 mJ, 30 Hz repetition rate and a beam size of 2x2 μm (FWHM). The forward scattering was recorded on a Octal MPCCD detector located 100 mm downstream of the

X-ray interaction point. Diffraction images from 7469 crystals were merged to achieve a resolution of 2.24 Å.

Data sets were then collected at the macromolecular femtosecond crystallography (MFX) experimental hutch at LCLS.[177] The drop on tape (DOT) method was used to deliver sMMOH:MMOB crystals into the XFEL X-ray interaction region.[172] In short, micro-crystal suspensions were loaded in gas-tight Hamilton syringes under inert gas conditions inside a glove box. The syringe was then connected via a single silica capillary to the sample reservoir inside the He-enclosure of the DOT setup. The crystal suspension was dispensed at a flow rate of 8 μl/min using a syringe pump (KD Scientific). The sample was pushed into a 6 μl well underneath and at the focal point of an acoustic transducer, forming droplets of 2.5 - 4 nl volume. The droplets were deposited onto a Kapton tape belt running at a speed of 300 mm/s that transported the droplets into the X-ray interaction region.[172] The He-enclosure around the setup ensured anaerobic conditions and limited air scattering of X-rays. The residence time of the droplets inside the He atmosphere (O_2 level below 0.1%) was around 0.8 s.

For *in-crystallo* O_2 incubation experiments, an *in-situ* gas incubation setup was used as previously described.[172] In this case, the gas reaction chamber was continuously filled with pure O_2 gas at a flow rate of 0.5 - 0.75 liter/min and monitored by an oxygen sensor in the chamber during the experiment. The travel speed of the Kapton belt transporting the sample droplets was reduced to 15 mm/s, thus resulting in a 4 s travel time of individual sample droplets through the O_2 reaction chamber and an additional incubation time of 6 s before reaching the X-ray interaction region. To avoid dehydration of the sample droplets, the O_2 gas and He gas in the direct environment of the incubation region was first routed through water-filled gas wash bottles, leading to a relative humidity of 35% around the sample.

X-ray diffraction was generated by ~35 fs long X-ray pulses at 9.5 keV with a pulse energy of around 4.0 mJ, 20 Hz repetition rate and a beam size of 4 μm (FWHM). The forward scattering

was recorded on a Rayonix MX340 detector at 194 mm downstream of the X-ray interaction point. In addition, diffraction data was collected with the same DOT setup installed at the NCI beam line of the PAL-XFEL facility.[178] Here ~35 fs long X-ray pulses at 9.4 keV with a pulse energy of 0.8 mJ, a beam size of 2.5 μm (FWHM) at 15 Hz repetition rate were used and diffraction was measured on a Rayonix MX200 detector located 130 mm downstream of the sample.

X-ray emission data was collected concomitant with diffraction data using a multi-crystal wavelength-dispersive hard X-ray spectrometer based on the von Hamos geometry.[172, 179] Four Ge (440) crystals were placed 250 mm from the interaction point, with the center of the crystals at 75.41° with respect to the interaction point covering both Fe Kα lines. The focused X-ray emission signal was collected on an ePIX-100 detector (LCLS) or on a 500k Jungfrau detector (PAL-XFEL). Calibration was performed using aqueous solutions of 10 mM $Fe(III)(NO_3)_3$ and $Fe(II)Cl_2$ as reference.

Diffraction images were processed with *cctbx.xfel*[180] and DIALS.[181] The sMMOH:MMOB structure was solved using molecular replacement by PHASER,[182] with truncated coordinates from the *Mc* Bath sMMOH:MMOB complex crystal structure PDB: 4GAM used as the starting model. The structure was initially modeled in space group $P4_1$ with two complexes (eight polypeptide chains) per asymmetric unit; however, after running the program *labelit.check_pdb_symmetry*,[183] it was realized that the model was consistent with space group $P4_12_12$ with one complex (four polypeptide chains) per asymmetric unit. Therefore, we used *cctbx* to merge the $P4_1$ reflection file into the higher symmetry, and thus proceeded to refinement in $P4_12_12$. Refinement of the structure was performed using PHENIX.refine[184, 185] and model building was done in COOT.[186] Individual atomic coordinates, isotropic B factor and TLS parameters were used during refinement. Solvent molecules were added using PHENIX.refine,[184, 185] followed by manual addition. **Table 2-1** was generated using PHENIX.table_one.[184, 185]

2.3.3 Probing the Active Site Cavity in Protein Structures.

The interior active site cavity in the protein structures was identified with the MOLE 2.5 program.[187] Heteroatoms were ignored in the calculation. A probe radius of 3.0 Å, interior threshold of 1.59 Å, and minimum depth of 5.0 Å were used to assess the cavity.

Table 2-1 X-ray Data Collection and Refinement Statistics for sMMOH:MMOB Complex in the Diferric, Diferrous, Reoxidized States, and the t = 0 Diferrous State Before O_2 Exposure.

Dataset (PDB Code)	Diferric sMMOH:MMOB (PDB 6YD0)	Diferrous sMMOH:MMOB (PDB 6YDI)	Reoxidized sMMOH:MMOB (PDB 6YDU)	t = 0 Diferrous sMMOH:MMOB (PDB 6YY3)
Wavelength	1.30644	1.30448	1.30396	1.318066
XFEL source	LCLS MFX	LCLS MFX	LCLS MFX	PAL-XFEL NCI
Spacegroup	$P4_12_12$	$P4_12_12$	$P4_12_12$	$P4_12_12$
Cell dimensions (Å)	106.9, 106.9, 303.9	106.9, 106.9, 303.9	106.9, 106.9, 304.1	106.0, 106.0, 301.0
Cell angles (deg)	90, 90, 90	90, 90, 90	90, 90, 90	90, 90, 90
Resolution range[a] (Å)	33.00-1.95 (2.02-1.95)	33.71-1.95 (2.02-1.95)	33.96-1.95 (2.02-1.95)	24.66-2.0 (2.07-2.0)
Merged lattices	25274	14980	15629	13596
Reflections observed (unique)[b]	16675375 (128780)	10382513 (128981)	9590816 (128969)	9549089 (116482)
Mean $\langle I\rangle/\sigma\langle I\rangle$ [a,b,c]	34.3 (0.8)	27.5 (0.6)	25.2 (0.6)	1.78 (0.32)
CC1/2 [a,b]	0.944 (0.282)	0.949 (0.175)	0.945 (0.077)	0.933 (0.25)
Completeness (%) [a,b]	99.93 (99.90)	99.91 (99.70)	99.84 (99.16)	99.06 (92.35)
R, R_{free}, test (%)[d]	16.24, 18.96, 1.55	17.54, 19.54, 1.55	16.77, 19.64, 1.55	20.36, 23.50, 1.71
R_{split} (%)	20.8 (100.6)	20.6 (110.8)	21.6 (119.8)	24.1 (90.8)
RMSD [e] bond length (Å)	0.017	0.004	0.010	0.007
RMSD [e] angles (deg)	1.33	0.72	0.99	0.81
Average B-factor	45.40	46.07	46.51	45.36
Ramachandran favored, allowed and outlier regions (%)	96.50, 3.33, 0.17	97.42, 2.58, 0.00	97.09, 2.91, 0.00	97.17, 2.83, 0.00

[a] Values for the highest resolution shell are given in parentheses. [b]These statistics are for merging the data in $P4_1$. The data were subsequently merged into $P4_12_12$, essentially halving the number of unique reflections and improving the completeness, $\langle I\rangle/\sigma\langle I\rangle$, and CC1/2 beyond what is reported here. [c]Columns 1-3: σ was computed using the Ha14 error model as described in Hattne, et al.[180] and Brewster et al. 2018.[188] Column 4: σ was computed using the Ev11 error model (see Brewster et al. 2018[188] and 2019[189]). The difference in error models accounts for the large difference in $\langle I\rangle/\sigma\langle I\rangle$ values when comparing columns 1-3 with column 4; see Brewster et al.[189] for more information. [d] $R = (\sum|F_{obs}-kF_{calc}|)/\sum|F_{obs}|$, where k is a scale factor. The R_{free} value was calculated with the indicated percentage of reflections not used in the refinement. [e] Root-mean-square deviation (RMSD) from ideal geometry in the final models.

2.4 Results

2.4.1 High Resolution Crystal Structures of the sMMOH:MMOB Complex in Diferric and Diferrous Oxidation States.

Crystals of the *Mt* OB3b sMMOH:MMOB complex in the resting diferric oxidation state were prepared as described in Experimental Procedures and found to diffract to 2.45 Å at the ID30B beamline, European Synchrotron Radiation Facility (data not shown). Microcrystals were then prepared as described in Experimental Procedures and analyzed by XFEL at room temperature. Microcrystals of the diferrous state of the sMMOH:MMOB complex were obtained by chemical reduction of the oxidized sMMOH:MMOB complex crystal slurry under anaerobic conditions. No notable decrease in the diffraction quality of these crystals was observed despite the rigorous reduction procedure. In order to test whether O_2 is capable of initiating enzymatic turnover with the reduced sMMOH:MMOB protein complex in crystals, a microcrystal slurry of chemically reduced crystals was washed of excess reductant and then passed through a chamber filled with pure O_2 for 4 s before injection into the XFEL beam. The total time from exposure to O_2 to diffraction in the beam was 10 s. This sample behaved similarly to the diferric and diferrous crystal slurry. All three structures were refined to a resolution of 1.95 Å (**Table 2-1**). As a control, diffraction data were collected from a washed slurry of chemically reduced crystals prior to O_2 incubation, and a structure was refined to a resolution of 2.0 Å (**Table 2-1**, "t=0 Diferrous"). In parallel, Fe Kα XES was collected for the diferric, diferrous and reoxidized samples.

The overall structure of the *Mt* OB3b sMMOH:MMOB complex is shown in **Figure 2-1**A for the diferric state (PDB: 6YD0). The asymmetric unit contains one molecule of MMOB bound to one αβγ protomer of the $(\alpha\beta\gamma)_2$ sMMOH protein. The quaternary structure of the protein complex is unaltered upon reduction of the diiron cluster (PDB: 6YDI) or following reaction of the diferrous complex with O_2 (PDB: 6YDU). MMOB binds primarily to the α-subunit of sMMOH in

the ‘canyon’ region at the interface of the sMMOH protomers (**Figure 2-1**A). This binding site is immediately above the buried active site diiron cluster (**Figure 2-1**A and B).

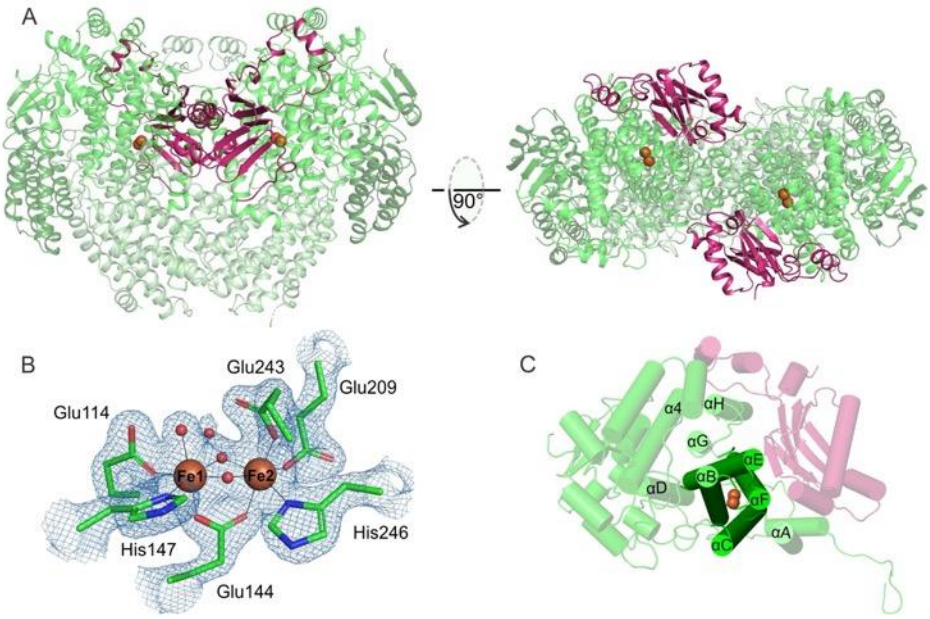

Figure 2-1 The diferric *Mt* OB3b sMMOH:MMOB complex (PDB: 6YD0).
(A) Two perspectives of the overall complex. The α, β, and γ subunits of the sMMOH protein are shown in different shades of green while MMOB is colored purple. The iron atoms in the sMMOH active site are represented as orange spheres. The dimeric sMMOH:MMOB is shown by generating the symmetry related monomer in PyMOL (B) 2Fo-Fc map of the oxidized diiron cluster contoured to 2 σ. (C) Cartoon of the α-subunit with the helix nomenclature illustrated.

2.4.2 Complex Formation Leads to Localized Structural Reorganization of MMOB as well as the sMMOH Interface.

The availability of a room temperature, high resolution, fully oxidized structure of the *Mt* OB3b sMMOH:MMOB complex allows a critical evaluation of the changes in both diferric sMMOH and MMOB upon complex formation. A comparison of MMOB in this crystal structure with the NMR structure of *Mt* OB3b MMOB in isolation (PDB:2MOB)[44] shows that there is a significant conformational reorganization of MMOB upon complex formation. These changes are present not only in the well-ordered core region (residues 35 – 125) but also in the N-terminal tail (residues 1 – 35) and C-terminal tail (residues 127 -138) (**Figure 2-2**). The reorganization is significant as suggested by the r.m.s.d value of 3.5 Å between isolated MMOB and MMOB in complex with sMMOH. In the absence of sMMOH, the MMOB core region is composed of two domains, where domain 1 (residues 36 – 81) contains a βαββ motif and domain 2 (residues 82 –126) contains a βααββ motif.[44] Upon binding to sMMOH, the α-helices on the two domains move closer to each other (**Figure 2-2**). In addition, a long helix in domain 2 of MMOB is restructured into a short helix, while an unstructured loop is converted into a β-sheet (**Figure 2-2**). This newly formed β-sheet is involved in hydrogen-bonding interactions with the β-sheets of domain 1. The extent of reorganization of the MMOB core seen in this structure is not observed in the *Mc* Bath sMMOH:MMOB complex crystal structure.

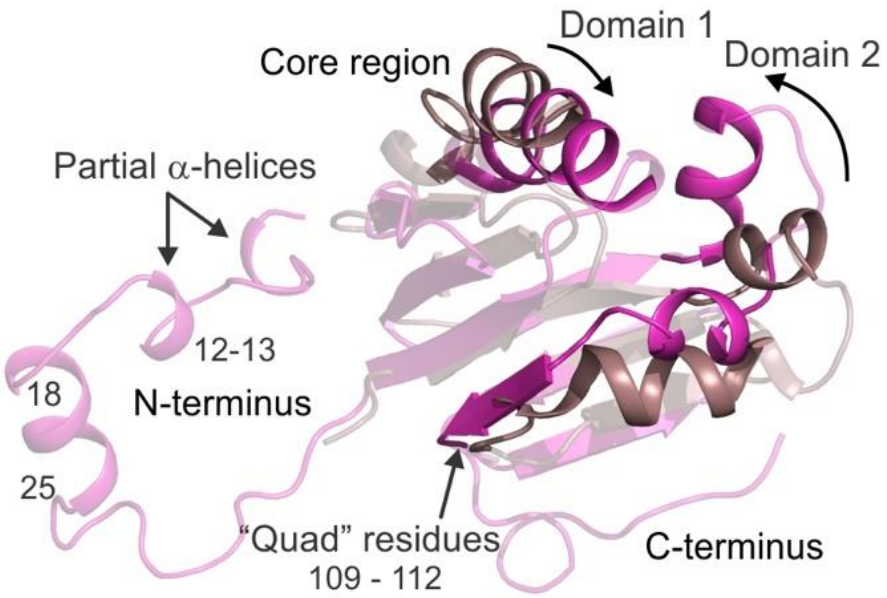

Figure 2-2 The structure of MMOB changes conformation when bound to sMMOH
An alignment of the MMOB protein structure in the uncomplexed state (PDB: 2MOB; brown cartoon) and sMMOH bound complex (PDB: 6YD0; magenta cartoon).
Both the N-terminal and C-terminal tails of MMOB are ordered in the protein complex with additional secondary structure being generated in the N-terminal tail. The MMOB core also becomes reorganized in the complex as highlighted by the region in focus (opaque cartoon). MMOB domains 1 and 2 reorient closer together upon complex formation with sMMOH.

The residues present on the new β-sheet include Ser109, Ser110, Thr111 and Val112. This sequence of MMOB, termed the "Quad region" is important because three of these residues specifically interact with residues on sMMOH and affect catalysis (*vide infra*).[65-67, 71] The N-terminal tail of isolated MMOB is disordered, as it cannot be observed in the NMR structures. However, upon complex formation, this region on MMOB is arranged in a ring-like fashion on the surface of sMMOH (**Figure 2-1** and **Figure 2-3**), as observed previously with the 2.9 Å cryo-temperature *Mc* Bath sMMOH:MMOB complex structure.[70] A short α-helix is formed in this N-terminal tail (residues 18 – 25) upon complex formation with sMMOH, which is in agreement with previous solution NMR studies.[46] In addition, there are two short regions where a partial helix is formed, which can be seen only in the higher resolution *Mt* OB3b protein complex structure (**Figure 2-2**). These helices appear to form as a result of the insertion of multiple conserved non-polar MMOB residues (Ile12, Met13, Phe20, Phe24, Phe25 and Gln30, **Figure 2-3**B and **Figure 2-4**) into a predominantly polar region (Helices H and 4, see **Figure 2-1**C for helix nomenclature) on the sMMOH surface. Steric clashes, hydrophobic interactions and avoiding non-favorable contacts with the polar residues lead to the stabilization of an α-helix in MMOB. Finally, the C-terminal tail of MMOB, which is disordered in the isolated NMR solution structure, is ordered in the protein complex, although it does not acquire any secondary structure (**Figure 2-2**). The higher resolution of the *Mt* OB3b sMMOH:MMOB crystal structure compared to the *Mc* Bath structure enables this observation, as the C-terminal tail cannot be observed in the latter structure.

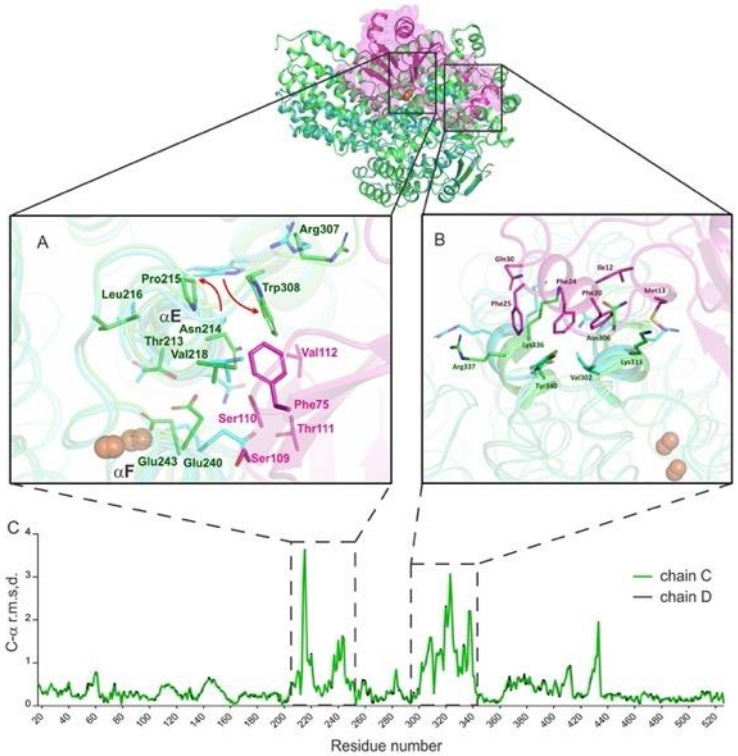

Figure 2-3 Conformational changes in the alpha subunit of sMMOH upon MMOB binding.

An alignment of the α-subunit of sMMOH in unbound (1MHY) and MMOB-bound (6YD0) states shows that specific regions in sMMOH undergo a large reorganization as depicted by the C-α r.m.s.d. values (panel C). These regions (Helix E – residue 213 – 223 ; Helix F – residue 237 – 252; Helix H and 4 – residue 302 – 341) are shown in more detail in the square boxes (Panel A: Helices E and F; Panel B: Helices H and 4). MMOB residues responsible for the reorganization are shown in the boxes as magenta sticks. sMMOH in isolation is shown as the cyan cartoon; $sMMOH^{ox}$:MMOB is shown as the green cartoon. Hydrogen bonds are depicted as black lines.

Localized structural reorganization also occurs in the sMMOH protein upon MMOB binding. A comparison of the superposed structures of oxidized sMMOH from *Mt* OB3b (PDB:1MHY, also solved using data collected at room temperature) [40] and the *Mt* OB3b sMMOH:MMOB complex provides a clear picture of these changes. The reorganization involves two of the four helices of the 4-helix bundle (E and F) and two additional helices on the sMMOH surface (H and 4) (**Figure 2-3** and **Figure 2-1**). All of these regions are located on the sMMOH interface with MMOB.

A comprehensive list of structural changes in *Mt* OB3b sMMOH due to MMOB binding is given in **Table 2-2**. A long section of sMMOH residues (213 – 223; α-subunit; Helix E) reorganize (**Figure 2-3** and **Figure 2-5**) as a result of the formation of a hydrogen bond between Asn214 (sMMOH) and Ser110 (MMOB) and steric clashes of Val218 (sMMOH) with Phe75 (MMOB). It is important to note that Helix E contains sections that possess the relatively rare π-helical secondary structure. π–helices are evolutionarily conserved features in proteins and their presence is strongly associated with active site residues involved in catalysis.[190] The π–helices in the ferritin-like superfamily, of which sMMO is a member along with other bacterial multicomponent monooxygenases (BMM), ribonucleotide reductases (RNR), acyl-ACP desaturases, ferritins and bacterioferritins, are important because they provide some of the ligands to the carboxylate-bridged di-metal cofactors (Glu209 in sMMOH).[190] In unbound sMMOH, Helix E contains two small π-helical sections from residues 202 – 205 and 208 – 209 along with residues bereft of intra-main chain hydrogen bonds (206, 210 – 211, 214). MMOB binding reorganizes the second π-helix to 207 – 208 and induces the formation of an additional π-helical section from residues 213 – 215 (**Figure 2-5**). The Helix E residues lacking intra-main chain hydrogen bonds in the complex are 206, 209 – 211 and 216 – 217. Such a dramatic reorganization is possible due to a kink in Helix E at Pro215. Prolines in the middle of α-helices are conserved for their structural and functional significance and have also been found to be present at the point of transition from a π-

helix to an α-helix.[190, 191] Upon MMOB binding, Pro215 undergoes the largest r.m.s.d shift of 3.6 Å from its position in the sMMOH alone structure (**Figure 2-3**C). Pro215 is a strictly conserved residue in sMMOH (**Figure 2-6**), but not in other BMM enzyme

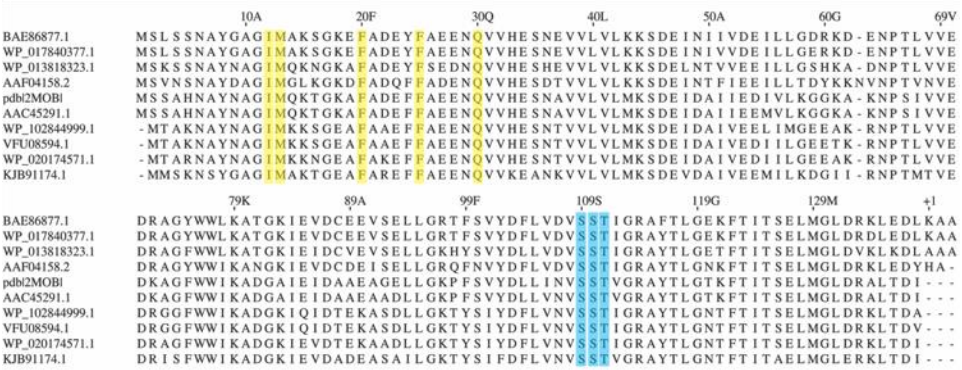

Figure 2-5 Multiple sequence alignment of MMOB in sMMO enzymes.
The strictly conserved residues on the N-terminal MMOB tail that interact with Helices H and 4 of sMMOH are highlighted in yellow. The strictly conserved residues in the core of MMOB that interact with sMMOH Helices E and F are highlighted in cyan. Sequences compared include - BAE86877.1 - *Methylomicrobium japanense*; WP_017840377.1 *Methylomicrobium buryatense*; WP_013818323.1 *Methylomonas methanica*; AAF04158.2 *Methylococcus capsulatus* Bath; pdb|2MOB| *Methylosinus trichosporium* OB3b; AAC45291.1 *Methylocystis sp.* M; WP_102844999.1 *Methylocella silvestris*; VFU08594.1 *Methylocella tundra*; WP_020174571.1 *Methyloferula stellate*; KJB91174.1 *Skermanella aerolata* KACC 11604.

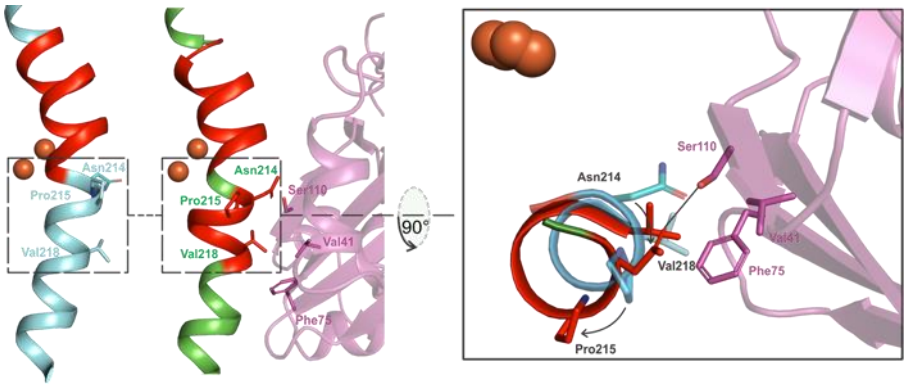

Figure 2-4 sMMOH π-helicies.
The π-helical portion (red) in Helix E of sMMOH is extended in the sMMOH^{ox}:MMOB complex (6YD0, green helix) as opposed to sMMOH in isolation (1MHY, cyan helix). The reorganization is caused primarily by the hydrogen-bond interaction between Ser110 (MMOB) and Asn214 (sMMOH) and a steric clash between Val218 (sMMOH) and Phe75 (MMOB). This leads to the large movement of Pro215. π-Helix assignment was performed using DSSP with the DSSP & Stride plugin for PyMOL (The PyMOL Molecular Graphics System, Version 2.0 Schrödinger, LLC).

Table 2-2 List of sMMOH (α-Subunit) Residues that Undergo a Large Structural Rearrangement upon MMOB Binding.[a]

Position	Residues reorganized	Specific interaction with MMOB
Loop 2	A53, N54, E55, T56, K57, E58, Q59, F60, K61, V62	K57 hydrogen bond to D137 Q59 steric clash with A115 K61 hydrogen bond to T136
Helix A	R69	R69 hydrogen bond to D103
Helix A	R77	R77 hydrogen bond to E47
Helix B	L110	L110 steric clash with L216 (MMOH)
Helix C	H156	
Helix C	K160	K160 hydrogen bond to D46 (of other MMOB)
Helix D	F188, F192	
Helix E	L204, Q205, L206, V207, G208, E209, A210, C211, F212, T213, N214, P215, L216, I217, V218, A219, V220, T221, E222, W223	N214 hydrogen-bond to S110 V218 steric clash with F75 E222 steric clash with F75
Helix F	E230, I231	
Helix F	L237, S238, V239, E240, T241, D242, E243, L244, R245, H246, M247, A248, N249, G250, Y251, Q252	E240 steric clash with S109 L244 steric clash with T111 Y251 steric clash with L128
Loop 9	S256, I257, A258, N259, D260, P261, A262, S263	
Helix G	W276, F282, T283, L286, F290	
Loop 10	V298, E299	E299 hydrogen bond to Y8
Helix H, Loop 11 and Helix 4	V302, K303, T304, W305, N306, R307, W308, V309, Y310, E311, D312, W313, G314, G315, I316, W317, I318, G319, R320, L321, G322, K323, Y324, G325, V326, E327, S328, P329, A330, S331, L332, R333, D334, A335, K336, R337, D338, A339, Y340, W341, A342, H343	K303 hydrogen bond to backbone L15 N306 steric clash with F24 R307 steric clash with Y8 W308 steric clash with P215 (MMOH) Y310 steric clash with N29 Y310 hydrogen bond to V31(b) D312 hydrogen bond to K79 I316 steric clash with S35 R320 steric clash with R114 K323 steric clash with L128 K323 hydrogen bond to E34 Y324 steric clash with L131 Y324 hydrogen bond to D132 R333 steric clash with Q30 R333 hydrogen bond with E27 K336 hydrogen bond to F24(b) and N29(b) Y340 steric clash with F24 and F25

[a] The 1MHY and the 6YD0 structure have been compared in order to generate this table. The specific interactions between sMMOH and MMOB residues are listed in the right-most column. Some sMMOH residues interact with the main-chain atoms in MMOB and these have been indicated with the (b) symbol. Some sMMOH residues reorganize as an indirect effect of MMOB binding for they interact with sMMOH residues that rearrange as a result of direct interaction with MMOB.

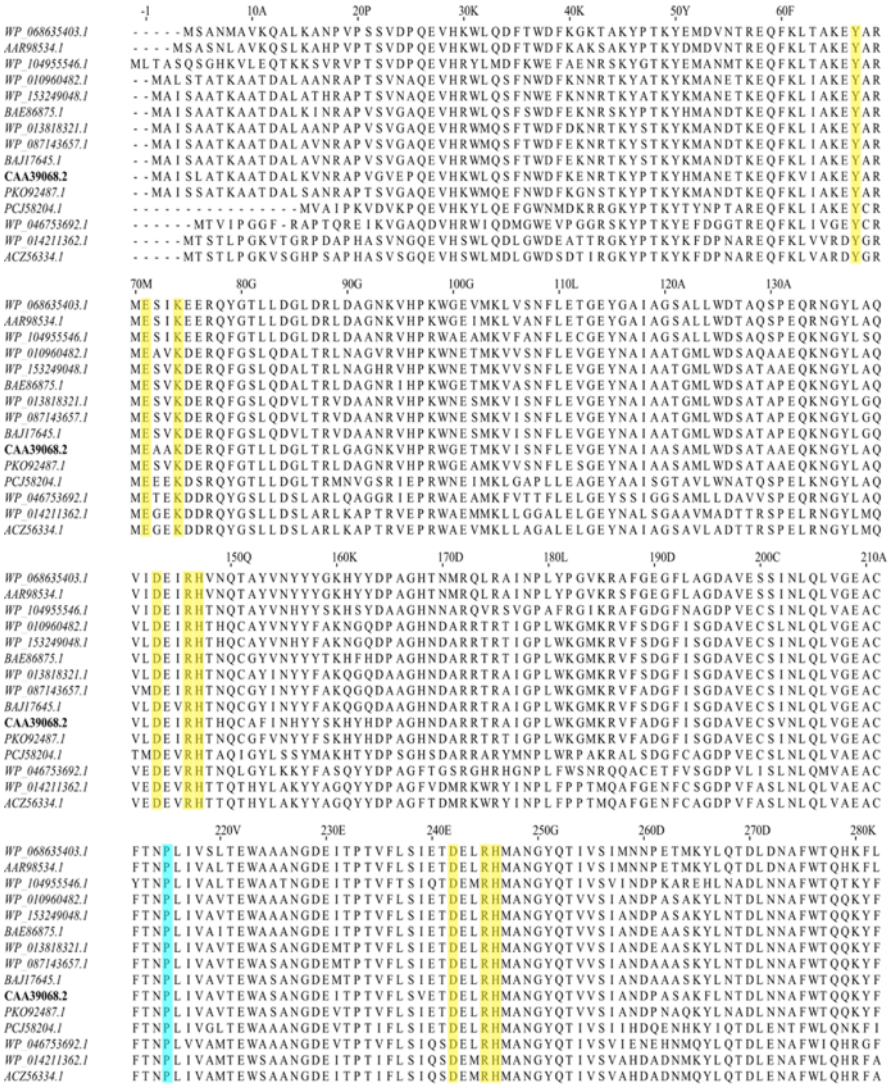

Figure 2-6 Multiple sequence alignment of a portion of the α-subunit of sMMOH
The strictly conserved residues of the hydrogen bonding network distal to the histidine ligands are highlighted in yellow. The strictly conserved Pro215 residue in Helix E is highlighted in cyan. Sequences compared include the α-subunit of hydroxylase proteins for a butane monooxygenase - AAR98534.1 *Brachymonas petroleovorans*. The remaining sequences are for the α-subunit of hydroxylase proteins for methane monooxygenases - WP_068635403.1 *Thauera butanivorans*; WP_104955546.1 *Sphingobium sp*. SCG-1; WP_010960482.1 *Methylococcus capsulatus* Bath; WP_153249048.1 *Candidatus Methylospira mobilis*; BAE86875.1 *Methylomicrobium japanense*; WP_013818321.1 *Methylomonas methanica*; WP_087143657.1 *Crenothrix polyspora*; BAJ17645.1 *Methylovulum miyakonense* HT12; PKO92487.1 *Betaproteobacteria bacterium* HGW-Betaproteobacteria-1; PCJ58204.1 *Rhodospirillaceae bacterium*; WP_046753692.1 *Mycolicibacterium elephantis*; WP_014211362.1 *Mycolicibacterium rhodesiae*; ACZ56334.1 *Mycolicibacterium chubuense* NBB4.

Another long chain of residues (236 – 252; α-subunit; Helix F) reorganize upon MMOB binding (**Figure 2-3**A) with the largest change occurring at Glu240. The side chain of Glu240 swings away from being solvent exposed to project into the interior of the protein in order to avoid a steric clash with Ser109 of MMOB. In this new position, Glu240 forms a hydrogen bond with Thr213, which has undergone a 180° rotation of the side chain residue. This hydrogen bond formation, and MMOB coverage of the surrounding sMMOH surface, block access to the active site in the diferric sMMOH:MMOB complex. A similar structural change was also observed in the *Mc* Bath sMMOH:MMOB protein complex.[70] The stretch of residues from 237 – 252 is additionally important, because it contains two coordinating ligands, Glu243 and His246 to the Fe2 iron atom. The reorganization of both Helices E and F arise as a result of hydrogen bond interactions and steric clashes with strictly conserved residues Ser109, Ser110 and Thr111 of MMOB (**Figure 2-2** and **Figure 2-4** and **Table 2-2**).

A combination of hydrogen bond interactions and steric clashes (**Table 2-3**) cause the reorganization of a stretch of 40 residues in sMMOH (302 – 341; α-subunit; Helices H and 4 along with intervening loop) (**Figure 2-3**B). Helix H also contains a section with the rare π-helical secondary structure, but unlike Helix E, does not contain either ligands to the diiron cluster or residues in the active site cavity. The π-helical portion of Helix H (residue 306 – 313) is rearranged in the MMOB-bound complex (residues 306 – 309 and 314 – 315). Helix 4 is a short helix in unbound sMMOH (332 – 338) that becomes part of a longer bent helix (331 – 356) in the sMMOH:MMOB protein complex. The extension of this helix in turn rearranges an adjacent unstructured loop region (428 – 435; α-subunit) (**Figure 2-3**C). Most of the sMMOH:MMOB interactions leading to the reorganization of Helices H and 4 arise from the N-terminal tail of MMOB (**Figure 2-3**B).

Table 2-3 List of Hydrogen Bond Donor-Acceptor Distances (in Angstroms) in sMMOH Alone (1MHY) and the Diferric (6YD0) and Diferrous Forms (6YDI) of the sMMOH:MMOB Complex.

Donor Acceptor pair	1MHY	6YD0	6YDI
D242-H147	2.67	2.60	2.66
D242-R146	2.92	2.86	2.81
D242-E71	2.80	2.60	2.66
D242-K74	2.78	2.71	2.69
D143-H246	2.76	2.75	2.83
D143-R245	2.95	2.76	2.81
D143-Y67	2.68	2.62	2.61

It is pertinent to note that specific interactions can be found between all the three regions of MMOB (N-terminal tail, C-terminal tail and core) with sMMOH (**Table 2-2**). These discrete interactions of MMOB residues with their counterparts on sMMOH result in very ordered regions of the MMOB protein as indicated by lower B-factors (**Figure 2-7**).

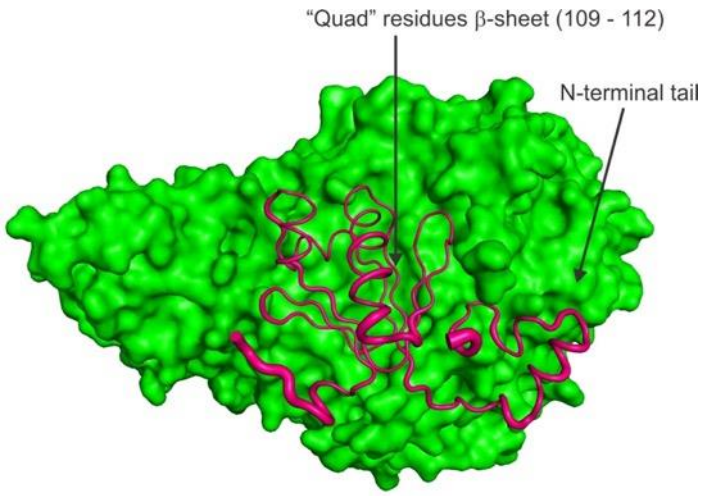

Figure 2-7 B-factor representation of MMOB in complex with sMMOH
The B-factors of the MMOB protein in the diferric sMMOH:MMOB structure are represented as a putty cartoon figure in magenta. The sMMOH surface is represented in green. Thicker secondary structure elements indicate high B-factor while thin regions indicate low B-factors.

2.4.3 MMOB Reorganizes the Active Site Cavity in sMMOH.

The active site cavity of sMMOH lies along one face of the diiron cluster (**Figure 2-8**). It is predominantly lined with non-polar residues on the surface facing the iron atoms (Leu110, Gly113, Ala117, Phe188, Phe192, Leu204, Thr213, Leu216, Ile217) along with the iron ligands Glu209, Glu243, and Glu114. This sMMOH active site cavity is reduced in volume upon MMOB binding (198 $Å^3$ to 156 $Å^3$) primarily due to the projection of the side chains of Leu110, Leu216 and Ile217 further into the cavity (**Figure 2-8**) The movement of the latter two residues is due to the reorganization of Helix E upon complex formation with MMOB. The side chain of Leu110 rotates in order to avoid a steric clash with the altered position of Leu216. In addition to size changes, the overall polarity of amino acid side chains that line the cavity is also altered upon MMOB binding. The hydrophobic character is further increased as a result of the rotamer shift of Thr213, which leads to the projection of the methyl group of Thr213 into the active site cavity in place of the hydroxyl moiety. In the unbound sMMOH resting state structure, the side chain hydroxyl group of Thr213 is in hydrogen bonding distance of two water molecules (**Figure 2-9**). These water molecules are not found in the active site cavity after MMOB binds sMMOH. Another water molecule that is hydrogen bonded to the backbone carbonyl group of Leu110 and the side-chain carboxylate of Glu114 is also lost. The loss of three crystallographically ordered water molecules and the side-chain hydroxyl group of Thr213 results in a more non-polar active site cavity in the sMMOH:MMOB protein complex. The loss of ordered solvents from the active site cavity not only opens up room for substrates to bind, it also increases the affinity for hydrophobic molecules such as oxygen and methane. The change in hydrophobicity and volume of the active site cavity is a direct result of MMOB binding that induces the extension of the π–helix in Helix E of sMMOH.

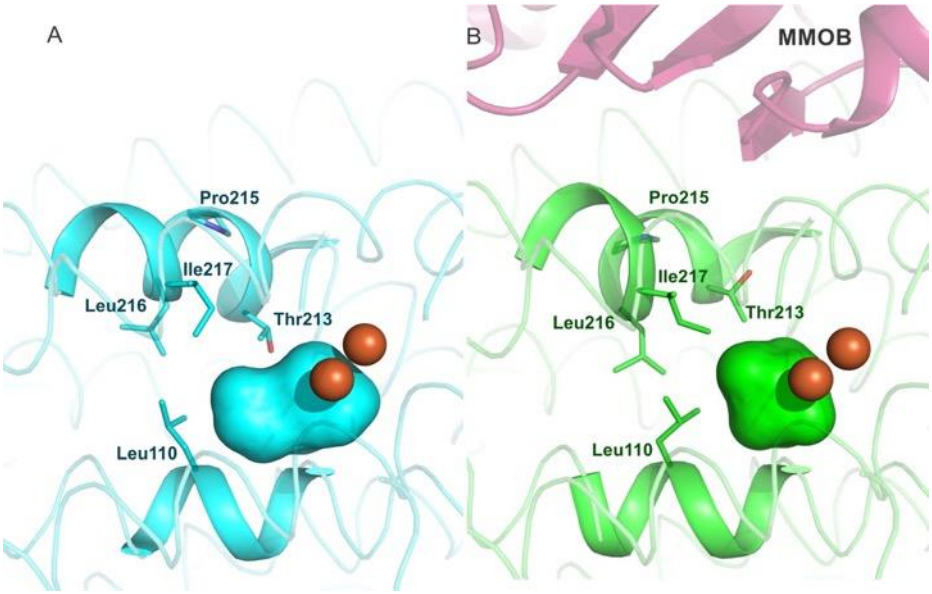

Figure 2-8 Reduction in size of the active site cavity.
The sMMOH active site cavity (colored surface representation) reduces in size upon MMOB binding, as calculated using HOLLOW.77 Diferric sMMOH in isolation (A) is represented as a cyan cartoon while the diferric sMMOH:MMOB complex (B) is shown as a green cartoon. MMOB is shown as a magenta cartoon. The iron atoms are shown as orange spheres. The active site cavity is indicated by cyan and green surfaces, respectively.

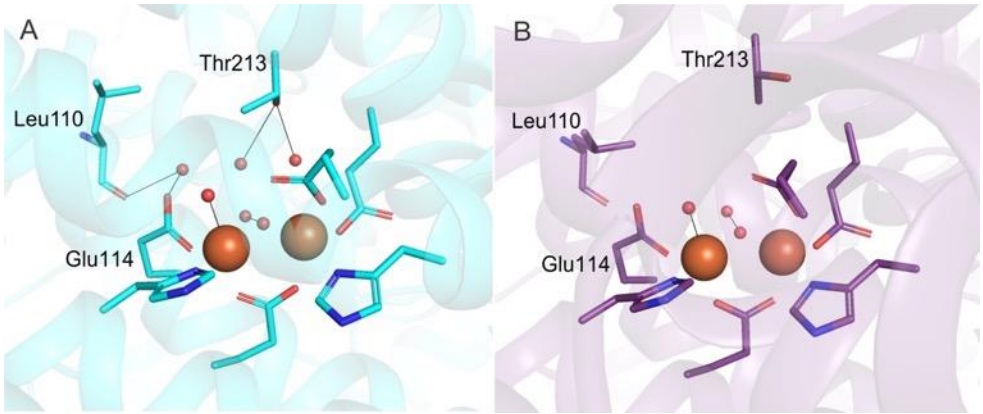

Figure 2-9 Active site water molecules
Comparison of active site water molecules between the sMMOH (A) and sMMOH:MMOB complex (B) structures. Color scheme – 1MHY (cyan carbon atoms); 6YDU (purple carbon atoms); water molecules and bridging μ-hydroxo groups (red spheres). Hydrogen bonds between residues and water molecules are shown by black lines. The rotamer shift of T213 and L110 leads to the loss of three active site water molecules upon MMOB binding.

2.4.4 The Binding of MMOB Causes Subtle Changes in the Structure of the Oxidized Dinuclear Iron Cluster.

Considering that two of the four diiron cluster-coordinating α-helices (E and F) undergo structural reorganization upon MMOB binding, it is essential to critically evaluate any changes in the metal coordinating environment. Viewed from the superposition of the secondary structure of the α-subunit, MMOB binding leads to a shift of the entire diiron cluster by ~ 0.6 Å. However, the relative arrangement of the ligands with respect to the iron atoms is roughly maintained based upon a superposition of only the metals and ligating residues (r.m.s.d = 0.14 Å) (**Figure 2-10**A). Most of the minor reorganization is localized on Fe2 because the E and F helices donating ligands to this iron atom also interact directly with MMOB. There is a small rotameric shift of Glu243 away from the plane of the iron atoms, but the binding mode stays monodentate and non-bridging. The two bridging hydroxo/aquo ligands to the diiron cluster characteristic of oxidized sMMOH are retained.

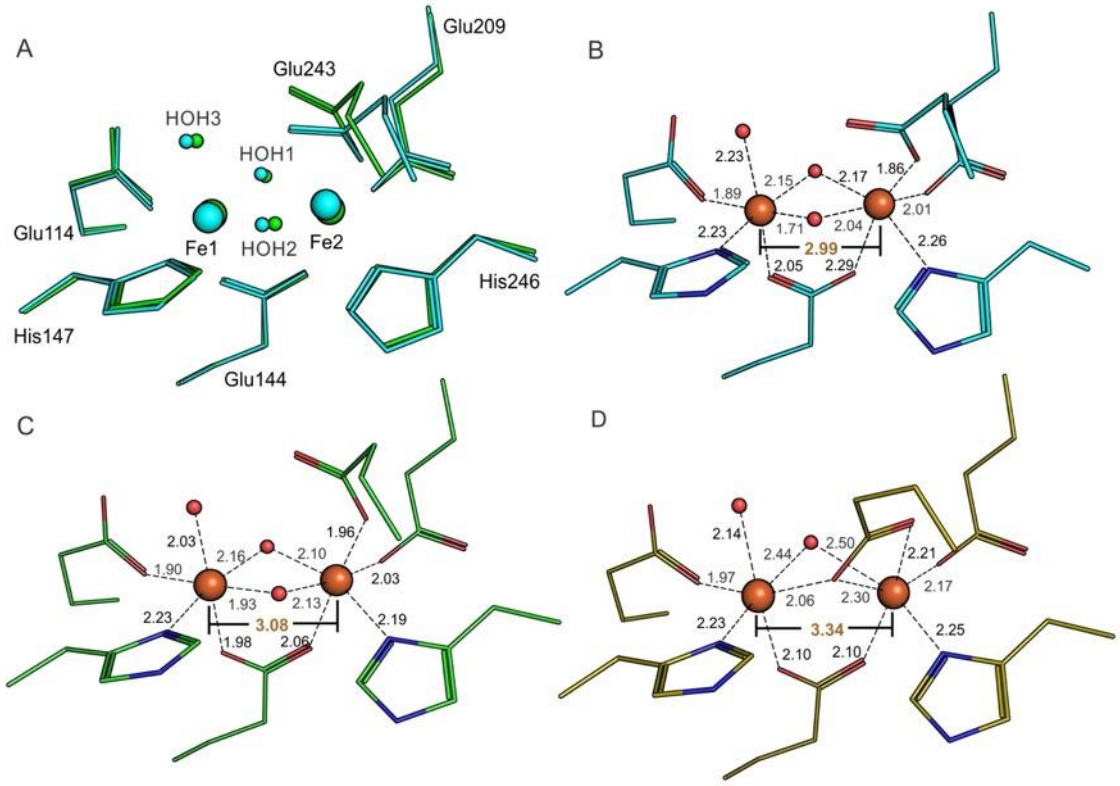

Figure 2-10 Changes in the diferric sMMOH diiron cluster induced by MMOB and reduction
The ligands and iron atoms are identified as per the labels in panel A. (A) Alignment of the oxidized diiron clusters of unbound sMMOH with the sMMOH^{ox}:MMOB complex based on just the first-sphere ligands and iron atoms. Cyan – sMMOH alone (1MHY); Green – diferric sMMOH:MMOB complex (6YD0). (B) Ligand to Fe distances for isolated diferric sMMOH (1MHY). (C) Ligand to Fe distances for diferric sMMOH:MMOB (6YD0). (D) Ligand to Fe distances for anaerobic diferrous sMMOH:MMOB (6YDI). The Fe-Fe distance is labeled in orange text.

2.4.5 The 'Carboxylate Shift' of Glu243 Occurs Upon Reduction of the Dinuclear Iron Cluster.

The canonical carboxylate shift of Glu243 to replace one of the bridging hydroxo/aquo ligands (HOH2) is observed upon a chemical reduction of the diiron cluster in the *Mt* OB3b sMMOH:MMOB complex crystals (**Figure 2-10**D). Reduction of the diiron cluster is also evident from the concomitantly measured Fe Kα XES spectra of the microcrystals (**Figure 2-11**Kα XES chemical sensitivity has been reported for some transition metal systems.[192, 193] Subtle changes in the peak positions and shapes, as well as the ratios between the $K\alpha_1$ and $K\alpha_2$ peak height, have

been described to be correlated with the number of unpaired d-electrons and hence with the transition metal oxidation state.[194-197] The reduced - oxidized difference spectrum (**Figure 2-11**blue line) shows an asymmetric shift in the $K\alpha_1$ peak as well as a decrease in intensity and a shift in position for the $K\alpha_2$ peak. This trend is similar to the difference observed between Fe^{2+} and Fe^{3+} standards in aqueous buffers collected under the same conditions as the sMMOH:MMOB samples (**Figure 2-11**, green line). While ligation environment of the Fe centers are not identical between the two systems, the observation of similar trends in both difference spectra is indicative of a predominant change from Fe^{3+} to Fe^{2+} in the sMMOH:MMOB samples. Similar features were also found previously for the Fe/Mn containing ribonucleotide reductase (RNR) R2c, where a transition between Fe oxidation states (orange trace in **Figure 2-11**, taken from ref.[172]) was observed. The observed oxidation is also supported by a change in the full width at half maximum (FWHM) of the $K\alpha_1$ peak and a change of the intensity ratio of the $K\alpha_1$ vs. the $K\alpha_2$ peak, as both have previously been reported as an indicator for the oxidation state.[194, 195] An increase of the FWHM by 0.17 eV was observed when comparing the diferric with the diferrous sMMOH:MMOB samples. In comparison, an increase of the FWHM by 0.29 eV was observed between the Fe^{2+} and Fe^{3+} standards and by 0.1 eV for these states of RNR R2c;[53] These numbers are in line with previously reported values for transition metal $K\alpha$ spectra.[194-197]

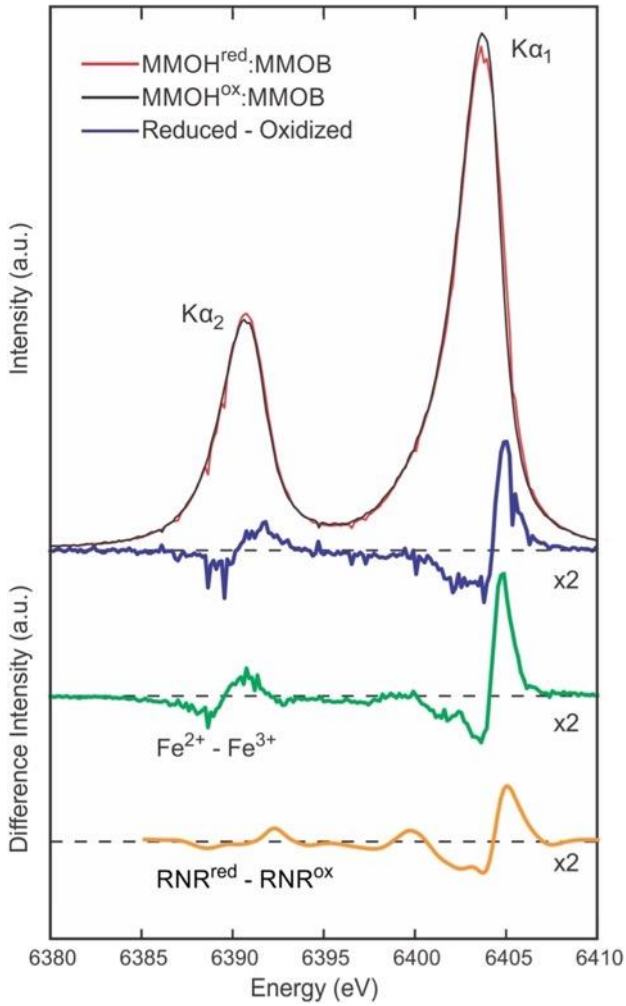

Figure 2-11 The Fe-Kα XES spectra diferric and diferrous sMMOH. Area-normalized Fe-Kα XES of microcrystals of chemically reduced (red) and oxidized (black) sMMOH:MMOB, and a subtraction (blue, 2× magnification) of the reduced minus oxidized spectra showing a clear asymmetric shift in the $K\alpha_1$ peak as well as a weakening in intensity and a slight shift in position for the $K\alpha_2$ peak. For comparison the difference spectra for aqueous Fe^{2+} - Fe^{3+} (green, 2× magnification), collected in the same experiment, and for solutions of reduced and oxidized ribonucleotide reductase (RNR) R2c (yellow, smoothed by wavelet denoising and 2× magnification), collected previously at LCLS are shown.

The magnitudes of these changes are consistent with the full reduction indicated by the occupancy of the shifted Glu243 in the crystal structure, but the extent of reduction cannot be unequivocally determined from the XES data. In the diferrous state, reorientation of Glu243 is

achieved by a rotameric shift at the β-carbon position. The iron-iron distance increases from 3.04 Å in the oxidized state to 3.29 Å in the reduced state, which is in close agreement to previous EXAFS studies (3.056 Å to 3.270 Å).[198] In concert, the ligand-to-iron distances increase, especially for HOH3 – Fe1 (2.08 Å to 2.21 Å), Glu144 – Fe1 (1.95 Å to 2.09 Å) and Glu243 – Fe2 (1.96 Å to 2.18 Å). The bridging aquo ligand that faces the active site cavity (HOH1) moves away significantly (~ 0.3 Å) from the iron atoms upon the change of oxidation state. The B-factors for the iron atoms are higher in the reduced state as compared to the resting diferric state (**Figure 2-12**). Furthermore, Fe2 specifically has a higher B-factor than Fe1, which is not surprising considering that it is ligated by residues from Helices E and F. The ligands coordinating Fe2 also appear to have higher B-factors, as opposed to the ligands of Fe1. Apart from the carboxylate shift of Glu243 and the lengthening of ligand to iron bond distances, there is no structural reorganization of either sMMOH or MMOB upon diiron cluster reduction. Structural alignments of the sMMOH α-subunits and their respective MMOBs before and after reduction provide r.m.s.d values of 0.08 Å (sMMOH) and 0.13 Å (MMOB). This means that the myriad of the structural changes identified above that occur in oxidized sMMOH upon MMOB binding also pertain in the fully reduced, O_2 reactive complex. In the active site, these changes include (i) compression of the active site cavity by shifts in Leu110, Leu216 and Ile217, (ii) closure of an access route from bulk solvent into the active site by reorganization of Glu240 and Thr213, (iii) generation of a more non-polar active site cavity with the loss of water molecules and rotamer shift of Thr213, and (iv) realignment of several of the iron ligands, especially those of Fe2.

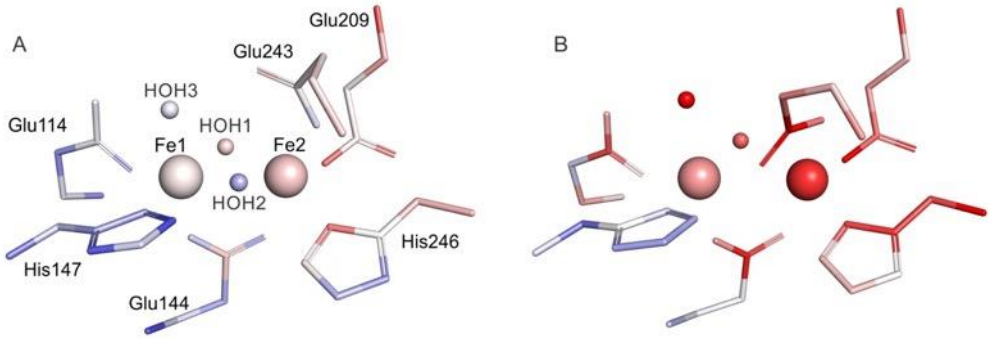

Figure 2-12 The diiron clusters of the sMMOH:MMOB complex. (6YD0, panel A) and diferrous sMMOH:MMOB complex (6YDI, panel B) are colored according to the atomic B-factors. A color spectrum from red to white to blue represent the B-factors, where red = 45, white = 35 and blue = 25.

2.4.6 Reduced sMMOH:MMOB Complex Reacts Rapidly with O_2 in the Microcrystals.

The sMMO catalytic cycle is initiated by the reaction of dioxygen with the diferrous sMMOH:MMOB complex and continues through a well-established series of intermediates to restore the diferric resting state.[5, 14, 68, 75, 76] While this process occurs readily in solution, it is important to test whether O_2 can access and react with the diiron cluster in crystals. This can uniquely be accomplished during the XFEL experiment because the reduced crystals on the tape of the DOT system can be briefly exposed to O_2 before being transported into the XFEL interaction region. Moreover, the experiment is conducted at room temperature with very fast XFEL pulses, so structural changes occurring during the reaction can be observed. The crystal structure of the sample after a 4 s exposure to pure O_2 atmosphere plus a 6 s travel to the XFEL interaction region (PDB: 6YDU) indicates that the diiron cluster rapidly reacts with O_2 to regenerate the diferric complex. The Fe Kα XES difference spectrum for the reduced (t=0) minus 10s O_2 incubated sMMOH:MMOB samples, albeit limited due to a higher noise level, is very similar to that for the reduced minus oxidized sMMOH:MMOB samples. This is consistent with the observation from the diffraction data for the *in-situ* re-oxidized sample, where Glu243 shifts back to the monodentate

coordination mode to Fe2 that is characteristic of the diferric cluster (**Figure 2-13**). Also, the Fe-Fe distance of the diiron cluster is restored to 3.02 Å and the bridging hydroxo ligand that is lost upon reduction is reacquired. The ligand-to-iron distances are similar to those of the oxidized diiron cluster. Passage of similarly reduced and washed crystals through a chamber filled with helium rather than O_2 retained all the structural features of diferrous sMMOH:MMOB (PDB: 6YY3) (**Figure 2-13**A and **Figure 2-13**B), showing that the diferrous state is preserved under these conditions in the absence of O_2. The 10 s oxidized crystal structure suggests that the reduced sMMOH:MMOB protein complex is indeed capable of binding oxygen, activating it, and completing a single turnover *in-crystallo* on a similar time scale to that observed in solution.[15, 68]

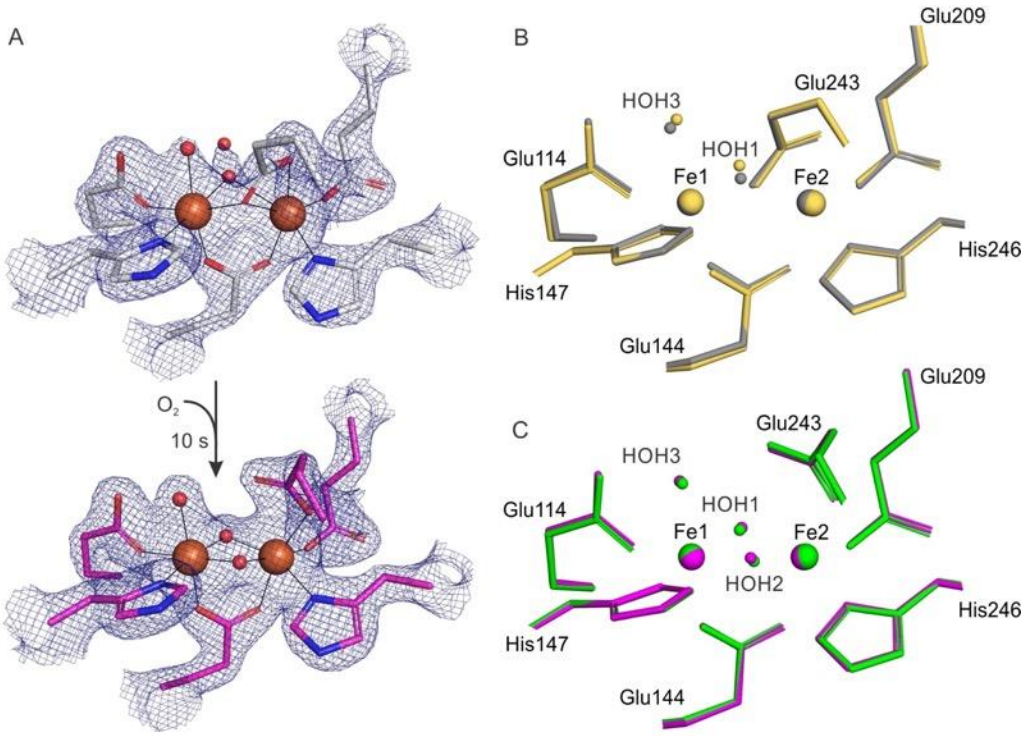

Figure 2-13 *In crystallo* reoxidation of diferrous sMMOH:MMOB microcrystals. Diferrous sMMOH:MMOB crystals washed of reductant undergo reoxidation upon exposure to O_2 in the reaction region of the DOT (drop on tape) system while staying reduced if exposed to helium under identical conditions. Panel A: 2Fo-Fc map of the diiron cluster of $sMMOH^{red}$:MMOB immediately prior to O_2 exposure (6YY3, top) and after post-4 s O_2 exposure, 6 s aging (6YDU, bottom) contoured to 2 σ. Panel B: An alignment of the diiron cluster of 6YY3 (grey atoms) with that of the diferrous sMMOH:MMOB complex (6YDI; yellow atoms) indicates that the sMMOH:MMOB crystals stay reduced in the absence of O_2 after removal of the dithionite reductant. Panel C: An alignment of 6YDU (purple atoms) with that of the diferric sMMOH:MMOB complex (6YD0; green atoms) indicates that the reduced sMMOH:MMOB crystals oxidize completely to the resting diferric state in this timeframe.

During the single turnover *in-crystallo* reaction, a region of unmodeled electron density disappears from the active site cavity (**Figure 2-14**). This density is present in both diferric and diferrous structures and is close to the expected binding location of hydrocarbon substrates. The unmodeled density is too large to be accounted for by methane or methanol, but the sMMO system is known to oxidize a remarkably wide range of other small hydrocarbons and similar molecules.[35] One explanation for this density and its loss after O_2 incubation is that it may represent an

adventitious substrate from the crystallization media, which is oxidized during turnover and diffuses out of the active site. This possibility will be further explored in ongoing studies.

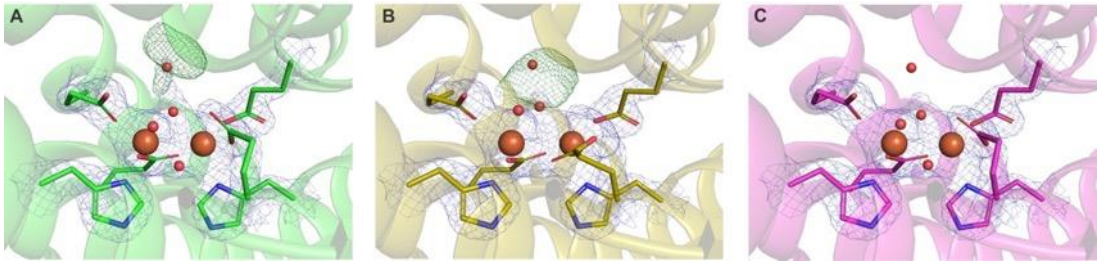

Figure 2-14 Loss of unassigned electron density upon reoxidation of microcrystals. (Fo-Fc electron density map (green mesh) contoured at 3σ, 2Fo-Fc Fo-Fc electron density map (blue mesh) contoured at 2σ) from the active site post in-crystallo single turnover. Panel A: Diferric sMMOH:MMOB complex (6YD0), Panel B: Reduced sMMOH:MMOB complex (6YDI) and Panel C: Re-oxidized sMMOH:MMOB complex (6YDU).

2.5 Discussion

This report describes for the first time the crystal structures of the sMMOH:MMOB protein complex in the fully diferric and O_2-reactive diferrous oxidation states. The resolutions of the crystal structures of these complexes offer a significant improvement over the previously reported *Mc* Bath protein complex structure.[70] A comparison of the diferric protein complex crystal structures for *Mc* Bath and *Mt* OB3b shows that the overall structure of the protein complex is similar. However, the enhanced resolution of the current structures enables detection of important structural reorganization in sMMOH upon binding MMOB not possible in the *Mc* Bath sMMOH:MMOB crystal structure. These include (i) alteration in the π-helical character of sMMOH Helices E and H, (ii) compression of the active site cavity, (iii) increase in hydrophobicity of the active site cavity due to loss of discrete water molecules, and (iv) MMOB binding-induced modulation of the hydrogen bonding network to the histidine ligands to the diiron cluster (*vide infra*). A clearer view of the structural reorganization in sMMOH caused by MMOB binding results from these structures and this lies at the heart of the many regulatory roles played by MMOB during catalysis. Furthermore, it is shown that the reduced sMMOH:MMOB protein complex binds and

activates O_2 *in-crystallo* to complete a single turnover cycle. This ability, in conjunction with high resolution diffraction and concomitant measurements at 298 K of both crystallographic and Fe Kα XES data, bodes well for future experiments designed to structurally characterize reaction cycle intermediates. Here, the structural changes induced by MMOB binding are discussed in the context of the current understanding of the roles played by MMOB in regulating catalysis.

2.5.1 Structures of sMMOH:MMOB Complexes without Radiation Induced Alterations.

The previously reported comparison of the structures of diferric *Mc* Bath sMMOH (PDB: 1MTY) and the *Mc* Bath sMMOH:MMOB protein complex (PDB: 4GAM) led to the conclusion that MMOB binding is sufficient to cause the characteristic 'carboxylate shift' of Glu243 in sMMOH without requiring reduction of the diiron cluster.[70] In the *Mt* OB3b sMMOH:MMOB complex structures reported here, this reorientation of Glu243 is only observed in the diferrous oxidation state of sMMOH (**Figure 2-10**). There are several possible explanations for this discrepancy including: (i) slight protein differences, (ii) crystal structure resolution and space group, (iii) temperature (93 K versus 298 K), and (iv) light sources (synchrotron versus XFEL). Of these, the light source is the most likely factor because synchrotron radiation has been demonstrated to cause partial or complete reduction of redox-active metal centers in many different types of proteins.[152, 153, 199-201] This dose-dependent radiation induced effect arises from solvated electrons generated *in situ* by the X-ray beam. The serial-femtosecond crystallographic (SFX) approach at XFELs addresses this issue by using significantly shorter and more intense X-ray pulses than produced by synchrotrons. XFEL pulses yield diffraction images from crystals on time scales of 10 - 35 fs, which is much less than the time required for radiation damage to occur by diffusion of solvated electrons or radicals even at room temperature. The concomitantly measured Fe Kα XES spectra in this study showed a clear difference between the oxidized and reduced species, indicating no noticeable photo-induced changes taking place under our experimental conditions. This is in line

with previous reports on several proteins and model compounds under conditions similar to the ones used in this study.[161, 166, 172, 173, 202]

Some evidence for radiation-mediated partial reduction of the diiron clusters in the *Mc* Bath sMMOH:MMOB crystal comes from the wide range of Fe-Fe distances observed in four protomers within the asymmetric unit (2.9 – 3.2 Å).[70] The largest of these values are close to that observed for diferrous clusters in the structure of reduced sMMOH.[38] In contrast, different distances are observed for the diferric and diferrous *Mt* OB3b sMMOH:MMOB crystals, and these distances correlate well with those from the more accurate solution EXAFS measurements.[198]

Another line of evidence suggesting a mixed oxidation state in the *Mc* Bath sMMOH:MMOB crystal derives from the predicted overall charge of the diiron cluster. It has been observed in structures of diferric sMMOH that the six positive charges of the iron atoms are balanced by the negative charges of the four glutamate residues and two bridging hydroxo ligands.[73] This neutral net charge is maintained after reduction of the iron atoms to the diferrous state by either the loss or protonation of the bridging hydroxo ligands, thereby avoiding the thermodynamic penalty of having a charged moiety inside the non-polar environment of the sMMOH active site. This charge-maintenance principle can even be extended to the high-valent intermediates generated during catalysis, wherein the increasing oxidation state of the iron atoms is balanced by the negative charges of the bridging peroxo and bis-μ-oxo (or equivalent) ligands.[73, 76] The diiron cluster in the crystal structure of diferric *Mc* Bath sMMOH:MMOB would have a net 1+ charge due to the loss of a hydroxo ligand without a change in iron oxidation state. In contrast, the structures of the *Mt* OB3b sMMOH:MMOB complexes show that the dinuclear iron cluster remains charge-neutral during the redox change, as expected. Thus, based upon the range of Fe-Fe distances, the charged active site, and comparison to the *Mt* OB3b protein complex structures, it is likely that the *Mc* Bath diferric sMMOH:MMOB protein complex was partially reduced as a result of radiation damage during data collection.

The success of the SFX technique in obtaining accurate representations of the oxidized and reduced diiron cluster in sMMOH:MMOB is especially important towards the future goal of capturing structures of enzymatic reaction cycle intermediates. The reduction potential of the key methane-reactive intermediate **Q** (dinuclear Fe^{IV}) has not been measured, but it is expected to be significantly higher than that of the diferric resting state. A reasonable estimate of ~ +1.4 to +1.6 V can be made based on the measured value of +1.0 V for the isoelectronic Compound I intermediate of heme oxygenases, which is incapable of breaking the strong C-H bond of methane except in the presence of strong chemical oxidants.[203, 204] The high positive redox potential of **Q** makes reduction in the X-ray beam very likely, as observed for highly oxidizing intermediates studied in other proteins using synchrotron light sources.[152, 153, 201] One solution to this problem has been to merge low X-ray radiation dose diffraction data from multiple crystals or multiple positions on one crystal to yield a complete dataset.[153, 205] The XFEL-based SFX methodology avoids X-ray induced reduction, and thus it does not have to be tailored to each new protein and unique reaction intermediate. The promise of this technique was recently demonstrated by a study that revealed structures for several intermediate states of the Mn_4CaO_5 cluster of photosystem II,[161, 166] as well as numerous other types of biological molecules.[162-165, 167-171]

2.5.2 Rationalizing the Regulatory Roles of MMOB.

MMOB exhibits regulatory effects throughout the catalytic cycle of sMMOH **Scheme 2-1**.[5, 71] The high-resolution structure of the *Mt* OB3b sMMOH:MMOB complex allows the basis for some of these effects to be examined. One dramatic effect of MMOB is to control the interaction of substrates with the activated oxygen of the diiron cluster in intermediate **Q** during the reaction cycle. The most important of these effects is to selectively increase the quantum tunneling component of the reaction with methane, which gives a large kinetic advantage to methane over undesirable substrates such as ethane.[66, 67, 89] Reactions of larger adventitious substrates *in vitro* are also affected. For example in the case of isopentane, the regiospecificity of hydroxylation shifts from the tertiary to the primary carbon upon formation of the sMMOH:MMOB complex.[114] Both

of these results suggest that MMOB binding must reorganize the sMMOH active site cavity to ensure optimal positioning of methane with respect to the activated oxygen of compound **Q** in order to enhance tunneling.[206] Indeed, the structure of the sMMOH:MMOB complex shows that the volume of the sMMOH active site cavity is decreased by 21 % in the sMMOH:MMOB complex (**Figure 2-8**), which would presumably position methane in the site closer to the reactive oxygen species. The same restricted active site architecture may constrain the motion of isopentane so that the primary carbon with the strongest C-H bond, but in the least sterically hindered position, is brought closest to the reactive oxygen of **Q** and thus is preferentially oxidized. It is interesting to note that a variant of MMOB termed the Quad mutant (N107G/S109A/S110A/T111A) leads to a significant decrease in the methane ^{2}H-KIE for the reaction of compound **Q** with methane (50 decreased to 6), indicating a loss of the quantum tunneling contribution to the reaction coordinate.[66, 67] The *Mt* OB3b sMMOH:MMOB structure shows that three of the four residues of this MMOB variant, Ser109, Ser110 and Thr111, directly interact with residues on Helices E and F of sMMOH; this interaction causes the reduction in volume of the active site cavity (**Figure 2-3**, **Figure 2-8** and **Table 2-2**). A mutation to smaller residues in positions Ser109 and Thr111, which make steric clashes with sMMOH residues, and a removal of the hydrogen-bond interaction of Ser110 with N214 of sMMOH would impair the structural reorganization of sMMOH Leu216, Ile217 and Leu110 (**Figure 2-3**A and **Figure 2-8**). This would lead to an expanded sMMOH active site cavity, which would be expected to perturb the optimal positioning of methane with respect to **Q**.

Another effect of MMOB binding to sMMOH is to lower the mid-point reduction potential of the diiron cluster by 132 mV (cf. +48 mV to -84 mV),[143] thereby increasing the thermodynamic driving force for the step of O_2 binding and activation at the reduced diiron cluster. There are many mechanisms by which structure can affect the redox potential of a metalloprotein, and these primarily involve changes in hydrophobicity of the metal environment and charge donation by the first sphere ligands.[207-210] It is shown above that the structural changes evoked by MMOB binding result in a more constricted active site with increased hydrophobicity due to excluding water and

introducing more aliphatic residues into the boundary of the substrate binding cavity (**Figure 2-8**, **Figure 2-9** and **Figure 2-15**). An increase in hydrophobicity would be expected to increase the redox potential of the diiron cluster and decrease its affinity for O_2.[207, 211] This outcome is opposite to that experimentally observed in solution. However, the increase in hydrophobicity would lead to an increase in the affinity for O_2 binding in the active site prior to forming a complex with the diiron cluster. The appropriate balance between binding substrates and activating O_2 on the diiron cluster may be achieved through other structural changes revealed by the high resolution structure of *Mt* OB3b sMMOH:MMOB complex. For example, an increased negative charge density on first sphere ligands that stabilizes the Fe^{III} state over the Fe^{II} state will decrease the redox potential. A comparison of the coordination environment of the diferric cluster in sMMOH to that in the sMMOH:MMOB complex shows that the first sphere ligands do not rearrange significantly upon MMOB binding (**Figure 2-10**A, B and C). The only reorganization of note is the small change in the rotamer configuration of Glu243 with respect to the diiron cluster, which moves the distal oxygen of the carboxylate function out of hydrogen bonding range of the water ligand (HOH3) on Fe1. However, this change and several additional small second sphere changes cause some of the ligand-to-iron distances to shorten upon complex formation with MMOB, namely HOH3-Fe1, Glu144-Fe1 and Glu144-Fe2 (**Figure 2-10**B and C). These shorter bonds reflect a greater charge donation by the ligands to the iron atoms, thereby lowering the reduction potential.

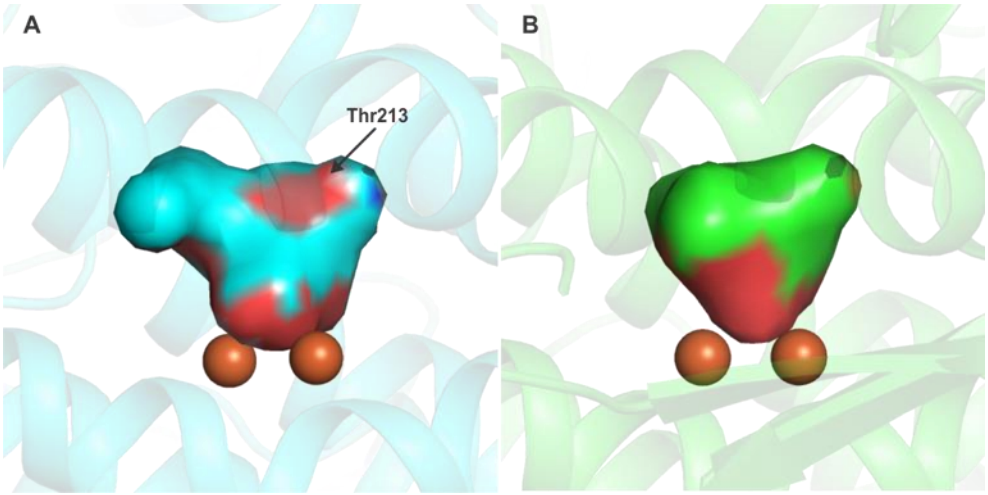

Figure 2-15 Change in active site polarity when MMOB binds to sMMOH.
Surface representation of the sMMOH active site cavity depicts the difference in polarity in diferric sMMOH (panel A) and the diferric sMMOH:MMOB complex (panel B) as a result of the reorganization of Thr213.The side-chain of residues that project into the active site cavity are colored according to the following scheme; carbon atoms = cyan in sMMOH, green in sMMOH:MMOB; oxygen atoms = red; nitrogen atoms = blue. The iron atoms are shown as orange spheres.

The charge donation by the first sphere ligands may also be affected by hydrogen bonding networks involving second sphere residues. As one example, MMOB binding causes displacement of an active site water that hydrogen bonds to Glu114 in uncomplexed sMMOH, thereby increasing charge density on Glu114 (**Figure 2-9**). A potentially much more important example is described in the following section.

2.5.3 Role of Hydrogen Bonding in Second Sphere Active Site Residues.

A set of strictly conserved second-sphere amino acid residues near the diiron cluster histidine ligands has been observed to be present in sMMOH and the entire family of bacterial multicomponent monooxygenases (BMMs) and structurally related enzymes (**Figure 2-6** and **Figure 2-16**).[212] In these enzyme systems, the second sphere aspartate to histidine hydrogen bonds are strictly conserved such that the typical diiron cluster binding motif [E/D-$X_{\sim 30}$-E-X_2-H] is better described as [E/D-$X_{\sim 29}$-DE-X-(R)H].[213] In the BMM enzyme sub-family, the penultimate Arg is completely conserved [E/D-$X_{\sim 29}$-DE-X-RH] and the hydrogen bond network is extended further

beyond the aspartate residues to the surface of the protein. The function of this network remains undefined in the BMM enzymes. However, the current high resolution structure of *Mt* OB3b sMMOH:MMOB allows the network of hydrogen bonds to be described in detail for the first time (**Figure 2-15** and **Figure 2-16**).

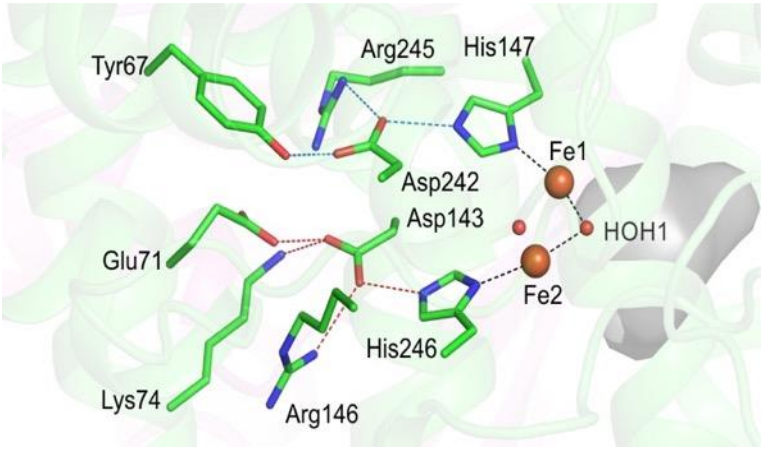

Figure 2-16 Strictly conserved hydrogen bond network extending from diiron cluster. The iron atoms are represented as orange spheres while the bridging μ-hydroxo groups are shown as red spheres. The active site cavity is shown as a grey surface. Black dashed lines depict the *trans* positioning of the histidine ligands with respect to the μ-hydroxo moiety facing the active site. Red and blue dashed lines show the hydrogen bond network to each of the two histidine residues (His147 – blue, His246 – red).

One role that has been suggested for the hydrogen bonding network is electron transfer to the diiron cluster from the reductase MMOR.[212] However, this role is unlikely because the exterior sMMOH protein surface from which the hydrogen bond network starts, lies at the dimerization interface between the two sMMOH monomers. As a result, this surface of sMMOH is occluded and cannot be involved in binding MMOR or in electron transfer. A more likely role for this network appears to be a structural stabilization of the diiron cluster, as the hydrogen bonds are arranged in a crisscross manner that would brace the position of the histidine ligands (**Figure 2-16** and **Figure 2-17**)Accordingly, the helices containing the residues involved in the hydrogen bond network have the lowest B-factors in the entire sMMOH protein structure (**Figure 2-17**)

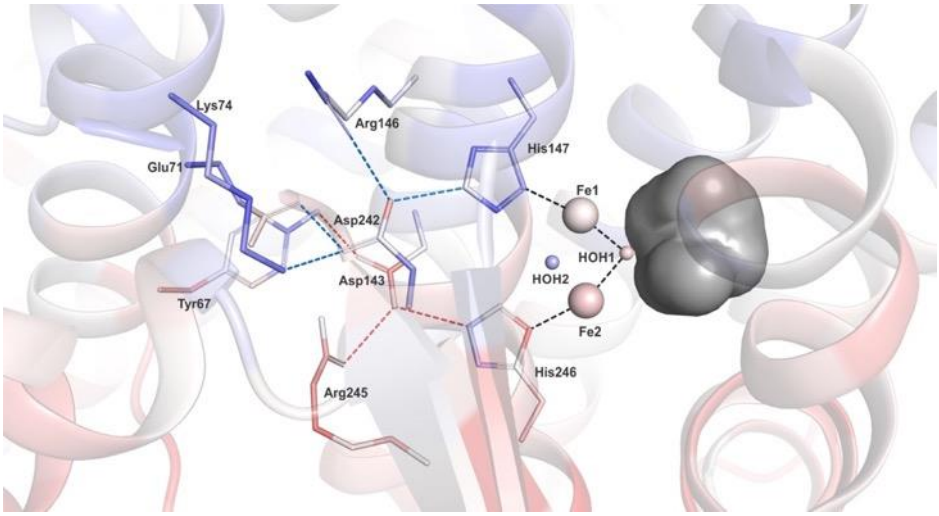

Figure 2-17 Alternative view of the hydrogen-bonding network.
The residues are colored according to its B-factor where blue indicates the lowest B-factor (25), red the highest (45) and white an intermediate value (35). The iron atoms are represented as larger spheres while the bridging μ-hydroxo groups are shown as smaller spheres. The active site cavity is shown as a grey surface. Black dashed lines depict the trans-positioning of the histidine ligands with respect to the μ-hydroxo moiety facing the active site. Red and blue dashed lines show the hydrogen bond network.

Another potential role of the hydrogen bond network might be to tune the electronic properties of the diiron cluster by modulating charge donation from the diiron cluster histidine ligands. A comparison of the hydrogen bonding network in diferric *Mt* OB3b sMMOH alone (PDB:1MHY) to that in sMMOH:MMOB shows an overall shortening of the hydrogen bonds (**Table 2-3**). In particular, the two aspartate-to-histidine ligand hydrogen bonds are relatively short as measured in the oxidized *Mt* OB3b sMMOH:MMOB complex (average donor acceptor distance = 2.7 Å) (**Figure 2-16** and **Figure 2-17** and **Table 2-3**). A strong hydrogen bond between the aspartate and histidine residues would partially deprotonate the histidine ligand, thereby increasing its imidazolate character and thus increasing electron donation to the iron atoms and decreasing the redox potential.

2.5.4 Implications of the sMMOH:MMOB Hydrogen Bonding Network for Reactivity.

It is well established that a hydrogen bonding Asp-His motif plays a vital role in increasing the basicity of the active-site histidine residue in both serine proteases and in heme-containing oxygenases and peroxidases.[214, 215] In the latter enzyme systems, greater charge donation from the axial histidine/cysteine ligand is positively correlated with increased reactivity towards C-H bond activation.[122, 216, 217] This effect has been rationalized as arising from an increase in the p*K*a of the Fe^{IV}-OH compound II species, resulting in a stronger Fe^{IV}-O-H bond in compound II after hydrogen atom abstraction from the substrate C-H bond. This increases the driving force for the compound I mediated hydrogen atom abstraction step and reduces the activation energy barrier.

Similar considerations may apply to sMMO, which must generate an even more potent reactive species to effect the oxygenation of methane. The histidine ligands are positioned opposite to the active site cavity (**Figure 2-16** and **Figure 2-17**). In the compound **Q** species of sMMO, the reactive iron-oxygen moiety is expected to be either a Fe^{IV}-O-Fe^{IV} group or a terminal Fe^{IV}=O group that projects into the active site cavity.[85, 92, 198] One or both of the histidine ligands are *trans* to the reactive oxygen species. Thus, modulation in the electron donating capacity of the histidine ligands can have very important effects on the reactivity of **Q** towards methane oxidation. This modulation is linked in part to the conformational changes induced by MMOB as it binds (**Table 2-3**), which may contribute to the dramatic effects MMOB has on the reactivity of **Q**.[71] Unfortunately, it is not currently possible to experimentally examine the role of the conserved hydrogen bonding network by creating variants because efforts to heterologously express sMMOH in numerous laboratories have not been successful.

2.5.5 Correlation of *Mt* OB3b sMMOH:MMOB Complex Structures with Past Spectroscopic Studies.

The high resolution crystal structures of the sMMOH:MMOB complex also enable a correlation between MMOB binding-induced changes in structure and electronic environment of the diiron

cluster. EPR spectroscopic studies of the $S = ½$ mixed-valent state of sMMOH and the diferric state radiolytically one-electron-reduced at 79K (a probe of the diferric state) have provided evidence for a weakening of the antiferromagnetic coupling between the iron atoms upon MMOB binding.[63, 218] The antiferromagnetic coupling constant J for the spin-exchanged mixed-valent diiron cluster is reduced from ~30 cm^{-1} to ~5 cm^{-1} in the presence of MMOB. Accordingly, the structure of the sMMOH:MMOB complex shows that the bridging Fe-O bonds (Fe1-HOH2, Fe2-HOH2) are lengthened (**Figure 2-10**B and C), which would be expected to moderate the spin-exchange coupling between the iron atoms.

The electronic environment of the reduced diiron cluster of sMMOH has also been probed in the presence and absence of MMOB with circular dichroism (CD) and magnetic circular dichroism (MCD) spectroscopies.[219, 220] These studies showed that the ligand field environment of only one of the two iron atoms of the diiron cluster changes upon MMOB binding to sMMOH. The crystal structure of the protein complex clearly shows that this insight is correct and identifies the affected iron atom as Fe2 (**Figure 2-18**). The ligand field of each iron atom of the reduced diiron cluster was additionally calculated in order to match the experimental ligand field transitions of the sMMOH:MMOB complex.[127] A predicted Fe1-Fe2-Glu209 angle of 135° was shown to best match the experimental ligand field transitions. This angle would represent an increase from 120° observed for the diferrous sMMOH alone and would expose a site for O_2 binding to Fe2 in the absence of a bridging aquo-ligand (**Figure 2-18**). The MCD spectra show that both irons are 5-coordinate in solution, and thus the weak bridging water (HOH1) seen in the crystal structure is lost. In accord with the spectroscopic and computational results, the Fe1-Fe2-Glu209 angle in the reduced sMMOH:MMOB complex is observed to be 143°. It is pertinent to note here that the Glu209 backbone is not anchored by an intra main-chain hydrogen bond upon MMOB binding. Moreover, the B-factors of the first and second sphere residues of Fe2 are large compared to those of Fe1, suggesting that flexibility in this region may be associated with preparing the diiron cluster to bind O_2 (**Figure 2-12**). Finally, analysis of the CD spectra showed that changes in protein

structure occur in the active site away from the diiron cluster upon MMOB binding to diferrous sMMOH that are essential for a rapid reaction with O_2.[127] The crystal structure of the diferrous complex demonstrates numerous changes in second sphere residue positions and solvent occupancy (**Figure 2-18**) that will affect the accessibility to the active site and the geometry of small molecule binding.

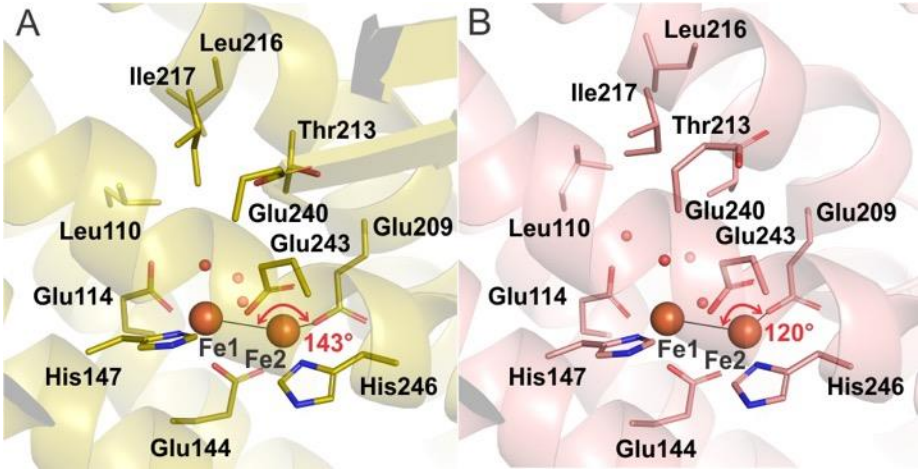

Figure 2-18 Angle change of E209 enhances O_2 reactivity
Reduced sMMOH^{red}:MMOB complex (PDB: 6YDI, panel A) and reduced sMMOH from *M. capsulatus* Bath (PDB: 1FYZ, panel B) shows reorganization prior to O_2 binding and activation. The iron atoms are shown as orange spheres while red spheres represent water molecules.

2.6 Conclusion

The use of the XFEL SFX technique in combination with highly diffracting crystals of the *Mt* OB3b sMMOH:MMOB complex have significantly advanced structural studies of the sMMO enzyme system. This new approach has resulted in a high resolution crystal structure of the fully oxidized resting state of sMMOH:MMOB and the first crystal structure of the O_2-reactive diferrous state. The SFX methodology is shown here to circumvent the most common problem in determining the crystal structure of oxidized metalloenzymes, which is reduction during the long duration synchrotron experiment. This conclusion is further supported by the concomitantly collected XES data that indicate a clear change in oxidation state of the Fe site between the oxidized resting state and the diferrous state. The high-resolution crystal structures presented here illustrate in detail the extensive structural reorganization of both sMMOH and MMOB upon complexation. Some of these conformational changes shed light on the MMOB mediated regulation of catalysis by providing structural explanations for previous mutation and spectroscopic results. Most importantly, the crystal structures show the manner in which the active site cavity is altered in the protein complex, which is vital for enhancing the reaction with O_2 and ultimately methane. Finally, the rapid reoxidation of the diiron cluster in the crystal of reduced sMMOH:MMOB upon exposure to O_2 without loss of diffraction quality is very promising for ongoing XFEL SFX experiments designed to capture crystal structures of reaction cycle intermediates such as **Q**.

Chapter 3 Structural Studies of *Methylosinus trichosporium* OB3b Soluble Methane Monooxygenase Hydroxylase and Regulatory Component Complex Reveal a Transient Substrate Tunnel

Portions of this chapter are reprinted and adapted with permission from: Jason C. Jones, Rahul Banerjee, Ke Shi, Hideki Aihara, and John D. Lipscomb* *Biochemistry*, **2020**, *59*, 2946-2961.

My contributions to this project were: conceiving and planning the experiments, sample preparation, perform the experiments, analyze the results, draft manuscript preparation, and review/approve the final manuscript.

3.1 Synopsis

The metalloenzyme soluble methane monooxygenase (sMMO) consists of hydroxylase (sMMOH), regulatory (MMOB), and reductase components. When sMMOH forms a complex with MMOB, the rate constants are greatly increased for the sequential access of O_2, protons, and CH_4 to an oxygen-bridged diferrous metal cluster located in the buried active site. Here, we report high resolution X-ray crystal structures of the diferric and diferrous states of both sMMOH and the sMMOH:MMOB complex using the components from *Methylosinus trichosporium* OB3b. These structures are analyzed for O_2 access routes enhanced when the complex forms. Previously reported, lower resolution structures of the sMMOH:MMOB complex from the sMMO of *Methylococcus capsulatus* Bath revealed a series of cavities through sMMOH postulated to serve as the O_2 conduit. This potential role is evaluated in greater detail using the current structures. Additionally, a search for other potential O_2 conduits in *Methylosinus trichosporium* OB3b sMMOH:MMOB revealed a narrow molecular tunnel, termed the W308-Tunnel. This tunnel is sized appropriately for O_2 and traverses the sMMOH-MMOB interface before accessing the active site. Kinetics of O_2 reaction with diferrous sMMOH:MMOB in solution show that use of the MMOB V41R variant decreases the rate constant for O_2 binding >25,000-fold without altering component affinity. The location of Val41 near the entrance to the W308-Tunnel is consistent with the tunnel serving as the primary route for O_2 transfer into the active site. Accordingly, the crystal structures show that formation of the diferrous sMMOH:MMOB complex restricts access through the chain of cavities while opening the W308-Tunnel.

3.2 Introduction

Methane monooxygenase (MMO) catalyzes the conversion of methane to methanol with the incorporation of one atom of oxygen from O_2.[5]

$$CH_4 + O_2 + NADH + H^+ \rightarrow CH_3OH + H_2O + NAD^+$$

Two forms of the enzyme have been identified in methanotrophic bacteria. A copper-containing particulate form (pMMO) is present when the soluble copper:biomass ratio is > 5.7 μmol/g protein, while an iron-containing soluble form (sMMO) is present in some methanotrophs at lower copper concentrations.[221] Together, the MMOs prevent a significant fraction of the 10 billion tons of biogenic methane produced annually from entering the atmosphere.[16, 222]

The sMMOs from *Methylosinus trichosporium* (*Mt*) OB3b and *Methylococcus capsulatus* (*Mc*) Bath are very similar multicomponent metalloenzymes despite significant differences in the cellular structure and metabolism of the two host organisms.[5, 14, 15, 35, 174] Both sMMOs consist of the following protein components: i) a 40 kDa FAD and Fe_2S_2 cluster-containing reductase (MMOR), ii) a 245 kDa $(\alpha\beta\gamma)_2$ hydroxylase (sMMOH) containing an oxygen-bridged, nonheme diiron cluster, and iii) a 16 kDa regulatory protein termed MMOB.[5, 14, 15, 33, 35, 37, 38, 40] The catalytic cycle begins with the transfer of two electrons from MMOR to the sMMOH diiron cluster, priming it to react with O_2. In the presence of MMOB, a series of intermediates is generated at the diiron cluster during the oxygen activation process (termed **O**, **P***, and **P**) that culminates in the formation of a diiron(IV) intermediate termed compound **Q**.[5, 14, 33, 68, 75, 76, 85, 86, 90, 92, 198, 223] **Q** is observed to react directly with methane by a hydrogen atom abstraction and hydroxyl radical rebound mechanism.[78, 80, 89, 104]

Regulation of the catalytic cycle by MMOB is a critical aspect of sMMO catalysis. At the beginning of the catalytic cycle, complex formation between reduced sMMOH and MMOB increases the rate constant for the reaction of O_2 with the diiron cluster to form **P*** by at least 1000-fold over that for reduced sMMOH alone.[68, 69] Formation of the sMMOH:MMOB complex is also key for maintaining the specificity of sMMO for methane in an environment that may contain numerous alternative substrates, almost all of which have much weaker C-H bond strengths than methane (bond dissociation energy of 105 kcal/mol).[35, 224, 225] MMOB apparently alters the reactivity and specificity of **Q** by two mechanisms.[66, 67, 71, 74, 75, 89, 104] In the first mechanism, the

formation of the sMMOH:MMOB complex opens a route into the active site which is size selective for methane. In the second mechanism, the hydrogen atom abstraction reaction between **Q** and methane in the sMMOH:MMOB complex is accelerated by quantum tunneling; this mechanism of acceleration is not observed for larger substrates or when MMOB variants are utilized. The structural aspects of the sMMOH:MMOB complex that enforce regulation of O_2 and CH_4 binding and reaction are poorly understood, but they are essential, because methane is the only growth substrate for the methanotrophs.

A general theme of all of these regulatory events in sMMO is a strict control of the entry and exit of substrates and products, respectively, during the catalytic cycle.[14, 15, 66, 70, 71, 131] X-ray crystal structures of sMMOH have provided evidence for two putative routes of substrate entry (**Scheme 3-1**). First, a set of three large, internal voids termed cavities have been identified in the α-subunit of sMMOH, one of which (Cavity 1, Cav 1 in **Scheme 3-1**) is the active site containing the diiron cluster.[37, 38, 40, 43] It has been proposed that O_2 and methane could traverse from solvent to the buried nonheme diiron active site by filling these cavities.[70, 134] However, the passage between Cavities 2 and 1 is greatly restricted in the structure of sMMOH alone.[43, 50] The 2.9 Å X-ray crystal structure of the oxidized sMMOH:MMOB complex from *Mc* Bath showed that a structural change occurs which widens the bottleneck between Cavities 2 and 1.[70] This observation could provide an explanation for the dramatic effects of MMOB on O_2 and methane binding and reactivity if it can be shown to extend to the reduced sMMOH:MMOB complex and intermediates in the reaction cycle.

Scheme 3-1 Proposed Substrate Access Routes in the sMMOH α-Subunit

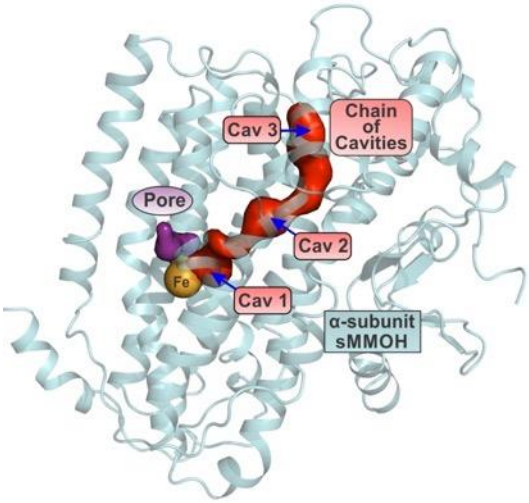

Another potential route for O_2 and methane entry was identified as a short, narrow path termed the Pore, which extends from the sMMOH surface directly into the active site.[39, 212, 226] However, this route is made less likely by the observation that, in the oxidized *Mc* Bath sMMOH:MMOB crystal structure, the Pore is blocked by shifts of sMMOH residues and by the fact that MMOB covers the Pore.[70]

In order to critically examine the potential substrate entry routes, it is vital to obtain a crystal structure of the diferrous sMMOH:MMOB complex, which is the state primed to react with O_2. Structural changes in sMMOH and MMOB must also be analyzed in reference to solution transient kinetic studies that depict the influence of MMOB and its variants on substrate regulation at defined points within the catalytic cycle. In the current study, higher resolution crystal structures of *Mt* OB3b sMMOH alone and in complex with MMOB in both the oxidized and reduced states are used to evaluate the effects of MMOB binding and sMMOH reduction on the proposed substrate entry routes. We also introduce a third potential category of substrate entry route termed a tunnel, which is defined as a narrow, convoluted path that only allows one dimensional substrate migration. One such tunnel that involves the sMMOH-MMOB interface is identified in the complex.

Mutagenesis of key MMOB residues lining this tunnel are shown to affect O_2 entry in a manner consistent with the kinetics and selectivity of the process.

3.3 Experimental procedures

3.3.1 Reagents, Protein Expression and Purification.

Water used in all experiments was purified with a Millipore Super-Q system. Standard reagents used in this study were purchased from Fisher Scientific. Chemicals for crystallization of proteins including PEG/Ion Screen Reagents 18 and 40, Tacsimate®, PEG6000, and PEG3350 were purchased from Hampton Research unless otherwise stated. Glass rods for crushing crystals and crystal seed bead tubes were also supplied by Hampton Research. Ultra-high purity grades of 3-(N-morpholino)propanesulfonic acid (MOPS) buffer, PEG3350 (alternative source) and sodium phosphate dibasic were obtained from Sigma-Millipore. sMMOH, MMOR, MMOB, and variants of MMOB were produced and purified as previously described. [34, 76]

3.3.2 Protein Mutagenesis.

A Thermo Scientific™ Phusion Site-Directed Mutagenesis Kit was used to introduce point mutations at residues 39 and 41 of the pT7-7 derived plasmid pBWJ400 containing the wild type *M. trichosporium* OB3b MMOB gene.[44] The primers shown in **Table 3-1** were synthesized at the University of Minnesota Genomics Center.

Table 3-1 MMOB Variant Primers

MMOB Mutant	Mutagenesis Forward Primer 5'-3'	Mutagenesis Reverse Primer 5'-3'
V41(WT)	GTGGTTCTGGTGCTGATGAAGAG	GGCGTTGGACTCGTGGAC
V41F	GTGGTTCTGTTCCTGATGAAGAG	GGCGTTGGACTCGTGGAC
V41R	GTGGTTCTGCGTCTGATGAAGAG	GGCGTTGGACTCGTGGAC
V41E	GTGGTTCTGGAGCTGATGAAGAG	GGCGTTGGACTCGTGGAC
V39F	AACGCCGTGTTTCTGGTGCT	GGACTCGTGGACGACCTG
V39R	AACGCCGTGCGTCTGGTGCT	GGACTCGTGGACGACCTG

3.3.3 Crystallization of sMMOH.

All crystallization was performed at room temperature. *Mt* sMMOH was crystallized using the hanging drop vapor diffusion method by first mixing 1.5 μl of protein solution containing 45 μM sMMOH (90 μM active sites) and 90 μM MMOB in 25 mM MOPS, pH 7 with 1.5 μl of crystallization solution containing 5% (w/v) PEG6000 in the same buffer. Whisker-like long thin crystals appeared within 2 days. The crystals were pulverized and added to a seed bead tube, brought up to a total volume of 50 μl with mother liquor and vortexed for 3 min in 30 s intervals. The seed stock was used to set up a second hanging drop experiment by first mixing 1.0 μl of protein solution containing 45 μM sMMOH (90 μM active sites) and 90 μM MMOB in 25 mM MOPS, pH 7 with 2.0 μl of crystallization solution containing 0.2 M $Na_2HPO_4 \cdot 2H_2O$ and 20% (w/v) PEG3350. Subsequently, 0.5 μl of seed stock suspension was added to this drop. Over-nucleated crystals formed within a few days. Crystals were pulverized with a glass rod and added to a seed bead tube. They were then brought to a total volume of 50 μl and vortexed for 3 min in 30 s intervals. The seed stock was used to conduct a third hanging drop experiment by first mixing 1.0 μl of protein solution containing 45 μM sMMOH (90 μM active sites) and 90 μM MMOB in 25 mM MOPS, pH 7 with 2.0 μl of crystallization solution containing 8% Tacsimate® and 20% (w/v) PEG3350. Then 0.5 μl of seed stock solution was added to this drop. Disc-shaped crystals formed after 1 week. Diferric sMMOH crystals were cryo-protected with 10% ethylene glycol and frozen in liquid nitrogen. sMMOH crystals were chemically reduced in an anaerobic chamber (Belle Technology) by soaking in a solution containing 8% Tacsimate®, 20% PEG3350 (w/v), 5 mM sodium dithionite and 200 μM methyl viologen for 30 min, cryo-protected with mineral oil, and then frozen in liquid nitrogen. Despite the absence of MMOB in these crystals, the presence of MMOB is vital in the crystallization solution. This crystal form is the same as the Form 2 diferric *Mt* sMMOH crystals that were described in the original crystallography study for this enzyme.[40]

The diferric sMMOH structure obtained is nominally the same as that from the Form 1 crystals obtained in the absence of MMOB, albeit with higher resolution.

3.3.4 Crystallization of sMMOH-MMOB Complex.

A Rigaku CrystalMation fully integrated platform for protein crystallization was used to screen for conditions that would produce sMMOH:MMOB crystals. PEG/Ion Screen Reagent 18 (8% v/v Tacsimate® pH 8.0, 20% w/v PEG3350) and Reagent 40 (0.2 M Sodium phosphate dibasic dihydrate, 20% w/v PEG3350) each produced bipyramidal crystals and harvesting trays were made by repeating each condition 96 times using the Rigaku CrystalMation instrument. Oxidized crystals were looped directly from the 96-well plate and transferred to a cryo-solution containing 8% Tacsimate®, 20% (w/v) PEG3350 and 10% (v/v) ethylene glycol, and then they were plunged into liquid nitrogen. Crystals were chemically reduced in an anaerobic chamber by soaking in a solution containing 8% (v/v) Tacsimate®, 20% (w/v) PEG3350, 5 mM sodium dithionite and 200 μM methyl viologen. sMMOH:MMOB crystals were soaked for 2 h, cryo-protected in mineral oil and then frozen in liquid nitrogen.

Crystal growth was scaled up using the sitting-drop vapor diffusion method in 24-well plates (Cryschem M). Both Reagent 18 and 40 solutions were made in lab so that the crystallization conditions could be optimized. A seed stock suspension of the sMMOH:MMOB complex was made from crystals grown in a 96-well plate created by the Rigaku robot. A glass rod crystal crusher was used to pulverize the crystals. The crushed crystals were added to a seed bead tube, brought to a total volume of 50 μl and vortexed for 3 min in 30 s intervals. Sitting-drop experiments were set up by mixing 1.5 μl of protein with 1.5 μl of the well solution and then adding of the 0.5 μl seed stock suspension. The well solution contained 500 μl of precipitant (Reagent 18 or 40). Bipyramidal crystals started to grow in 2 days at room temperature.

3.3.5 Crystal Data Collection, Structure Solution and Refinement.

The crystals were exposed to X-ray radiation at the Advanced Photon Source (Argonne National Laboratory, Lemont, IL) on Beamline 24-ID-C and 24-ID-E at 0.979 Å wavelength at 100 K. A total of 675 frames were collected with an oscillation step of 0.2º. Datasets were subsequently processed using XDS [227] and merged using PHENIX[184]. Molecular replacement calculation were done with PHASER[182] using the X-ray crystal structure of *Mt* OB3b sMMOH and the NMR structure of *Mt* OB3b MMOB [40, 44] (PDBID: 1MHZ and 2MOB) as initial search models. The 2Fo-Fc map after the first round of refinement revealed significant structural differences between the sMMOH and the sMMOH:MMOB complex. A structural model was built using COOT[186] and refinement was carried out using PHENIX.[184]

3.3.6 PyMol Analysis.

PyMol version 2.3.3 (Schrödinger) was used to visualize, analyze, and design figures of *Mt* OB3b sMMO crystal structures. Structural alignments were calculated using the align command available *via* the user interface. In order to find internal cavities in protein structures, the following PyMol settings were used: Display quality = maximum, Surface = cavities and pockets (culled), Cavity detection radius = 3 solvent radii, Cavity detection cutoff = 5 solvent radii, Ignore HETATMs. The solvent radius was additionally set to 1.1 Å instead of the default value of 1.4 Å. The calculated cavities were then manually inspected to determine the amino acids lining the surface of cavities.

The intra-chain hydrogen bonding network of all helices in the α-subunit was determined by the following steps: i) The α-subunit was colored by secondary structure, ii) Each helix was made a separate object, iii) The find polar contacts within selection command was applied to all helices, and iv) Every helix was manually inspected to determine the *i and i+x* hydrogen bonding pattern for each amino acid.

3.3.7 MOLE Tunnel Calculations.

MOLE 2.5 is an advanced software tool designed to analyze molecular channels and pores.[187] The diiron cluster was chosen as the starting point for all sMMOH MOLE 2.5 calculations presented here. The default parameters yielded no tunnels for substrate entry when the diiron cluster is chosen as the starting point. The interior threshold and bottleneck radius had to be then adjusted to discover biologically relevant tunnels. The Interior Threshold (IT) parameter allows the user to identify all voids wider than double the chosen IT value. The Bottleneck Radius (BNR) parameter defines the minimum radius of the tunnel at any point along its length. In order to minimize redundancy, the parameter Cutoff Ratio is adjusted to filter out tunnels that are too similar. The parameter values were used to identify the tunnels in the crystal structure were IT = 0.9 Å, BNR = 0.8 Å and cutoff ratio = 0.5.

3.3.8 Steady-State Experiments.

A Hansatech Instruments Oxytherm+ system equipped with an S1 Clark-type oxygen electrode was used to measure O_2 consumption over time. The total volume of the reactions was 1 ml. The reaction components were: 0.2 μM sMMOH (0.4 μM active sites), 0.4 μM wild-type MMOB (WT-MMOB), 1.2 μM MMOR, 200 μM methane, 250 μM O_2, 400 μM NADH, 25 mM MOPS pH 7.5, 23 °C and varying concentrations of the MMOB variant. NADH was used to initiate the reaction. The O2view software package was used to calculate the initial rate of O_2 consumption.

3.3.9 Stopped-Flow Experiments.

The Applied Photophysics stopped-flow spectrophotometer model SX.18MV was used to rapidly mix reaction components and observe single wavelength absorbance over time. sMMOH was reduced as previously described.[34, 85] One syringe contained 55 μM $sMMOH^{red}$ (110 μM active sites) and 110 μM V41R-MMOB in anaerobic 50 mM MOPS buffer, pH 7.0. The second syringe contained dissolved gaseous O_2 in buffer at varying concentrations that were all high enough to establish pseudo first order conditions in the reaction. Solutions from the two syringes were rapidly

mixed and single wavelength time-dependent absorbance data at 330 nm were collected. At 330 nm, oxidized sMMOH absorbs more strongly than reduced sMMOH. For other experiments of this type in which a saturated O_2 solution was used, the reaction was also monitored at 430 and 700 nm where reaction cycle intermediates **Q** and **P**, respectively, absorb.[5] All stopped-flow experiments were performed at 4.5 °C. The multi-step first order or pseudo-first order reaction time courses were fit to a multiple summed-exponential expression using the nonlinear regression fitting package in Applied Photophysics Pro-Data Viewer software as previously described.[74, 76, 228] The analysis yields the number of phases required to fit the time course as well as the amplitude and reciprocal relaxation time ($1/\tau$) for each exponential phase. Data analysis is described in Supporting Information.

3.3.10 Analysis of Stopped-Flow Data.

For a linear series of first order or pseudo-first order reactions, the time course can be fit by summing exponential expressions where the number of exponentials is equal to the number of steps, *n* (Eq. 3.1). If the steps are irreversible, then the reciprocal relaxation times ($1/\tau$) give the rate constants for individual steps, although it is not possible to assign a specific reciprocal relaxation time to the rate constant for a specific step without additional information. When the steps are reversible, the reciprocal relaxation times become coupled, so that they do not correlate with a specific rate constant. In some cases, the rate constants can be determined from the ligand concentration dependence of the reciprocal relaxation times.[229]

$$Abs_t = \left(\sum_{i=1}^{n} Amp_i\, e^{-\frac{t}{\tau i}}\right) + Abs_{inf} \qquad \text{(Eq. 3.1)}$$

The kinetic data were fit to Eq. 3.1 using the nonlinear regression function of the Applied Photophysics ProData Viewer program. In this equation, Abs_t is the observed absorbance at time t, Amp_i is the observed amplitude for exponential phase *i*, τ_i is the relaxation time for phase *i*, and Abs_{inf} is the final absorbance at the end of the reaction. Fitting statistics were reported by the fitting

program, and each reaction was repeated multiple times to determine the average fitting parameters and errors.

For a single step reaction (Eq. 3.2) only one exponential phase is observed under pseudo-first order conditions in ligand, allowing Eq. 3.3 to be used to determine the forward (k_r) and reverse (k_r) rate constants as well as the K_D from their ratio.

$$\text{E + ligand} \underset{k_r}{\overset{k_f}{\rightleftarrows}} \text{E·ligand} \qquad \text{(Eq. 3.2)}$$

$$\frac{1}{\tau_{obs}} = k_f[\text{ligand}] + k_r \quad \text{(Eq. 3.3)}$$

For a two-step reaction where the first step is fast, reversible ligand binding (Eq. 3.4), only one exponential phase may be observed. A plot of $1/\tau_{obs}$ versus the concentration of the binding ligand will be hyperbolic if the rate constant k_{r1} is at least 3 fold greater than k_{f2} (Eq. 3.5).[230] The K_{D1} for the first step, k_{f2}, and k_{r2} are given by a non-linear regression fit to the hyperbolic plot.

$$\text{E + ligand} \underset{k_{r1}}{\overset{k_{f1}}{\rightleftarrows}} \text{E·ligand} \underset{k_{r2}}{\overset{k_{f2}}{\rightleftarrows}} \text{E-ligand'} \quad \text{(Eq. 3.4)}$$

$$\frac{1}{\tau_{obs}} = \frac{k_{f2}[\text{ligand}]}{(\frac{k_{r1}}{k_{f1}})+[\text{ligand}]} + k_{r2} \qquad \text{(Eq. 3.5)}$$

3.3.11 EPR Measurements.

Electron paramagnetic resonance (EPR) spectra were recorded using a Bruker Elexsys E-500 spectrometer equipped with a Bruker dual mode cavity and an Oxford ESR 910 liquid helium cryostat. Experimental conditions are given in the figure legend.

3.4 Results

3.4.1 Crystal Forms of *Mt* OB3b sMMOH and sMMOH:MMOB Complex.

In past studies, most preparations of sMMOH from *Mc* Bath and *Mt* OB3b contained a sizable fraction of unreactive enzyme without evidence for misfolding or aberrant diiron cluster structure.[75, 76] Although never successfully characterized, it is likely that the unreactive fraction resulted from small sMMOH surface modifications that interfered with the precise interaction between sMMOH and MMOB required for full activity.[71] Recently, advances have been made in the *Mt* OB3b sMMOH purification protocol that double the active fraction.[34] We find that the new preparation allows for the development of tractable methods to form a co-crystal of sMMOH and MMOB that diffracts to high resolution. Here, we evaluate the structures of oxidized, diferric *Mt* sMMOH ($sMMOH^{ox}$, PDB:6VK6, 1.52 Å), chemically reduced diferrous *Mt* sMMOH ($sMMOH^{red}$, PDB:6VK7, 2.12 Å), *Mt* $sMMOH^{ox}$:MMOB (Form 1, PDB:6VK5, 1.86 Å and Form 2, PDB:6VK8, 2.03 Å), and *Mt* $sMMOH^{red}$:MMOB (PDB:6VK4, 2.35 Å) (**Table 3-2**). These structures are also evaluated in the context of structures of oxidized and reduced *Mt* sMMOH:MMOB determined using room temperature X-ray free electron laser (RT-XFEL) technology published recently by some of us.

Table 3-2 Data Collection and Refinement Statistics

	sMMOH^{ox}	sMMOH^{red}	sMMOH^{ox}:MMOB Form 1	sMMOH^{ox}:MMOB Form 2	sMMOH^{red}:MMOB
Data collection					
PDB Code	6VK6	6VK7	6VK5	6VK8	6VK4
Resolution range (Å)	63.8-1.52 (1.57 - 1.52)	49.1-2.12 (2.20 - 2.12)	73.5-1.86 (1.93 - 1.86)	86.0-2.03 (2.10 - 2.03)	52.6-2.35 (2.43 - 2.35)
Space group	$C222_1$	$C222_1$	$P2_12_12_1$	$P2_12_12_1$	$P2_12_12_1$
Unit cell (Å)	63.07 292.63 141.79	62.46 290.45 139.2	102.62 105.46 299.42	101.87 105.35 297.72	102.86 105.21 300.88
Total reflections	628962 (60913)	363811 (33807)	1365173 (131835)	858293 (87118)	576343 (57098)
Unique reflections	197515 (19628)	71995 (7050)	271076 (26707)	203936 (19538)	133740 (11725)
Multiplicity	3.2 (3.1)	5.1 (4.8)	5.0 (4.9)	4.2 (4.3)	4.3 (4.3)
Completeness (%)	98.25 (98.37)	99.37 (98.84)	99.65 (99.26)	97.85 (95.35)	96.27 (86.80)
I/σI	11.58 (1.14)	6.69 (1.08)	8.21 (0.97)	8.09 (0.95)	5.71 (0.65)
R-merge	0.06956 (1.023)	0.1599 (1.366)	0.131 (1.511)	0.137 (2.025)	0.1447 (2.263)
R-meas	0.08342 (1.234)	0.1784 (1.534)	0.1463 (1.691)	0.152 (2.316)	0.1641 (2.574)
R-pim	0.04492 (0.6755)	0.07791 (0.6875)	0.06397 (0.7467)	0.096 (1.105)	0.07547 (1.195)
$CC_{1/2}$	0.998 (0.532)	0.994 (0.442)	0.996 (0.39)	0.992 (0.387)	0.993 (0.392)
Refinement					
Reflections	197477 (19613)	71994 (7048)	270965 (26698)	202459 (19516)	131580 (11717)
# used for R-free	9858 (1002)	3609 (398)	13530 (1336)	10347 (1019)	6689 (597)
R-work	0.1392 (0.3111)	0.1600 (0.2659)	0.1721 (0.2965)	0.1664 (0.3154)	0.2088 (0.3991)
R-free	0.1585 (0.3048)	0.2027 (0.3213)	0.1933 (0.3108)	0.2073 (0.3445)	0.2379 (0.4275)
# of non-H atoms	10110	9437	21007	20999	19851
Macromolecules	8814	8697	19498	19498	19475
Ligands	201	2	123	116	78
Solvent	1095	738	1386	1385	298
RMS deviation					
Bond lengths (Å)	0.011	0.010	0.005	0.007	0.003
Bond angles (º)	1.03	1.00	0.86	0.85	0.57
Ramachandran plot					
Favored (%)	97.18	97.37	96.96	97.13	96.51
Allowed (%)	2.82	2.63	2.95	2.87	3.37
Outliers (%)	0.00	0.00	0.08	0.00	0.12
Average B-factor	22.14	36.94	28.46	36.59	63.63
Macromolecules	20.29	36.44	28.28	36.15	63.57
Ligands	46.47	34.96	34.43	51.86	102.92
Solvent	32.52	42.89	30.50	41.52	57.03

The 1.52 Å *Mt* sMMOH^{ox} structure (PDB:6VK6) is the highest resolution sMMOH structure reported to date.[39, 40] The two αβγ protomers of sMMOH protein in the crystal are related by 2-fold crystallographic symmetry. The experimental data allowed for accurate modeling of the amino acids and aquo/hydroxo ligands coordinated to the diiron cluster (**Figure 3-1**A). Interatomic distances are summarized in

Table 3-3. Throughout this report, when referring to sMMOH, the established nomenclature for the secondary structural elements of the α-subunit is used (**Figure 3-1**B).[37]

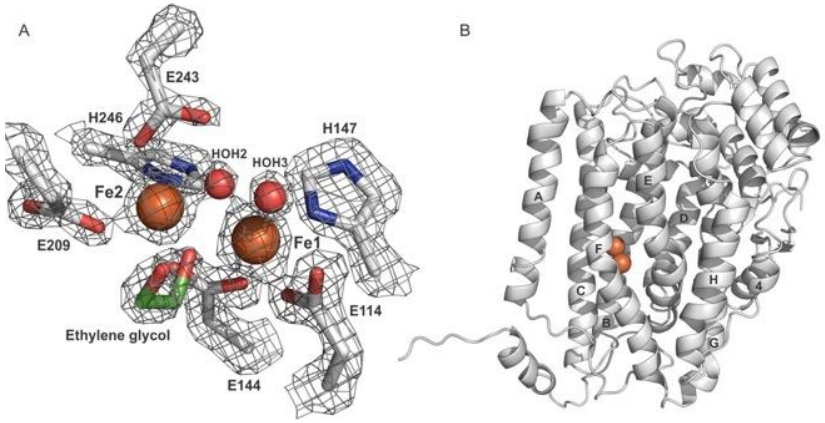

Figure 3-1 The 1.52 Å sMMOH active site and helix nomenclature. (A) Image of the active site diiron cluster along with the electron density map (1.9 σ contour). Electron density (2Fo-Fc) is colored gray, the irons are shown as orange spheres, amino acids are represented as sticks (white = carbon, red = oxygen, blue = nitrogen), bridging and terminal aquo/hydroxo ligands are shown as red spheres. In this structure ($sMMOH^{ox}$, PDB:6VK6), the second bridging hydroxo ligand is replaced by a hydroxyl group of ethylene glycol (green = carbon) from the cryo-stabilization solution. B) The α-subunit of sMMOH is shown as a black and white cartoon. The principal helices are labeled A-H and 4, and the diiron cluster is shown as orange spheres. The four helices providing ligands to the diiron cluster are B, C, E and F.

Chemical reduction of the *Mt* sMMOH crystals caused *in crystallo* structural rearrangements to occur in the α-subunit. **Figure 3-2** highlights all the pertinent amino acid side chains that change rotometric conformation and/or move ≥1.0 Å in the 2.12 Å structure (PDB:6VK7). For example, the Pore residues N214 and E240 located on Helices E and F change rotameric conformation as well as shift a notable 2.0-2.2 Å upon chemical reduction (**Figure 3-2**, Helices E and F, see below). The other regions of the α-subunit and the β and γ subunits of sMMOH remain relatively unchanged. One important change at the diiron cluster is a shift of E243 from a monodentate ligand of Fe2 to a position where it forms a monodentate bridge between the irons

and a bidentate coordination to Fe2. The same "carboxylate shift" has been reported for *Mc* sMMOH^{red}. [38]

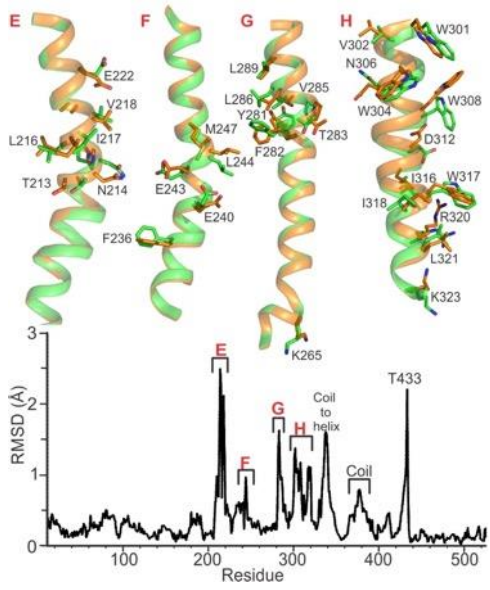

Figure 3-2 Structural rearrangements in *Mt* sMMOH α-subunit upon reduction. Top: Diferric sMMOH (6VK6) is colored green and chemically reduced diferrous sMMOH (6VK7) is colored orange. Helices E, F, G, and H are labeled and are represented as cartoons. Amino acid side chains that move at least 1 Å upon chemical reduction are represented as sticks (green/orange = carbon, red = oxygen, blue = nitrogen). Bottom: Main chain Cα RMSD of the α-subunit residues upon alignment between the oxidized and reduced states using the CCP4 analysis package.

The *Mt* sMMOH:MMOB complex crystallizes with the complete $(\alpha\beta\gamma)_2$ sMMOH and 2 bound MMOBs in the asymmetric unit. Form 1 (PDB:6VK5) and Form 2 (PDB:6VK8) *Mt* sMMOH^{ox}:MMOB complex crystal structures (1.86 and 2.03 Å, respectively) are nearly identical except for the exogenous ligands bound to the diiron cluster, as discussed in detail below. The crystal structures exhibit the same overall changes upon complex formation between *Mt* sMMOH and MMOB. These changes have been detailed in a parallel room temperature XFEL (RT-XFEL) structure study, so they are not described further here.

Chemical reduction of Form 1 crystals resulted in a structure (2.35 Å) that has one protomer reduced (diferrous) and the other protomer oxidized (diferric, PDB: 6VK4). The phenomenon of two different oxidation states in the sMMOH homodimer has been observed before in an X-ray crystallographic study of chemically reduced *Mc* sMMOH crystals.[38] The presence of two oxidation states in different protomers facilitates identification of structural changes under otherwise identical conditions and resolution.

Table 3-3 Interatomic Distances for sMMOH

Ligand-Fe	sMMOH^{ox} (6VK6)	sMMOH^{red} (6VK7)
Resolution	1.52 Å	2.12 Å
Fe1-Fe2	3.1	3.3
Fe1-E114 OE1	2.0	2.1
Fe1-E144 OE1	2.1	2.3
Fe1-E243 OE2	3.9	2.2
Fe1-H147 ND1	2.2	2.2
Fe1-HOH 1	2.2	2.4
Fe1-HO(H) 2[a]	2.1	2.5
Fe1-EDO O2[a]	2.1	N/A
Fe2-E209 OE2	1.9	2.0
Fe2-E243 OE2	3.4	2.4
Fe2-E243 OE1	2.2	2.2
Fe2-E144 OE2	2.2	2.2
Fe2-H246 ND1	2.2	2.2
Fe2-EDO O2[a]	2.4	N/A
Fe2-HO(H) 2[a]	1.9	2.3

[a]Bridging

Many of the sMMOH α-subunit helices contain regions of π-helix and/or 3_{10}-helix which increase or decrease flexibility, respectively. Close inspection of the *Mt* sMMOH and *Mt* sMMOH:MMOB crystal structures obtained in this study provided detailed information about the helical composition of the sMMOH α-subunit. Principal helices A, D, E, H, and a helix formed by residues W379 to L393 contain π-helices, where the backbone carbonyl of residue i hydrogen bonds to the backbone NH moiety of the i+5 residue in at least 2 consecutive residues (**Figure 3-3**). Two of these π-helices (in Helices E and H) have been described previously in limited detail.[37, 40, 50] The helix composed of residues W379 to L393 is involved in making crystal contacts, and the backbone carbonyl group of residue W379 is engaged in a rare trifurcated acceptor hydrogen bond, which initiates the π-helix. Because this π-helix is involved in crystal contacts, we assume it an artifact of protein crystallization, and therefore not functionally important. When the complex with MMOB forms, Helix E residues N214 and P215 as well as Helix H residues G314 and G315 form additional π-helices (**Figure 3-3**). The π-helix in Helix D, composed of residues K185 and R186, becomes a coiled region as a result of large exogenous molecules present in the active site in Forms 1 and 2 crystals. It is interesting to note that many of the residues that stabilize the α-helices throughout the α-subunit also form hydrogen bonds to the i + 3 residue a 3_{10} helix. Typically, 3_{10} helices are located at the ends of α-helices, but this is not universally the case in sMMOH. The partial 3_{10} helix character causes the α-helices to be tightly wound, further highlighting the flexibility of the interspersed π-helical segments.

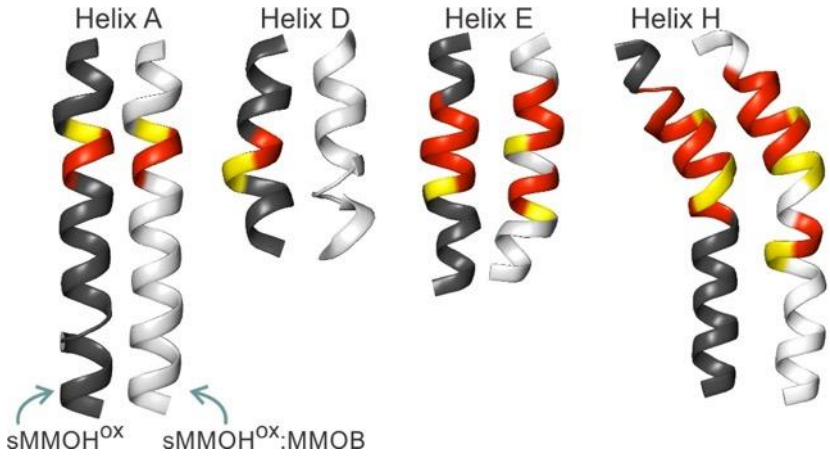

Figure 3-3 sMMOH π-helices altered by MMOB
The π-helices of *Mt* sMMOH^{ox} (6VK6) and *Mt* sMMOH^{ox}:MMOB (6VK5) crystal structures. sMMOH and sMMOH:MMOB Helices A, D, E, and H are represented as grey and white cartoons, respectively. The π-helices are colored red and sections of the protein that do not form intra-main chain hydrogen bonds are colored yellow.

3.4.2 Exogenous Ligands Bound to the Diiron Cluster of the sMMOH:MMOB Complex Induce Conformational Changes.

Typically, only aquo/hydroxo exogenous molecules are found coordinated to the diiron cluster of sMMOH in crystal structures.[37, 38, 40] In contrast, the large exogenous ligands benzoate and succinate are found bound to the diiron cluster of the Form 1 and Form 2 *Mt* sMMOH^{ox}:MMOB structures, respectively (**Figure 3-4**A and B). The benzoate carboxylate oxygens bridge between the irons of the cluster of Form 1 symmetrically, whereas the succinate carboxylate oxygens bind strongly to Fe1 and weakly to Fe2 in Form 2 (interatomic distances shown in **Table 3-4**). The Fe-Fe distance in both structures is an atypically long 3.5 Å, presumably due to the presence of the exogenous ligand carboxylate group. The source of the benzoate in Form 1 was identified as a contaminant in the PEG3350 precipitant present in the mother liquor. Changing the supplier of the PEG eliminated the benzoate in sMMOH^{ox}:MMOB Form 2, but it was replaced by succinate from the Tacsimate® mixture of organic acids. We attempted to crystallize the sMMOH^{ox}:MMOB complex without succinic acid bound to the diiron cluster by lowering the concentration of Tacsimate® to 2% (v/v),

but the structure was unchanged. It is known that larger molecules such as single and double ring aromatic compounds are adventitious substrates of sMMO,[35, 114] and thus they can at least slowly access the active site.

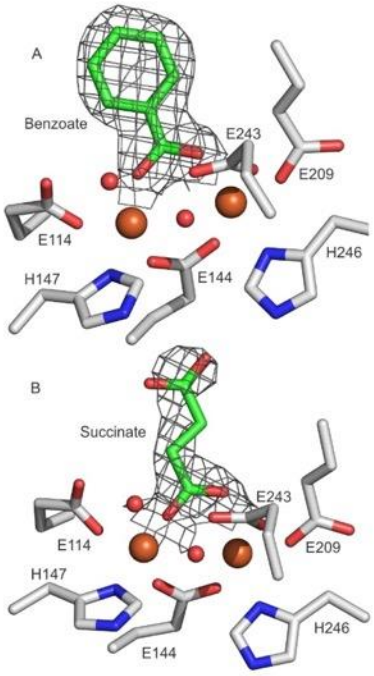

Figure 3-4 Exogenous ligands bound to the active site.
Active site structures of (A) Form 1 (6VK5) and (B) Form 2 (6VK8). Stick colors: green/white = carbon, red = oxygen, blue = nitrogen. Fe atoms shown as orange spheres and aquo/hydroxo are shown as smaller red spheres. Where shown, the 2Fo-Fc electron density is modeled at 1 σ. Interatomic distances can be found in Table 3-4.

Table 3-4 Interatomic Distances sMMOH:MMOB

Complex	sMMOH^{ox}:MMOB				sMMOH^{red}:MMOB	
Type	Form 1 (6VK5)		Form 2 (6VK8)		(6VK4)	
	Protomer 1	Protomer 2	Protomer 1	Protomer 2	Protomer 1	Protomer 2
Resolution	1.86 Å	1.86 Å	2.03 Å	2.03 Å	2.35 Å	2.35 Å
Fe1-Fe2	3.5	3.5	3.4	3.5	3.5	3.2
Fe1-E114 OE1	2.1	1.9	2.0	1.9	1.9	2.0
Fe1-E144 OE1	2.1	2	2.1	2.1	2.1	2.0
Fe1-E243 OE2	3.7	3.8	3.9	3.9	3.4	2.2
Fe1-H147 ND1	2.3	2.2	2.2	2.2	2.1	2.3
Fe1-HOH 1	2.2	2.0	2.2	2.2	2.1	2.1
Fe1-HOH 2[a]	2.0	2.0	2.0	1.9	1.9	N/A
Fe1-BEZ/SIN O1	2.1	2.1	1.9	1.9	2.0	1.9
Fe2-E209 OE2	2.1	2.2	2.3	2.1	2.1	2.1
Fe2-E243 OE2	3.2	3.4	3.5	3.6	3.3	2.2
Fe2-E243 OE1	2.3	2.2	2.2	2.2	2.0	2.1
Fe2-E144 OE2	2.2	2.1	2.3	2.2	2.0	2
Fe2-H246 ND1	2.3	2.2	2.3	2.2	2.2	2.1
Fe2-BEZ /SIN O2	2.2	2.2	2.5	2.3	2.1	2.2
Fe2-HOH 2[a]	2.0	1.9	1.8	2.0	1.9	N/A

[a]bridging

The exogenous ligands bound to the diiron cluster in Form 1 and 2 crystal structures have an effect on the sMMOH α-subunit structure. Inspection of the electron density maps shows that both benzoate and succinate extend to the outer boundary of the active site cavity, causing the side chain of F188 to change rotameric conformation (**Figure 3-5**A and B). This conformational change is not observed in the RT-XFEL structures of *Mt* sMMOH^{ox}:MMOB (PDB:6YD0), which have

only solvent and possibly a small exogenous molecule near the diiron cluster (**Figure 3-5**C). A notable observation is that F188 is located adjacent to a π-helix. In both the *Mt* sMMOH^{ox} and *Mt* sMMOH^{red} crystal structures, K185 and R186 of Helix D form i, i+5 hydrogen bonds while V187 and F188 do not have intra-main chain hydrogen bonds. This region remains unchanged upon MMOB binding in the RT- XFEL structures, but it is converted to a coil in the 100 K *Mt* sMMOH^{ox}:MMOB crystal structures reported here (**Figure 3-3** Helix D). A structural alignment of the substrate-free RT-XFEL sMMOH^{ox}:MMOB with the Form 1 sMMOH^{ox}:MMOB structure depicts the regions where the α-subunit of sMMOH is reorganized by the presence of a large exogenous substrate in the active site (**Figure 3-6**). Apart from the conformational change of F188 and the adjoining residues on Helix D as described above, three of the four helices of the 4-helix bundle (C, E and F) reorganize. This change leads to an alteration in the structure of Helix H along with an unstructured coiled region that interacts with Helices C, E and F. Overall, the structures of sMMOH:MMOB from data at 100 K and at room temperature are very similar, with differences confined to the α-subunits due to the effects of the exogenous ligands in the 100 K structure.

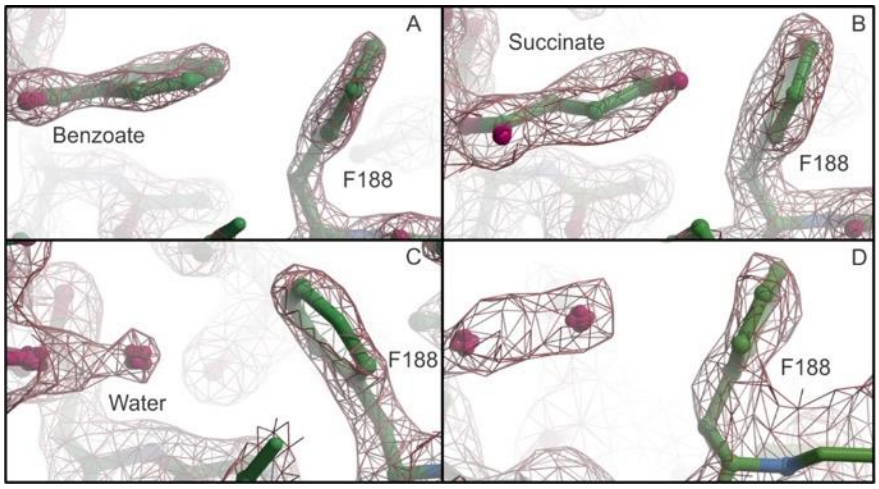

Figure 3-5 Exogenous ligands bound to the diiron cluster alter the conformation of F188. In all panels, 2Fo-Fc electron density is shown as mesh contoured at 1 σ, F188 and ligands bound to the diiron cluster are shown as sticks and spheres (Green = carbon, Blue = nitrogen, Red = oxygen). A) Benzoate bound to the diiron cluster of the *Mt* sMMOH^{ox}:MMOB Form 1 (6VK5) structure. B) Succinate bound to the diiron cluster of the *Mt* sMMOH^{ox}:MMOB Form 2 structure (6VK8). C) Active site of RT-XFEL *Mt* sMMOH^{ox}:MMOB structure (6YD0). D) *Mc* sMMOH:MMOB structure from PDB:4GAM. The 2Fo-Fc electron density in the active site extends to the outer edge of Cavity 1, causing a shift in F188 as seen in panels A and B. Two waters were modeled into the density at the active site in the 4GAM structure, but a larger exogenous ligand is possible on the basis of additional unassigned density (see text and **Figure 3-7**).

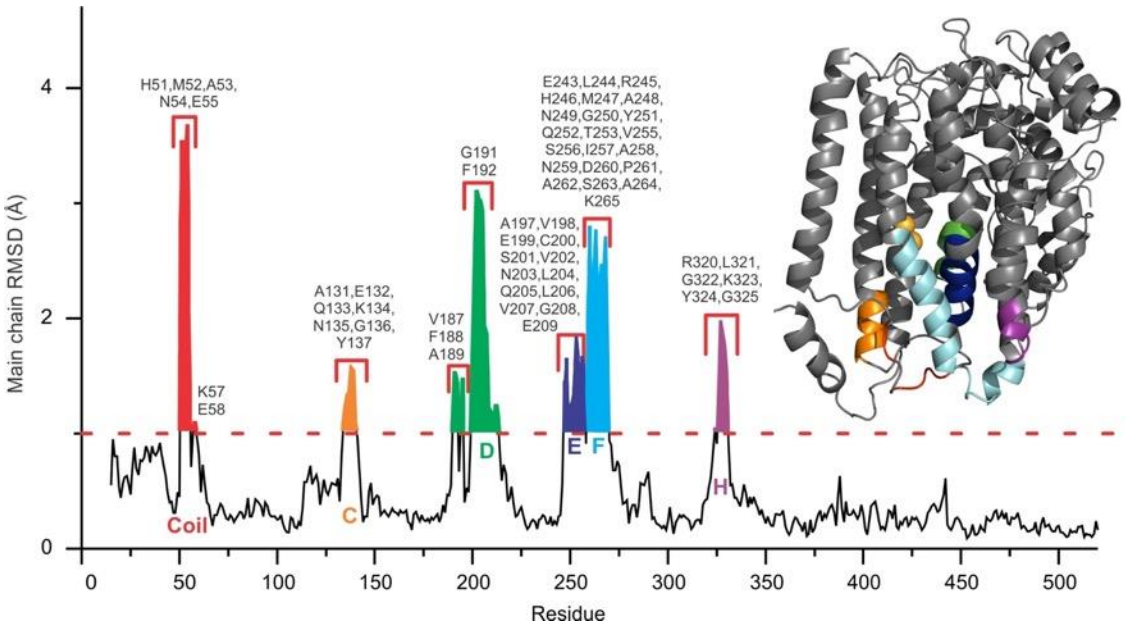

Figure 3-6 Main chain Cα RMSD comparison of the structures of the α-subunits of Form 1 sMMOH^{ox}:MMOB (6VK5) with RT-XFEL sMMOH^{ox}:MMOB (6YD0).
These structural changes occur as a result of binding of an exogenous molecule (benzoate) in the active site of sMMOH. The majority of the changes occur in three out of four helices of the four-helix bundle housing the diiron cluster (C, E and F) and Helix D that forms the outer border of the active site cavity. This reorganization in turn rearranges an extended coil region in contact with Helices C, E and F and Helix H that is in contact with Helix E. *Inset*: Cartoon of the α-subunit with color coding to showing the regions that change in structure. The diiron cluster is shown as gold spheres.

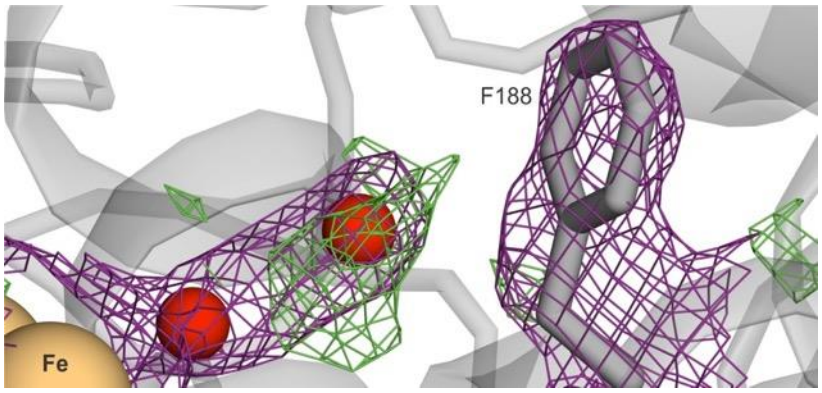

Figure 3-7 Unassigned electron density in the active site of *Mc* sMMOH^{ox} (PDB:4GAM, Chain A).
The 2Fo-Fc map (1.2 σ) is represented as purple isomesh and the Fo-Fc map (+3 σ) is represented as green isomesh. The green Fo-Fc isomesh indicates that the two waters (red spheres) modeled into the active site do not account for all of the experimental density. Three of the four subunits in the asymmetric unit of the 4GAM model have positive sigma density altering the position of F188 and enlarging the connection between Cavities 2 and 1

3.4.3 Bottlenecks Between Cavities are Regulated by Flexible Residues.

As noted in the introduction, the current model of substrate binding proposed by Cho and colleagues suggests that O_2 and CH_4 diffuse from solvent to the active site *via* a chain of three internal cavities located in the sMMOH α-subunit. [43, 50, 70] The detection of the cavities in the most recent of these studies was conducted using PyMol. The ability to identify cavities is based on PyMol parameters termed cavity detection radii and cutoff values. These parameters are varied in units of a separately entered solvent radius (See Experimental Procedures). The program default values are set for a solvent radius of 1.4 Å (water), and cavity detection radii and cutoff values of 5 and 3 solvent radii, respectively. These parameter values provide a useful, albeit conservative, evaluation of the internal void geometry. However, in the case of sMMOH^{red}, we are seeking a highly restricted substrate access route such that it slows O_2 access (see kinetic evaluation below) and can differentiate between the size of methane and ethane.[74] Setting the solvent radius to 1.1 Å with concomitant decrease in the cavity detection parameters (estimates for the effective radius of

O_2 range from 1.17 to 1.7 Å)[231-235] allows a more relevant detection of the cavities and the bottlenecks between them (**Figure 3-8**).

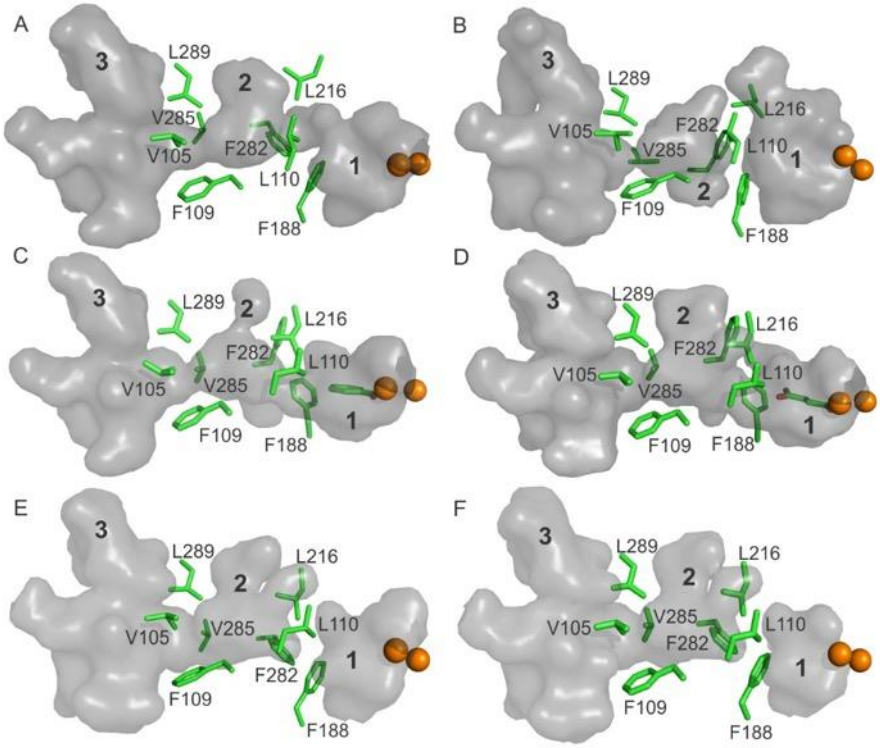

Figure 3-8 Cavity gating residues of *Mt* sMMOH and sMMOH:MMOB. The internal cavities of A) sMMOH^{ox} (6VK6), B) sMMOH^{red} (6VK7), C) sMMOH^{ox}:MMOB Form 1 (6VK5), D) sMMOH^{ox}:MMOB, Form 2 (6VK8), E) RT-XFEL sMMOH^{ox}:MMOB (6YD0), and F) RT-XFEL sMMOH^{red}:MMOB (6YDI), are shown as a grey colored surface. Amino acids involved in determining the connectivity of the cavities are shown as green sticks. The diiron cluster atoms are represented as orange spheres. Benzoate and succinate are shown bound to the diiron cluster in Forms 1 and 2, respectively.

This analysis shows that a bottleneck regulated by residues V105, F109, V285, and L289 is located between Cavities 3 and 2. Cavity 2 is separated from the active site Cavity 1 by another bottleneck controlled by residues L110, F188, L216, F282 and F286. Cavities 3 and 2 are connected in all of the *Mt* sMMOH and sMMOH:MMOB crystal structures (**Figure 3-8**A-D). However, Cavities 2 and 1 are only connected in the sMMOH^{ox} and Form 1 and 2 sMMOH^{ox}:MMOB structures (**Figure 3-8**A, C-D). These cavities are disconnected in sMMOH^{red}

(**Figure 3-8**B) along the route used in sMMOH^{ox} due to shifts in the gating residues. Importantly, Cavities 1 and 2 are not connected in the RT-XFEL sMMOH^{ox}:MMOB and sMMOH^{red}:MMOB crystal structures (PDB:6YD0 and 6YDI) (**Figure 3-8**E and F). The MMOB binding-induced reorganization of the bottleneck residues L216 and L110 in sMMOH serves to isolate Cavity 1 from Cavity 2 in the complex. While the reorganization of L216 and L110 is also observed in the sMMOH^{ox}:MMOB Form 1 and Form 2 crystal structures, the altered position of bottleneck residue F188 due to benzoate or succinate binding in Cavity 1 enables a larger connection with Cavity 2 (**Figure 3-5**A and B, **Figure 3-8**C and D).

3.4.4 The Pore is Blocked upon Reduction and MMOB Binding.

The Pore is located between Helices E and F and has been proposed to be involved in regulating the access of substrates (e^- and H^+) and release of products (CH_3OH) to and from the active site, respectively.[226] The strictly conserved amino acids T213, N214, and E240 are considered the Pore gating residues that regulate these processes (**Figure 3-9**). The Pore is a uniquely polar region on the sMMOH surface as it is flanked by hydrophobic amino acids A210, V218, L237, L244, and M247 on Helices E and F. In the *Mt* sMMOH^{ox} crystal structure, the side chains of N214 and E240 are solvent exposed, ~4.0 Å apart, and coordinate 5 water molecules. The side chain of T213 lines the active site cavity and the hydroxyl moiety points towards the diiron cluster. Chemical reduction of the diiron cluster causes the middle of Helix E to twist, resulting in T213 and N214 to shift 2.2 Å and 3.2 Å, respectively. The rotameric conformation of E240 is altered and the distance between this residue and N214 becomes 3.0 Å. The rotameric conformations of the hydrophobic residues V218, L244, and M247 are altered as well, helping to create a chemical environment that does not favor stable binding of water molecules to the region around the Pore.

MMOB binding to sMMOH causes structural rearrangement of the Pore residues as well. The side chain of E240 is no longer solvent exposed, and instead, traverses the width of the Pore. This new conformation blocks the access of substrates through the Pore into the active site cavity. The side chain of T213 is shifted 2.2 Å compared to its position in *Mt* sMMOH^{ox} and rotated ~180°

compared to its position in *Mt* sMMOH^{red}. This new conformation positions the side chain hydroxyl moiety of T213 to face away from the diiron cluster and form a hydrogen bond with E240. It is important to note that MMOB covers the Pore while in complex with sMMOH, further limiting access to the active site by this route.

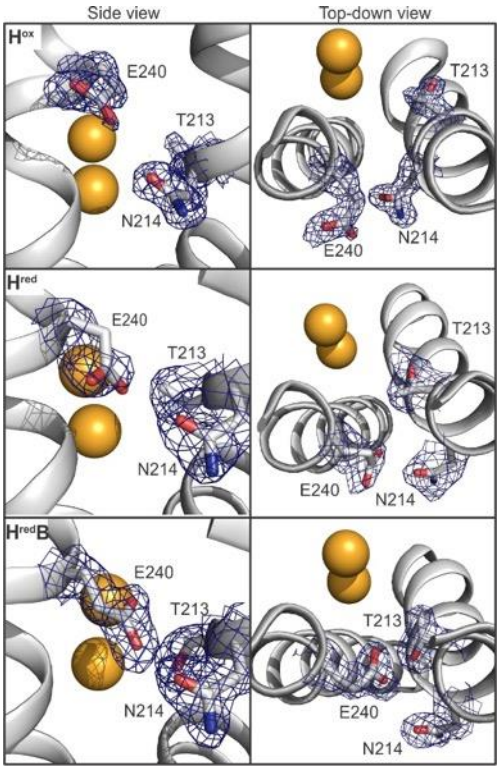

Figure 3-9 Views of the Pore region in *Mt* sMMOH in various states and in complex with MMOB.
H^{ox} = $sMMOH^{ox}$ (6VK6), H^{red} = $MMOH^{red}$ (6VK7), $H^{red}B$ = RT-XFEL $sMMOH^{red}MMOB$ (6YDI). Diiron cluster reduction partially closes the Pore while complex formation with MMOB completely seals off the Pore. Electron density is shown as 2Fo-Fc and modeled at 1 σ.

3.4.5 Binding of MMOB Results in the Optimization of a New Transient Molecular Tunnel into the Active Site.

Past kinetic studies have provided a wealth of experimental evidence suggesting that the access of O_2 and methane to the active site is precisely regulated by the binding of MMOB.[5, 14, 68, 71, 75] The high resolution *Mt* sMMOH:MMOB crystal structures, especially that of the particularly relevant sMMOH^{red}:MMOB state, afford the opportunity to search for alternative substrate entry routes involving the sMMOH-MMOB interface. Using the program MOLE 2.5, a narrow tunnel (the W308-Tunnel named for the gating tryptophan residue 308, see below) was identified in the Form 1 and Form 2 *Mt* sMMOH^{ox}:MMOB, *Mt* sMMOH^{red}:MMOB and RT-XFEL *Mt* sMMOH$^{ox/red}$:MMOB crystal structures (**Figure 3-10** and **Figure 3-11**A and B). The W308-Tunnel is primarily lined by hydrophobic residues, which are well-suited to the non-polar nature of sMMO substrates. See

Table 3-5 for a list of the residues lining the W308-Tunnel.

Cavity analysis using PyMol with the lower solvent radius parameters described above allows detection of internal voids along the W308-Tunnel route, which correlates very well with the Mole 2.5 prediction (**Figure 3-11**B). All the amino acids lining the W308-Tunnel in sMMOH and MMOB are highly conserved in the small hydrocarbon-oxidizing, diiron enzyme family (

Table 3-5).

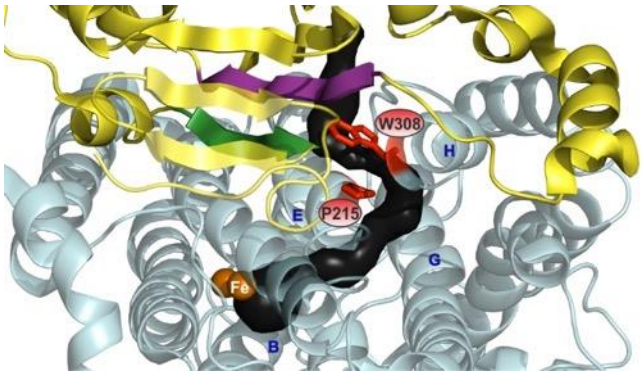

Figure 3-10 The W308-Tunnel.
Starting from bulk solvent, the W308-Tunnel traverses the sMMOH:MMOB interface before reaching the entrance into the sMMOH α-subunit. The α-subunit entrance is gated by sMMOH residues W308 and P215 on Helices H and E respectively. After traveling between Helices H and E the W308-Tunnel curves away from Helix G and turns a corner around Helix E. Finally, the W308-Tunnel goes between Helices E and B into the active site. Colors: sMMOH α-subunit, cyan; W308-Tunnel, black; sMMOH gating residues, red; MMOB, yellow; MMOB "Quad" regulatory residues, green; MMOB W308-Tunnel interface mutated residues, purple; active site diiron cluster, orange. PDB code: 6YDI

Variations of the W308-Tunnel can also be identified by MOLE 2.5 in the *Mt* sMMOH^{ox} and sMMOH^{red} (**Figure 3-11**A) structures. In the sMMOH^{ox} structure (**Figure 3-12**, top), the entrance into the sMMOH interior is severely constricted by sMMOH residues W308 and P215. Reduction of the diiron cluster leads to structural reorganization of Helix E and H in the sMMOH^{red} structure that partially alleviates this bottleneck (**Figure 3-2** and **Figure 3-12**, bottom). However, another significant bottleneck in this tunnel remains within sMMOH^{red} at F282 and F212 (**Figure 3-11**A). MMOB binding to sMMOH^{red} removes this constriction, as is apparent in a comparison of the W308-Tunnel in the *Mt* sMMOH^{red} and RT-XFEL sMMOH^{red}:MMOB structures (**Figure 3-11**A and B). Mole 2.5 also allows detection of a route through the chain of cavities to the active site in both of these structures. A constriction between Cavities 2 and 1 is detected by analysis of the sMMOH^{red} structure (**Figure 3-11**A). However, in the RT-XFEL sMMOH^{red}:MMOB structure, the changes caused by complex formation result in closure of the Mole 2.5 tunnel between Cavity 2 and 1 (**Figure 3-11**B). The same changes occur in the W308-Tunnel found in the 100K sMMOH^{red}:MMOB structure reported here, but the alteration of the active site structure caused by

the presence of the large exogenous ligand prevents the complete closure of the Cavity 2 to 1 passageway.

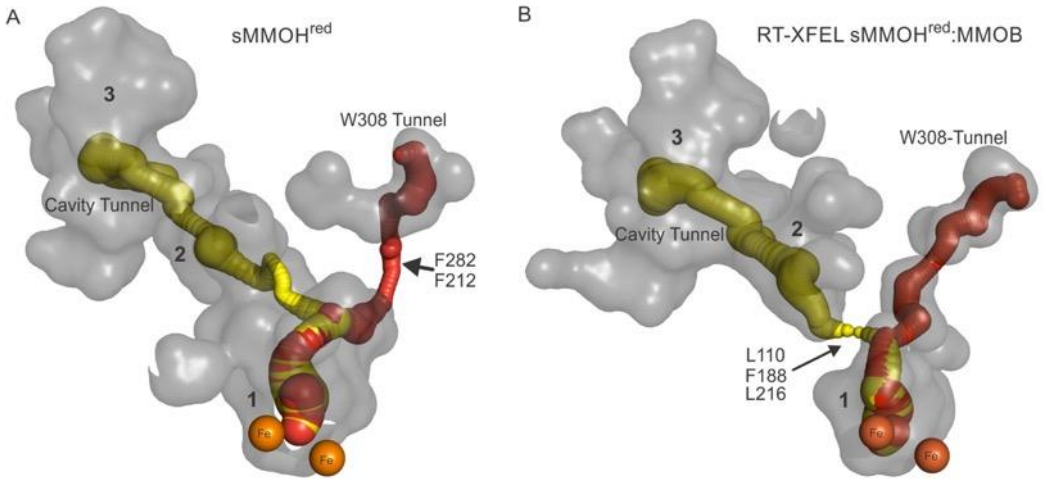

Figure 3-11 Correlation of voids in the protein identified using PyMol and tunnels computed by MOLE 2.5.
A) Tunnels (red and yellow solid spheres) calculated by Mole 2.5 into the active site of sMMOH in the *Mt* sMMOH^{red} (6VK7) are show superimposed on the cavities computed by PyMol (transparent gray). The diameter of the spheres representing the tunnel depicts the computed width. The significant restriction in the W308-Tunnel is marked with an arrow. The restriction in the computed tunnel between Cavities 2 and 1 is less than in sMMOH:MMOB (see panel B), but rotation around the vertical axis of the view shown reveals that the cavities remain distinct. B) Analogous computations for the *Mt* sMMOH^{red}:MMOB complex (6YDI). Tunnels are found through the chain of cavities (yellow, severely restricted where marked) and through the W308-Tunnel (red).

Table 3-5 The W308 Tunnel Residues are Conserved Amongst 15 Small Hydrocarbon Oxidizing Strains[a]

	Sub[b]	110	188	192	212	213	215	216	217	219	222	223	282	286	290	299	301	304	305	308	309
Methylosinus trichosporium OB3b	CH_4	L	F	F	F	T	P	L	I	A	E	W	F	L	F	E	W	T	W	W	V
Methylococcus capsulatus Bath	CH_4	L	F	F	F	T	P	L	I	A	E	W	F	L	F	E	W	T	W	W	V
Sphingobium sp. SCG-1	CH_4	L	F	F	F	T	P	L	I	A	E	W	F	L	F	E	W	T	W	W	V
Methylospira mobilis	CH_4	L	F	F	F	T	P	L	I	A	E	W	F	L	F	E	W	T	W	W	V
Methylomicrobium japanense	CH_4	L	F	F	F	T	P	L	I	A	E	W	F	L	F	E	W	T	W	W	V
Methylomonas methanica	CH_4	L	F	F	F	T	P	L	I	A	E	W	F	L	F	E	W	T	W	W	V
Crenothrix polyspora	CH_4	L	F	F	F	T	P	L	I	A	E	W	F	L	F	E	W	T	W	W	V
Methylovulum miyakonense HT12	CH_4	L	F	F	F	T	P	L	I	A	E	W	F	L	F	E	W	T	W	W	V
Betaproteobacteria bacterium	CH_4	L	F	F	F	T	P	L	I	G	E	W	F	L	F	E	W	T	W	W	V
Rhodospirillaceae bacterium	CH_4	L	L	F	F	T	P	L	I	A	E	W	I	V	L	E	W	T	W	W	V
Mycolicibacterium elephantis	CH_4	L	A	F	F	T	P	L	V	A	E	W	L	V	F	E	W	T	W	W	V
Mycolicibacterium rhodesiae	CH_4	L	F	F	F	T	P	L	I	A	E	W	A	V	F	E	W	V	W	W	V
Mycobacterium chubuense NBB4	C_3H_8	L	F	F	F	T	P	L	I	A	E	W	A	V	F	E	W	V	W	W	V
Thauera butanivorans	CH_4	L	F	F	F	T	P	L	I	S	E	W	L	V	L	E	W	S	W	W	V
Brachymonas petroleovorans	C_4H_{10}	L	F	F	F	T	P	L	I	A	E	W	L	V	L	D	W	M	W	W	V

[a]BLAST alignment of α-subunit W308-tunnel residues, *Methylosinus trichosporium* OB3b numbering. NCBI GenBank sequence ID: *Methylosinus trichosporium* OB3b - CAA39068.2, *Methylococcus capsulatus Bath* - WP_010960482.1, *Sphingobium* sp. SCG-1 - WP_104955546.1, *Methylospira mobilis* - WP_153249048.1, *Methylomicrobium japanense* - BAE86875.1, *Methylomonas methanica* - WP_013818321.1, *Crenothrix polyspora* - WP_087143657.1, *Methylovulum miyakonense* HT12 - BAJ17645.1, Betaproteobacteria bacterium - PKO92487.1, *Rhodospirillaceae* bacterium - PCJ58204.1, *Mycolicibacterium elephantis* - WP_046753692.1, *Mycolicibacterium rhodesiae* - WP_014211362.1, *Mycobacterium chubuense* NBB4 - ACZ56334.1, *Thauera butanivorans* - WP_068635403.1, *Brachymonas petroleovorans* - AAR98534.1.

[b]Substrate for the diiron monooxygenase

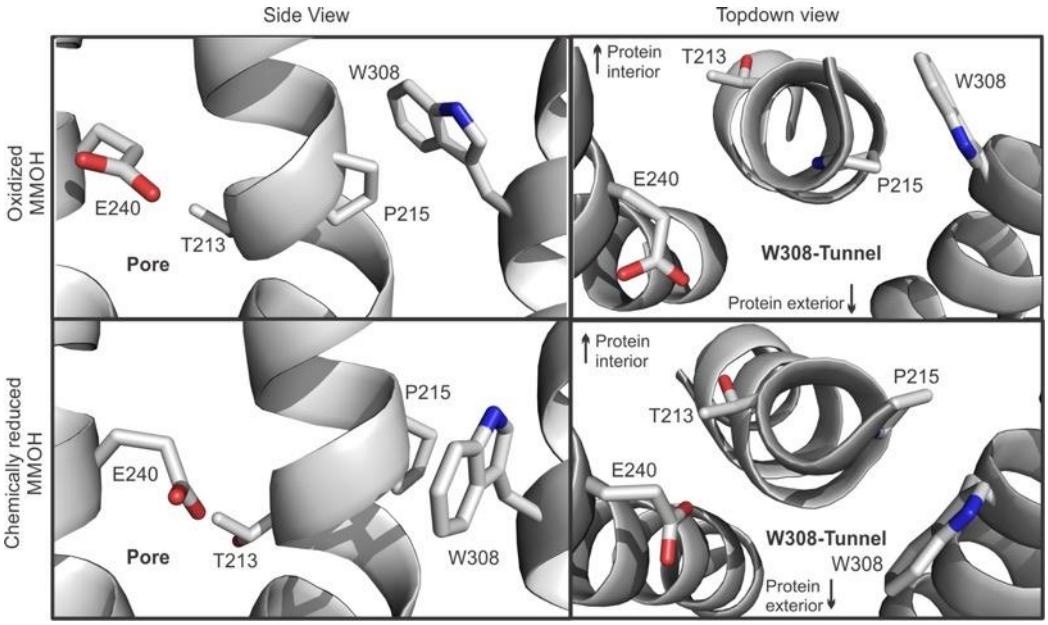

Figure 3-12 Effect of diiron cluster reduction on the Pore and the W308-Tunnel. Reduction of sMMOH causes the Pore (left) to partially close and opens the entrance into the W308-Tunnel (right). However, a bottleneck remains at sMMOH F282 and F212 that is not relieved until a complex is formed with MMOB The Pore is fully closed in the sMMOH:MMOB complex (see **Figure 3-10**). $sMMOH^{ox}$ = PDB:6KV6; $sMMOH^{red}$ = PDB:6VK7.

3.4.6 Kinetic Analysis of V41R-MMOB.

Past studies of enzymes such as NiFe hydrogenase that allow selective passage of gases to the active site have shown that small changes in the diameter of the putative gas tunnel via mutagenesis cause large changes in the efficiency of transit.[236] Accordingly, the importance of the W308-Tunnel was evaluated by altering access to the tunnel through mutagenesis. Variants of MMOB are easily generated,[71] whereas this is not the case for sMMOH. MMOB residue V41 was chosen as a target for mutagenesis to determine if the W308-Tunnel is involved in trafficking substrates to the active site. It is positioned near the W308-Tunnel entrance into the α-subunit (**Figure 3-13**A), and it is a part of a β-sheet involved in the sMMOH-MMOB interaction interface. The only intra/intermolecular polar contacts V41 makes are between its backbone NH and carbonyl oxygen and the backbone atoms of S109 and S110 located on an adjacent β-sheet of MMOB. Residues S109 and S110 have been experimentally shown to strongly influence hydrocarbon substrate selectivity and reactivity.[65, 67, 71] Residues with larger side chains were introduced at MMOB position 41 in an attempt to block access into the W308-Tunnel (**Figure 3-13**B). The following V41 MMOB mutations were created and biochemically assessed: V41R, V41E, and V41F. In addition, the nearby V39 residue was evaluated by generating the V39R and V39F variants. Each variant nearly halted the reaction of the reconstituted sMMO system (**Table 3-6**), but V41R-MMOB exhibited the most dramatic effects, so its reaction will be described in more detail here.

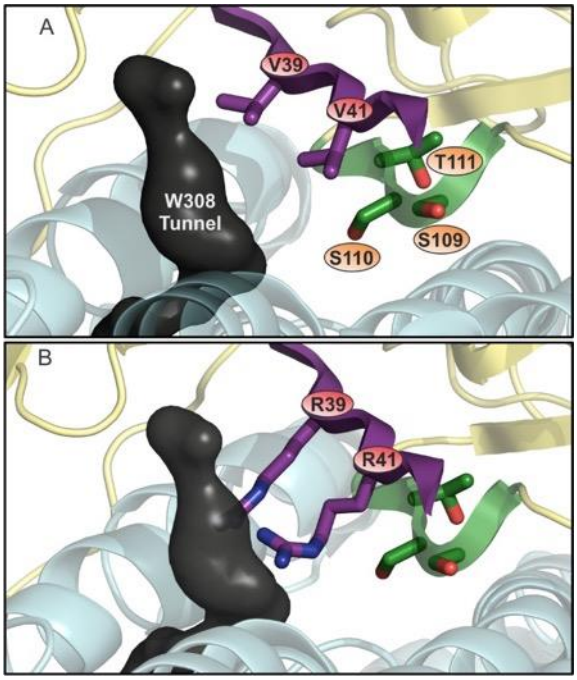

Figure 3-13 V41R-MMOB mutation theoretical representation.
Panel A depicts the orientation of V39 and V41 in the Form 1 *Mt* sMMOH:MMOB complex (6VK5) crystal structure. Panel B is the result of using the mutagenesis feature in PyMol to mutate V39 and V41 to R39 and R41, respectively. The new Arg residues have no obvious side chain electrostatic interactions and so a number of rotomeric conformations are possible, of which only one is illustrated. The W308-Tunnel is represented as a tube (black), MMOB (yellow) and sMMOH α-subunit (cyan) are shown as cartoons, and amino acid side chains are represented as sticks (purple = carbon, blue = nitrogen). The nearby "Quad" residues of MMOB are shown in green.

Table 3-6 Steady State O_2 Uptake in the Reconstituted sMMO System with MMOB Variant

MMOB Variant	Variant Alone % Activity	Variant 1:1 with MMOB % Activity	Variant 5:1 with MMOB % Activity
None (MMOH alone)	0	N/A	N/A
WT-MMOB	100	100	100
V39F	< 0.1	100	86
V39R	< 0.1	84	42
V41E[b]	< 0.1	100	100
V41F[b]	< 0.1	100	100
V41R	< 0.1	53	4

[a]Conditions: 0.2 μM sMMOH (0.4 μM active sites), 0.4 μM MMOB, 0.4 μM or 2.0 μM MMOB variant when present 1.2 μM MMOR, 200 μM CH_4, 250 μM O_2, 400 μM NADH, 25 mM MOPS pH 7.5, 23 °C

[b]Steady state data alone do not demonstrate binding for these variants. However, a perturbation in the EPR spectrum of reduced sMMOH shows that these variants do form a complex (see below).

In the absence of MMOB, steady state O_2 utilization during CH_4 turnover by the reconstituted sMMO system is very slow, but it increases 150-fold when MMOB is added in a 1:1 ratio with the sMMOH diiron sites.[33] In contrast, this concentration of V41R-MMOB caused almost no increase in the rate of O_2 uptake (**Figure 3-14**) The loss of reactivity when using V41R-MMOB could derive either from blocked O_2 (or CH_4) binding or failure to form a complex with sMMOH. In order to determine if V41R-MMOB can bind to sMMOH, a competitive steady-state experiment was performed in which both MMOB and V41R-MMOB were present. If V41R-MMOB binds to sMMOH with a similar binding affinity as MMOB, then the steady state initial velocity will decrease as V41R-MMOB is added. It was found that the initial velocity of O_2 consumption decreased nearly 50% in the presence of equal molar concentrations of V41R-MMOB and MMOB (**Figure 3-14**). The initial velocity continued to decrease upon subsequent additions of the MMOB variant. This finding suggests that the mutation does not significantly alter MMOB affinity for sMMOH. The same experiment using V39R-MMOB showed a similar competitive effect, but the affinity of this variant appears to be less than that of WT-MMOB (**Figure 3-15**). The other variants tested showed even lower affinity relative to that of WT-MMOB, but perturbation of the integer spin EPR signal of $sMMOH^{red}$ demonstrated that each forms a protein-protein complex (**Figure 3-16**).

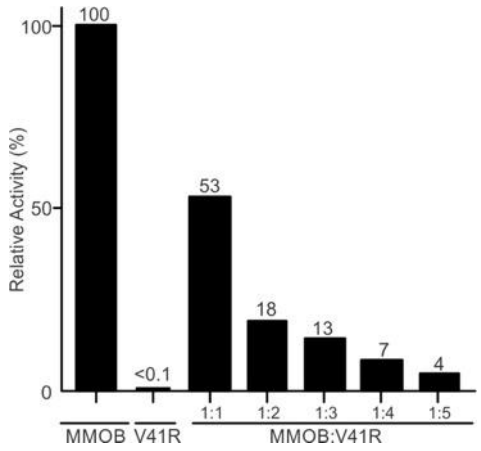

Figure 3-14 Competition between WT-MMOB and V41R-MMOB during steady state turnover.

Mt sMMOH was present at the same concentration in all experiments. When WT-MMOB or V41R-MMOB was added alone, it was present at the same concentration as sMMOH (active sites). For experiments in which WT-MMOB and V41R were added together in the ratios shown, WT-MMOB was present at the same concentration as sMMOH (active sites). Other conditions for the experiment are given in Experimental Procedures.

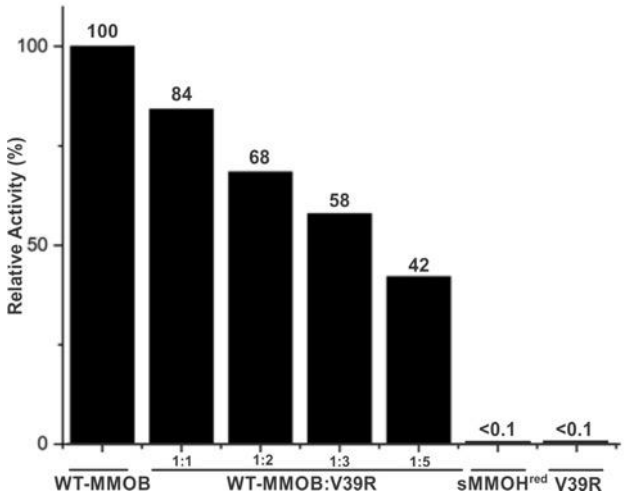

Figure 3-15 Competition between WT-MMOB and V39R-MMOB during steady state turnover.

Mt sMMOH is present at the same concentration in all experiments. When WT-MMOB or V39R-MMOB was added alone, it was present at the same concentration as sMMOH (active sites). For experiments in which WT-MMOB and V39R are added together in the ratios shown, WT-MMOB is present at the same concentration as sMMOH (active sites). Other conditions for the experiment are given in Experimental Procedures.

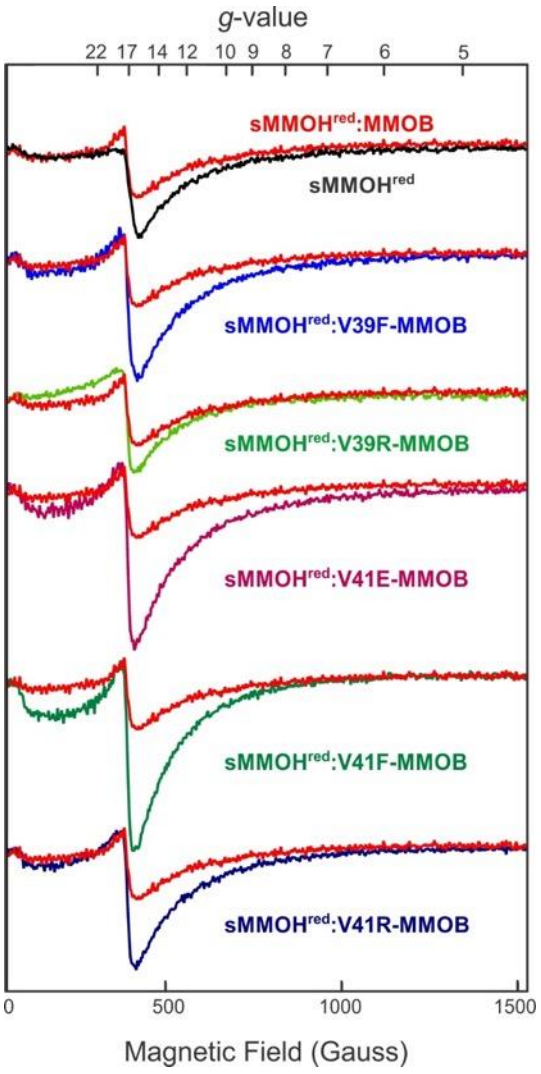

Figure 3-16 Parallel mode EPR spectra of sMMOH^{red} with MMOB and MMOB variants.

sMMOH^{red} exhibits a characteristic EPR spectrum at g = 16 due to ferromagnetic coupling of the two high-spin Fe(II) ions of the diiron cluster The resulting integer spin system gives an enhanced EPR signal when recorded with the microwave field aligned parallel with the magnetic field. The signal is perturbed when MMOB is present due to the formation of a protein-protein complex (compare the black and red spectra in the top trace). Each of the MMOB variants used in this study gives a similar perturbation, albeit with distinct intensities, showing that each forms a complex with MMOH^{red} (red trace from sMMOH:MMOB show for comparison in each case). Moreover, each perturbs the diiron cluster environment slightly differently. Conditions: sMMOH^{red}, 300 μM (active sites); MMOB (or variant), 300 μM, 25 mM MOPS, pH 7.5. EPR conditions: frequency, 9.400 GHz; time constant, 2.56 ms; microwave power, 2 mW, temperature, 2.0 K, cavity tuned for parallel mode detection.

Single turnover stopped-flow experiments were performed in which a 1:1 mixture of anaerobic sMMOH^{red} and V41R-MMOB was rapidly mixed with a large excess of O_2 in order to determine whether this MMOB variant affects the formation and decay of chemical intermediates in the sMMOH catalytic cycle. MMOB is required to accelerate the start of the reaction cycle so that reaction cycle intermediates **P***, **P**, and **Q** build up and can be detected.[68] In the presence of V41R-MMOB, none of these intermediates were seen. Instead, the diferrous sMMOH decayed slowly to the diferric state.

As sMMOH^{red} oxidizes, a weak chromophore in the near-UV region develops, allowing the kinetics of reoxidation to be monitored. In the case of the *Mt* sMMOH^{red}:MMOB complex, the initial reaction with O_2 is apparently too fast to follow with stopped-flow, because no O_2-dependent phase is observed in multi-exponential fits of the time course.[68, 69] The lack of O_2 concentration dependence in the reciprocal relaxation times of the observed phases implies that the (unobserved) O_2 binding is effectively irreversible.[69] The reaction following O_2 binding in the sMMOH^{red}:MMOB active site, which results in a complex with the diferrous cluster (intermediate **P***), occurs with a rate constant of 26 s^{-1} at 4 °C as monitored by rapid freeze quench EPR and Mössbauer spectroscopies.[33, 68, 69, 77] **P*** then decays at 9 s^{-1} to the diferric peroxo intermediate **P** with the resulting chromophoric change.[68, 76] The rate constant of 26 s^{-1} is 1-2 orders of magnitude slower than typically observed for O_2 reaction with a metalloenzyme, [124, 237, 238] but it is much faster than that observed for O_2 reaction with sMMOH^{red} in the absence of MMOB (**Figure 3-17**A). The observed reciprocal relaxation time for the latter reaction exhibits a hyperbolic dependence on O_2 concentration, suggesting that it occurs in two steps (**Figure 3-17**B, inset). Nominally, these steps are reversible binding (K_{D1} = 0.44 mM ± 0.02 mM) followed by a slower irreversible oxidation step (k = 0.019 ± 0.001 s^{-1}). Interestingly, the reaction of *Mt* sMMOH^{red}:V41R-MMOB with O_2 occurs even slower with a O_2-dependent second order rate constant of 1.5 ± 0.2 M^{-1} s^{-1} at 4 °C (pseudo first order $k \approx 0.001$ s^{-1} at 720 μM O_2) (**Figure 3-17**A and B). The linear O_2-concentration dependence suggests that this reaction is rate-limited by the initial O_2 binding reaction. Thus, the

initial O_2 binding reaction occurs at least 25,000-fold slower when V41R-MMOB is used in place of WT-MMOB (>26 s^{-1}/0.001 s^{-1}). The fundamentally different reactions with O_2 indicated in **Figure 3-17**B for $sMMOH^{red}$:V41R-MMOB versus $sMMOH^{red}$ alone have implications for the mechanism of O_2 access as discussed below.

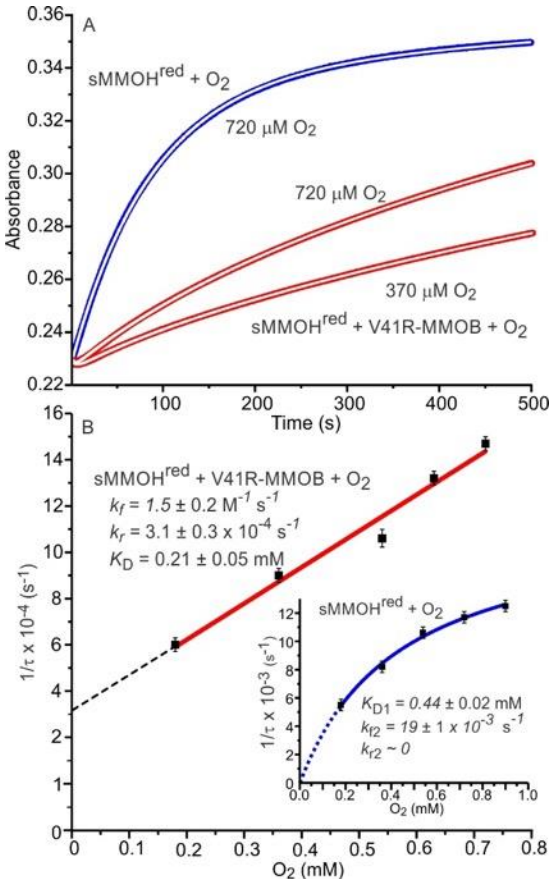

Figure 3-17 Stopped-flow experiments using the V41R-MMOB variant. Reaction after stopped-flow mixing of 28.5 μM sMMOH^{red} (57 μM active sites) with O_2 in the presence (red) and absence (blue) of 57 μM V41R-MMOB (after mixing). (A) Time course of the oxidation reaction monitored at 330 nm at the concentration (after mixing) of O_2 shown. Three-summed exponential fits to the data are shown superimposed in white on the time courses. All time courses have the same endpoint at infinite time. The faster two, very low amplitude phases are seen in all reactions in the presence or absence of V41R-MMOB and are apparently an artifact of mixing. In the presence of WT-MMOB, the time course would be coincident with the y-axis for the time scale shown. Conditions: 50 mM MOPS buffer pH 7, 4 °C. (B) Plot of observed reciprocal relaxation times of the large amplitude, slowest phase from fits of data like those in panel A for reactions using V41R-MMOB versus O_2 concentration. Inset: The same plot from fits of reactions containing MMOH^{red} alone. Data analysis is described in the methods section.

3.5 Discussion

Presented here and in another recent study are the first X-ray crystallographic structures of the sMMOH^{ox}:MMOB and sMMOH^{red}:MMOB complexes using protein components isolated from the Type II methanotroph *Methylosinus trichosporium* OB3b. These structures complement those previously published of the complex of the oxidized sMMO components from the Type Ia methanotroph[239] *Methylococcus capsulatus* strain Bath.[70] While the structures are clearly similar, the much higher current resolution of the *Mt* OB3b complex structures now allows the effects of complexation and reduction to be evaluated in detail. We also report the highest resolution structure of sMMOH^{ox} to date, as well as the first structure of reduced *Mt* sMMOH. These studies are used in the following discussion to evaluate the changes in the sMMOH structure caused by MMOB that specifically influence O_2 (and potentially methane) access to the active site during the catalytic cycle.

3.5.1 Effect of Molecules in the Active Site.

The *Mt* sMMOH^{ox}:MMOB Form 1 (6VK5) and Form 2 (6VK8) structures reported here show benzoate and succinate, respectively, bound in the active site to the diiron cluster (**Figure 3-4**). The presence of these molecules is particularly revealing because the structures demonstrate the flexibility of the active site and its potential influence on substrate access. While sMMOH is clearly tailored to facilitate methane oxidation, the enzyme will oxidize hundreds of larger adventitious substrates.[35, 114] These reactions are not beneficial to the methanotroph, but they do indicate that the active site can expand to accommodate larger molecules. The metrics of the diiron cluster itself with benzoate bound are essentially unchanged from those of the substrate-free enzyme with the exception of the Fe-Fe distance, which is lengthened by approximately 0.4 Å. In contrast, the active site cavity is significantly altered, which can be seen by comparing the benzoate-bound *Mt* sMMOH^{ox}:MMOB Form 1 structure to the RT-XFEL *Mt* sMMOH^{ox}:MMOB structure, in which

water is modeled as a ligand to the diiron cluster in place of benzoate (**Figure 3-5**A vs C and **Figure 3-8**C vs E). Changes occur in three of the four helices (C, E, and F) that house the nonheme diiron cluster (**Figure 3-6**). The ability of Helices E and F to shift is important because they carry with them residues E209, E243, and H246, which are three of the six ligands that coordinate the diiron cluster. The flexibility of these helices permit Fe2 to change its distance from Fe1 during the catalytic cycle, which allows formation of structurally diverse intermediates.[92, 198] It is likely that part of this flexibility derives from the π-helical segment in Helix E adjacent to the cluster.

The mechanistic significance of large substrates in the active site of the *Mt* sMMOH:MMOB complex remains unknown. In addition to the benzoate and succinate demonstrated here, relatively large alcohols have been structurally characterized as ligands to the diiron cluster in *Mc* sMMOH^{ox} crystals in soaking experiments (see for example PDB:1XVG).[42, 50] In contrast, no large molecules that perturb the active site are observed in the structures of *Mt* sMMOH^{ox}, *Mt* sMMOH^{red}, and only a small molecule that causes no change in structure was observed in RT-XFEL *Mt* sMMOH:MMOB experiments. Thus, the presence of larger exogenous molecules in the active site of crystallized enzyme appears to be dependent on both the sMMO protein components present and the crystallization conditions. Past single turnover kinetic experiments have shown that molecules larger than methane such as C2 to C8 hydrocarbons bind slowly to the enzyme after **Q** is formed in the reaction cycle and are hydroxylated.[5, 68, 74, 86] The route of entry of these large molecules into the active site is unclear, but the current results suggest that the variable volume of the active site is likely to be an important factor in the ability of sMMO to oxidize such a large range of substrates.

It is proposed here that the binding of large molecules in the active site is the direct cause of the shift in the position of F188 and coordinated changes in the π-helical region of Helix D (**Figure 3-5**A and B). This observation contradicts the conclusion of Lee, et al. that MMOB binding is the cause of this shift.[70] The latter conclusion was based on the observation of the shift in F188

in a structure of *Mc* sMMOH:MMOB (4GAM) thought to be devoid of a substrate. However, close inspection of the 4GAM electron density map shows that there is additional positive density in the Fo-Fc omit map of the active site (**Figure 3-5**D and **Figure 3-7**) in the position where we model large molecules in Form 1 and Form 2 *Mt* sMMOH:MMOB. This observation suggests the likely possibility that there is also a substrate-like molecule present in the *Mc* sMMOH:MMOB crystal, and that this molecule is the cause of the F188 shift. This new insight is important because the shift in the position of F188 completely removes the barrier between Cavities 2 and 1 (compare **Figure 3-8**C with **Figure 3-8**E, **Table 3-7**). The observation of this pathway opening as an effect of MMOB binding in the *Mc* Bath sMMOH:MMOB complex was proposed as explanation for the regulatory effect of MMOB on O_2 and CH_4 binding,[70] which we believe should be reevaluated. Indeed, the results presented here indicate that MMOB binding constricts the bottleneck between Cavities 1 and 2 due to the reorganization of L110 and L216 and blocks access to the active site through the chain of cavities. This change is only visualized in the absence of adventitious substrate binding in the active site cavity.

Table 3-7 Potential Passages into the sMMOH Active Site

	sMMOH^{ox} 6VK6	sMMOH^{red} 6VK7	sMMOH^{ox}:MMOB Form 1 6VK5	sMMOH^{red}:MMOB 6VK4	sMMOH^{ox}:MMOB RT-XFEL 6YD0	sMMOH^{red}:MMOB RT-XFEL 6YDI
Chain of Cavities	Cavities 3 to 2 Connected	Cavities 3 to 2 Connected	Cavities 3 to 2 Connected	Cavities 3 to 2 Connected	Cavities 3 to 2 Connected	Cavities 3 to 2 Connected
	Cavities 2 to 1 Connected	Cavities 2 to 1 Disconnected[a]	Cavities 2 to 1 Connected[b]	Cavities 2 to 1 Connected[b]	Cavities 2 to 1 Disconnected	Cavities 2 to 1 Disconnected
W308-Tunnel	Closed	Closed	Open	Open	Open	Open
Pore	Open	Partially closed	Closed	Closed	Closed	Closed

3.5.2 The W308-Tunnel as an Alternative Route for O_2 Access.

The structures currently available are those of the states leading directly to formation of the O_2 complex. As described in the introduction, two routes for the entry of substrates into the active site have been proposed: (i) direct entry through the Pore region, and (ii) transit through a long assembly of three cavities. The structures presented here and in previous studies of the *Mc* Bath sMMOH:MMOB suggest that the route through the Pore is unlikely because MMOB physically covers the Pore and residues shift within the Pore upon MMOB binding to block access.[70] Access through the chain of cavities remains a possibility, but it is made less likely by the structural, kinetic, and mutagenic studies presented here and in our previous studies.[65, 68, 69, 71] We suggest here that passage of O_2 through the W308-Tunnel is a third possible transit route, which is consistent with all of the available studies. Several observations favor the W308-Tunnel over the chain of cavities. First, the residues that define the W308-Tunnel, are highly conserved in the known sMMOH enzymes as well as in similar diiron cluster-containing enzymes that catalyze oxidation of small hydrocarbons (

Table 3-5). This conservation is not observed for enzymes structurally related to sMMOH that oxidize larger substrates such as the toluene 4-monooxygenase (T4MO), toluene/o-xylene monooxygenase (ToMOH), and phenol hydroxylase (PHH). In the latter enzymes, a relatively large tunnel in the vicinity of the sMMOH W308-Tunnel has been detected.[212] However, these tunnels follow a different path to the active site, and close rather than open when complexes are formed with the cognate regulatory proteins.[55] Second, the proposed route for O_2 through the W308-Tunnel in the sMMOH:MMOB complex would take it past V41 shown here to profoundly affect the rate of diiron cluster oxidation when mutated to a larger residue (**Figure 3-17**). Third, the tunnel also passes the sMMOH-MMOB interface region that includes the MMOB "Quad-residues" (N107, S109, S110, T111)[71] that control many aspects of the size selectivity of hydrocarbon substrates (**Figure 3-10** and **Figure 3-13**). Fourth, the binding of MMOB causes many structural changes in

the W308-Tunnel that are likely to affect O_2 binding. Specifically, a dome of conserved, hydrophobic residues is organized above the entry to the W308-Tunnel by MMOB (**Figure 3-18**).

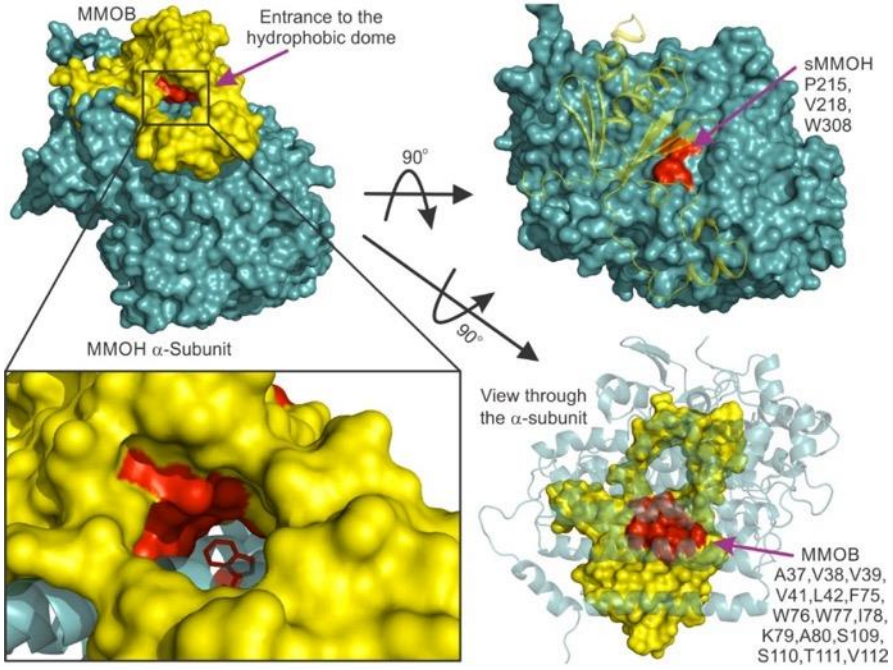

Figure 3-18 The hydrophobic entrance to the W308-Tunnel. Hydrophobic entry into the W308-Tunnel results from the formation of the sMMOH^{red}:MMOB complex (6YDI). Colors: sMMOH α-subunit, teal; MMOB, yellow; residues forming the hydrophobic dome, red. The red colored surface representation of the hydrophobic dome at the protein complex interface is visualized more clearly by making one of the two proteins transparent in the structures to the right.

This structural feature would enhance the binding of O_2 because the W308-Tunnel entrance is otherwise exposed to solvent and surrounded by polar residues in the sMMOH^{red} structure. Fifth, the bottlenecks in the W308-Tunnel widen in the sMMOH:MMOB complex sufficiently to permit O_2 to pass at the critical choke points, whereas the passage through the chain of cavities effectively closes (**Figure 3-11** and **Figure 3-19**).

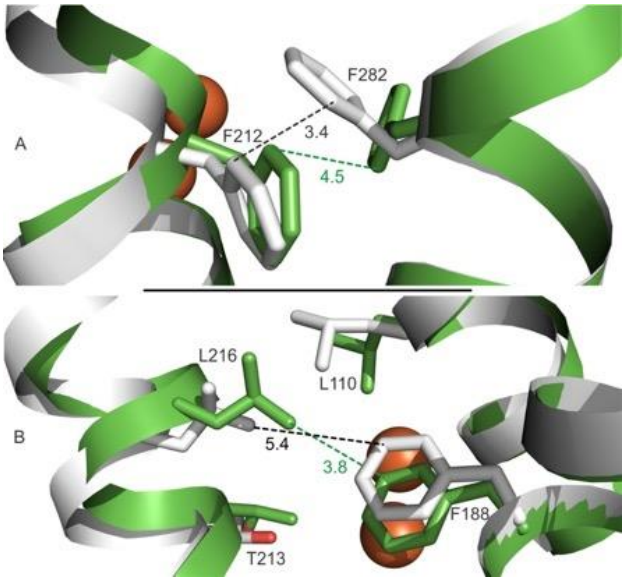

Figure 3-19 Structural changes in constriction points in access routes for O_2 into the actives site resulting from MMOB binding.
Structures for sMMOH^{red} (6VK7, white) and RT-XFEL sMMOH^{red}:MMOB (6YDI, green) are shown at constriction points in (A) the W308-Tunnel and (B) the passage from Cavity 2 to Cavity 1. The large shift in the position of F282 opens the W308-Tunnel, while the shifts in the Cavity 2 to 1 passage greatly restrict that route of entry.

The state of the potential passageways into the active site as seen in the crystal structures are summarized in **Table 3-7**. Sixth, the W308-Tunnel entrance is positioned in a structural region in sMMOH between two π-helical sections of adjacent Helices E and H (**Figure 3-20**). Often π-helices are evolutionary conserved for their functional roles in enzyme activity.[190, 240-242] Finally, all structures of the sMMOH:MMOB complex show that the 30-residue unstructured N-terminal region of isolated MMOB becomes ordered as it binds to sMMOH.[45, 46, 70, 243] Truncation of this region shifts the rate-limiting step of the catalytic cycle to O_2 binding.[46] The RT-XFEL study of the sMMOH:MMOB complex showed that the MMOB N-terminal residues selectively reorganize sMMOH Helices H and 4. Helix H provides many of the residues for the W308-Tunnel once it enters sMMOH. Indeed, both the N-terminal tail of MMOB and the distinctive tryptophan-rich sequence of Helix H in sMMOH are uniquely conserved in sMMO enzymes within the larger family of bacterial multicomponent monooxygenases (**Figure 3-21**). The novelty of the W308-Tunnel entrance is further highlighted by the observation that the MMOB induced reorganization of Helices E, F and H closes the Pore and opens the W308-tunnel. It is perhaps not coincidental that this conformational change opens up a non-polar route into sMMOH at the expense of a polar route in preparation for the start of the catalytic cycle.

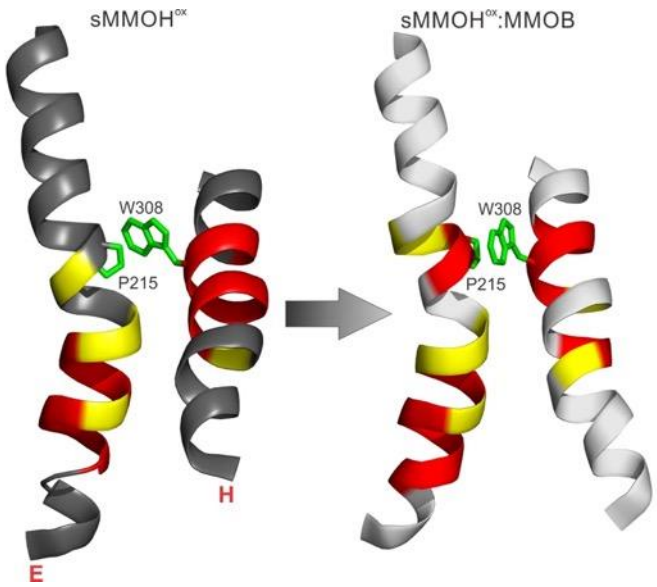

Figure 3-20 The W308-Tunnel molecular gate.
sMMOH amino acids P215 (Helix E) and W308 (Helix H) shift dramatically upon formation of the MMOB complex, acting as a molecular gate. The gate movement is possible because of the α-helices (red) and sections of the helix that do not form intra-main chain hydrogen bonds (yellow). As a result, the helices are more flexible allowing the molecular gate to open and close. $sMMOH^{ox}$ = PDB:6VK6; $sMMOH^{ox}$:MMOB = PDB:6YD0.

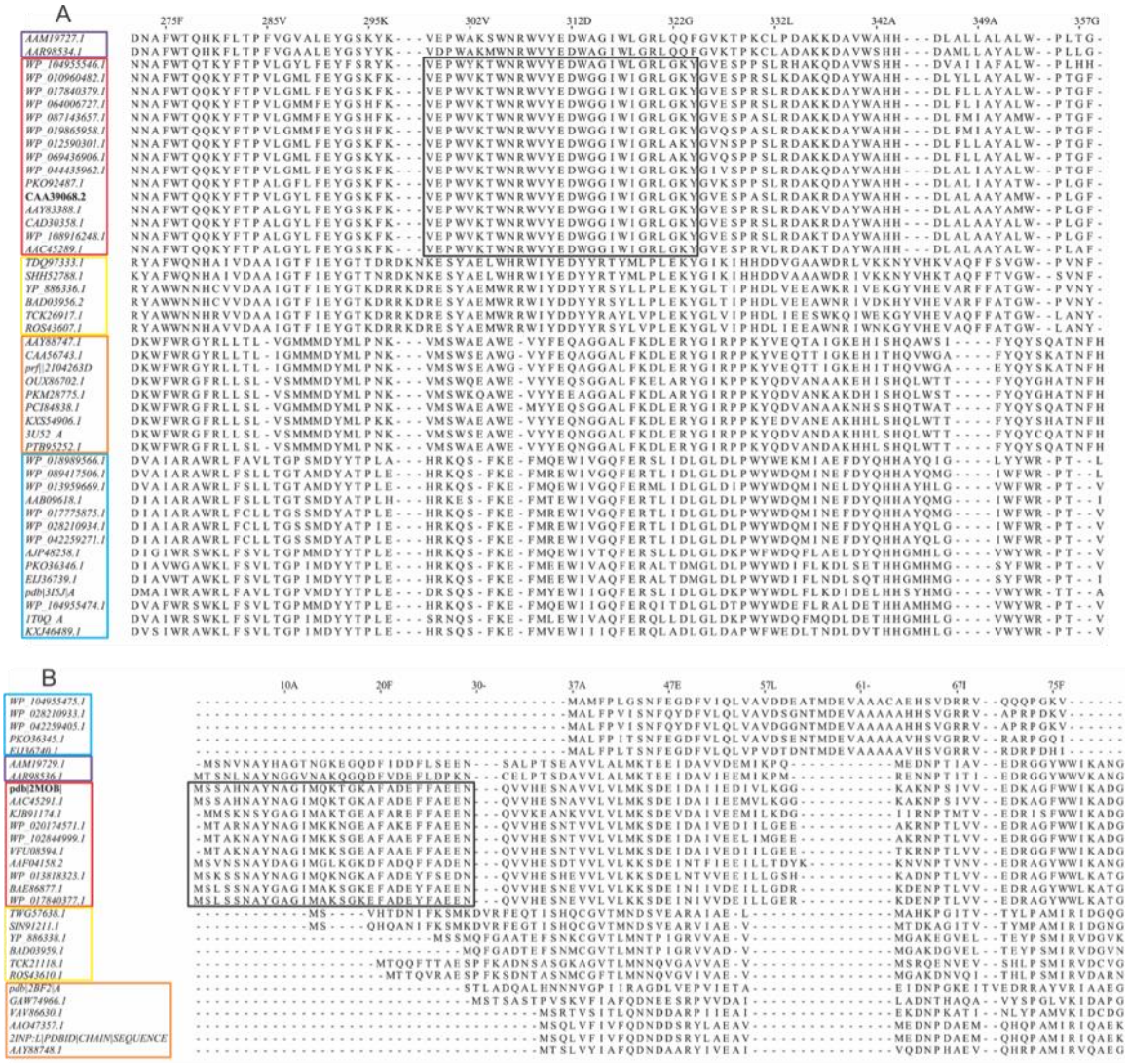

Figure 3-21 Sequence alignments of key regions of hydroxylase and regulatory proteins.
Portions of the α-subunit of the hydroxylase components (panel A) and the regulatory protein components (panel B) of the bacterial multicomponent monooxygenase family are illustrated. Enzyme sub-families are identified by colored boxes; methane monooxygenase – red, butane monooxygenase – purple, propane monooxygenase – yellow, phenol hydroxylase – orange, toluene monooxygenase – cyan. The unique extended N-terminal tail of the regulatory component and the tryptophan-rich Helix H of the α-subunit in sMMOH have been highlighted by black boxes.

3.5.3 Insight from Studies of the Evolution of Bacterial Multicomponent Monooxygenases.

A recent study of the evolution of bacterial multicomponent monooxygenases suggests that sMMO was the last to emerge and is significantly diverged from the monooxygenases that oxidized larger substrates.[51] It is interesting to speculate that the chain of cavities in sMMOH has been carried over from an earlier ancestor, but has been functionally replaced by the narrow W308-Tunnel to provide selectivity for small substrates. Also, it is noteworthy that the critical N-terminal region of MMOB that regulates the W308-Tunnel region in the sMMOH:MMOB complex is missing or truncated in the monooxygenases that oxidize larger substrates (**Figure 3-21**). Thus, caution must be exercised when using the structures of these enzymes to draw conclusions regarding substrate access into the active site of sMMOH.

3.5.4 Insight from Diiron Cluster Oxidation Kinetics.

Additional support for the importance of the W308-Tunnel derives from an examination of the kinetics of $sMMOH^{red}$ diiron cluster reoxidation under various conditions (**Figure 3-17**). Overall, the rate constant for O_2 access into the active site is at least 25,000-fold larger when $sMMOH^{red}$ is complexed with WT-MMOB rather than V41R-MMOB. However, the comparison of the reaction without MMOB versus that with V41R-MMOB present also provides insight. The reaction using V41R-MMOB is much slower, and the rate constant for the reaction displays a first order dependence on O_2 concentration rather than the hyperbolic dependence seen for that of the isolated $sMMOH^{red}$ reaction (**Figure 3-17**B). A possible scenario to account for these observations is based on a change in the rate-limiting step from: (i) O_2 gaining access to the protein at a location remote from the diiron cluster in the V41R-MMOB $sMMOH^{red}$ reaction, to (ii) O_2 binding to the diiron cluster in the isolated $sMMOH^{red}$ reaction. If V41R-MMOB restricts the W308-Tunnel, the slow step becomes O_2 binding from solution, the rate constant for which would exhibit the observed first

order dependence on O_2 concentration. In the absence of MMOB, the hyperbolic O_2 concentration dependence of the observed rate constant suggests that another step following reversible O_2 binding is rate-limiting. Our previous magnetic circular dichroism/circular dichroism[127] and RT-XFEL studies of the *Mt* sMMOH:MMOB complex show that discrete changes occur in the diiron cluster environment as MMOB binds that are predicted to enhance its ability to bind and activate O_2. In the absence of these changes, the binding of O_2 to the cluster may be slower than the O_2 transit to a position where it would be poised to react with the cluster. This condition would be satisfied if the transit time through the W308-Tunnel is faster than binding to the diiron cluster. However, the severe constriction in the W308-Tunnel and polar residues at its entry into $sMMOH^{red}$ in the absence of MMOB may greatly slow or even block O_2 entry via this route (**Figure 3-11**). Alternatively, in the absence of MMOB or its V41R variant, O_2 might still slowly enter the active site through the constriction in the channel between Cavities 1 and 2 in the chain of cavities. Accumulation of O_2 in the chain of cavities prior to binding to the diiron cluster would result in the observed hyperbolic dependence of the rate constant. In this scenario, the route through the cavities is responsible for the slow background rate of cluster reoxidation in the absence of MMOB, which is shut off when MMOB binds. It should be noted that this analysis implies two separate roles for MMOB. The structural changes it engenders both activate the cluster to react with O_2, while also opening the W308-Tunnel for size-selective, bottleneck free, one-dimensional rapid transit of O_2 to the cluster.

3.5.5 Relevance to Methane Binding.

Past studies have shown that methane and most adventitious substrates of sMMO react directly with intermediate **Q** in the sMMOH catalytic cycle.[86] These substrates do not affect the kinetics of earlier cycle steps, but their reaction with **Q** is first order in substrate in the accessible concentration range. Our previous transient kinetic studies demonstrate that MMOB is bound to sMMOH when substrates react with **Q**.[71] MMOB variants with smaller residues in the Quad region (Green β-sheet

in **Figure 3-10** and **Figure 3-13**) adjacent to the W308-Tunnel allow larger substrates to react more rapidly, consistent with easier passage into the active site.[71] Accordingly, larger substrates exhibit no deuterium KIE when reacting with **Q** unless the MMOB variants with smaller residues in the Quad region are used in place of WT-MMOB.[66] In contrast, a deuterium KIE of 50 is observed for the methane reaction when WT-MMOB is utilized.[65, 74, 89] These results are consistent with the W308-Tunnel also serving as an access route for hydrocarbon substrates. When the substrate is larger than methane, the constraints of the tunnel cause binding to the protein to be rate-limiting rather than C-H bond cleavage, hence giving first order kinetics in substrate concentration with no deuterium KIE. Methane may give both first order kinetics and a KIE because it is small enough to pass efficiently through the MMOB-modified tunnel. The transit of methane might be faster than expected through the narrow tunnel because it can only move in one- rather than three-dimensions. A parallel can be drawn to the accelerated localization of DNA binding factors to consensus sites due to one-dimensional transit on the DNA polymer.[244] In essence, methane behaves kinetically as if it does not accumulate in the tunnel but rather collides directly from solution with the diiron cluster in the highly reactive **Q** intermediate state. The cleavage of the strong bond of methane would then be rate-limiting to give the detectable KIE. The passage of methane through the chain of cavities is also possible, but the cavities are large enough to accumulate many methane molecules. Indeed, we find multiple solvent molecules in the cavities (**Figure 3-22**)and the binding of Xe and small hydrophobic molecules have been reported in the cavities of the *Mc* Bath sMMOH.[43] This accumulation of substrates in the cavities would mean that the substrate would react with **Q** from within the protein rather than from solution, thereby yielding hyperbolic or concentration independent response of the rate constants.

An important caveat is that the asynchronous binding of O_2 and hydrocarbon substrates during the catalytic cycle implies a significant structural change that cannot be investigated using the available crystal structures. In particular, a change that allows the binding of molecules slightly larger than O_2 at the **Q** stage of the reaction cycle would account for the existing kinetic data.

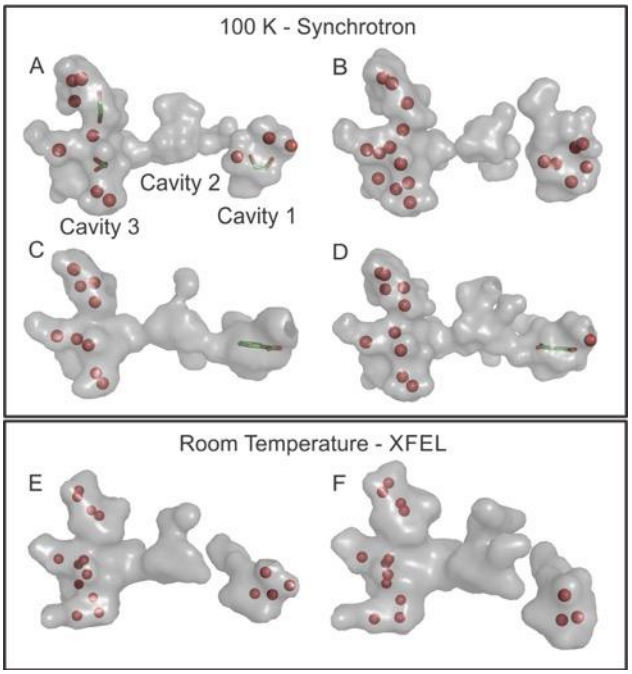

Figure 3-22 Exogenous molecules bound inside the cavities.
The chain of *Mt* sMMOH internal cavities is represented as transparent gray surface. Water molecules are represented as red spheres. Alternative substrate molecules are shown as sticks where green is carbon and red is oxygen. A.) *Mt* sMMOH^{ox} (6VK6), B.) *Mt* sMMOH^{red} (6VK7), C.) *Mt* sMMOH^{ox}:MMOB, Form 1, protomer 1 (6VK5), D.) *Mt* sMMOH^{ox}:MMOB, Form 2, protomer 1 (6VK8), E.) RT-XFEL *Mt* sMMOH^{ox}:MMOB (6YD0), F.) RT-XFEL *Mt* sMMOH^{red}:MMOB (6YDI).

Chapter 4 Soluble Methane Monooxygenase Component Interactions Monitored by ^{19}F-NMR

Portions of this chapter are adapted from a manuscript currently under review authored by Jason C. Jones, Rahul Banerjee, Manny Semonis, Ke Shi, Hideki Aihara, William C. K. Pomerantz and John D. Lipscomb*

My contributions to this project were: conceiving and planning the experiments, sample preparation, perform the experiments, analyze the results, draft manuscript preparation, and review/approve the final manuscript.

4.1 Synopsis

Soluble methane monooxygenase is a multi-component metalloenzyme capable of catalyzing the fissure of the C-H bond of methane and insertion one atom of oxygen from O_2 to yield methanol. Efficient multiple-turnover catalysis occurs only in the presence of all three sMMO protein components; the hydroxylase (sMMOH), the reductase (MMOR), and the regulatory protein (MMOB). The complex series of sMMO protein component interactions that regulate the formation and decay of sMMO reaction cycle intermediates is not fully understood. Here, the two tryptophan residues in MMOB and the single Trp residue in MMOR are converted to 5-fluorotryptophan (5FW) by expression in media containing 5-fluoroindole. In addition, the mechanistically significant N-terminal region of MMOB is ^{19}F-labeled by reaction of the K15C variant with 3-bromo-1,1,1-trifluoroacetone (BTFA). The 5FW and BTFA modifications cause minimal structural perturbation, allowing detailed studies of the interactions with sMMOH using ^{19}F-NMR. Resonances from the 275 kDa complexes of sMMOH with 5FW-MMOB and BTFA-K15C-5FW-MMOB complex are readily detected at 5 μM labeled protein concentration. This approach shows directly that MMOR and MMOB competitively bind to sMMOH with similar K_D values, independent of the oxidation state of the diiron cluster of sMMOH. These findings suggest a new model for regulation in which dynamic equilibration of the MMOR and MMOB with sMMOH allows transient formation of key reactive complexes that irreversibly pull the reaction cycle forward. The slow kinetics of exchange of the sMMOH:MMOB complex is proposed to prevent MMOR-mediated reductive quenching of the high-valent reaction cycle intermediate **Q** before it can react with methane.

4.2 Introduction

Soluble methane monooxygenase (sMMO) is a multicomponent metalloenzyme capable of catalyzing the conversion of methane to methanol at ambient temperature and pressure.[5, 14] The enzyme consists of three protein components: a 245 kDa $(\alpha\beta\gamma)_2$ hydroxylase (sMMOH), a 38 kDa FAD and 2Fe-2S cluster-containing reductase (MMOR), and a 15 kDa cofactorless regulatory component (MMOB).[15, 33, 35] As shown in **Scheme 4-1**, the sMMOH active site contains a dinuclear iron cluster which serves to activate molecular oxygen for insertion into the C-H bond of methane (bond dissociation energy = 105 kcal/mol).[37, 40, 68, 151]

Scheme 4-1 Reaction Cycle of sMMO and Structure of the sMMOH:MMOB Complex.

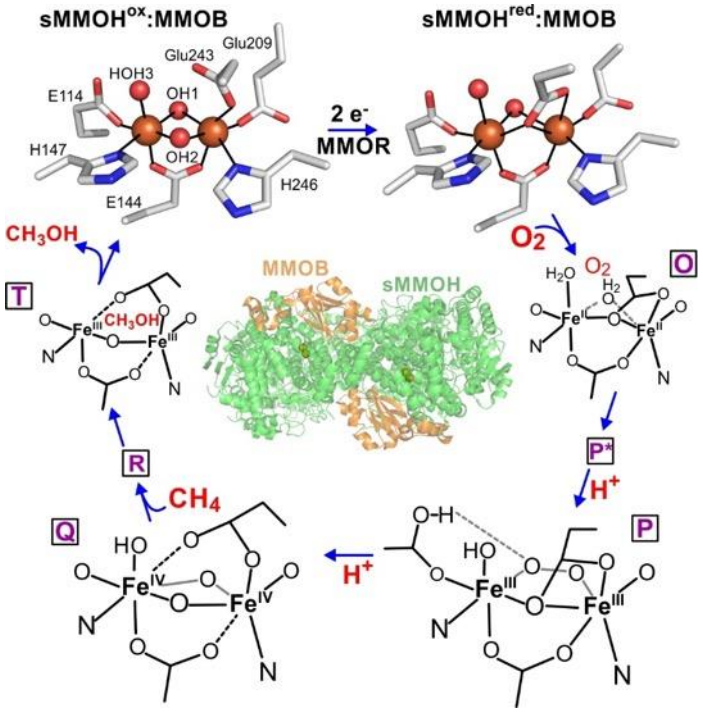

The resting state of sMMOH contains a diferric cluster ($Fe^{3+}Fe^{3+}$, $sMMOH^{ox}$) in which the irons are bridged by two solvent (OH^- or H_2O) molecules in addition to the carboxylate of Glu144. $sMMOH^{ox}$ can form a complex with MMOR and receive two electrons to form the diferrous cluster

($Fe^{2+}Fe^{2+}$, $sMMOH^{red}$) in which Glu243 shifts to bridge the irons via one carboxylate oxygen, one bridging solvent is lost, and the bond to the second solvent is weakened. In this new configuration, the diiron cluster can bind O_2 between the irons upon dissociation of the weakly bound solvent. However, O_2 binding is observed to be very slow in the absence of the regulatory component MMOB (Structure of the complex shown in **Scheme 4-1**).[69, 245] Binding of MMOB effects a 1,000-fold increase in the rate constant for the O_2 binding to the diiron cluster to form the first spectroscopically distinct intermediate of the reaction cycle, termed **P***. [68, 69, 75, 76, 245]. Recent structural studies indicate that one cause of the decreased rate of O_2 binding in the sMMOH active site in the absence of MMOB is the near closure of the molecular tunnel that mediates the transit of O_2 from the solvent.[245] This bottleneck is relieved by conformational changes in both MMOB and $sMMOH^{red}$ when the $sMMOH^{red}$:MMOB complex forms.[245] A second cause of the low reactivity of O_2 with $sMMOH^{red}$ is the position of the Glu209 ligand to the diiron cluster which blocks the approach to the open iron coordination site.[246] An angle change of this residue in the $sMMOH^{red}$:MMOB complex exposes the site for O_2 binding. The formation of intermediate **P*** is followed by spontaneous formation of a peroxo-intermediate **P**, and finally, O-O bond cleavage to yield the reactive dinuclear Fe^{IV} intermediate **Q**.[68, 86] **Q** can react directly with methane to form methanol with incorporation of one atom of oxygen sourced from O_2.

Intermediate **Q** is generated and stabilized by precisely coordinated sMMO protein component interactions.[64, 66, 70, 71, 131, 144, 245] Although two electrons are required to generate **Q**, subsequent stabilization of this intermediate requires that further transfer of electrons from MMOR be blocked in order to prevent quenching of the highly electrophilic dinuclear Fe^{IV} cluster. Early chemical cross-linking studies of the sMMO components from *Methylosinus trichosporium* OB3b showed that complexes between sMMOH and MMOB or MMOR can readily form.[63] Fluorescence quenching experiments utilizing either endogenous sMMOH tryptophan fluorescence or MMOB labeled with fluorophores demonstrated the formation of a $sMMOH^{ox}$:MMOB complex with a K_D value of 68 nM.[63, 131] However, measurement of the redox potential of sMMOH showed that a shift

of -132 mV occurred upon complex formation with MMOB, indicating that MMOB binds much more weakly to diferrous sMMOH.[69, 143, 145] While this finding might favor dissociation of MMOB upon reduction of sMMOH, subsequent studies based on site directed mutations in MMOB showed that this was not the case.[71] Remarkably, mutations in different regions of MMOB caused the rate constants for different individual steps in the reaction cycle to significantly change. When two different MMOB variants were added in succession in a single turnover reaction of $sMMOH^{red}$, only the step affected by the first MMOB variant added was observed to change. Thus, the first MMOB variant cannot equilibrate with the second in the sMMOH complex during the time required for a single turnover. A nondissociating MMOB might serve to physically block the ability of MMOR to transfer electrons to **Q** provided MMOB and MMOR share a binding spot on sMMOH. One conflict with this scenario is that MMOR must have access to resting sMMOH ($sMMOH^{ox}$) in order to transfer electrons at the start of the cycle, so MMOB cannot entirely block the reaction at this stage of the reaction cycle. Dissociation of MMOB from $sMMOH^{ox}$ promoted by MMOR would resolve this problem, but this suggestion seems at odds with the high affinity of MMOB for $sMMOH^{ox}$.

Two current models for the regulation of electron transfer in the sMMO system are illustrated in **Scheme 4-2**. Model A was motivated by the observation in the chemical cross-linking study referenced above that MMOB and MMOR cross-link to different subunits of sMMOH.[63] In this model sMMOH and MMOB have independent binding sites and electron transfer at the **Q** stage of the reaction cycle might be blocked by a conformational change at either the MMOR-MMOB or sMMOH alpha-beta subunit interface. Model B is based on studies of the protein components isolated from *Methylococcus capsulatus* (*Mc*) Bath.[64, 144] An MMOR construct composed of just the domain containing the 2Fe-2S cluster, termed the Fd domain, was utilized to simplify the experiments. Results from hydrogen−deuterium exchange coupled to mass spectrometry (HDX-MS) and fluorescence anisotropy titration experiments using a 5-((((2-iodoacetyl) amino) ethyl) amino) naphthalene-1-sulfonic Acid (IAEDANS)-labeled MMOB D36C variant suggested that the

MMOB and Fd-MMOR binding sites overlap on sMMOH. The HDX-MS data showed that the Fd domain interacts with sMMOH surface residues located in the canyon region of the alpha subunit. This is the same location that X-ray crystal structures of the sMMOH:MMOB complex revealed to be the binding site for MMOB for both *Mc* Bath and *Mt* OB3b components.[70, 245] Fluorescence anisotropy titration in *Mc* Bath sMMO experiments showed that Fd-MMOR can displace MMOB from sMMOH. Furthermore, the Fd-MMOR was more effective at displacing a Δ (2-23) MMOB variant than full length MMOB. [64, 144] The researchers hypothesized that the N-terminal region of MMOB serves as an anchor which prevents MMOB from fully dissociating from sMMOH while MMOR is interacting with sMMOH. However, the shift in the MMOB position opens the binding site necessary for MMOR to transfer electrons to sMMOH. Finally, the affinity of MMOB for sMMOH was found to increase rather than decrease upon reduction of the diiron center, suggesting that MMOB might remain bound and block reduced MMOR from rebinding at later points in the reaction cycle.

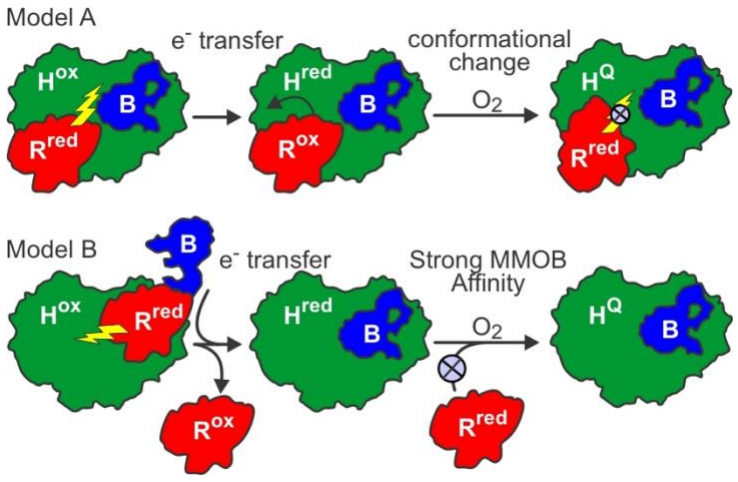

Scheme 4-2 Models for Regulation of Electron Transfer to sMMOH.
H^{ox} = diferric sMMOH^{ox}, H^{red} = diferrous sMMOH^{red}, B = MMOB, R^{ox} = fully oxidized MMOR, R^{red} = two electron reduced MMOR^{red}, H^Q = Intermediate **Q** of the reaction cycle.

The studies of the interaction of sMMO components from *Mc* Bath and *Mt* OB3b differ primarily in the reported affinity of sMMOH^{ox}:MMOB (K_D^{Mc} = 550 nM;[144] K_D^{Mt} = 68 nM.[63, 131]) and sMMOH^{ox}:MMOR (K_D^{Mc} = 900 nM;[142] K_D^{Mt} = 10 nM[129]) complexes and the change in affinities for MMOB upon sMMOH reduction (K_D^{Mc} = 170 nM; [144] K_D^{Mt} = 2.2 μM[131]). It is possible that part of the disparity in these measurements stems from techniques used to measure the affinities, which often involved major structural modifications in the protein components from attaching large fluorophores. In this study, we have prepared *Mt* OB3b MMOB and MMOR in which the native tryptophan residues are conservatively changed to 5-fluorotryptophan (5FW).[247-249] Also, an MMOB variant in the N-terminal region is modified with a small ^{19}F-containing label such that the modified residue mimics the size of the original lysine.[250] These changes are found not to alter the overall structure or regulatory functions of MMOB or MMOR. They permit the use of ^{19}F-NMR to study labeled-MMOB complex formation with sMMOH in the presence or absence of MMOR. The sensitivity of the NMR spectrum to changes in the environment and mobility of the tryptophans allows insight into the effects of component concentration and sMMOH oxidation state on complex formation in the absence of large external labels or truncated component variants. The studies support a new model for regulation in which progress through the reaction cycle is promoted by sMMO component exchange that is kinetically coupled to effectively irreversible downstream reactions.

4.3 Experimental procedures

4.3.1 Hydroxylase and Reductase Preparation.

sMMOH was purified from *Methylosinus trichosporium* OB3b according to purification protocols described previously.[34] A modification in previous methods for MMOR purification and purification was utilized. A gBLOCKs® gene fragment with the MMOR *E. coli* codon optimized sequence was purchased from Integrated DNA Technologies. The MMOR gene sequence used is from the PacBio single-molecule real-time complete genome sequence of *M. trichosporium*

OB3b.[251] The MMOR gBLOCKs® was inserted into a pET100/D-TOPO® vector using NdeI and XhoI restriction enzymes following the protocol for the In-Fusion® HD Cloning Kit. The following two vectors were transformed into BL21(DE3) *E. coli* cells: i.) an MMOR vector with an ampicillin resistance cassette, and ii.) a pACYC-isc vector with a chloramphenicol resistance cassette. The pACYC-isc vector contains genes involved in the assembly of iron-sulfur clusters in *E. coli*.[252]The transformed BL21(DE3) *E. coli* cells were spread onto Luria Broth plates supplemented with the 100 μg/ml carbenicillin and 100 μg/ml chloramphenicol and allowed to incubate overnight at 37 °C. Colonies that grew over night were used to inoculate 3 x 50 ml flasks of LB supplemented with carbenicillin and chloramphenicol then grown overnight at 37 °C. On the next day, 10 ml of the overnight liquid culture was added to 12 x 800 ml LB liquid media flasks supplemented with 100 μg/ml carbenicillin and 100 μg/ml chloramphenicol. The liquid cultures were grown to an OD_{600} of 1.0, and then overexpression was induced by adding ITPG to a final concentration of 1 mM. The transformed BL21(DE3) cells overexpressed for 22 hours at 20 °C. Cell paste was resuspended in 25 mM Trizma pH 8 (5 ml/g of cell paste) followed by sonication to rupture the cells (1/2 inch disrupter horn, 80% power output, 80% duty cycle). The sonicated cell solution was centrifuged at 43,000 x *g* for 30 minutes at 4 °C. The supernatant was loaded onto a Q-sepharose fast flow column equilibrated with 25 mM Trizma buffer pH 8 containing 5 mM thioglycolic acid and 0.2 M NaCl at 4 °C. The Q-Sepharose fast flow column was washed with 25 mM Trizma buffer pH 8 containing 5 mM thioglycolic acid and 0.2 M NaCl at 4 °C. MMOR was eluted from the column with a 900-ml gradient from 0.2 M to 0.4 M NaCl in 25 mM Trizma pH 8 containing 5 mM thioglycolic acid. The MMOR protein elutes at a salt concentration of 0.27 M NaCl. Fractions containing MMOR were pooled together then concentrated to 25 ml using an Amicon stirred cell equipped with a 10 kDa filter. Next, a Sephadex G-75 size exclusion column was equilibrated with 25 mm MOPS pH 7 buffer containing 5 mM thioglycolic acid. The concentrated MMOR was loaded onto the equilibrated Sephadex G-75 column and a peristaltic pump was used to deliver the elution buffer

(25 mM MOPS pH 7 containing 5 mM thioglycolic acid). Chosen fractions were pooled and concentrated to 25 ml using an Amicon stirred cell equipped with a 10 kDa filter then further concentrated to 200 µl using a 10 MWCO centrifugal filter. Purity of the final protein solution was assessed by SDS-PAGE. The extinction coefficients for MMOR and sMMOH are 18.6 $mM^{-1}cm^{-1}$ at 458 nm and 539 $mM^{-1}cm^{-1}$ at 280 nm, respectively.

4.3.2 Mutation of the MMOB Gene.

A Thermo Scientific Phusion Site Directed Mutagenesis Kit was used to introduce the point mutation W77F in the pT7-7-derived plasmid pBWJ400 containing the wild type *M. trichosporium* OB3b MMOB gene.[71] Additionally, a variant of pBWJ400 containing a K15C point mutation was used in this study.[131] Primers listed in **Table 4-1**were synthesized at the University of Minnesota Genomics Center.

Table 4-1 Primers Used in This Study

Plasmid	Mutation	Primers
PBWJ400	K15C	5'-GCCGGCATCATGCAGTGCACCGGCAAGGCCTTC- 3' 5'-GAAGGCCTTGCCGGTGCACTGCATGATGCCGGC- 3'
PBWJ400	W77F	5'-GGCTTCTGGTTTATCAAGGCCG-3' 5'-CGCCTTGTCCTCGACGAC-3'

4.3.3 MMOB Preparation and Biosynthetic Incorporation of 5-Fluorotryptophan.

Plasmids for wild type MMOB and the two variants described above were transformed into *Escherichia coli* BL21(DE3) chemically competent cells. The cells were grown to an optical density of 1.0 (600 nm) and then transferred from Luria Broth media to a defined medium which included 5-fluoroindole.[253, 254] In the absence of the amino acid tryptophan, 5-fluoroindole is biosynthetically transformed into 5-fluorotryptophan by *E. coli*. IPTG (1 mM final concentration) was added to the defined medium and the BL21(DE3) *E. coli* cells were allowed to overexpress for 20 hours at 20 ºC. The cells were then centrifuged at 3800 rpm for 25 minutes and the supernatant was removed. Centrifuged cells were washed with 25 mM MOPS pH 7 buffer. The cells were then pooled together and centrifuged for 30 minutes at 19,000 rpm. After centrifugation the supernatant was discarded and 5 ml of 25 mM MOPS pH 7 buffer per gram of cell paste was added to resuspend the cells. The resuspended cells where then sonicated for 5 minutes in 1-minute intervals. The sonicated solution was centrifuged for 30 minutes at 19,000 rpm. While the heterologous expression of unlabeled MMOB in Luria Broth media leads to the predominant presence of MMOB in inclusion bodies, the expression of ^{19}F-labeled MMOB in a defined media leads to the predominant expression of MMOB in the soluble fraction. Hence, the purification protocol for MMOB was altered. The supernatant was collected and loaded onto a DEAE Q sepharose fast flow ion exchange column equilibrated with 25 mM Tris pH 8 at 4 ºC. The column was developed using

a 900 ml gradient from 0.15 M NaCl to 0.35 M NaCl. Fractions containing protein were identified using UV/Vis spectroscopy and then assessed by SDS-PAGE gel to verify the presence of MMOB. The fractions of interest were pooled and then concentrated to ~25 ml using an Amicon stirred cell equipped with a 10 kDa filter under argon pressure at 4 ºC. The concentrated solution was loaded onto a G75 Sephadex size exclusion column equilibrated with 25 mM MOPS pH 7 at 4 ºC. Fractions were assessed by UV/Vis spectroscopy and SDS-PAGE analysis. Chosen fractions were pooled and concentrated to 25 ml using an Amicon stirred cell equipped with a 10 kDa filter then further concentrated to 200 µl using a 10 MWCO centrifugal filter. Purity of the final protein solution was assessed by SDS-PAGE. The extinction coefficient used to determine the final concentration of the 5FW-MMOB is 23.2 $mM^{-1}cm^{-1}$ at 280 nm. Unmodified MMOB has an extinction of 20.8 $mM^{-1}cm^{-1}$ at 280 nm.

4.3.4 Biosynthetic Incorporation of 5FW into MMOR.

The following two vectors were transformed into BL21 (DE3) E. coli cells: i.) an MMOR vector with an ampicillin resistance cassette, and ii.) a pACYC-isc vector with a chloramphenicol resistance cassette. The cells were grown to an optical density of 1.0 (600 nm) and then transferred from Luria Broth media to a defined medium which included 5-fluoroindole.[253] IPTG (1 mM final concentration) was added to the defined medium and the BL21(DE3) *E. coli* cells were allowed to overexpress for 20 hours at 20 ºC. Cell paste was resuspended in 25 mM Trizma pH 8 (5 ml/g of cell paste) followed by sonication to rupture the cells (1/2 inch disrupter horn, 80% power output, 80% duty cycle). The sonicated cell solution was centrifuged at 43,000 x *g* for 30 minutes at 4 °C. The supernatant was loaded onto a Q-Sepharose fast flow column equilibrated with 25 mM Trizma buffer pH 8 containing 5 mM thioglycolic acid at 4 ˚C. The Q-Sepharose fast flow column was washed with 25 mM Trizma buffer pH 8 containing 5 mM thioglycolic acid and 0.2 M NaCl at 4 ˚C. Fractions containing MMOR were pooled and then concentrated to 25 ml using an Amicon stirred cell equipped with a 10 kDa filter. Next, a Sephadex G-75 size exclusion column was equilibrated with 25 mM MOPS pH 7 buffer containing 5 mM thioglycolic acid. The concentrated

MMOR was loaded onto the equilibrated Sephadex G-75 column and a peristaltic pump was used to deliver the elution buffer (25 mM MOPS pH 7 containing 5 mM thioglycolic acid). Chosen fractions were pooled and concentrated to 25 ml using an Amicon stirred cell equipped with a 10 kDa filter then further concentrated to 200 µl using a 10 MWCO centrifugal filter. Purity of the final protein solution was assessed by SDS-PAGE. Wild type MMOB containing both Trp residues converted to 5FW is termed 5FW-MMOB. The labeled MMOB from the W77F variant is termed W77F-5FW-MMOB. The K15C-5FW-MMOB variant containing two 5FW residues is additionally labeled by modifying the new Cys residue as described below.

4.3.5 3-Bromo-1,1,1-trifluoroacetone (BTFA) Labeling of K15C-5FW-MMOB and MMOR.

BTFA was used to introduce fluorine into a cysteine residue based on established protocols.[250, 255, 256] 100 µM of purified K15C-5FW-MMOB, 1 mM TCEP, and 400 µM BTFA were added to 100 mM MOPS buffer pH 7, to a final volume of 2.5 ml. The solution was allowed to stir for at least 1 hour at 4 ºC. The solution was then passed through a PD-10 column to remove excess TCEP and BTFA. The PD-10 eluent containing BTFA-K15C-5FW-MMOB or MMOR was added to an Amicon Ultra-15 10K MWCO centrifugal filter and centrifuged for 15 minutes at 4700 rpm. Quantification of free sulfhydryl groups after BTFA modification using Ellman's reagent (5,5'-dithio-bis-[2-nitrobenzoic acid]) showed that >90% of the Cys was labeled.

4.3.6 Crystallization of the sMMOH:5FW-MMOB and sMMOH:BTFA-K15C-5FW-MMOB Complexes.

The sitting-drop vapor diffusion method was used to crystallize the sMMOH:5FW-MMOB complex. 1.5 µl of protein solution (60 µM sMMOH, 120 µM 5FW-MMOB in 100 mM MOPS pH 7 was mixed with 1.5 µl of the well solution (20% PEG3350 and 0.2 M sodium phosphate dibasic pH 8). The well solution volume was 500 µl. Bipyramidal crystals started to grow within two days and had an average size of about 100 µm. The crystals were cryoprotected in 20% PEG3350, 0.2

M sodium phosphate dibasic pH 8, and 10% ethylene glycol, mounted in nylon loops, and flash cooled by plunging in liquid nitrogen. The structure was solved using diffraction data collected at the Advanced Photon Source (Argonne National Laboratory, Lemont, IL) on Beamline 24-ID-C and 24-ID-E using a wavelength of 0.979 Å at 100 K. A total of 675 frames were collected with an oscillation step of 0.2°. The data was processed and structure refined as previously described.[245]

The sitting-drop vapor diffusion method was used to crystallize the sMMOH:BTFA-K15C-5FW-MMOB complex. First, a seed stock solution was created from a sitting-drop containing sMMOH:5FW-MMOB crystals by adding 5 µl of the well solution to the drop. The crystals were crushed with a glass rod and then transferred to a seed bead tube containing 30 µl of well solution. The seed bead tube was vortexed on high for 6 min in 30 s intervals. The tube was placed on ice in between vortexes. Next, 1.5 µl of protein solution (60 µM sMMOH, 120 µM BTFA-K15C-5FW-MMOB in 100 mM MOPS pH 7.0 was mixed with 1.5 µl of the well solution (21% PEG3350 and 0.2 M sodium phosphate dibasic pH 6.8). The well solution volume was 500 µl. Bipyramidal crystals started to grow within four days. The crystal harvesting, data collection and structure determination were done as described above for the sMMOH:5FW-MMOB complex.

4.3.7 Preparation of NMR samples.

All NMR experiments were performed in 100 mM MOPS buffer, pH 7, containing 10% D_2O and less than 0.01% TFA. TFA was used to calibrate the chemical shifts, setting the value of TFA to -76.55 ppm. Samples were first prepared in microfuge tubes and then transferred to an NMR tube. Reduced sMMOH samples were prepared in a Coy vinyl anaerobic chamber. The solutions needed for sMMOH reduction experiments were made anaerobic on a Schlenk line using argon gas. The procedure for reducing sMMOH is described elsewhere.[34] The NMR tubes were capped with a rubber septa and parafilm was applied around the rubber septa and NMR tube to prevent O_2 from entering.

The binding constants for MMOB binding to diferric and diferrous sMMOH were determined by direct ^{19}F-NMR monitored titration. Aliquots of diferric or diferrous (anaerobic)

sMMOH were added to a constant concentration (5 μM) ^{19}F-labeled MMOB in 100 mM MOPS buffer pH 7 at 25 °C while maintaining a constant overall volume in an NMR tube. The intensities of resonances from free ^{19}F-labeled MMOB decrease as sMMOH is added. The change in intensity was divided by the overall change in intensity at saturation to determine a fraction for the complex formed. The sMMOH added contains a fraction (~30%) that cannot bind MMOB,[76] but remains as a contribution to the free sMMOH during the titration. This fraction complicates the direct fitting of the data to a binding isotherm. Also, the low K_D in the case of diferric sMMOH (~80 nM, see Results) is 60-fold below the accessible concentration for NMR detection (~5 μM), further limiting the ability to directly fit the data. As a result, the observed titration is compared to computed curves for given K_D values using Equations 4.1, 4.2, and 4.3 where free [H] is the total concentration of sMMOH sites not bound to MMOB, H'_{Tot} is the total concentration of sMMOH sites added that can potentially bind MMOB (~70% of the total sMMOH), $H_{Inactive}$ is the total concentration of sMMOH that cannot bind MMOB, B_{Tot} is the total concentration of MMOB, [H'B] is the concentration of the sMMOH:MMOB complex and K_D is the trial dissociation constant for the sMMOH:MMOB complex. The equivalent formulas were used to simulate the titration of labeled MMOR with sMMOH.

$$[H'B] = \frac{H'_{Tot} + B_{Tot} + K_D - \sqrt{(H'_{Tot} + B_{Tot} + K_D)^2 - 4(H'_{Tot} \bullet B_{Tot})}}{2} \qquad \text{Eq.4.1}$$

$$\text{Free } [H] = (H'_{Tot} - [H'B]) + H_{Inactive} \qquad \text{Eq.4.2}$$

$$\text{Fraction bound} = \frac{[H'B]}{B_{Tot}} \qquad \text{Eq.4.3}$$

The fraction of active sMMOH that can bind MMOB was determined for each experiment based on the amount of intermediate **Q** formed in a single turnover stopped-flow experiment. The intermediate **Q** to bound MMOB ratio has been established by Mössbauer spectroscopy.[76, 198]

The K_D value for MMOR binding to sMMOH was determined by competition with MMOB. The approximately stoichiometric ^{19}F-labeled MMOB (12 μM) complex with sMMOH (18 μM sites of which ~ 12.6 μM can form the MMOB complex) was formed using either diferric or diferrous (anaerobic) sMMOH. Aliquots of MMOR were added and the increase in the NMR resonances from free MMOB quantified. The fraction of MMOB released was determined as the ratio of the increase in intensity divided by the difference between the intensity of the starting complex and free MMOB. The resulting curve was fit by non-linear regression to a regular hyperbola. The half saturation MMOR concentration value and the K_D values for the diferric or diferrous sMMOH:labeled-MMOB complexes were used with the online calculator BotDB to determine the K_D for MMOR binding to sMMOH.[257, 258]

4.3.8 ^{19}F-NMR spectroscopy.

Acquisition of spectra was performed using a Bruker 600-MHz Avance NEO equipped with a 5-mm triple resonance cryoprobe. Routine 1D-^{19}F-NMR spectrum were acquired utilizing the zg pulse program (Bruker TOPSPIN Version 4.0.3). Acquisition parameters for most of the NMR experiments were: spectrometer frequency = 565.1 MHz, temperature = 298.0 K, number of scans = 512, acquisition = 0.2 s, relaxation delay = 2.0 s, and receiver gain = 101.0. The raw data was processed using MestReNova version 14.1.2, released 03/23/2020. Processing consisted of the following steps: i.) import data, ii.) automatic phase correction followed by manual 0 and 1st order corrections, iii.) baseline correction along f1 using either polynomial fit or splines methodology, and iv.) line broadening of 30 to 90 Hz using an exponential function.

Chemical exchange saturation transfer (CEST) experiments were acquired by first obtaining a 1D ^{19}F-NMR spectrum of the sample. Next, the frequency values to be irradiated in the CEST experiment were chosen using the acquired 1D spectrum and saved as separate irradiation frequency lists containing three frequencies each. All irradiation frequency lists created contained at least one off-resonance frequency as a control. The stddiff pulse program was used to collect

CEST data and the acquisition settings were: number of scans = 512, acquisition time = 0.2 s, Relaxation time = 4 s, saturation time = 4 s, Gaussian pulse width = 50 ms, F2 channel- shaped pulse for saturation = 50 dB, File name for SP9 = Gaus1.1000, number of irradiation frequencies = 3, and number of FIDs = 3.

4.3.9 Stopped-Flow Experiments.

An Applied Photophysics stopped-flow spectrophotometer model SX.18MV with a SX Pro-data upgrade was used to rapidly mix anaerobic 110 μM (active sites), stoichiometrically-reduced sMMOH in 50 mM MOPS buffer, pH 6.9 with a stoichiometric (vs active sites) concentration of either 5FW-MMOB or BTFA-K15C-5FW-MMOB in the same buffer containing 1.8 mM O_2. Procedures for stoichiometric sMMOH reduction sMMOH have been previously described.[34, 76] The reaction was monitored using a diode array detector at 16 wavelengths between 330 and 700 nm. The entire data set was fit by global analysis using Applied Photophysics Pro-K software to a three irreversible step model: intermediates **P*** $\rightarrow$ **P** $\rightarrow$ **Q** $\rightarrow$ Diferric sMMOH as previously described.[76] The pseudo-first order conditions and first order irreversible steps allow use of a global multiple summed-exponential fitting equation where the reciprocal relaxation times give the rate constants of the individual steps. While the intermediates absorb throughout the spectral region monitored, absorbance at 700 nm and 430 nm are most definitive for intermediates **P** and **Q**, respectively.

4.4 Results

4.4.1 ^{19}F-Labeling of MMOB.

Past studies designed to characterize the sMMOH:MMOB complex in response to sMMOH oxidation state or the presence of MMOR have relied on changes in endogenous tryptophan fluorescence or spectral response from fluorescent or spin probes chemically added to cysteine residues introduced into MMOB.[63, 64, 129, 131, 142, 144] However, the sensitivity and size of the introduced probes have limited their utility, especially when placed in the sMMOH:MMOB

interface, where mutagenesis studies have shown precise interaction to be essential.[65, 71] Inspection of the X-ray crystal structure of the *Mt* OB3b sMMOH:MMOB complex suggested an alternative approach, because the only two Trp residues of MMOB (W76 and W77) were found to be in or near the sMMOH:MMOB interface.[70, 245] Replacement of these two Trp residues with 5-fluorotryptophan by growth of the MMOB overexpression strain on media containing 5-fluoroindole provides a sensitive ^{19}F-NMR probe that results in two well dispersed resonances which is consistent with a folded protein (**Figure 4-1**,inset).[247] The 5FW resonances were assigned to specific Trp residues by mutating W77 to Phe as shown in **Figure 4-2**.

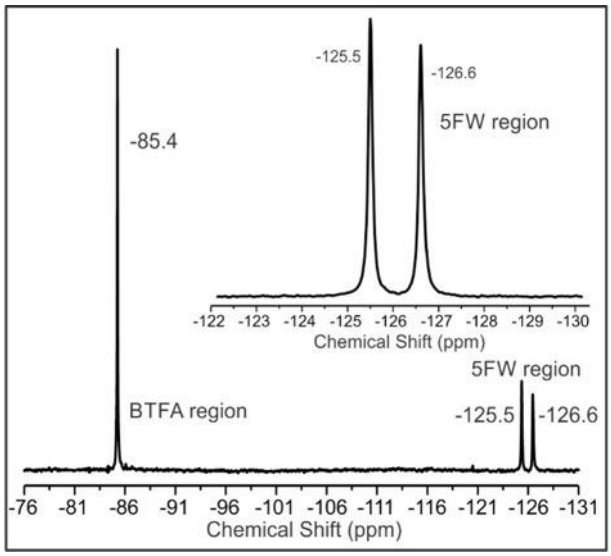

Figure 4-1 One dimensional ^{19}F-NMR spectra of ^{19}F-labeled MMOB. Main panel: Spectrum of BTFA-K15C-5FW-MMOB. The spectral regions for the resonances from the BTFA and 5FW labels are marked. Inset: Spectrum of 5FW-MMOB not containing the K15C mutation. 100 mM MOPS, pH 7, 25 °C

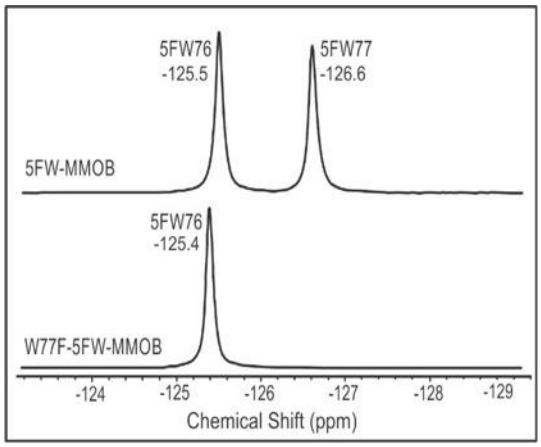

Figure 4-2 5-Fluorotryptophan resonance assignment.
Protein mutagenesis and overexpression of 5FW-W77F-MMOB allowed a definitive assignment of the 5FW resonances. 100 mM MOPS, pH 7, 25 °C. Spectrometer acquisition settings were: number of scans = 1520, acquisition = 0.05 s, and relaxation delay = 0.9 s.

A second objective of this study was to determine whether the core region of MMOB, which includes W76 and W77, responds differently than the N-terminal tail region to changes in sMMOH diiron cluster redox state or to the binding of MMOR to the complex. To address these questions, a BTFA fluorine probe was introduced in the N-terminal region by chemically modifying the K15C MMOB variant, which has been shown in previous studies to not interact significantly with other residues in the sMMOH:MMOB complex and to not cause large changes in sMMO catalysis upon labeling.[131, 245] Post translational modification of the K15C-5FW-MMOB with BTFA was confirmed by 1D-^{19}F-NMR (**Figure 4-1 One dimensional ^{19}F-NMR spectra of ^{19}F-labeled MMOB.**

Main panel: Spectrum of BTFA-K15C-5FW-MMOB. The spectral regions for the resonances from the BTFA and 5FW labels are marked. Inset: Spectrum of 5FW-MMOB not containing the K15C mutation. 100 mM MOPS, pH 7, 25 °C). The BTFA resonance at -85.4 ppm is more intense than the resonances from the labeled Trp residues because of the three ^{19}F atoms in the probe and its increased mobility, leading to a narrow linewidth. It is important to note that the 5FW resonances upfield of the K15C-BTFA resonance are unchanged (compare **Figure 4-1** and **Figure 4-1**, inset and see other examples below).

4.4.2 Impact of Incorporation of 5-Fluorotryptophan and BTFA on sMMO Steady State and Single-Turnover Kinetics.

Both 5FW-MMOB and BTFA-K15C-5FW-MMOB allowed efficient turnover of methane by the reconstituted sMMO system (**Figure 4-3 Steady state kinetics of the ^{19}F labeled MMOB variants**

An oxygen electrode was used to monitor the velocity of O_2 consumption for the reaction of 0.4 μM sMMOH (active sites), 1.2 μM MMOR and the indicated concentration of either MMOB (black squares) or 5FW-MMOB (red circles) or 5FW-BTFA-K15C-MMOB (green triangles). The other reaction components were 200 μM methane, 250 μM O_2, 400 μM NADH in 25 mM MOPS buffer pH 7.5 at 23 °C. Past studies have shown that the velocity maximizes at approximately stoichiometric sMMOH-MMOB complex formation and then declines.). Past observations have shown that the initial velocity of oxygen uptake or NADH utilization increases to a maximum when the MMOB and sMMOH active sites concentrations are approximately equal, followed by a decline in velocity.[33] This result was interpreted to indicate that a complex of one MMOB with each α-subunit of sMMOH is necessary for rapid turnover. Moreover, this complex apparently forms nearly stoichiometrically, even at sub-micromolar concentrations of the components used in the

experiment. The same concentration dependence is observed when 5FW-MMOB is used in place of wild-type MMOB (**Figure 4-3 Steady state kinetics of the ^{19}F labeled MMOB variants**
An oxygen electrode was used to monitor the velocity of O_2 consumption for the reaction of 0.4 μM sMMOH (active sites), 1.2 μM MMOR and the indicated concentration of either MMOB (black squares) or 5FW-MMOB (red circles) or 5FW-BTFA-K15C-MMOB (green triangles). The other reaction components were 200 μM methane, 250 μM O_2, 400 μM NADH in 25 mM MOPS buffer pH 7.5 at 23 °C. Past studies have shown that the velocity maximizes at approximately stoichiometric sMMOH-MMOB complex formation and then declines.). However, when BTFA-K15C-5FW-MMOB is used, an approximate 2-fold excess over sMMOH active sites is required to maximize the initial velocity, suggesting a somewhat lower affinity. The same maximum initial velocity is reached using each of the MMOBs, suggesting that the fluorine labeling does not interfere with function or the rate limiting step in the reaction cycle.

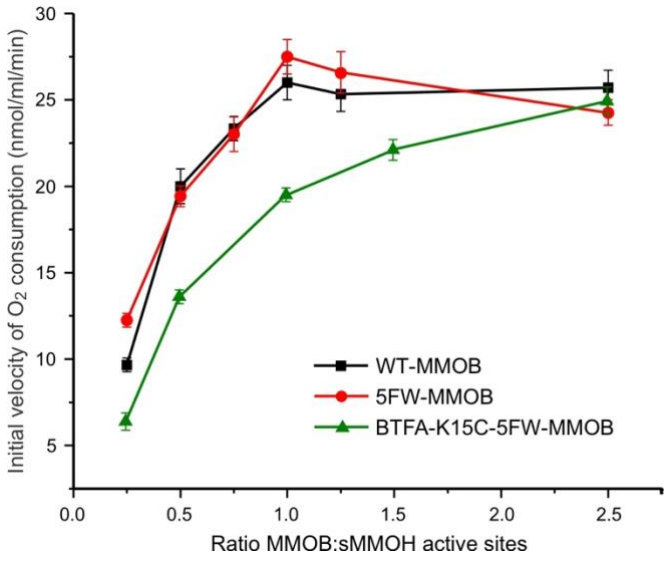

Figure 4-3 Steady state kinetics of the ^{19}F labeled MMOB variants
An oxygen electrode was used to monitor the velocity of O_2 consumption for the reaction of 0.4 μM sMMOH (active sites), 1.2 μM MMOR and the indicated concentration of either MMOB (black squares) or 5FW-MMOB (red circles) or 5FW-BTFA-K15C-MMOB (green triangles). The other reaction components were 200 μM methane, 250 μM O_2, 400 μM NADH in 25 mM MOPS buffer pH 7.5 at 23 °C. Past studies have shown that the velocity maximizes at approximately stoichiometric sMMOH-MMOB complex formation and then declines.

The potential for perturbation of the individual steps in the sMMO reaction cycle kinetics was evaluated by conducting single-turnover transient kinetics studies. Anaerobic, stoichiometrically reduced sMMOH was rapidly mixed with either MMOB, 5FW-MMOB, or BTFA-K15C-5FW-MMOB in a buffer containing a large excess of O_2 using a stopped-flow device (see Experimental Procedures). These pseudo-first order conditions allowed the rate constants for formation and decay of the intermediates to be obtained by multiple-summed exponential fitting of the time courses (**Figure 4-4 Transient kinetics of the sMMO reaction cycle using ^{19}F-labeled MMOB.**

Anaerobic stoichiometrically reduced sMMOH (110 μM sites) was mixed in a 1:1 active site ratio with ^{19}F-labeled MMOB in O_2 saturated (~1.8 mM) 50 mM MOPS buffer, pH 6.9 at 4 °C using a stopped-flow device. The time courses at 430 nm (blue, where intermediate **Q** absorbs strongly) and 700 nm (red, where intermediate **P** and **Q** both absorb weakly) were fit using nonlinear regression to a 3-summed exponential equation (white dashed lines). A: 5FW-MMOB. B: BTFA-K15C-5FW-MMOB. The rate constants derived from the fits are reported in **Table 4-2**.,

Table 4-2).[68, 74, 76] The rate constants for **P*** to **P**, **P** to **Q** and **Q** decay steps in the reaction cycles when using wild type MMOB and 5FW-MMOB showed either no or minor perturbation. Use of the BTFA-K15C-5FW-MMOB caused decreases in the rate constants for the **P*** to **P** and **P** to **Q** steps, while leaving the **Q** decay step unchanged. However, this ^{19}F-labeled MMOB remained highly functional as a reaction cycle regulator.

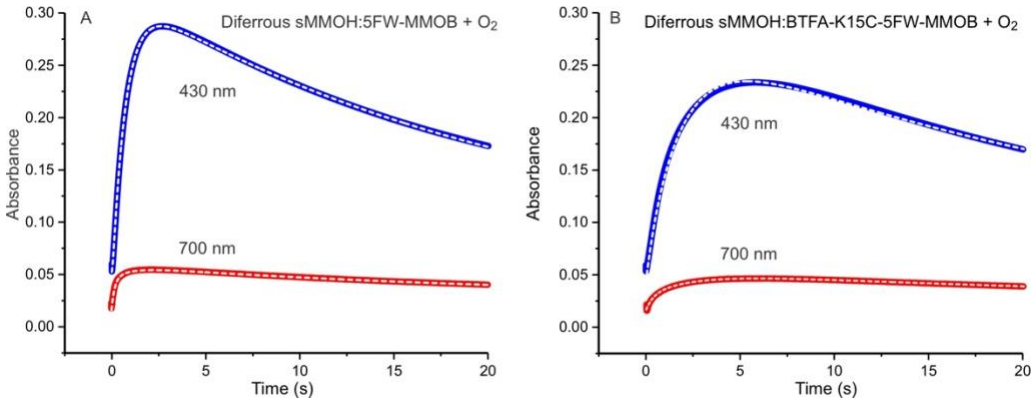

Figure 4-4 Transient kinetics of the sMMO reaction cycle using ^{19}F-labeled MMOB. Anaerobic stoichiometrically reduced sMMOH (110 μM sites) was mixed in a 1:1 active site ratio with ^{19}F-labeled MMOB in O_2 saturated (~1.8 mM) 50 mM MOPS buffer, pH 6.9 at 4 °C using a stopped-flow device. The time courses at 430 nm (blue, where intermediate **Q** absorbs strongly) and 700 nm (red, where intermediate **P** and **Q** both absorb weakly) were fit using nonlinear regression to a 3-summed exponential equation (white dashed lines). A: 5FW-MMOB. B: BTFA-K15C-5FW-MMOB. The rate constants derived from the fits are reported in **Table 4-2**.

Table 4-2 Rate Constants or Single Turnover Reactions

	MMOB species utilized in reaction		
Rate constants (s^{-1})	MMOB	5FW-MMOB	BTFA-K15C-5FW-MMOB
$k_{\mathbf{P}}$ formation	6.6 ± 0.6	5.9 ± 0.6	2.6 ± 0.8
$k_{\mathbf{P}}$ decay/$_{\mathbf{Q}}$ formation	2.4 ± 0.3	1.4 ± 0.3	0.5 ± 0.1
$k_{\mathbf{Q}}$ decay	0.04 ± 0.01	0.04 ± 0.01	0.04 ± 0.01

4.4.3 Molecular Structures of the sMMOH:5FW-MMOB and sMMOH:BTFA-K15C-5FW-MMOB Complexes.

To assess whether incorporation of 5FW or BTFA into MMOB perturbs the structure of the sMMOH:MMOB complex, we crystallized both the sMMOH:5FW-MMOB and sMMOH:BTFA-K15C-5FW-MMOB complexes and obtained crystals structures solved at 2.08 Å (PDBID:7M8Q) and 2.22 Å (PDBID:7M8R), respectively (**Table 4-3**). In both crystals, the native $(\alpha\beta\gamma)_2$ sMMOH and two bound MMOBs occupy the asymmetric unit. The structures show that the sidechain of 5FW77 points towards the sMMOH interface while the sidechain of 5FW76 points away (**Figure 4-5**A and B). Additionally, all of the polar contacts that each 5FW makes are the same as those made by the respective tryptophans in the sMMOH complex with unlabeled MMOB. Structural alignment of the protein backbones of 7M8Q or 7M8R with that of the sMMOH:MMOB complex (PDBID: 6VK5) yields RMSD values of 0.097 Å and 0.149 Å, respectively, indicating that the structures are nearly identical. The overall structure of the sMMOH:MMOB complex and the conformational changes induced by MMOB have been discussed in detail elsewhere, and thus they are not described further here.[245] It is important to note that conservation of structure upon substitution of 5FW for tryptophan has been commonly observed in other proteins.[249, 259-261]

To the best of our knowledge, the X-ray crystal structure of sMMOH:BTFA-K15C-5FW-MMOB is the first to show BTFA in a protein-protein complex. The K15C-BTFA probe is located

on the N-terminal tail of MMOB and is solvent exposed (**Figure 4-6**A and B) A polar contact between MMOB residues K15 and E23 is lost as a result of the mutation to cysteine and addition of the BTFA probe. Comparison of the two MMOBs in the asymmetric unit reveals different rotomeric conformations of the BTFA probe (**Figure 4-6**C). Also, the electron density of the three ^{19}F atoms on BTFA is somewhat less than those on 5FW76 and 5FW77, likely due to the increased mobility of BTFA in the complex.

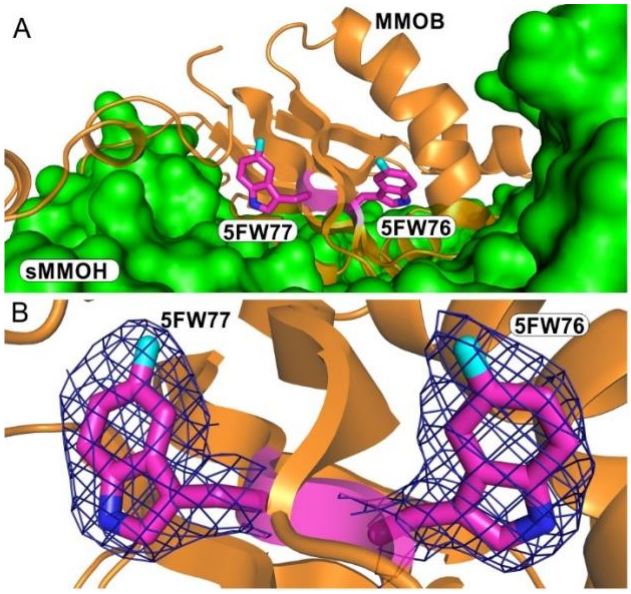

Figure 4-5 Structure of fluorine-labeled positions in sMMOH:5FW-MMOB and sMMOH:BTFA-K15C-5FW-MMOB.
A: Structure of the sMMOH:5FW-MMOB complex (PDB: 7M8Q) showing the interface region containing 5FW76 and 5FW77. 5FW77 is buried in the interface whereas 5FW76 is partially solvent exposed. B: Detailed view of the interface region with 2Fo-2Fc electron density contoured at 1σ. Overlaid on the atomic model

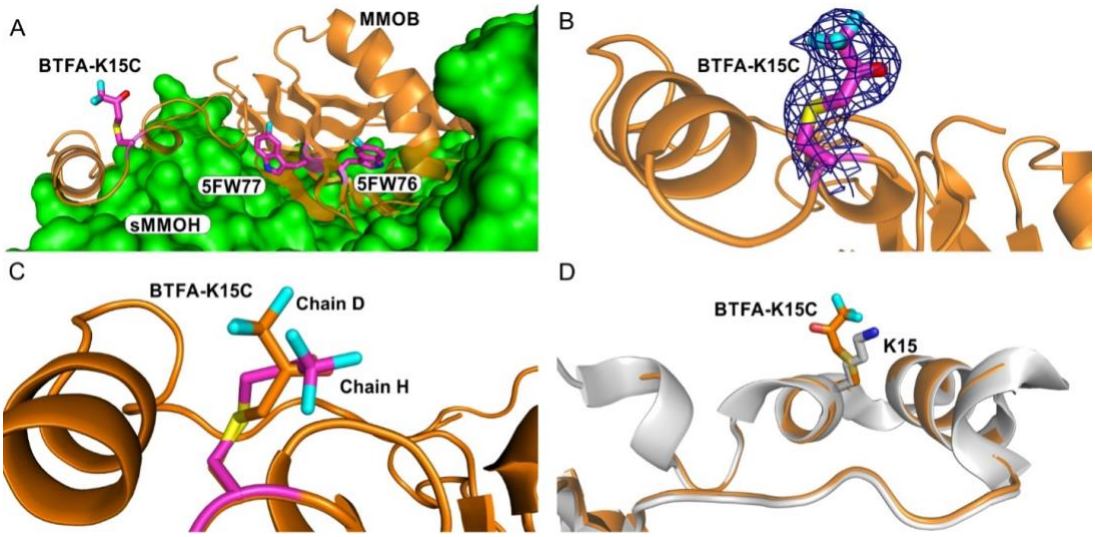

Figure 4-6 Structure of the sMMOH:BTFA-K15C-5FW-MMOB complex (PDB:7M8R)
A: Interface region showing the relative position of the BTFA and 5FW ^{19}F-labels. B: Detailed view of the BTFA probe with 2Fo-2Fc electron density contoured at 1σ overlaid on the atomic model C: Superimposed views of the BTFA probe in the two labeled MMOBs present in the asymmetric unit (Chains D and H) revealing different rotomeric conformations. D: Superposition of structures of sMMOH: MMOB (PDB:6VK5) and sMMOH:BTFA-K15C-5FW-MMOB showing relative size of BTFA-K15C and the native K15.

Table 4-3 Data Collection and Refinement Statistics

Data Collection	sMMOH:5FW-MMOB	sMMOH:BTFA-K15C-5FW-MMOB
PDBID	7M8Q	7M8R
Wavelength	0.9791	0.9791
Resolution range	84.6 - 2.08 (2.15 - 2.08)	84.4 - 2.22 (2.23 - 2.22)
Space group	$P2_12_12_1$	$P2_12_12_1$
Unit cell (*a*,*b*,*c* in Å)	102.493 105.623 299.704	102.39 105.47 298.18
Total reflections	991930 (99363)	827515 (81159)
Unique reflections	194439 (19235)	158458 (15645)
Multiplicity	5.1 (5.1)	5.2 (5.2)
Completeness (%)	99.08 (99.35)	98.98 (98.78)
I/σI	7.65 (1.58)	9.11 (1.51)
R-merge	0.178 (0.989)	0.1473 (1.04)
R-meas	0.199 (1.102)	0.1625 (1.15)
R-pim	0.08755 (0.4804)	0.0668 (0.4778)
$CC_{1/2}$	0.986 (0.500)	0.999 (0.881)
Refinement		
Refl in refinement	193619 (19225)	158215 (15638)
Refl for R-free	9526 (906)	7771 (795)
R-work	0.1820 (0.3147)	0.1562 (0.2456)
R-free	0.2122 (0.3263)	0.2018 (0.2827)
Number of non-H atoms	21830	21601
macromolecules	19477	19556
ligands	71	189
solvent	2282	1856
Protein residues	2418	2416
RMS(bonds in Å)	0.005	0.005
RMS(angles in °)	0.5	0.63
Ramachandran favored (%)	97.57	97.24
Ramachandran allowed (%)	2.34	2.72
Ramachandran outliers (%)	0.08	0.00
Average B-factor	32.15	39.36
macromolecules	31.01	38.43
ligands	36.05	59.78
solvent	41.71	47.02

4.4.4 Complex of ^{19}F-Labeled MMOB with Diferric or Diferrous sMMOH.

One-dimensional ^{19}F-NMR experiments were performed to investigate the interaction between oxidized or reduced sMMOH and ^{19}F-labeled MMOB. Both 5FW and BTFA resonances observed for unbound labeled MMOB decrease sharply in intensity and do not shift or broaden upon addition of oxidized or reduced sMMOH. Additionally, new resonances emerge in the ^{19}F-spectra. Specifically, when diferric sMMOH is added two sharp resonances emerge downfield of the resonance from unbound BTFA-K15C and one broad resonance emerges downfield of the resonances from unbound 5FW (**Figure 4-7**A). Addition of diferrous sMMOH also elicits two sharp resonances downfield of the resonance from unbound BTFA-K15C, but they occur at different frequencies than observed after addition of diferric sMMOH (**Figure 4-7**B)

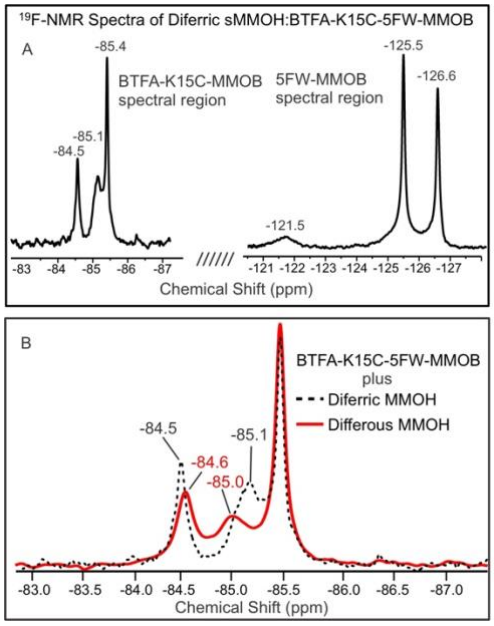

Figure 4-7 One dimensional ^{19}F NMR spectra of sMMOH complexed with BTFA-K15C-5FW MMOB.
Panel A: On the left is the spectral region where the BTFA signals are located and on the right is where the 5FW signals are located. New resonances at -84.5 ppm, -85.1 ppm and -121.5 ppm are labeled in addition to the resonances from a small fraction of residual unbound MMOB. Panel B: Effect of the oxidation state of sMMOH on the spectrum of the BTFA-labeled MMOB in the sMMOH:BTFA-K15C-5FW MMOB complex. 100 mM MOPS, pH 7, 25 °C

4.4.5 Resonance Assignment of the 275 kDa sMMOH:MMOB Complex.

The origin of the new resonances that arise from sMMOH:MMOB complex formation were probed using ^{19}F-Chemical Exchange Saturation Transfer (^{19}F-CEST).[262-265] In this experiment, weak selective Gaussian pulses are applied in small steps across the regions of interest in the ^{19}F-NMR spectra of a sample containing sMMOH and BTFA-K15C-5FW-MMOB. This pulse is then followed by a hard non-selective 90° pulse. If the weak Gaussian pulse is applied to a region of the ^{19}F-spectrum away from frequencies corresponding to either the bound or unbound state, no change in intensity will be observed in either set of resonances. However, if the weak Gaussian pulse is applied to a region near or directly on frequencies corresponding to the bound or unbound state, a decrease in intensity of both resonances will be observed following the strong pulse as a result of chemical exchange.

As shown in **Figure 4-8**A, when the weak Gaussian pulses are applied to the spectral region downfield of the resonance at -85.4 ppm from BTFA on the unbound MMOB N-terminal tail, the intensities decrease for the -85.4 ppm resonance and both of the downfield resonances. A complementary result is found when monitoring the intensity of the downfield resonances after the weak pulse is applied to the -85.4 ppm resonance (**Figure 4-8**B and C). These results shows that -85.4 ppm and downfield resonances are due to bound and free ^{19}F-labeled MMOB in chemical exchange and supports the conclusion that the downfield resonances arise from the sMMOH:BTFA-K15C-5FW MMOB complex. Moreover, because both downfield resonances decrease upon irradiation at -85.4 ppm or when the weak pulse is applied to either resonance, there are two separate interconverting conformational states of the complex in slow exchange.

The spectral region near the resonances from 5FW in the MMOB core region was similarly probed (**Figure 4-8**, right). The results support the assignment of the broad -121.5 ppm resonance as arising from the sMMOH:BTFA-K15C-5FW MMOB complex. However, when the weak pulse

was applied at -121.5 ppm, only the 5FW77 signal intensity at -126.6 ppm was observed to decrease (**Figure 4-8**D and E). The complementary result was observed when the -126.6 ppm resonance was irradiated (**Figure 4-8**F). Thus, it appears that the -121.6 ppm resonance reports on the chemical environment of 5FW77 while bound to sMMOH, in accord with its placement in the sMMOH-MMOB interface revealed by the structure (**Figure 4-5**A and B). This result is confirmed by the lack of a resonance at -121.5 ppm from the sMMOH:5FW-W77F-MMOB complex.

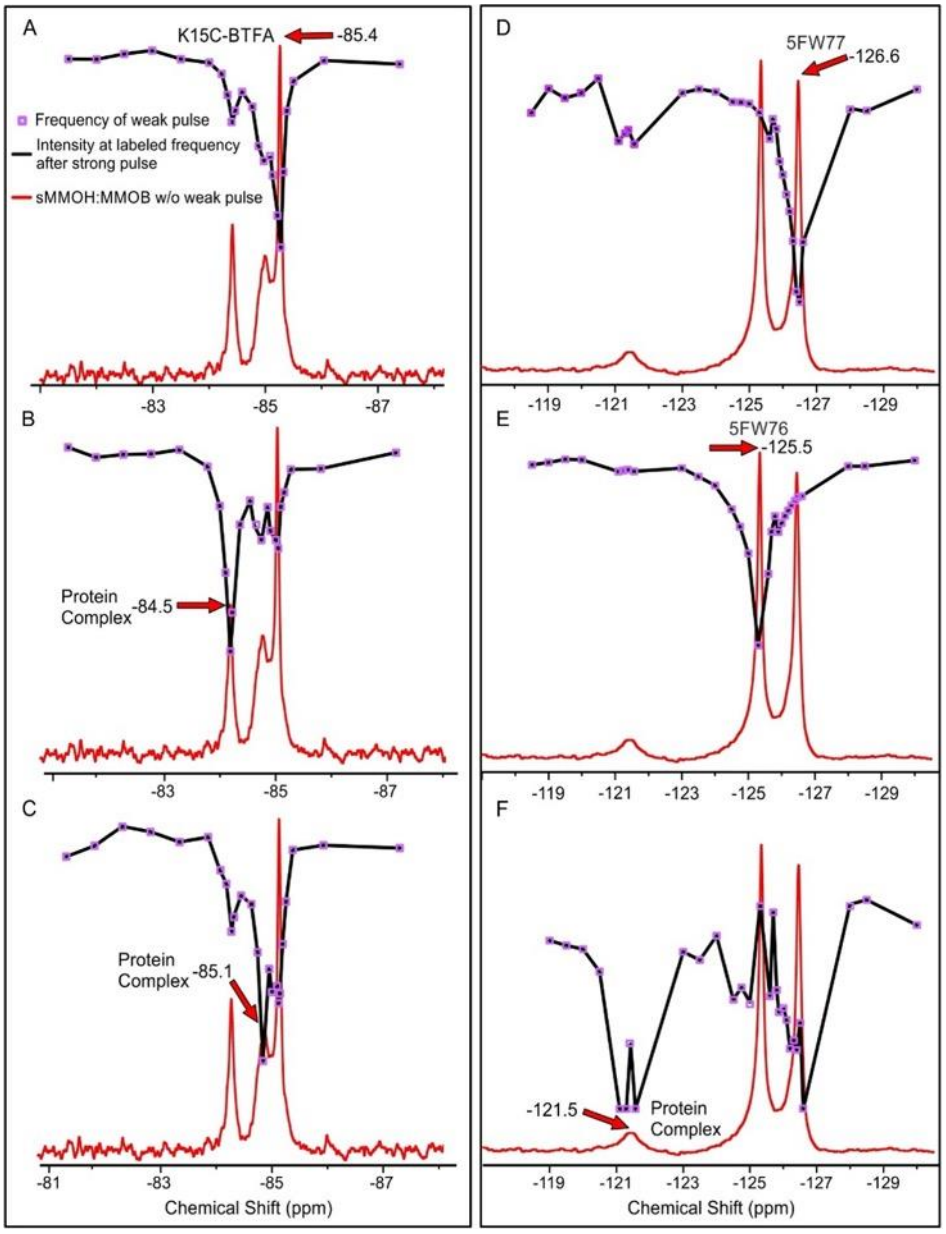

Figure 4-8. **^{19}F-NMR Chemical exchange saturation transfer (^{19}F-NMR CEST) of sMMOH:BTFA-K15C-5FW MMOB complex.**

A selective Gaussian pulse was applied to the ^{19}F spectra at locations indicated by purple boxes. The black line indicates the loss of intensity of the resonances indicated by the labeled frequency and red arrow. If slow exchange is occurring between bound and free states, the black line should mirror the spectrum shown in red. A-C: BTFA spectral region. D-F: 5FW spectral region.

4.4.6 5FW-Labeled MMOR.

The primary structure of OB3b MMOR contains one tryptophan residue. MMOR was labeled with 5FW in the same manner as MMOB. The 1D ^{19}F-NMR spectrum of heterologously expressed 5FW-MMOR is shown in **Figure 4-9**A. Two resonances of quite different intensity, but similar width are observed in the spectrum. Treatment with TCEP failed to eliminate either resonance, so dimerization via a disulfide linkage is not responsible for the two environments observed for a single Trp. Another possibility is that there is a single form of the enzyme, but two conformations exist in slow exchange. To test this hypothesis, a CEST experiment was performed (**Figure 4-10**). It was observed that irradiation of either resonance resulted in very little decrease in intensity of the other resonance. This result contrasts sharply with the CEST experiments involving sMMOH and ^{19}F-labeled MMOB shown in **Figure 4-8**. Consequently, it seems likely that there are major and minor forms of the enzyme that do not interconvert on the NMR timescale.

Addition of stoichiometric sMMOH (active sites) resulted in elimination of the spectrum from MMOR (**Figure 4-9**B). No new resonances are observed. It is likely that the resonances from 5FW are broadened into the baseline by formation of a tight sMMOH:MMOR complex. Titration of 5FW-MMOR with sMMOH gives a linear decrease in the -125.1 ppm resonance demonstrating high affinity. The concentration of 5FW-MMOR required for reasonable S/N (μ 20 μM) is too high for accurate determination of the K_D value for this tight complex. Another approach to determination of this K_D is described below.

MMOR was also labeled with BTFA in the same manner as described for MMOB. However, the presence of nine cysteine residues led to incorporation of multiple labels and a ^{19}F-NMR spectrum that was too complex to allow definitive studies.

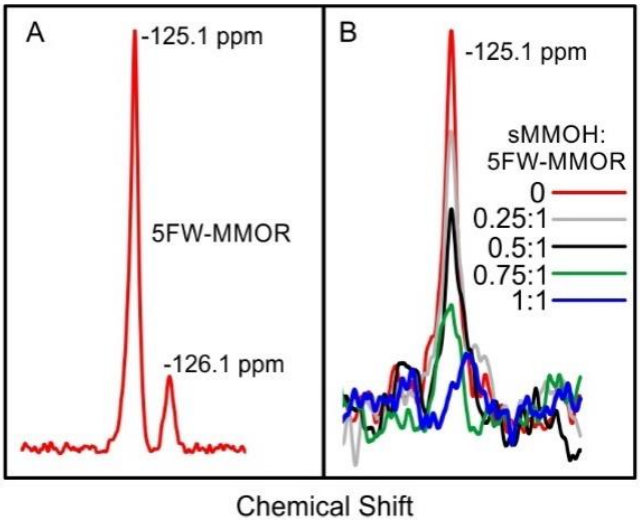

Figure 4-9 ^{19}F-NMR spectra of 5FW-MMOR
A: Spectrum of 20 μM 5FW-MMOR in the absence of sMMOH (5000 scans). B: Spectrum of 20 μM 5FW-MMOR (red, 512 scans) after adding the ratio of sMMOH (active sites) shown. The minor -126.1 ppm feature is not resolved due to the decreased number of scans, but in other experiments was found to also disappear after addition of stoichiometric sMMOH.

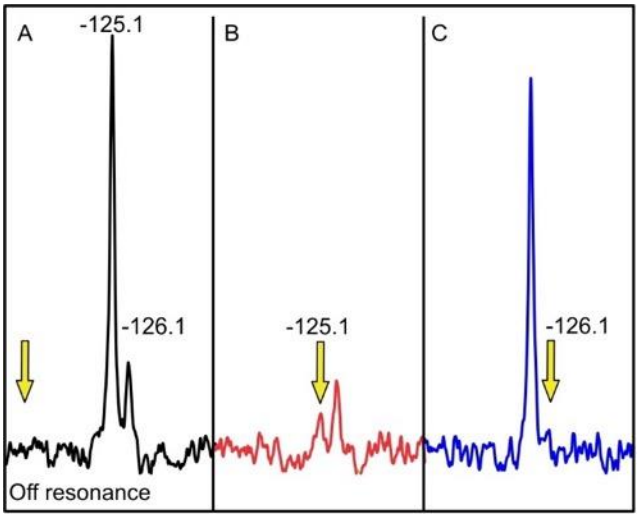

Figure 4-10 5FW-MMOR CEST
Panel A shows the 1D ^{19}F NMR CEST spectrum when a Gaussian pulse is applied to a region of the spectrum away from the 5FW-MMOR resonances. Panel B shows the effects when irradiated at -125.1 ppm. Panel C shows the effects when irradiated at -126.1 ppm. The arrow indicates the frequency of the Gaussian pulse used.

4.4.7 Binding Affinity of sMMOH for ^{19}F-Labeled MMOB

The relatively sharp and intense resonances from the relative low molecular weight 5FW-MMOB and BTFA-K15C-5FW MMOB allows quantification of a titration with sMMOH (an example is shown in **Figure 4-11**. The affinity for sMMOH is very high, and thus, the minimum concentration of ^{19}F-labeled MMOB with acceptable S/N is higher than optimal for a precise K_D determination. Nevertheless, the titration plots allow boundaries to be set for K_D values for both diferric and diferrous sMMOH as shown in **Figure 4-12**. The dashed curves shown in **Figure 4-12** are not fits of the data, but rather computed binding isotherms under the assumption that 70 % of the sMMOH is capable of binding to the ^{19}F-labeled MMOB (see below and Experimental Procedures). The good match between the computed curve and the titration of 5FW-MMOB suggests a K_D value of roughly 80 nM for both diferric and diferrous sMMOH (**Figure 4-12**A). The relatively intense -85.4 ppm resonance of BTFA allows a more accurate titration of BTFA-K15C-5FW MMOB by sMMOH. BTFA-K15C-5FW MMOB show a high affinity (K_D ~ 80 nM) for diferric sMMOH, but a 10-fold lower (K_D ~ 800 nM) affinity for diferrous sMMOH (**Figure 4-12** B). Similar values are obtained from analysis of the titrations monitored using the resonances from the 5FW labels in BTFA-K15C-5FW MMOB.

The high affinity of diferric sMMOH for BTFA-K15C-5FW MMOB allows a check on the proposal that there is a fraction of sMMOH that cannot bind MMOB. As shown in **Figure 4-13**) the titration of ^{19}F-labeled MMOB with sMMOH at an MMOB concentration over 1000-fold above the 80 nM K_D value results in the expected linear dependence on total sMMOH. However, complete saturation of the complex requires an excess of sMMOH consistent with the presence of a 30-40 % fraction that cannot bind the regulatory protein.

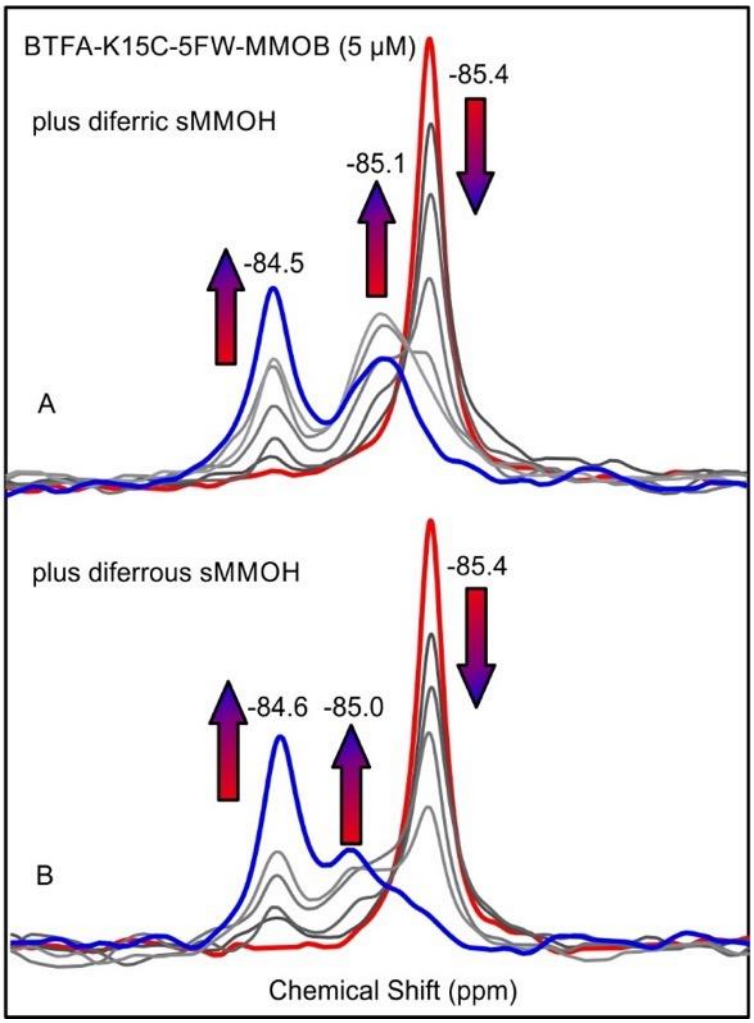

Figure 4-11 Typical titration of BTFA-K15C-5FW MMOB with sMMOH. BTFA-K15C-5FW MMOB (5 μM, red spectrum) was progressively titrated with sMMOH (gray spectra) to a final concentration of 50 μM (active site concentration, blue spectrum). The BTFA spectral region is shown. A: diferric sMMOH, B: diferrous sMMOH.

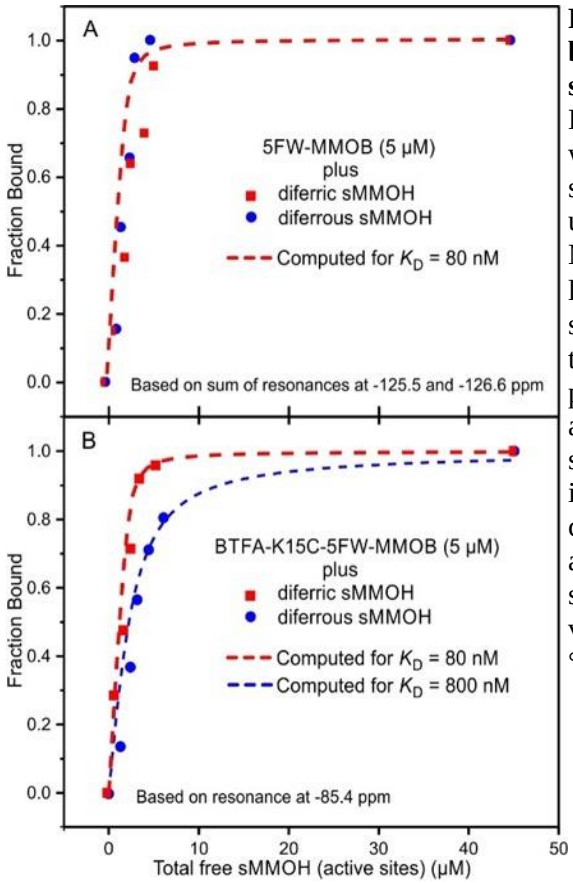

Figure 4-12 Plot of fraction of sMMOH bound versus concentration of free sMMOH.

Data such as that shown in **Figure 4-11** were normalized using an internal TFA standard and a fraction bound determined using the spectra of free ^{19}F-labeled MMOB and that of nearly fully bound ^{19}F-labeled MMOB after additon of 50 μM sMMOH (sites). The fraction bound times the concentration of ^{19}F-labeled MMOB present subtracted from the sMMOH added yields the concentration of free sMMOH. The free concentration shown includes the portion of sMMOH which cannot bind MMOB. The dashed curves are computed assuming that 70% of the sMMOH can bind MMOB and for the K_D values shown for 100 mM MOPS, pH 7, 25 °C.

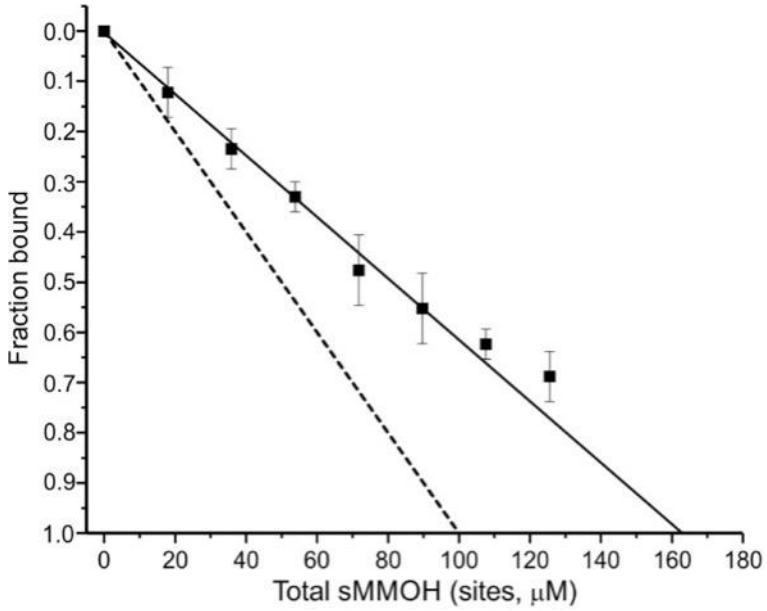

Figure 4-13 ^{19}F-NMR titration of 5FW-MMOB with sMMOH^{ox} at high concentrations. 5FW-MMOB (100 μM) was titrated with sMMOH at the concentrations shown (■, active sites). The fraction bound represents the change in the sum of the intensities for the two ^{19}F-NMR resonances in the 5FW spectral region divided by the sum of the intensities of these resonances from unbound 100 μM MMOB. The characterization of the sMMOH via stopped-flow (**Q** formation) and Mössbauer techniques predicted that 35% of this batch sMMOH would not bind MMOB. The observed linear dependence is consistent with the K_D value of 80 nM for the sMMOH:MMOB complex reported here. However, the dashed line is the computed dependence for these conditions. The difference in X-axis intercept reflects the inactive fraction of sMMOH (~39%). 100 mM MOPS buffer pH 7, 25 °C.

4.4.8 Binding Affinity of MMOR for the sMMOH:5FW-MMOB Complex.

As described in the introduction, a key question is whether MMOB and MMOR can form a ternary complex with sMMOH. The high affinity of 5FW-MMOB for diferric and diferrous sMMOH allow a nearly complete complex formation when μ10 μM of each (sites) are mixed in an NMR tube. Under these conditions, the -125.5 and -126.6 ppm resonances from the 5FW label of 5FW-MMOB are nearly extinguished. Incremental addition of MMOR is found to restore these resonances showing that the 5FW-MMOB is displaced by MMOR (**Figure 4-14**A). As shown in **Figure 4-14**B, a plot of the fraction of the original sMMOH:5FW-MMOB complex dissociated versus MMOR added is hyperbolic for both the diferric and diferrous forms of sMMOH:5FW-MMOB. In each case, the half dissociation values of 9.1 ± 2.3 and 13.7 ± 3.5 μM for the diferric and diferrous forms, respectively, are similar to the concentration of MMOB present (12 μM total). Computation[257, 258] of the K_D values for the diferric and diferrous sMMOH:MMOR complex from this competitive titration gives values of K_D = 60 ± 16 nM and 90 ± 23 nM, respectively. Thus, MMOR and MMOB appear to have a similar K_D values for sMMOH in each oxidation state. It is interesting to note that for both diferric and diferrous sMMOH:5FW-MMOB titrations, ~30% of the starting complex either does not dissociate or the characteristic resonance is decreased in intensity by an unidentified interaction when MMOR is added. Simple addition of MMOR to 5FW-MMOB in the absence of sMMOH does not decrease the resonance intensity.

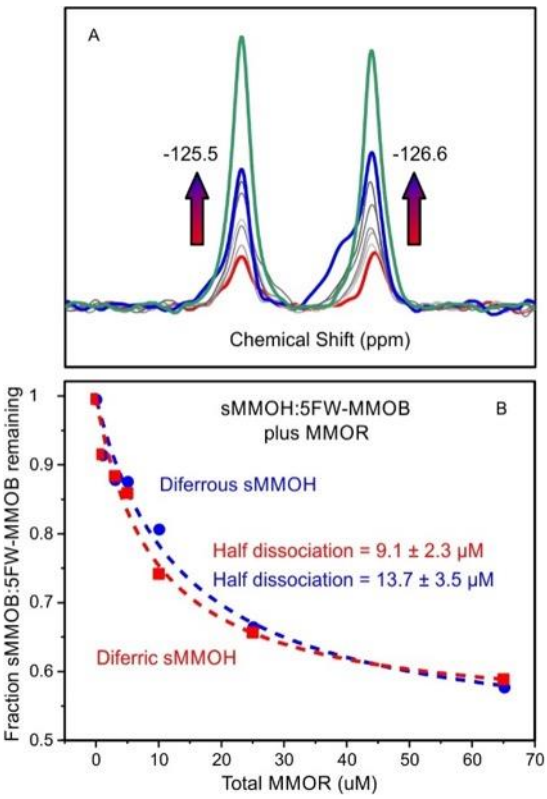

Figure 4-14 Titration of the sMMOH:5FW-MMOB complex with MMOR.
A: The ^{19}F-NMR resonances of unbound 5FW-MMOB (green spectrum) appear as MMOR is added (grey spectra) to diferric sMMOH:5FW-MMOB (red spectrum, represents residual unbound labeled MMOB under the starting conditions). Saturation (blue spectrum) occurs without full restoration of the spectrum of unbound 5FW-MMOB. B: Plot of the fraction of 5FW-MMOB released from the complex with sMMOH versus concentration of MMOR added. The fraction of dissociated sMMOH:5FW-MMOB complex was determined as the change in intensity of the resonance at -126.6 ppm relative to maximum possible change in the intensity of this resonance. The starting concentration of the sMMOH:5FW-MMOB complex was approximately 12 µM (18 µM total sMMOH, 70% active). The dashed lines are hyperbolic fits to the data. The half dissociation value is the amount of MMOR required for half of the observed dissociation reaction to be complete. 100 mM MOPS buffer pH 7, 25 °C.

4.4.9 MMOR Causes Both the N-terminal Tail and the Core Region of MMOB to Dissociate from sMMOH.

The presence of fluorine labels in two regions of MMOB allows their dissociation from the sMMOH:BTFA-K15C-5FW-MMOB upon MMOR binding to be independently evaluated. The spectra in **Figure 4-15**A and B show that the resonances characteristic of free, ^{19}F-labeled MMOB in the BTFA and 5FW spectral regions emerge during the titration of diferric sMMOH:BTFA-K15C-5FW-MMOB with MMOR. Thus, the binding of MMOR results in dissociation of both the core (5FW) and N-terminal (BTFA) regions of MMOB from sMMOH.

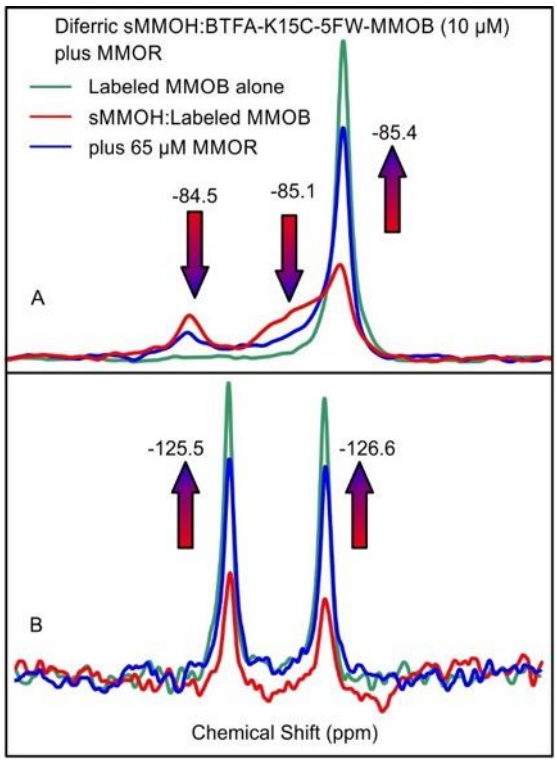

Figure 4-15 ^{19}F-NMR monitored addition of MMOR to diferric sMMOH:BTFA-K15C-5FW-MMOB complex. Aliquots of MMOR were added to sMMOH:BTFA-K15C-5FW-MMOB complex (12 µM labeled MMOB, 18 µM of 70% active sMMOH sites) leading to progressive release of labeled MMOB. A: BTFA spectral region. B: 5FW spectral region. Red spectra: Spectrum under starting conditions listed above (mixture of residual unbound labeled MMOB and sMMOH-labeled MMOB complex, Green spectra: 12 µM MMOB alone, Blue spectra: after addition of 65 µM MMOR. 100 mM MOPS buffer pH 7, 25 °C.

4.5 Discussion

This study has shown that the incorporation of fluorine into the protein components of an enzyme either by replacing the endogenous tryptophans with 5FW or by modifying a cysteine residue with BTFA allows detailed studies of component interactions via ^{19}F-NMR. These modifications cause minimal steric disruption, making them ideal as probes of protein-protein interfaces. In the current case, the combined mass of the dimeric sMMOH with 2 MMOBs bound is 277 kDa, a value often considered beyond the reach of NMR investigation. Nevertheless, this large particle gives easily distinguishable, well-resolved ^{19}F-resonances, particularly in the case of BTFA labeling, that can be used for structural interrogation and quantification in the 5 μM protein concentration range. Large changes in the NMR spectra show that complex formation between sMMOH and ^{19}F-labeled MMOB causes structural changes in both the compactly folded core region of MMOB and the N-terminal region as it transitions from disordered to ordered upon binding. Titration studies show that MMOB and MMOR both form tight complexes with sMMOH, but they are competitive with each other for a binding site. The approximate component affinities that emerge from these studies suggest a new model for electron transfer and regulation in the sMMO system which is discussed here.

4.5.1 Structural Changes that Occur as MMOB binds to sMMOH.

The appearance of a new resonance at -121.5 ppm upon formation of the sMMOH:^{19}F-labeled-MMOB complex is shown by mutagenesis and CEST measurements to arise from a large change in the environment of W77. The downfield shift relative to the resonance from W77 in free MMOB is consistent with movement of this Trp to a more hydrophobic environment.[266, 267] No new resonance is observed from W76 as the complex forms. However, a slight broadening of the base of the resonance from W76 is consistently observed (compare Figures 2 and 4A), suggesting that the resonance is not shifted, and thus, the environment of W76 is largely unchanged. These findings showcase the sensitivity of the ^{19}F-NMR in probing these types of interactions, and they also

correlate with the crystal structures of the complex reported here (**Figure 4-5**) and in other recent studies.[245, 268] Importantly, the 5FW-MMOB is found to be comparable to wild type MMOB both in steady state and single turnover kinetic studies, so 5FW substitution does not appear to alter either the structural or functional aspects of the interaction of sMMOH and MMOB.

When both 5FW and BTFA labels are incorporated into MMOB, the same shift in the resonance from W77 is observed, so the change in the N-terminal region does not affect the environment of the sMMOH interface residue in the compactly folded core region of MMOB. This finding is important because W77 is adjacent to the W308-tunnel that we propose is used in the transit of O_2 and probably also CH_4 to the active site of sMMOH.[245] Accordingly, O_2 binding remains fast and non-rate-limiting, and the rate constant for **Q** decay is not greatly affected by the BTFA modification in the N-terminal region. However, the new resonances that appear in the ^{19}F-NMR spectrum of the sMMOH:5FW-BTFA-K15C-MMOB complex show that the environment of the BTFA has shifted to a more hydrophobic environment and that it occupies at least two distinct positions. Neither outcome is expected based on the crystal structure of the native sMMOH:MMOB complex where residue K15 is solvent exposed and occupies a single orientation, presumably due to the K15-E23 hydrogen bond which is lost upon mutation and BTFA labeling. The steady state kinetics using the doubly ^{19}F-labeled MMOB are largely unchanged in rate limiting step (likely product release), but the single turnover kinetics for the **P*** to **P** and **P** to **Q** steps are slowed. Past studies have shown that the rate constants for these steps are individually slowed by two distinct His to Ala mutations in the N-terminal region.[71] Consequently, it is possible that the more hydrophobic trifluoromethyl group of BTFA samples the more hydrophobic environment in the sMMOH-MMOB interface and perturbs this interaction slightly. However, the enzyme remains functional and all of the intermediates of the reaction cycle are formed in high yield. These observations highlight the precise interactions between the sMMOH and MMOB components that regulate every aspect of the sMMO reaction cycle.

4.5.2 Binding Affinity of Labeled-MMOB for sMMOH.

Past studies have used techniques such as fluorescence quenching, fluorescence anisotropy, and ITC to determine the binding affinity between components of the sMMO system. These reports are summarized in **Table 4-4** for comparison with the current results. The wide range of values may derive from the types of probes employed, protein preparations, or the sensitivity of the techniques. It is unlikely that the differences reflect the bacterial origin of the sMMO components from *Mc*. Bath or *Mt.* OB3b because many studies have shown that these enzymes are remarkably similar structurally and functionally.[5, 14, 70, 75, 221, 245, 268] The titration monitored by ^{19}F-NMR described here combines the advantages of a sensitive, easily quantified readout of the incorporation of labeled-MMOB as the complex forms with minimal perturbation of the protein structure. The latter advantage allows the probe to be placed in or near the protein-protein interface where the most perturbation in the environment of the probe is likely to occur, particularly in the case of the 5FW probes. The results show that the 5FW-MMOB and 5FW-BTFA-K15C-MMOB complexes with sMMOH are both very strong, in near perfect agreement with previous measurements made using fluorescence techniques and the *Mt.* OB3b components (**Table 4-4**). In contrast, the results show the same strong affinity of 5FW-MMOB for diferrous sMMOH, whereas previous results using fluorescent probes showed a 30-65 fold decrease in affinity (or a 3-fold increase in affinity in the case of the *Mc*. Bath components[144]). The similarity of the steady state and transient kinetic behavior of 5FW-MMOB and wild type MMOB suggests that the latter would also show little change in affinity for diferrous sMMOH. The 5FW-BTFA-K15C-MMOB exhibits 10-fold weaker affinity for diferrous sMMOH. The higher apparent K_D value of 800 M is consistent with a doubling of the concentration required to reach full activity in the steady state assay under the assumption that high sMMO activity requires formation of a 1:1 sMMOH:MMOB complex. It may be significant that all of the studies reporting K_D values for diferrous sMMOH:MMOB complex except the current application of 5FW probes involve mutations and addition of fluorophores in or near the N-terminal region. Thus, the wide range of reported K_D values may reflect changes in binding

affinity and/or alterations in the protein-protein interface similar to those reported here for the MMOB-K15C-BTFA probe.

Table 4-4 Reported K_D Values for sMMO Component Complexes at pH 7

Method	Organism	sMMOH^{ox}-MMOB	sMMOH^{red}-MMOB	sMMOH^{ox}-MMOR	sMMOH^{red}-MMOR	Reference
			nM			
ITC	*Mc.* Bath	3000		900		[142]
Fluorescence Anisotropy IEDANS[b]	*Mc.* Bath	550	170	8000[c]		[64, 144]
Fluorescence Tryptophan	*Mt.* OB3b	67[a]		10		[63]
Fluorescence BADAN[d]	*Mt.* OB3b	68[e]	4500[e]			[129]
Fluorescence BADAN[d]	*Mt.* OB3b	68 159[e]	2200 4500[e]			[131]
^{19}F-NMR	*Mt.* OB3b	80[f] 80[g]	80[f] 800[g]	60[c,f]	90[c,f]	This work

[a]Fit to a thermodynamic cycle

[b]IEDANS label on D35C-MMOB from *Mc.* Bath

[c]MMOB present in solution but displaced by MMOR

[d]BADAN label on A62C-MMOB from *Mt.* OB3b

[e]pH 7.4

[f]5FW-MMOB

[g]5FW-BTFA-K15C-MMOB

One conflict between the past and current results is the observation that the redox potential of sMMOH decreases substantially when complexed with MMOB.[143, 145] If the free energy of binding is coupled with the redox potential shift, as it should be for thermodynamic states, the observed decrease of 132 mV in potential of a two electron reduction would indicate an increase in K_D from 80 nM to over 2 mM. This value is unreasonably high given the known strong interactions between sMMOH and its regulatory protein. It is possible that under the conditions of the redox potential measurements (multiple redox dyes and mediators) interactions beyond the binding of the two components occurred. Alternatively, we have observed that, while crystals of sMMOH are reduced in seconds by chemical reductants, co-crystals of sMMOH:MMOB require up to 12 hours of incubation. [245, 268] Consequently, the 1-1.5 hour time at 4 °C allowed for equilibration in previous redox titrations may not have been sufficient. Additional studies are required to resolve this conflict. It is important to point out that one of the conclusions of this study is that MMOB is not bound to sMMOH when electron transfer occurs from MMOR (see below), so the redox potential of the sMMOH:MMOB complex is of decreased relevance.

4.5.3 Displacement of Labeled MMOB from the sMMOH Complex by MMOR.

Addition of MMOR to either the diferric or diferrous sMMOH:5FW-MMOB complex results in the release of MMOB as observed by the return of the ^{19}F-NMR spectrum of unbound labeled-MMOB. The amount of MMOR required to cause half of the 5FW-MMOB to dissociate in both titrations is approximately equal to the amount of 5FW-MMOB present, showing that 5FW-MMOB and MMOR have similar K_D values for formation of the complex with sMMOH. The similar kinetic behavior of 5FW-MMOB and MMOB itself imply that MMOB and MMOR also have similar K_D values. This finding suggests that MMOB and MMOR compete equally for an sMMOH binding site both before and after electron transfer to initiate the catalytic cycle.

4.5.4 Mechanistic Significance.

As noted above, past studies indicate that once sMMOH is reduced and binds O_2 in the catalytic cycle, MMOB remains bound at least up to the product release step. Another indication that this is true is the failure of reduced MMOR to reduce intermediate **Q** during turnover, which would diminish or eliminate product yield. The previously proposed models for regulation, product release, and electron transfer shown in **Scheme 4-2** invoke transit through discrete fully occupied states. In Model A, MMOB and MMOR bind fully in independent sites, while in Model B, MMOR completely dissociates the core region of MMOB while leaving the N-terminal region bound. Both of these models are made less likely by the current results which show that: (i) both the core and N-terminal regions of ^{19}F-labeled MMOB are completely displaced by a large excess of MMOR, (ii) labeled-MMOB and MMOR have similar K_D values for sMMOH implying an equilibrium state, and (iii) the K_D values for labeled MMOB and MMOR do not change appreciably with the oxidation state of sMMOH. The results support the new model shown in **Scheme 4-3** in which MMOR and MMOB compete continuously for the same binding site on sMMOH independent of oxidation state. The fractional occupancy of the binding site on sMMOH is biased by the relative concentrations of MMOB and MMOR in the cell, which favors MMOB by 20-fold.[33] Nevertheless, in the new model the reaction is pulled forward by effectively irreversible reactions that occur when a specific complex is formed (bold red arrows in **Scheme 4-3**). Dissociation of a small fraction of the sMMOH^{ox}:MMOB complex at the end of turnover would allow product release through the pore normally covered by bound MMOB. Subsequent binding of reduced MMOR would lead to rapid reduction (96 s^{-1} in the equivalent *Mc* Bath complex[142]) and formation of sMMOH^{red}:MMOR complex thereby removing it from the equilibrium of diferric sMMOH and its component complexes. In the next step, a small fraction of MMOR would dissociate from the sMMOH^{red}:MMOR complex, allowing MMOB to bind. The diferrous sMMOH:MMOB complex would very rapidly bind O_2 removing this fraction from the equilibrium of diferrous sMMOH and its complexes, again pulling the reaction forward. The current results do not give information about

the affinities of MMOB and MMOR for the intermediates in the reaction cycle after O_2 binds. However, only the sMMOH^{red}:MMOB complex can bind O_2 rapidly, so it is the only complex that can proceed in the reaction cycle. Subsequent binding of MMOR may be prevented by an increase in affinity for MMOB by the diiron(III) and (IV) intermediates **P**, **Q**, and **R**. Alternatively, the kinetics of flux through the reaction cycle may not allow significant dissociation of MMOB from the intermediates. Transient kinetic measurements of 5 μM BADAN-A62C-MMOB binding to sMMOH revealed a pseudo first order association rate constant at 4 °C of 400 s^{-1} and a dissociation rate constant of 2.4 s^{-1}.[131] These values are in reasonable accord with the ^{19}F-NMR spectrum presented here which shows a 5 ppm shift of the resonance from 5FW-MMOB as the complex with sMMOH forms. For a Larmor frequency of 565 MHz for ^{19}F, these values, and the lack of resonance broadening during titration, require that the exchange rate constant of 5FW-MMOB in and out of the sMMOH:5FW-MMOB complex (k_{on} + k_{off}) be very slow relative to 17,750 s^{-1} (5 ppm x 2π x 565 MHz). In a single turnover with a typical assay concentration of 100 μM CH_4 present, the reaction cycle prior to product release is rate-limited by **Q** formation at 2.4 s^{-1} (**Table 4-2**). All of the other intermediate steps are substantially faster, so MMOB would have a limited time window in which to exchange, and its 20:1 concentration advantage would help to protect **Q** from reduction by MMOR.

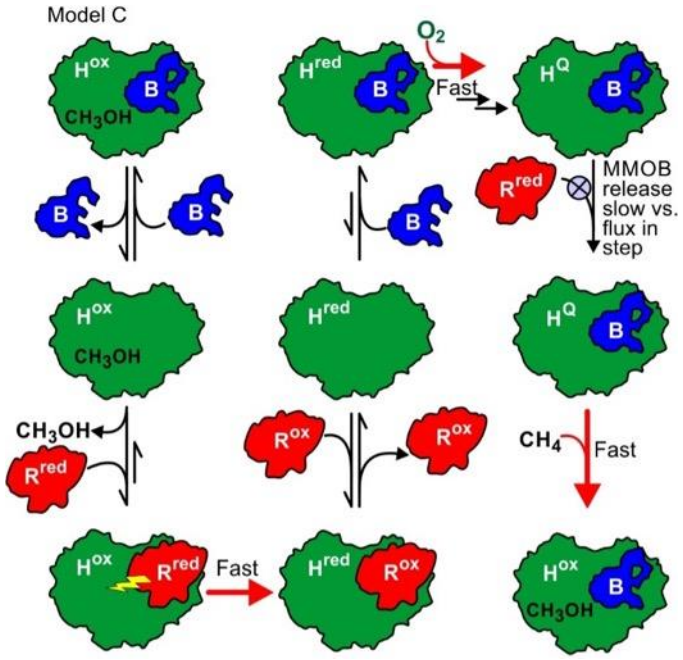

Scheme 4-3 New Model for Regulation of Electron Transfer and Substrate Binding. The cycle begins (upper left) and ends (lower right in the product complex (intermediate T in **Scheme 4-1**). Bold red arrows represent irreversible steps that pull the reaction cycle forward. H^{ox} = diferric sMMOH, H^{red} = diferrous $sMMOH^{red}$, B = MMOB, R^{ox} = fully oxidized MMOR, R^{red} = two electron reduced $MMOR^{red}$, H^Q = Intermediate **Q** of the reaction cycle.

4.6 Conclusion

A pervasive theme in oxygenase mechanistic studies is the requirement to carefully control the hyper-reactive intermediates that are generated to enable transfer of an oxygen atom into a stable substrate bond. The ultimate test of this principle is the reaction of the diiron(IV) intermediate **Q** of sMMO with the stable C-H bond of methane. The process of **Q** formation requires initial input of two electron to activate O_2, but the additional transfer of even a single additional electron after **Q** is formed would deactivate it sufficiently to obviate the attack on its only biologically relevant substrate. In sMMO, Nature has constructed a remarkable machine to control this process in which even minor changes in the interface between the catalytic sMMOH component the MMOB regulatory component compromise rate and specificity. It is shown here that labeling with 5FW allows the investigation of the MMOB interaction with sMMOH using ^{19}F-NMR in a manner that does not require perturbation of the interface. The frequent placement of Trp residues in

hydrophobic protein-protein interfaces, the relative rarity of this amino acid, and ability to study micromolar reactant concentrations suggest that this approach will continue to find wide application. The sensitivity of the MMOB-sMMOH interface is highlighted by the effects of replacing a lysine with the structurally conservative BTFA label in the N-terminal of the regulatory protein (**Figure 4-6**B). Even this small change decreases the binding affinity ten-fold and alters the rate constants of several steps in the catalytic cycle. Nevertheless, the BTFA and 5FW probes together very effectively demonstrate the regulatory importance of both the core and N-terminal structural regions of MMOB. It is often convenient to think of enzymatic reactions as occurring in a linear fashion with one step completing before the next initiates. However, it is increasingly apparent that many biological processes instead occur by shifts in equilibrium of the relevant complexes.[269-271] The current results suggest that a form of this dynamic equilibrium concept is at the heart of sMMO regulation. Nature forms and protects the key oxidative intermediate by controlling the concentrations, lifetimes, and irreversibility of reactions of specific protein-protein complexes.

Chapter 5 Future Directions

Collaboration is the hero of this dissertation, without it none of the work described above would have been possible. A team composed of biochemists, chemists, physicists, computer scientists, and engineers came together to obtain radiation-damage free high resolution X-ray crystal structures of the 275 kDa OB3b sMMOH:MMOB protein complex. The results provided new insight into the manner by which the diiron cluster and the active site environment are reorganized by the regulatory protein component in order to enhance the steps of oxygen activation and methane oxidation. A different collaboration between experts in biochemistry, X-ray crystallography, and ^{19}F-NMR at the University of Minnesota resulted in the discovery of the structural mechanism that regulates O_2 transport to the active site and also how sMMO protein interactions regulate catalysis. Because of these multidisciplinary teams, we have furthered our understanding of how Nature regulates enzymatic catalysis through protein-protein interactions. If we are to leverage the enzymatic activity of sMMO to prevent the escape of CH_4 into the atmosphere, then the collaborations that made this dissertation possible must continue to thrive and grow. The next paragraphs briefly describe a few experiments that may help answer questions that emerged from the research presented in this dissertation.

As shown in Chapter 2, *in crystallo* turnover without loss of diffraction quality is possible using sMMOH:MMOB microcrystal slurries. More SFX-XFEL experiments are needed to find the correct time in which chemically reduced sMMOH:MMOB microcrystals are exposed to O_2 using the drop-on-tape methodology if we are to obtain structures of sMMO chemical intermediates. Once we have the timing determined, the structure of radiation-damage-free chemical intermediates can potentially be obtained.

High-resolution structural data coupled with transient-kinetics data led to the discovery of the W308-Tunnel. The W308-Tunnel, pore, and chain of cavities are difficult to characterize because it is not possible to make and express sMMOH mutants. A high-throughput methodology to mutate and express sMMOH variants is needed to further investigate the proposed substrate

pathways. Until then, our understanding of how sMMO regulates the entry of CH_4, O_2, e^-, and H^+ will remain limited.

Quality sMMO protein preparations have propelled our structural biology research efforts. The ease at which we can crystallize milliliters of sMMOH:MMOB microcrystals warrants investigation of the potential to use the crystal slurries as catalysts to convert methane to methanol. A proof of principle study can be performed to determine if sMMOH:MMOB crystal slurries are capable of catalysis by first reducing the crystal slurry then mix with a aerobic buffer with substrate. If turnover occurred, product will be present indicating that the microcrystal slurries are capable of catalysis.

Limitations of the NMR methodology used in chapter 4 prevented the study of the interaction between reduced MMOR and $sMMOH^{ox}$. The only data available are of the interactions between oxidized MMOR and $sMMOH^{ox}$. Stopped-flow ^{19}F-NMR is a method that can be used to rapidly mix reduced MMOR with $sMMOH^{ox}$ and obtain time resolved information. Furthermore, we could rapidly mix reduced MMOR with a preformed $sMMOH^{ox}$:MMOB complex to learn if reduced MMOR is more effective at dissociating MMOB from $sMMOH^{ox}$.

Efforts to obtain the structure of the sMMOH:MMOR complex are necessary. One approach is to crystallize the protein complex, but our efforts thus far have not met with any success. An alternative and more promising methodology is to make cryo-EM samples containing sMMOH and MMOR. This method will likely be the methodology that first obtains the structure of the sMMOH:MMOR complex. Also, it may be possible to determine if a ternary complex between sMMOH, MMOB, and MMOR exists using cryo-EM.

Chapter 6 Bibliography

1. Luo, G.; Ono, S.; Beukes, N. J.; Wang, D. T.; Xie, S.; Summons, R. E., Rapid oxygenation of Earth's atmosphere 2.33 billion years ago. *Science Advances* **2016,** *2* (5), 0-10.
2. Kump, L. R.; Barley, M. E., Increased subaerial volcanism and the rise of atmospheric oxygen 2.5 billion years ago. *Nature* **2007,** *448* (7157), 1033-1036.
3. Bekker, A.; Holland, H. D.; Wang, P. L.; Rumble, D.; Stein, H. J.; Hannah, J. L.; Coetzee, L. L.; Beukes, N. J., Dating the rise of atmospheric oxygen. *Nature* **2004,** *427* (6970), 117-120.
4. Sessions, A. L.; Doughty, D. M.; Welander, P. V.; Summons, R. E.; Newman, D. K., The continuing puzzle of the great oxidation event. *Curr Biol* **2009,** *19* (14), R567-R574.
5. Banerjee, R.; Jones, J. C.; Lipscomb, J. D., Soluble methane monooxygenase. *Ann. Rev. Biochem.* **2019,** *88*, 409-431.
6. Kump, L. R., The rise of atmospheric oxygen. *Nature* **2008,** *451* (7176), 277-278.
7. Catling, D. C.; Glein, C. R.; Zahnle, K. J.; McKay, C. P., Why O_2 is required by complex life on habitable planets and the concept of planetary "oxygenation time". *Astrobiology* **2005,** *5* (3), 415-438.
8. Raymond, J.; Segre, D., The effect of oxygen on biochemical networks and the evolution of complex life. *Science* **2006,** *311* (5768), 1764-1767.
9. Xing, G.; Barr, E. W.; Diao, Y.; Hoffart, L. M.; Prabhu, K. S.; Arner, R. J.; Reddy, C. C.; Krebs, C.; Bollinger, J. M., Jr., Oxygen activation by a mixed-valent, diiron(II/III) cluster in the glycol cleavage reaction catalyzed by myo-inositol oxygenase. *Biochemistry* **2006,** *45* (17), 5402-5412.
10. Vu, V. V.; Emerson, J. P.; Martinho, M.; Kim, Y. S.; Münck, E.; Park, M. H.; Que, L., Jr., Human deoxyhypusine hydroxylase, an enzyme involved in regulating cell growth, activates O_2 with a nonheme diiron center. *Proc. Nat. Acad. Sci. USA* **2009,** *106* (35), 14814-14819.
11. Han, Z.; Sakai, N.; Boettger, L. H.; Klinke, S.; Hauber, J.; Trautwein, A. X.; Hilgenfeld, R., Crystal structure of the peroxo-diiron(III) intermediate of deoxyhypusine hydroxylase, an oxygenase involved in hypusination. *Structure* **2015,** *23* (5), 882-892.
12. Jasniewski, A. J.; Que, L., Jr., Dioxygen activation by nonheme diiron enzymes: diverse dioxygen adducts, high-valent intermediates, and related model complexes. *Chem Rev* **2018,** *118* (5), 2554-2592.
13. Kovaleva, E. G.; Lipscomb, J. D., Versatility of biological non-heme Fe(II) centers in oxygen activation reactions. *Nat. Chem. Biol.* **2008,** *4* (3), 186-193.
14. Tinberg, C. E.; Lippard, S. J., Dioxygen activation in soluble methane monooxygenase. *Accounts of Chemical Research* **2011,** *44* (4), 280-288.
15. Wallar, B. J.; Lipscomb, J. D., Dioxygen activation by enzymes containing binuclear non-heme iron clusters. *Chemical Reviews* **1996,** *96* (7), 2625-2657.
16. Reay, D. S.; Smith, P.; Christensen, T. R.; James, R. H.; Clark, H., Methane and global environmental change. *Annu. Rev. Environ. Resour.* **2018,** *43* (1), 165-192.
17. Fletcher, S. E. M.; Schaefer, H., Rising methane: A new climate challenge. *Science* **2019,** *364* (6444), 932-933.
18. Clomburg, J. M.; Crumbley, A. M.; Gonzalez, R., Industrial biomanufacturing: The future of chemical production. *Science* **2017,** *355* (6320), 38-39.
19. Haynes, C. A.; Gonzalez, R., Rethinking biological activation of methane and conversion to liquid fuels. *Nature Chemical Biology* **2014,** *10* (5), 331-339.
20. Hanson, R. S.; Hanson, T. E., Methanotrophic bacteria. *Microbiological Reviews* **1996,** *60* (2), 439-447.
21. Nazaries, L.; Murrell, J. C.; Millard, P.; Baggs, L.; Singh, B. K., Methane, microbes and models: fundamental understanding of the soil methane cycle for future predictions. *Environ Microbiol* **2013,** *15* (9), 2395-2417.

22. Knief, C., Diversity and habitat preferences of cultivated and uncultivated aerobic methanotrophic bacteria evaluated based on pmoA as molecular marker. *Frontiers in Microbiology* **2015,** *6*, 1346.
23. Kalyuzhnaya, M. G.; Puri, A. W.; Lidstrom, M. E., Metabolic engineering in methanotrophic bacteria. *Metab. Eng.* **2015,** *29*, 142-152.
24. Knief, C.; Vanitchung, S.; Harvey, N. W.; Conrad, R.; Dunfield, P. F.; Chidthaisong, A., Diversity of methanotrophic bacteria in tropical upland soils under different land uses. *Applied and Environmental Microbiology* **2005,** *71* (7), 3826-3831.
25. Koo, C. W.; Rosenzweig, A. C., Biochemistry of aerobic biological methane oxidation. *Chemical Society Reviews* **2021,** *50*, 3424-3436.
26. Sirajuddin, S.; Barupala, D.; Helling, S.; Marcus, K.; Stemmler, T. L.; Rosenzweig, A. C., Effects of zinc on particulate methane monooxygenase activity and structure. *J. Biol. Chem.* **2014,** *289* (31), 21782-21794.
27. Lieberman, R. L.; Rosenzweig, A. C., Crystal structure of a membrane-bound metalloenzyme that catalyzes the biological oxidation of methane. *Nature* **2005,** *434* (7030), 177-182.
28. Hakemian, A. S.; Kondapalli, K. C.; Telser, J.; Hoffman, B. M.; Stemmler, T. L.; Rosenzweig, A. C., The metal centers of particulate methane monooxygenase from methylosinus trichosporium OB3b. *Biochemistry* **2008,** *47* (26), 6793-6801.
29. Smith, S. M.; Rawat, S.; Telser, J.; Hoffman, B. M.; Stemmler, T. L.; Rosenzweig, A. C., Crystal structure and characterization of particulate methane monooxygenase from *Methylocystis* species strain M. *Biochemistry* **2011,** *50* (47), 10231-10240.
30. Ro, S. Y.; Ross, M. O.; Deng, Y. W.; Batelu, S.; Lawton, T. J.; Hurley, J. D.; Stemmler, T. L.; Hoffman, B. M.; Rosenzweig, A. C., From micelles to bicelles: Effect of the membrane on particulate methane monooxygenase activity. *The Journal of Biological Chemistry* **2018,** *293* (27), 10457-10465.
31. Ro, S. Y.; Schachner, L. F.; Koo, C. W.; Purohit, R.; Remis, J. P.; Kenney, G. E.; Liauw, B. W.; Thomas, P. M.; Patrie, S. M.; Kelleher, N. L.; Rosenzweig, A. C., Native top-down mass spectrometry provides insights into the copper centers of membrane-bound methane monooxygenase. *Nature Communications* **2019,** *10* (1), 1-12.
32. Ross, M. O.; Macmillan, F.; Wang, J.; Nisthal, A.; Lawton, T. J.; Olafson, B. D.; Mayo, S. L.; Rosenzweig, A. C.; Hoffman, B. M., Particulate methane monooxygenase contains only mononuclear copper centers. *Science* **2019,** *364* (6440), 566-570.
33. Fox, B. G.; Froland, W. A.; Dege, J. E.; Lipscomb, J. D., Methane monooxygenase from *Methylosinus trichosporium* OB3b. Purification and properties of a three-component system with high specific activity from a type II methanotroph. *J. Biol. Chem.* **1989,** *264* (17), 10023-10033.
34. Banerjee, R.; Komor, A. J.; Lipscomb, J. D., Use of isotopes and isotope effects for investigations of diiron oxygenase mechanisms. *Methods Enzymol.* **2017,** *596*, 239-290.
35. Pilkington, S. J.; Dalton, H., Soluble methane monooxygenase from *Methylococcus capsulatus* (Bath). *Methods Enzymol.* **1990,** *188*, 181-190.
36. Baik, M.-H.; Newcomb, M.; Friesner, R. A.; Lippard, S. J., Mechanistic studies on the hydroxylation of methane by methane monooxygenase. *Chemical Reviews (Washington, DC, United States)* **2003,** *103* (6), 2385-2419.
37. Rosenzweig, A. C.; Frederick, C. A.; Lippard, S. J.; Nordlund, P., Crystal structure of a bacterial non-haem iron hydroxylase that catalyses the biological oxidation of methane. *Nature* **1993,** *366* (6455), 537-543.
38. Rosenzweig, A. C.; Nordlund, P.; Takahara, P. M.; Frederick, C. A.; Lippard, S. J., Geometry of the soluble methane monooxygenase catalytic diiron center in two oxidation states. *Chem. Biol.* **1995,** *2* (6), 409-418.
39. Rosenzweig, A. C.; Brandstetter, H.; Whittington, D. A.; Nordlund, P.; Lippard, S. J.; Frederick, C. A., Crystal structures of the methane monooxygenase hydroxylase from

Methylococcus capsulatus (Bath): implications for substrate gating and component interactions. *Proteins* **1997,** *29* (2), 141-152.
40. Elango, N.; Radhakrishnan, R.; Froland, W. A.; Wallar, B. J.; Earhart, C. A.; Lipscomb, J. D.; Ohlendorf, D. H., Crystal structure of the hydroxylase component of methane monooxygenase from *Methylosinus trichosporium* OB3b. *Protein Sci.* **1997,** *6* (3), 556-568.
41. Whittington, D. A.; Lippard, S. J., Crystal structures of the soluble methane monooxygenase hydroxylase from *Methylococcus capsulatus* (Bath) demonstrating geometrical variability at the dinuclear iron active site. *J. Am. Chem. Soc.* **2001,** *123* (5), 827-838.
42. Whittington, D. A.; Sazinsky, M. H.; Lippard, S. J., X-ray crystal structure of alcohol products bound at the active site of soluble methane monooxygenase hydroxylase. *J. Am. Chem. Soc.* **2001,** *123* (8), 1794-1795.
43. Whittington, D. A.; Rosenzweig, A. C.; Frederick, C. A.; Lippard, S. J., Xenon and halogenated alkanes track putative substrate binding cavities in the soluble methane monooxygenase hydroxylase. *Biochemistry* **2001,** *40* (12), 3476-3482.
44. Chang, S. L.; Wallar, B. J.; Lipscomb, J. D.; Mayo, K. H., Solution structure of component B from methane monooxygenase derived through heteronuclear NMR and molecular modeling. *Biochemistry* **1999,** *38* (18), 5799-5812.
45. Walters, K. J.; Gassner, G. T.; Lippard, S. J.; Wagner, G., Structure of the soluble methane monooxygenase regulatory protein B. *Proc. Natl. Acad. Sci. U. S. A.* **1999,** *96* (14), 7877-7882.
46. Chang, S. L.; Wallar, B. J.; Lipscomb, J. D.; Mayo, K. H., Residues in *Methylosinus trichosporium* OB3b methane monooxygenase component B involved in molecular interactions with reduced- and oxidized-hydroxylase component: A role for the N-terminus. *Biochemistry* **2001,** *40* (32), 9539-9551.
47. Muller, J.; Lugovskoy, A. A.; Wagner, G.; Lippard, S. J., NMR structure of the [2Fe-2S] ferredoxin domain from soluble methane monooxygenase reductase and interaction with its hydroxylase. *Biochemistry* **2002,** *41* (1), 42-51.
48. Chatwood, L. L.; Mueller, J.; Gross, J. D.; Wagner, G.; Lippard, S. J., NMR structure of the flavin domain from soluble methane monooxygenase reductase from *Methylococcus capsulatus* (Bath). *Biochemistry* **2004,** *43* (38), 11983-11991.
49. Sazinsky, M. H.; Merkx, M.; Cadieux, E.; Tang, S.; Lippard, S. J., Preparation and X-ray structures of metal-free, dicobalt and dimanganese forms of soluble methane monooxygenase hydroxylase from *Methylococcus capsulatus* (Bath). *Biochemistry* **2004,** *43* (51), 16263-16276.
50. Sazinsky, M. H.; Lippard, S. J., Product bound structures of the soluble methane monooxygenase hydroxylase from *Methylococcus capsulatus* (Bath): Protein motion in the alpha-subunit. *Journal of the American Chemical Society* **2005,** *127* (16), 5814-5825.
51. Osborne, C. D.; Haritos, V. S., Beneath the surface: Evolution of methane activity in the bacterial multicomponent monooxygenases. *Mol. Phylogen. Evol.* **2019,** *139*.
52. Kim, H.; An, S.; Park, Y. R.; Jang, H.; Park, S. H.; Lee, S. J.; Cho, U. S., MMOD-induced structural changes of hydroxylase in soluble methane monooxygenase. *bioRxiv* **2018,** (October), 1-9.
53. Sazinsky, M. H.; Dunten, P. W.; McCormick, M. S.; DiDonato, A.; Lippard, S. J., X-ray structure of a hydroxylase-regulatory protein complex from a hydrocarbon-oxidizing multicomponent monooxygenase, *Pseudomonas* sp. OX1 phenol hydroxylase. *Biochemistry* **2006,** *45* (51), 15392-15404.
54. McCormick, M. S.; Sazinsky, M. H.; Condon, K. L.; Lippard, S. J., X-ray crystal structures of manganese(II)-reconstituted and native toluene/o-xylene monooxygenase hydroxylase reveal rotamer shifts in conserved residues and an enhanced view of the protein interior. *Journal of the American Chemical Society* **2006,** *128*, 15108-15110.
55. Bailey, L. J.; McCoy, J. G.; Phillips, G. N., Jr.; Fox, B. G., Structural consequences of effector protein complex formation in a diiron hydroxylase. *Proc. Nat. Acad. Sci. USA* **2008,** *105* (49), 19194-19198.

56. Sazinsky, M. H.; Lippard, S. J., Methane monooxygenase: Functionalizing methane at iron and copper. *Met. Ions Life Sci.* **2015,** *15*, 205-256.
57. Lund, J.; Woodland, M. P.; Dalton, H., Electron transfer reactions in the soluble methane monooxygenase of Methylococcus capsulatus (Bath). *European Journal of Biochemistry* **1985,** *147* (2), 297-305.
58. Fox, B. G.; Froland, W. A.; Dege, J. E.; Lipscomb, J. D., Methane Monooxygenase from Methylosinus trichosporium OB3b. *Journal of Bacteriology* **1989,** *264* (17), 10023-10033.
59. Müller, J.; Lugovskoy, A. A.; Wagner, G.; Lippard, S. J., NMR structure of the [2Fe-2S] ferredoxin domain from soluble methane monooxygenase reductase and interaction with its hydroxylase. *Biochemistry* **2002,** *41* (1), 42-51.
60. Chatwood, L. L.; Miller, J.; Gross, J. D.; Wagner, G.; Lippard, S. J., NMR structure of the flavin domain from soluble methane monooxygenase reductase from Methylococcus capsulatus (Bath). *Biochemistry* **2004,** *43* (38), 11983-11991.
61. Jeong, H. S.; Hong, S.; Yoo, H. S.; Kim, J.; Kim, Y.; Yoon, C.; Lee, S. J.; Kim, S. H., EPR-derived structures of flavin radical and iron-sulfur clusters from: *Methylosinus sporium* 5 reductase. *Inorganic Chemistry Frontiers* **2021,** *8* (5), 1279-1289.
62. Kopp, D. A.; Gassner, G. T.; Blazyk, J. L.; Lippard, S. J., Electron-transfer reactions of the reductase component of soluble methane monooxygenase from *Methylococcus capsulatus* (Bath) †. *Biochemistry* **2001,** *40* (49), 14932-14941.
63. Fox, B. G.; Liu, Y.; Dege, J. E.; Lipscomb, J. D., Complex formation between the protein components of methane monooxygenase from *Methylosinus trichosporium* OB3b. Identification of sites of component interaction. *J. Biol. Chem.* **1991,** *266* (1), 540-550.
64. Wang, W.; Iacob, R. E.; Luoh, R. P.; Engen, J. R.; Lippard, S. J., Electron transfer control in soluble methane monooxygenase. *J. Am. Chem. Soc.* **2014,** *136* (27), 9754-9762.
65. Brazeau, B. J.; Lipscomb, J. D., Key amino acid residues in the regulation of soluble methane monooxygenase catalysis by component B. *Biochemistry* **2003,** *42* (19), 5618-5631.
66. Brazeau, B. J.; Wallar, B. J.; Lipscomb, J. D., Unmasking of deuterium kinetic isotope effects on the methane monooxygenase compound Q reaction by site-directed mutagenesis of component B. *Journal of the American Chemical Society* **2001,** *123* (42), 10421-10422.
67. Zheng, H.; Lipscomb, J. D., Regulation of methane monooxygenase catalysis based on size exclusion and quantum tunneling. *Biochemistry* **2006,** *45* (6), 1685-1692.
68. Lee, S. K.; Nesheim, J. C.; Lipscomb, J. D., Transient intermediates of the methane monooxygenase catalytic cycle. *Journal of Biological Chemistry* **1993,** *268* (29), 21569-21577.
69. Liu, Y.; Nesheim, J. C.; Lee, S.-K.; Lipscomb, J. D., Gating effects of component B on oxygen activation by the methane monooxygenase hydroxylase component. *J. Biol. Chem.* **1995,** *270* (42), 24662-246625.
70. Lee, S. J.; McCormick, M. S.; Lippard, S. J.; Cho, U.-S., Control of substrate access to the active site in methane monooxygenase. *Nature* **2013,** *494* (7437), 380-384.
71. Wallar, B. J.; Lipscomb, J. D., Methane monooxygenase component B mutants alter the kinetics of steps throughout the catalytic cycle. *Biochemistry* **2001,** *40* (7), 2220-2233.
72. Liu, K. E.; Valentine, A. M.; Wang, D. L.; Huynh, B. H.; Edmondson, D. E.; Salifoglou, A.; Lippard, S. J., Kinetic and spectroscopic characterization of intermediates and component interactions in reactions of methane monooxygenase from *Methylococcus capsulatus* (Bath). *J. Am. Chem. Soc.* **1995,** *117* (41), 10174-10185.
73. Lee, S. K.; Lipscomb, J. D., Oxygen activation catalyzed by methane monooxygenase hydroxylase component: Proton delivery during the O-O bond cleavage steps. *Biochemistry.* **1999,** *38* (14), 4423-4432.
74. Brazeau, B. J.; Lipscomb, J. D., Kinetics and activation thermodynamics of methane monooxygenase compound Q formation and reaction with substrates. *Biochemistry* **2000,** *39* (44), 13503-13515.

75. Tinberg, C. E.; Lippard, S. J., Revisiting the mechanism of dioxygen activation in soluble methane monooxygenase from *M. capsulatus* (Bath): Evidence for a multi-step, proton-dependent reaction pathway. *Biochemistry* **2009,** *48* (51), 12145-12158.
76. Banerjee, R.; Meier, K. K.; Münck, E.; Lipscomb, J. D., Intermediate P* from soluble methane monooxygenase contains a diferrous cluster. *Biochemistry* **2013,** *52* (25), 4331-4342.
77. Hendrich, M. P.; Münck, E.; Fox, B. G.; Lipscomb, J. D., Integer-spin EPR studies of the fully reduced methane monooxygenase hydroxylase component. *J. Am. Chem. Soc.* **1990,** *112*, 5861-5865.
78. Priestley, N. D.; Floss, H. G.; Froland, W. A.; Lipscomb, J. D.; Williams, P. G.; Morimoto, H., Cryptic stereospecificity of methane monooxygenase. *J. Am. Chem. Soc.* **1992,** *114*, 7561-7562.
79. Jin, Y.; Lipscomb, J. D., Mechanistic insights into C-H activation from radical clock chemistry: Oxidation of substituted methylcyclopropanes catalyzed by soluble methane monooxygenase from *Methylosinus trichosporium* OB3b. *Biochim. Biophys. Acta.* **2000,** *1543*, 47-59.
80. Brazeau, B. J.; Austin, R. N.; Tarr, C.; Groves, J. T.; Lipscomb, J. D., Intermediate Q from soluble methane monooxygenase hydroxylates the mechanistic substrate probe norcarane: evidence for a stepwise reaction. *Journal of the American Chemical Society* **2001,** *123* (48), 11831-11837.
81. Jasniewski, A. J.; Que, L., Jr., Dioxygen activation by nonheme diiron enzymes: Diverse dioxygen adducts, high-valent intermediates, and related model complexes. *Chem. Rev.* **2018,** *118* (5), 2554-2592.
82. Beauvais, L. G.; Lippard, S. J., Reactions of the peroxo intermediate of soluble methane monooxygenase hydroxylase with ethers. *Journal of the American Chemical Society* **2005,** *127* (20), 7370-7378.
83. Tinberg, C. E.; Lippard, S. J., Oxidation reactions performed by soluble methane monooxygenase hydroxylase intermediates H_{peroxo} and Q proceed by distinct mechanisms. *Biochemistry* **2010,** *49* (36), 7902-7912.
84. Do, L. H.; Hayashi, T.; Moenne-Loccoz, P.; Lippard, S. J., Carboxylate as the protonation site in (peroxo)diiron(III) model complexes of soluble methane monooxygenase and related diiron proteins. *J. Am. Chem. Soc.* **2010,** *132* (4), 1273-1275.
85. Banerjee, R.; Proshlyakov, Y.; Lipscomb, J. D.; Proshlyakov, D. A., Structure of the key species in the enzymatic oxidation of methane to methanol. *Nature* **2015,** *518* (7539), 431-434.
86. Lee, S. K.; Fox, B. G.; Froland, W. A.; Lipscomb, J. D.; Münck, E., A transient intermediate of the methane monooxygenase catalytic cycle containing a $Fe^{IV}Fe^{IV}$ cluster. *J. Am. Chem. Soc.* **1993,** *115*, 6450-6451.
87. Valentine, A. M.; Tavares, P.; Pereira, A. S.; Davydov, R.; Krebs, C.; Hoffman, B. M.; Edmondson, D. E.; Huynh, B. H.; Lippard, S. J., Generation of a mixed-valent Fe(III)Fe(IV) form of intermediate Q in the reaction cycle of soluble methane monooxygenase, an analog of intermediate X in ribonucleotide reductase R2 assembly. *Journal of the American Chemical Society* **1998,** *120* (9), 2190-2191.
88. Wilkinson, E. C.; Dong, Y. H.; Zang, Y.; Fujii, H.; Fraczkiewicz, R.; Fraczkiewicz, G.; Czernuszewicz, R. S.; Que, L., Jr., Raman signature of the Fe_2O_2 "diamond" core. *J. Am. Chem. Soc.* **1998,** *120* (5), 955-962.
89. Nesheim, J. C.; Lipscomb, J. D., Large isotope effects in methane oxidation catalyzed by methane monooxygenase: Evidence for C−H bond cleavage in a reaction cycle intermediate. *Biochemistry* **1996,** *35* (31), 10240-10247.
90. Shu, L.; Nesheim, J. C.; Kauffmann, K.; Münck, E.; Lipscomb, J. D.; Que, L., Jr., An $Fe^{IV}{}_2O_2$ diamond core structure for the key intermediate Q of methane monooxygenase. *Science* **1997,** *275* (5299), 515-518.

91. Rohde, J.-U.; In, J.-H.; Lim, M.-H.; Brennessel, W. W.; Bukowski, M. R.; Stubna, A.; Münck, E.; Nam, W.; Que, L., Jr., Crystallographic and spectroscopic characterization of a nonheme Fe(IV)=O complex. *Science* **2003,** *299* (5609), 1037-9.
92. Castillo, R. G.; Banerjee, R.; Allpress, C. J.; Rohde, G. T.; Bill, E.; Que, L., Jr.; Lipscomb, J. D.; DeBeer, S., High-energy-resolution fluorescence-detected X-ray absorption of the Q intermediate of soluble methane monooxygenase. *J Am Chem Soc* **2017,** *139*, 18024-18033.
93. Xue, G.; De Hont, R.; Münck, E.; Que, L., Jr., Million-fold activation of the $[Fe_2(\mu\text{-}O)_2]$ diamond core for C-H bond cleavage. *Nature Chemistry* **2010,** *2* (5), 400-405.
94. Siegbahn, P. E. M.; Crabtree, R. H., Mechanism of C-H activation by diiron methane monooxygenases: Quantum chemical studies. *Journal of the American Chemical Society* **1997,** *119* (13), 3103-3113.
95. Siegbahn, P. E. M., O−O bond cleavage and alkane hydroxylation in methane monooxygenase. *J. Biol. Inorg. Chem.* **2001,** *6* (1), 27-45.
96. Mai, B. K.; Kim, Y., Theoretical studies for large tunneling and the hydrogen-transfer mechanism in the C-H activation of CH_3CN by the di(μ-oxo)diiron(IV) complex: A model for intermediate Q in soluble methane monooxygenase. *Chemistry--A European Journal* **2013,** *19* (11), 3568-3572.
97. Basch, H.; Musaev, D. G.; Mogi, K.; Morokima, K., Theoretical studies on the mechanism of the methane -> methanol conversion reaction catalyzed by methane monooxygenase (MMO): The O-side vs N-side mechanisms. *Journal of Physical Chemistry A* **2001,** *105*, 3615-3622.
98. Gherman, B. F.; Dunietz, B. D.; Whittington, D. A.; Lippard, S. J.; Friesner, R. A., Activation of the C-H bond of methane by intermediate Q of methane monooxygenase: A theoretical study. *J. Am. Chem. Soc.* **2001,** *123* (16), 3836-3837.
99. Musaev, D. G.; Basch, H.; Morokuma, K., Theoretical study of the mechanism of alkane hydroxylation and ethylene epoxidation reactions catalyzed by diiron bis-oxo complexes. The effect of substrate molecules. *Journal of the American Chemical Society* **2002,** *124* (15), 4135-4148.
100. Yoshizawa, K., Two-step concerted mechanism for methane hydroxylation on the diiron active site of soluble methane monooxygenase. *Journal of Inorganic Biochemistry* **2000,** *78* (1), 23-34.
101. Yoshizawa, K., Nonradical mechanism for methane hydroxylation by iron-oxo complexes. *Acc. Chem. Res.* **2006,** *39* (6), 375-82.
102. Newcomb, M.; Tadic-Biadatti, M.-H. L.; Chestney, D. L.; Roberts, E. S.; Hollenberg, P. F., A nonsynchronous concerted mechanism for cytochrome P-450 catalyzed hydroxylation. *J. Am. Chem. Soc.* **1995,** *117*, 12085-12091.
103. Shestakov, A. F.; Shilov, A. E., Five-coordinate carbon hydroxylation mechanism. *J. Mol. Catal. A:* **1996,** *105*, 1-7.
104. Gherman, B. F.; Lippard, S. J.; Friesner, R. A., Substrate hydroxylation in methane monooxygenase: quantitative modeling via mixed quantum mechanics/molecular mechanics techniques. *Journal of the American Chemical Society* **2005,** *127* (3), 1025-1037.
105. Fox, B. G.; Borneman, J. G.; Wackett, L. P.; Lipscomb, J. D., Haloalkene oxidation by the soluble methane monooxygenase from *Methylosinus trichosporium* OB3b: mechanistic and environmental implications. *Biochemistry* **1990,** *29* (27), 6419-6427.
106. Groves, J. T., Key elements of the chemistry of cytochrome P-450. The oxygen rebound mechanism. *Journal of Chemical Education* **1985,** *62* (11), 928-31.
107. Groves, J. T., High-valent iron in chemical and biological oxidations. *Journal of Inorganic Biochemistry* **2006,** *100* (4), 434-447.
108. Valentine, A. M.; Wilkinson, B.; Liu, K. E.; Komarpanicucci, S.; Priestley, N. D.; Williams, P. G.; Morimoto, H.; Floss, H. G.; Lippard, S. J., Tritiated chiral alkanes as substrates for soluble methane monooxygenase from *Methylococcus capsulatus* (Bath) - probes for the mechanism of hydroxylation. *J. Am. Chem. Soc.* **1997,** *119* (8), 1818-1827.

109. Baik, M.-H.; Gherman, B. F.; Friesner, R. A.; Lippard, S. J., Hydroxylation of methane by non-heme diiron enzymes: Molecular orbital analysis of C-H bond activation by reactive intermediate Q. *Journal of the American Chemical Society* **2002,** *124* (49), 14608-14615.
110. Guallar, V.; Gherman, B. F.; Miller, W. H.; Lippard, S. J.; Friesner, R. A., Dynamics of alkane hydroxylation at the non-heme diiron center in methane monooxygenase. *Journal of the American Chemical Society* **2002,** *124* (13), 3377-3384.
111. Choi, S.-Y.; Eaton, P. E.; Kopp, D. A.; Lippard, S. J.; Newcomb, M.; Shen, R., Cationic species can be produced in soluble methane monooxygenase-catalyzed hydroxylation reactions; radical intermediates are not formed. *Journal of the American Chemical Society* **1999,** *121* (51), 12198-12199.
112. Jin, Y.; Lipscomb, J. D., Probing the mechanism of C-H activation: Oxidation of methylcubane by soluble methane monooxygenase from *Methylosinus trichosporium* OB3b. *Biochemistry* **1999,** *38* (19), 6178-6186.
113. Valentine, A. M.; LeTadic-Biadatti, M.-H.; Toy, P. H.; Newcomb, M.; Lippard, S. J., Oxidation of ultrafast radical clock substrate probes by the soluble methane monooxygenase from *Methylococcus capsulatus* (Bath). *Journal of Biological Chemistry* **1999,** *274* (16), 10771-10776.
114. Froland, W. A.; Andersson, K. K.; Lee, S.-K.; Liu, Y.; Lipscomb, J. D., Methane monooxygenase component B and reductase alter the regioselectivity of the hydroxylase component-catalyzed reactions. A novel role for protein-protein interactions in an oxygenase mechanism. *J. Biol. Chem.* **1992,** *267* (25), 17588-17597.
115. Valentine, A. M.; Stahl, S. S.; Lippard, S. J., Mechanistic studies of the reaction of reduced methane monooxygenase hydroxylase with dioxygen and substrates. *J. Am. Chem. Soc.* **1999,** *121* (16), 3876-3887.
116. Klinman, J. P., The role of tunneling in enzyme catalysis of C-H activation. *Biochim. Biophys. Acta, Bioenerg.* **2006,** *1757* (8), 981-987.
117. Carr, C. A. M.; Klinman, J. P., Hydrogen tunneling in a prokaryotic lipoxygenase. *Biochemistry* **2014,** *53* (14), 2212-2214.
118. Siebrand, W.; Smedarchina, Z., Mechanism of CH-bond cleavage catalyzed by enzymes. In *Isotope Effects in Chemistry and Biology*, Kohen, A.; Limbach, H.-H., Eds. Taylor & Francis: Boca Raton, FL, 2006; pp 725-741.
119. Arciero, D. M.; Lipscomb, J. D., Binding of ^{17}O-labeled substrate and inhibitors to protocatechuate 4,5-dioxygenase-nitrosyl complex. Evidence for direct substrate binding to the active site Fe^{2+} of extradiol dioxygenases. *Journal of Biological Chemistry* **1986,** *261* (5), 2170-2178.
120. Wolfe, M. D.; Parales, J. V.; Gibson, D. T.; Lipscomb, J. D., Single turnover chemistry and regulation of O_2 activation by the oxygenase component of naphthalene 1,2-dioxygenase. *J. Biol. Chem.* **2001,** *276* (3), 1945-1953.
121. Lipscomb, J. D.; Sligar, S. G.; Namtvedt, M. J.; Gunsalus, I. C., Autooxidation and hydroxylation reactions of oxygenated cytochrome $P450_{cam}$. *J. Biol. Chem.* **1976,** *251*, 1116-1124.
122. Poulos, T. L., Heme enzyme structure and function. *Chem. Rev.* **2014,** *114*, 3919-3962.
123. Pau, M. Y. M.; Lipscomb, J. D.; Solomon, E. I., Substrate activation for O_2 reactions by oxidized metal centers in biology. *Proc. Natl. Acad. Sci. U.S.A.* **2007,** *104* (47), 18355-18362.
124. Rivard, B. S.; Rogers, M. S.; Marell, D. J.; Neibergall, M. B.; Chakrabarty, S.; Cramer, C. J.; Lipscomb, J. D., Rate-determining attack on substrate precedes Rieske cluster oxidation during *cis*-dihydroxylation by benzoate dioxygenase. *Biochemistry* **2015,** *54* (30), 4652-4664.
125. Komor, A. J.; Rivard, B. S.; Fan, R.; Guo, Y.; Que, L., Jr.; Lipscomb, J. D., CmlI N-oxygenase catalyzes the final three steps in chloramphenicol biosynthesis without dissociation of intermediates. *Biochemistry* **2017,** *56* (37), 4940-4950.
126. Sutherlin, K. D.; Rivard, B. S.; Bottger, L. H.; Liu, L. V.; Rogers, M. S.; Srnec, M.; Park, K.; Yoda, Y.; Kitao, S.; Kobayashi, Y.; Saito, M.; Seto, M.; Hu, M.; Zhao, J.; Lipscomb,

J. D.; Solomon, E. I., NRVS studies of the peroxide shunt intermediate in a Rieske dioxygenase and its relation to the native Fe(II) O_2 reaction. *J Am Chem Soc* **2018,** *140* (16), 5544-5559.
127. Mitić, N.; Schwartz, J. K.; Brazeau, B. J.; Lipscomb, J. D.; Solomon, E. I., CD and MCD studies of the effects of component B variant binding on the biferrous active site of methane monooxygenase. *Biochemistry* **2008,** *47*, 8386-8397.
128. Rinaldo, D.; Philipp, D. M.; Lippard, S. J.; Friesner, R. A., Intermediates in dioxygen activation by methane monooxygenase: A QM/MM study. *J. Am. Chem. Soc.* **2007,** *129* (11), 3135-3147.
129. Brazeau, B. J.; Wallar, B. J.; Lipscomb, J. D., Effector proteins from $P450_{cam}$ and methane monooxygenase: lessons in tuning nature's powerful reagents. *Biochemical and Biophysical Research Communications* **2003,** *312* (1), 143-148.
130. Kopp, D. A.; Berg, E. A.; Costello, C. E.; Lippard, S. J., Structural features of covalently cross-linked hydroxylase and reductase proteins of soluble methane monooxygenase as revealed by mass spectrometric analysis. *Journal of Biological Chemistry* **2003,** *278* (23), 20939-20945.
131. Zhang, J.; Wallar, B. J.; Popescu, C. V.; Renner, D. B.; Thomas, D. D.; Lipscomb, J. D., Methane monooxygenase hydroxylase and B component interactions. *Biochemistry* **2006,** *45* (9), 2913-2926.
132. MacArthur, R.; Sazinsky, M. H.; Kuehne, H.; Whittington, D. A.; Lippard, S. J.; Brudvig, G. W., Component B binding to the soluble methane monooxygenase hydroxylase by saturation-recovery EPR spectroscopy of spin-labeled MMOB. *Journal of the American Chemical Society* **2002,** *124* (45), 13392-13393.
133. Wang, W.; Liang, A. D.; Lippard, S. J., Coupling oxygen consumption with hydrocarbon oxidation in bacterial multicomponent monooxygenases. *Acc. Chem. Res.* **2015,** *48* (9), 2632-2639.
134. Song, W. J.; Gucinski, G.; Sazinsky, M. H.; Lippard, S. J., Tracking a defined route for O_2 migration in a dioxygen-activating diiron enzyme. *Proceedings of the National Academy of Sciences of the United States of America* **2011,** *108* (36), 14795-14800.
135. Smith, T. J.; Slade, S. E.; Burton, N. P.; Murrell, J. C.; Dalton, H., Improved system for protein engineering of the hydroxylase component of soluble methane monooxygenase. *Applied and Environmental Microbiology* **2002,** *68* (11), 5265-5273.
136. Puri, A. W.; Owen, S.; Chu, F.; Chavkin, T.; Beck, D. A. C.; Kalyuzhnaya, M. G.; Lidstrom, M. E., Genetic tools for the industrially promising methanotroph *Methylomicrobium buryatense*. *Appl. Environ. Microbiol.* **2015,** *81* (5), 1775-1781/1-1775-1781/7, 7 pp.
137. Yan, X.; Chu, F.; Puri, A. W.; Fu, Y.; Lidstrom, M. E., Electroporation-based genetic manipulation in type I methanotrophs. *Appl. Environ. Microbiol.* **2016,** *82* (7), 2062-2069.
138. Nagel, Z. D.; Klinman, J. P., Tunneling and dynamics in enzymatic hydride transfer. *Chem. Rev. (Washington, DC, U. S.)* **2006,** *106* (8), 3095-3118.
139. Brandstetter, H.; Whittington, D. A.; Lippard, S. J.; Frederick, C. A., Mutational and structural analyses of the regulatory protein B of soluble methane monooxygenase from *Methylococcus capsulatus* (Bath). *Chem. Biol.* **1999,** *6* (7), 441-449.
140. Zhang, J.; Lipscomb, J. D., Role of the C-terminal region of the B component of *Methylosinus trichosporium* OB3b methane monooxygenase in the regulation of oxygen activation. *Biochemistry* **2006,** *45*, 1459-1469.
141. Liu, Y.; Nesheim, J. C.; Paulsen, K. E.; Stankovich, M. T.; Lipscomb, J. D., Roles of the methane monooxygenase reductase component in the regulation of catalysis. *Biochemistry* **1997,** *36* (17), 5223-5233.
142. Gassner, G. T.; Lippard, S. J., Component interactions in the soluble methane monooxygenase system from *Methylococcus capsulatus* (Bath). *Biochemistry* **1999,** *38* (39), 12768-12785.
143. Paulsen, K. E.; Liu, Y.; Fox, B. G.; Lipscomb, J. D.; Münck, E.; Stankovich, M. T., Oxidation-reduction potentials of the methane monooxygenase hydroxylase component from *Methylosinus trichosporium* OB3b. *Biochemistry* **1994,** *33* (3), 713-722.

144. Wang, W.; Lippard, S. J., Diiron oxidation state control of substrate access to the active site of soluble methane monooxygenase mediated by the regulatory component. *Journal of the American Chemical Society* **2014,** *136* (6), 2244-2247.
145. Liu, K. E.; Lippard, S. J., Redox properties of the hydroxylase component of methane monooxygenase from *Methylococcus capsulatus* (Bath). Effects of protein B, reductase, and substrate [published erratum appears in J Biol Chem 1991 266:24859]. *J. Biol. Chem.* **1991,** *266* (20), 12836-12839.
146. Blazyk, J., L.; Gassner, G., T.; Lippard, S., J., Intermolecular electron-transfer reactions in soluble methane monooxygenase: a role for hysteresis in protein function. *Journal of the American Chemical Society* **2005,** *127* (49), 17364-76.
147. Morton, J. D.; Hayes, K. F.; Semrau, J. D., Effect of copper speciation on whole-cell soluble methane monooxygenase activity in *Methylosinus trichosporium* OB3b. *Appl. Environ. Microbiol.* **2000,** *66* (4), 1730-1733.
148. De Visscher, A.; Boeckx, P.; Van Cleemput, O., Artificial methane sinks. In *Greenhouse Gas Sinks*, Reay, D. S.; Hewitt, C. N.; Smith, K. A.; Grace, J., Eds. CAB International: Wallingford, Oxfordshire, UK, 2007; pp 184-200.
149. Ravi, M.; Ranocchiari, M.; van Bokhoven, J. A., The direct catalytic oxidation of methane to methanol—A critical assessment. *Angewandte Chemie International Edition* **2017,** *56* (52), 16464-16483.
150. Shu, L. J.; Liu, Y.; Lipscomb, J. D.; Que, L., Jr., X-ray absorption spectroscopic studies of the methane monooxygenase hydroxylase component from *Methylosinus trichosporium* OB3b. *J. Biol. Inorg. Chem.* **1996,** *1* (4), 297-304.
151. Fox, B. G.; Surerus, K. K.; Münck, E.; Lipscomb, J. D., Evidence for a m-oxo-bridged binuclear iron cluster in the hydroxylase component of methane monooxygenase. Mössbauer and EPR studies. *J. Biol. Chem.* **1988,** *263* (22), 10553-10556.
152. Yano, J.; Kern, J.; Irrgang, K.-D.; Latimer, M. J.; Bergmann, U.; Glatzel, P.; Pushkar, Y.; Biesiadka, J.; Loll, B.; Sauer, K.; Messinger, J.; Zouni, A.; Yachandra, V. K., X-ray damage to the Mn_4Ca complex in single crystals of photosystem II: A case study for metalloprotein crystallography. *Proc. Natl. Acad. Sci. U. S. A.* **2005,** *102* (34), 12047-12052.
153. Meharenna, Y. T.; Doukov, T.; Li, H.; Soltis, S. M.; Poulos, T. L., Crystallographic and single-crystal spectral analysis of the peroxidase ferryl intermediate. *Biochemistry* **2010,** *49* (14), 2984-2986.
154. Ebrahim, A.; Moreno-Chicano, T.; Appleby, M. V.; Chaplin, A. K.; Beale, J. H.; Sherrell, D. A.; Duyvesteyn, H. M. E.; Owada, S.; Tono, K.; Sugimoto, H.; Strange, R. W.; Worrall, J. A. R.; Axford, D.; Owen, R. L.; Hough, M. A., Dose-resolved serial synchrotron and XFEL structures of radiation-sensitive metalloproteins. *IUCrJ* **2019,** *6* (4), 543-551.
155. De la Mora, E.; Coquelle, N.; Bury, C. S.; Rosenthal, M.; Holton, J. M.; Carmichael, I.; Garman, E. F.; Burghammer, M.; Colletier, J.-P.; Weik, M., Radiation damage and dose limits in serial synchrotron crystallography at cryo- and room temperatures. *Proceedings of the National Academy of Sciences* **2020,** *117* (8), 4142-4151.
156. Dickerson, J. L.; McCubbin, P. T. N.; Garman, E. F., RADDOSE-XFEL: femtosecond time-resolved dose estimates for macromolecular X-ray free-electron laser experiments. *Journal of Applied Crystallography* **2020,** *53* (2), 549-560.
157. Bury, C. S.; Brooks-Bartlett, J. C.; Walsh, S. P.; Garman, E. F., Estimate your dose: RADDOSE-3D. *Protein Science* **2018,** *27* (1), 217-228.
158. Inoue, I.; Inubushi, Y.; Sato, T.; Tono, K.; Katayama, T.; Kameshima, T.; Ogawa, K.; Togashi, T.; Owada, S.; Amemiya, Y.; Tanaka, T.; Hara, T.; Yabashi, M., Observation of femtosecond X-ray interactions with matter using an X-ray–X-ray pump–probe scheme. *Proceedings of the National Academy of Sciences* **2016,** *113* (6), 1492-1497.
159. Gruner, S. M., Expanding the femtosecond crystallography toolkit. *Proceedings of the National Academy of Sciences* **2014,** *111* (48), 16986-16987.

160. McNeil, B. W. J.; Thompson, N. R., X-ray free-electron lasers. *Nat. Photonics* **2010,** *4*, 814-821.
161. Kern, J.; Alonso-Mori, R.; Tran, R.; Hattne, J.; Gildea, R. J.; Echols, N.; Gloeckner, C.; Hellmich, J.; Laksmono, H.; Sierra, R. G.; Lassalle-Kaiser, B.; Koroidov, S.; Lampe, A.; Han, G.; Gul, S.; DiFiore, D.; Milathianaki, D.; Fry, A. R.; Miahnahri, A.; Schafer, D. W.; Messerschmidt, M.; Seibert, M. M.; Koglin, J. E.; Sokaras, D.; Weng, T.-C.; Sellberg, J.; Latimer, M. J.; Grosse-Kunstleve, R. W.; Zwart, P. H.; White, W. E.; Glatzel, P.; Adams, P. D.; Bogan, M. J.; Williams, G. J.; Boutet, S.; Messinger, J.; Zouni, A.; Sauter, N. K.; Yachandra, V. K.; Bergmann, U.; Yano, J., Simultaneous femtosecond x-ray spectroscopy and diffraction of photosystem II at room temperature. *Science* **2013,** *340* (6131), 491-495.
162. Chapman, H. N., X-Ray free-electron lasers for the structure and dynamics of macromolecules. *Annual Review of Biochemistry* **2019,** *88* (1), 35-58.
163. Schlichting, I., Serial femtosecond crystallography: the first five years. *IUCrJ* **2015,** *2* (2), 246-255.
164. Fromme, P., XFELs open a new era in structural chemical biology. *Nat. Chem. Biol.* **2015,** *11* (12), 895-899.
165. Spence, J., XFELs for structure and dynamics in biology. *IUCrJ* **2017,** *4* (4), 322-339.
166. Kern, J.; Chatterjee, R.; Young, I. D.; Fuller, F. D.; Lassalle, L.; Ibrahim, M.; Gul, S.; Fransson, T.; Brewster, A. S.; Alonso-Mori, R.; Hussein, R.; Zhang, M.; Douthit, L.; de Lichtenberg, C.; Cheah, M. H.; Shevela, D.; Wersig, J.; Seuffert, I.; Sokaras, D.; Pastor, E.; Weninger, C.; Kroll, T.; Sierra, R. G.; Aller, P.; Butryn, A.; Orville, A. M.; Liang, M.; Batyuk, A.; Koglin, J. E.; Carbajo, S.; Boutet, S.; Moriarty, N. W.; Holton, J. M.; Dobbek, H.; Adams, P. D.; Bergmann, U.; Sauter, N. K.; Zouni, A.; Messinger, J.; Yano, J.; Yachandra, V. K., Structures of the intermediates of Kok's photosynthetic water oxidation clock. *Nature* **2018,** *563* (7731), 421-425.
167. Suga, M.; Shimada, A.; Akita, F.; Shen, J.-R.; Tosha, T.; Sugimoto, H., Time-resolved studies of metalloproteins using X-ray free electron laser radiation at SACLA. *Biochim. Biophys. Acta* **2020,** *1864* (2), 129466.
168. Stagno, J. R.; Liu, Y.; Bhandari, Y. R.; Conrad, C. E.; Panja, S.; Swain, M.; Fan, L.; Nelson, G.; Li, C.; Wendel, D. R.; White, T. A.; Coe, J. D.; Wiedorn, M. O.; Knoska, J.; Oberthuer, D.; Tuckey, R. A.; Yu, P.; Dyba, M.; Tarasov, S. G.; Weierstall, U.; Grant, T. D.; Schwieters, C. D.; Zhang, J.; Ferré-D'Amaré, A. R.; Fromme, P.; Draper, D. E.; Liang, M.; Hunter, M. S.; Boutet, S.; Tan, K.; Zuo, X.; Ji, X.; Barty, A.; Zatsepin, N. A.; Chapman, H. N.; Spence, J. C. H.; Woodson, S. A.; Wang, Y. X., Structures of riboswitch RNA reaction states by mix-and-inject XFEL serial crystallography. *Nature* **2017,** *541* (7636), 242-246.
169. Tenboer, J.; Basu, S.; Zatsepin, N.; Pande, K.; Milathianaki, D.; Frank, M.; Hunter, M.; Boutet, S.; Williams, G. J.; Koglin, J. E.; Oberthuer, D.; Heymann, M.; Kupitz, C.; Conrad, C.; Coe, J.; Roy-Chowdhury, S.; Weierstall, U.; James, D.; Wang, D.; Grant, T.; Barty, A.; Yefanov, O.; Scales, J.; Gati, C.; Seuring, C.; Srajer, V.; Henning, R.; Schwander, P.; Fromme, R.; Ourmazd, A.; Moffat, K.; Van Thor, J. J.; Spence, J. C. H.; Fromme, P.; Chapman, H. N.; Schmidt, M., Time-resolved serial crystallography captures high-resolution intermediates of photoactive yellow protein. *Science* **2014,** *346*, 1242-1246.
170. Tosha, T.; Nomura, T.; Nishida, T.; Saeki, N.; Okubayashi, K.; Yamagiwa, R.; Sugahara, M.; Nakane, T.; Yamashita, K.; Hirata, K.; Ueno, G.; Kimura, T.; Hisano, T.; Muramoto, K.; Sawai, H.; Takeda, H.; Mizohata, E.; Yamashita, A.; Kanematsu, Y.; Takano, Y.; Nango, E.; Tanaka, R.; Nureki, O.; Shoji, O.; Ikemoto, Y.; Murakami, H.; Owada, S.; Tono, K.; Yabashi, M.; Yamamoto, M.; Ago, H.; Iwata, S.; Sugimoto, H.; Shiro, Y.; Kubo, M., Capturing an initial intermediate during the P450nor enzymatic reaction using time-resolved XFEL crystallography and caged-substrate. *Nature Communications* **2017,** *8* (1), 1585.
171. Fukuda, Y.; Tse, K. M.; Nakane, T.; Nakatsu, T.; Suzuki, M.; Sugahara, M.; Inoue, S.; Masuda, T.; Yumoto, F.; Matsugaki, N.; Nango, E.; Tono, K.; Joti, Y.; Kameshima, T.; Song,

C.; Hatsui, T.; Yabashi, M.; Nureki, O.; Murphy, M. E. P.; Inoue, T.; Iwata, S.; Mizohata, E., Redox-coupled proton transfer mechanism in nitrite reductase revealed by femtosecond crystallography. *Proceedings of the National Academy of Sciences* **2016,** *113* (11), 2928-2933.
172. Fuller, F. D.; Gul, S.; Chatterjee, R.; Burgie, E. S.; Young, I. D.; Lebrette, H.; Srinivas, V.; Brewster, A. S.; Michels-Clark, T.; Clinger, J. A.; Andi, B.; Ibrahim, M.; Pastor, E.; de Lichtenberg, C.; Hussein, R.; Pollock, C. J.; Zhang, M.; Stan, C. A.; Kroll, T.; Fransson, T.; Weninger, C.; Kubin, M.; Aller, P.; Lassalle, L.; Bräuer, P.; Miller, M. D.; Amin, M.; Koroidov, S.; Roessler, C. G.; Allaire, M.; Sierra, R. G.; Docker, P. T.; Glownia, J. M.; Nelson, S.; Koglin, J. E.; Zhu, D.; Chollet, M.; Song, S.; Lemke, H.; Liang, M.; Sokaras, D.; Alonso-Mori, R.; Zouni, A.; Messinger, J.; Bergmann, U.; Boal, A. K.; Bollinger Jr, J. M.; Krebs, C.; Högbom, M.; Phillips Jr, G. N.; Vierstra, R. D.; Sauter, N. K.; Orville, A. M.; Kern, J.; Yachandra, V. K.; Yano, J., Drop-on-demand sample delivery for studying biocatalysts in action at X-ray free-electron lasers. *Nat. Methods* **2017,** *14*, 443-449.
173. Ibrahim, M.; Fransson, T.; Chatterjee, R.; Cheah, M. H.; Hussein, R.; Lassalle, L.; Sutherlin, K. D.; Young, I. D.; Fuller, F. D.; Gul, S.; Kim, I.-S.; Simon, P. S.; deLichtenberg, C.; Chernev, P.; Bogacz, I.; Pham, C. C.; Orville, A. M.; Saichek, N.; Northen, T.; Batyuk, A.; Carbajo, S.; Alonso-Mori, R.; Tono, K.; Owada, S.; Bhowmick, A.; Bolotovsky, R.; Mendez, D.; Moriarty, N. W.; Holton, J. M.; Dobbek, H.; Brewster, A. S.; Adams, P. D.; Sauter, N. K.; Bergmann, U.; Zoun, A.; Messinger, J.; Kern, J.; Yachandra, V. K.; Yano, J., Untangling the sequence of events during the S2 → S3 transition in photosystem II and implications for the water oxidation mechanism. *Proceedings of the National Academy of Sciences (U.S.A.)* **2020,** *117*, 12624-12635.
174. Fox, B. G.; Froland, W. A.; Jollie, D. R.; Lipscomb, J. D., Methane monooxygenase from *Methylosinus trichosporium* OB3b. *Methods Enzymol.* **1990,** *188*, 191-202.
175. Sugahara, M.; Mizohata, E.; Nango, E.; Suzuki, M.; Tanaka, T.; Masuda, T.; Tanaka, R.; Shimamura, T.; Tanaka, Y.; Suno, C.; Ihara, K.; Pan, D.; Kakinouchi, K.; Sugiyama, S.; Murata, M.; Inoue, T.; Tono, K.; Song, C.; Park, J.; Kameshima, T.; Hatsui, T.; Joti, Y.; Yabashi, M.; Iwata, S., Grease matrix as a versatile carrier of proteins for serial crystallography. *Nat. Methods* **2015,** *12* (1), 61-63.
176. Tono, K.; Togashi, T.; Inubushi, Y.; Sato, T.; Katayama, T.; Ogawa, K.; Ohashi, H.; Kimura, H.; Takahashi, S.; Takeshita, K.; Tomizawa, H.; Goto, S.; Ishikawa, T.; Yabashi, M., Beamline, experimental stations and photon beam diagnostics for the hard x-ray free electron laser of SACLA. *New J. Phys.* **2013,** *15* (8), 083035.
177. Sierra, R. G.; Batyuk, A.; Sun, Z.; Aquila, A.; Hunter, M. S.; Lane, T. J.; Liang, M.; Yoon, C. H.; Alonso-Mori, R.; Armenta, R.; Castagna, J.-C.; Hollenbeck, M.; Osier, T. O.; Hayes, M.; Aldrich, J.; Curtis, R.; Koglin, J. E.; Rendahl, T.; Rodriguez, E.; Carbajo, S.; Guillet, S.; Paul, R.; Hart, P.; Nakahara, K.; Carini, G.; DeMirci, H.; Dao, E. H.; Hayes, B. M.; Rao, Y. P.; Chollet, M.; Feng, Y.; Fuller, F. D.; Kupitz, C.; Sato, T.; Seaberg, M. H.; Song, S.; van Driel, T. B.; Yavas, H.; Zhu, D.; Cohen, A. E.; Wakatsuki, S.; Boutet, S., The macromolecular femtosecond crystallography instrument at the linac coherent light source. *J. Synchrotron Rad.* **2019,** *26* (2), 346-357.
178. Ko, I.; Kang, H.-S.; Heo, H.; Kim, C.; Kim, G.; Min, C.-K.; Yang, H.; Baek, S.; Choi, H.-J.; Mun, G.; Park, B.; Suh, Y.; Shin, D.; Hu, J.; Hong, J.; Jung, S.; Kim, S.-H.; Kim, K.; Na, D.; Lee, K., Construction and commissioning of PAL-XFEL facility. *Appl. Sci.* **2017,** *7*, 479.
179. Alonso-Mori, R.; Kern, J.; Sokaras, D.; Weng, T.-C.; Nordlund, D.; Tran, R.; Montanez, P.; Delor, J.; Yachandra, V. K.; Yano, J.; Bergmann, U., A multi-crystal wavelength dispersive x-ray spectrometer. *Review of Scientific Instruments* **2012,** *83*, 073114-073122.
180. Hattne, J.; Echols, N.; Tran, R.; Kern, J.; Gildea, R. J.; Brewster, A. S.; Alonso-Mori, R.; Glöckner, C.; Hellmich, J.; Laksmono, H.; Sierra, R. G.; Lassalle-Kaiser, B.; Lampe, A.; Han, G.; Gul, S.; DiFiore, D.; Milathianaki, D.; Fry, A. R.; Miahnahri, A.; White, W. E.; Schafer, D. W.; Seibert, M. M.; Koglin, J. E.; Sokaras, D.; Weng, T.-C.; Sellberg, J.; Latimer,

M. J.; Glatzel, P.; Zwart, P. H.; Grosse-Kunstleve, R. W.; Bogan, M. J.; Messerschmidt, M.; Williams, G. J.; Boutet, S.; Messinger, J.; Zouni, A.; Yano, J.; Bergmann, U.; Yachandra, V. K.; Adams, P. D.; Sauter, N. K., Accurate macromolecular structures using minimal measurements from X-ray free-electron lasers. *Nat. Methods* **2014,** *11* (5), 545-548.
181. Winter, G.; Waterman, D. G.; Parkhurst, J. M.; Brewster, A. S.; Gildea, R. J.; Gerstel, M.; Fuentes-Montero, L.; Vollmar, M.; Michels-Clark, T.; Young, I. D.; Sauter, N. K.; Evans, G., DIALS: implementation and evaluation of a new integration package. *Acta crystallographica. Section D, Structural biology* **2018,** *74* (Pt 2), 85-97.
182. McCoy, A. J.; Grosse-Kunstleve, R. W.; Adams, P. D.; Winn, M. D.; Storoni, L. C.; Read, R. J., Phaser crystallographic software. *Journal of Applied Crystallography* **2007,** *40* (4), 658-674.
183. Poon, B. K.; Grosse-Kunstleve, R. W.; Zwart, P. H.; Sauter, N. K., Detection and correction of underassigned rotational symmetry prior to structure deposition. *Acta Crystallogr., Sect. D: Biol. Crystallogr.* **2010,** *66* (5), 503-513.
184. Adams, P. D.; Afonine, P. V.; Bunkóczi, G.; Chen, V. B.; Davis, I. W.; Echols, N.; Headd, J. J.; Hung, L.-W.; Kapral, G. J.; Grosse-Kunstleve, R. W.; McCoy, A. J.; Moriarty, N. W.; Oeffner, R.; Read, R. J.; Richardson, D. C.; Richardson, J. S.; Terwilliger, T. C.; Zwart, P. H., PHENIX: a comprehensive Python-based system for macromolecular structure solution. *Acta Crystallogr., Sect. D: Biol. Crystallogr.* **2010,** *D66*, 213-221.
185. Liebschner, D.; Afonine, P. V.; Baker, M. L.; Bunkóczi, G.; Chen, V. B.; Croll, T. I.; Hintze, B.; Hung, L.-W.; Jain, S.; McCoy, A. J.; Moriarty, N. W.; Oeffner, R. D.; Poon, B. K.; Prisant, M. G.; Read, R. J.; Richardson, J. S.; Richardson, D. C.; Sammito, M. D.; Sobolev, O. V.; Stockwell, D. H.; Terwilliger, T. C.; Urzhumtsev, A. G.; Videau, L. L.; Williams, C. J.; Adams, P. D., Macromolecular structure determination using X-rays, neutrons and electrons: recent developments in Phenix. *Acta Crystallogr., Sect. D: Biol. Crystallogr* **2019,** *75*, 861-877.
186. Emsley, P.; Cowtan, K., Coot: Model-building tools for molecular graphics. *Acta Crystallogr., Sect. E: Struct. Rep. Online* **2004,** *E60* (12, Pt. 1), 2126-2132.
187. Sehnal, D.; Svobodová Vařeková, R.; Berka, K.; Pravda, L.; Navrátilová, V.; Banáš, P.; Ionescu, C.-M.; Otyepka, M.; Koča, J., MOLE 2.0: advanced approach for analysis of biomacromolecular channels. *J. Cheminformatics* **2013,** *5* (1), 39.
188. Brewster, A. S.; Waterman, D. G.; Parkhurst, J. M.; Gildea, R. J.; Young, I. D.; O'Riordan, L. J.; Yano, J.; Winter, G.; Evans, G.; Sauter, N. K., Improving signal strength in serial crystallography with DIALS geometry refinement. *Acta Crystallogr., Sect. D: Struct. Biol.* **2018,** *74* (9), 877-894.
189. Brewster, A. S.; Bhowmick, A.; Bolotovsky, R.; Mendez, D.; Zwart, P. H.; Sauter, N. K., SAD phasing of XFEL data depends critically on the error model. *Acta Crystallogr., Sect. D: Struct. Biol.* **2019,** *75* (11), 959-968.
190. Cooley, R. B.; Arp, D. J.; Karplus, P. A., Evolutionary origin of a secondary structure: pi-helices as cryptic but widespread insertional variations of alpha-helices that enhance protein functionality. *J. Mol. Biol.* **2010,** *404* (2), 232-246.
191. Barlow, D. J.; Thornton, J. M., Helix geometry in proteins. *J. Mol. Biol.* **1988,** *201* (3), 601-619.
192. Glatzel, P.; Bergmann, U., High resolution 1s core hole X-ray spectroscopy in 3d transition metal complexes-electronic and structural information. *Coord. Chem. Rev.* **2005,** *249* (1-2), 65-95.
193. Schuth, N.; Zaharieva, I.; Chernev, P.; Berggren, G.; Anderlund, M.; Styring, S.; Dau, H.; Haumann, M., Kα X-ray emission spectroscopy on the photosynthetic oxygen-evolving complex supports manganese oxidation and water binding in the S3 state. *Inorganic Chemistry* **2018,** *57* (16), 10424-10430.
194. Vankó, G.; Neisius, T.; Molnár, G.; Renz, F.; Kárpáti, S.; Shukla, A.; de Groot, F. M. F., Probing the 3d spin momentum with X-ray emission spectroscopy: The case of molecular-spin transitions. *J. Phys. Chem. B* **2006,** *110* (24), 11647-11653.

195. Svyazhin, A.; Kurmaev, E.; Shreder, E.; Shamin, S.; Sahle, C. J., Local moments and electronic correlations in Fe-based Heusler alloys: Kα x-ray emission spectra measurements. *J. Alloys Compd.* **2016,** *679*, 268-276.
196. Baydas, E.; Oz, E., Chemical effects in the Kα and Kβ1,3 of X-ray emission spectra of Fe. *J. Electron Spectrosc. Relat. Phenom.* **2012,** *185* (1-2), 27-31.
197. Yasuda, S.; Kakiyama, H., X-ray K emission spectra of vanadium in various oxidation states. *X-Ray Spectrom.* **1978,** *7* (1), 23-25.
198. Cutsail, G. E.; Banerjee, R.; Zhou, A.; Que, L.; Lipscomb, J. D.; DeBeer, S., High-resolution extended x-ray absorption fine structure analysis provides evidence for a longer Fe···Fe distance in the Q intermediate of methane monooxygenase. *J. Am. Chem. Soc.* **2018,** *140* (48), 16807-16820.
199. Corbett, M. C.; Latimer, M. J.; Poulos, T. L.; Sevrioukova, I. F.; Hodgson, K. O.; Hedman, B., Photoreduction of the active site of the metalloprotein putidaredoxin by synchrotron radiation. *Acta Crystallographica Section D* **2007,** *63* (9), 951-960.
200. Liu, B.; Chen, Y.; Doukov, T.; Soltis, S. M.; Stout, C. D.; Fee, J. A., Combined microspectrophotometric and crystallographic examination of chemically reduced and X-ray radiation-reduced forms of cytochrome ba_3 oxidase from *Thermus thermophilus*: Structure of the reduced form of the enzyme. *Biochemistry* **2009,** *48* (5), 820-826.
201. Hersleth, H.-P.; Uchida, T.; Røhr, Å. K.; Teschner, T.; Schünemann, V.; Kitagawa, T.; Trautwein, A. X.; Görbitz, C. H.; Andersson, K. K., Crystallographic and spectroscopic studies of peroxide-derived myoglobin compound II and occurrence of protonated Fe^{IV}–O. *Journal of Biological Chemistry* **2007,** *282* (32), 23372-23386.
202. Alonso-Mori, R.; Kern, J.; Gildea, R. J.; Sokaras, D.; Weng, T.-C.; Lassalle-Kaiser, B.; Tran, R.; Hattne, J.; Laksmono, H.; Hellmich, J.; Glockner, C.; Echols, N.; Sierra, R. G.; Schafer, D. W.; Sellberg, J.; Kenney, C.; Herbst, R.; Pines, J.; Hart, P.; Herrmann, S.; Grosse-Kunstleve, R. W.; Latimer, M. J.; Fry, A. R.; Messerschmidt, M. M.; Miahnahri, A.; Seibert, M. M.; Zwart, P. H.; White, W. E.; Adams, P. D.; Bogan, M. J.; Boutet, S.; Williams, G. J.; Zouni, A.; Messinger, J.; Glatzel, P.; Sauter, N. K.; Yachandra, V. K.; Yano, J.; Bergmann, U., Energy-dispersive X-ray emission spectroscopy using an X-ray free-electron laser in a shot-by-shot mode. *Proc. Natl. Acad. Sci. U. S. A.* **2012,** *109* (47), 19103-19107.
203. Hayashi, Y.; Yamazaki, I., The oxidation-reduction potentials of compound I/compound II and compound II/ferric couples of horseradish peroxidases A2 and C. *Journal of Biological Chemistry* **1979,** *254* (18), 9101-9106.
204. Chen, M. M.; Coelho, P. S.; Arnold, F. H., Utilizing terminal oxidants to achieve P450-catalyzed oxidation of methane. *Adv. Synth. Catal.* **2012,** *354* (6), 964-968.
205. Berglund, G. I.; Carlsson, G. H.; Smith, A. T.; Szoke, H.; Henriksen, A.; Hajdu, J., The catalytic pathway of horseradish peroxidase at high resolution. *Nature* **2002,** *417* (6887), 463-468.
206. Klinman, J. P., Dynamically achieved active site precision in enzyme catalysis. *Acc. Chem. Res.* **2015,** *48* (2), 449-456.
207. Hosseinzadeh, P.; Lu, Y., Design and fine-tuning redox potentials of metalloproteins involved in electron transfer in bioenergetics. *Biochim. Biophys. Acta* **2016,** *1857* (5), 557-581.
208. Tezcan, F. A.; Winkler, J. R.; Gray, H. B., Effects of ligation and folding on reduction potentials of heme proteins. *J. Am. Chem. Soc.* **1998,** *120* (51), 13383-13388.
209. Moore, G. R.; Pettigrew, G. W.; Rogers, N. K., Factors influencing redox potentials of electron transfer proteins. *Proc. Natl. Acad. Sci. U. S. A.* **1986,** *83* (14), 4998-4999.
210. DiCarlo, C. M.; Vitello, L. B.; Erman, J. E., Effect of active site and surface mutations on the reduction potential of yeast cytochrome c peroxidase and spectroscopic properties of the oxidized and reduced enzyme. *J. Inorg. Biochem.* **2007,** *101* (4), 603-13.
211. Liu, J.; Chakraborty, S.; Hosseinzadeh, P.; Yu, Y.; Tian, S.; Petrik, I.; Bhagi, A.; Lu, Y., Metalloproteins containing cytochrome, iron–sulfur, or copper redox centers. *Chemical Reviews* **2014,** *114* (8), 4366-4469.

212. McCormick, M. S.; Lippard, S. J., Analysis of substrate access to active sites in bacterial multicomponent monooxygenase hydroxylases: X-ray crystal structure of xenon-pressurized phenol hydroxylase from *Pseudomonas sp*. OX1. *Biochemistry* **2011,** *50* (51), 11058-11069.
213. Pikus, J. D.; Studts, J. M.; Achim, C.; Kauffmann, K. E.; Münck, E.; Steffan, R. J.; McClay, K.; Fox, B. G., Recombinant toluene-4-monooxygenase: Catalytic and Mössbauer studies of the purified diiron and Rieske components of a four-protein complex. *Biochemistry* **1996,** *35* (28), 9106-9119.
214. Carter, P.; Wells, J. A., Dissecting the catalytic triad of a serine protease. *Nature* **1988,** *332* (6164), 564-568.
215. Poulos, T. L., The role of the proximal ligand in heme enzymes. *JBIC, J. Biol. Inorg. Chem.* **1996,** *1* (4), 356-359.
216. Krest, C. M.; Silakov, A.; Rittle, J.; Yosca, T. H.; Onderko, E. L.; Calixto, J. C.; Green, M. T., Significantly shorter Fe-S bond in cytochrome P450-I is consistent with greater reactivity relative to chloroperoxidase. *Nat Chem* **2015,** *7* (9), 696-702.
217. Onderko, E. L.; Silakov, A.; Yosca, T. H.; Green, M. T., Characterization of a selenocysteine-ligated P450 compound I reveals direct link between electron donation and reactivity. *Nat Chem* **2017,** *9* (7), 623-628.
218. Davydov, A.; Davydov, R.; Gräslund, A.; Lipscomb, J. D.; Andersson, K. K., Radiolytic reduction of methane monooxygenase dinuclear iron cluster at 77 K - EPR evidence for conformational change upon reduction or binding of component B to the diferric state. *J. Biol. Chem.* **1997,** *272* (11), 7022-7026.
219. Pulver, S.; Froland, W. A.; Fox, B. G.; Lipscomb, J. D.; Solomon, E. I., Spectroscopic studies of the coupled binuclear non-heme iron active site in the fully reduced hydroxylase component of methane monooxygenase: Comparison to deoxy and deoxy-azide hemerythrin. *J. Am. Chem. Soc.* **1993,** *115*, 12409-12422.
220. Pulver, S. C.; Froland, W. A.; Lipscomb, J. D.; Solomon, E. I., Ligand field circular dichroism and magnetic circular dichroism studies of component B and substrate binding to the hydroxylase component of methane monooxygenase. *J. Am. Chem. Soc.* **1997,** *119* (2), 387-395.
221. Ross, M. O.; Rosenzweig, A. C., A tale of two methane monooxygenases. *JBIC, J. Biol. Inorg. Chem.* **2017,** *22* (2-3), 307-319.
222. Singh, B. K.; Bardgett, R. D.; Smith, P.; Reay, D. S., Microorganisms and climate change: Terrestrial feedbacks and mitigation options. *Nat. Rev. Microbiol.* **2010,** *8*, 779-790.
223. Fox, B. G.; Hendrich, M. P.; Surerus, K. K.; Andersson, K. K.; Froland, W. A.; Lipscomb, J. D.; Münck, E., Mössbauer, EPR, and ENDOR studies of the hydroxylase and reductase components of methane monooxygenase from *Methylosinus trichosporium* OB3b. *J. Am. Chem. Soc.* **1993,** *115*, 3688-3701.
224. Leak, D. J.; Dalton, H., Studies on the regioselectivity and stereoselectivity of the soluble methane monooxygenase from *Methylococcus capsulatus* (Bath). *Biocatalysis* **1987,** *1*, 23-36.
225. Green, J.; Dalton, H., Substrate specificity of soluble methane monooxygenase. Mechanistic implications. *J. Biol. Chem.* **1989,** *264* (30), 17698-17703.
226. Liang, A. D.; Wrobel, A. T.; Lippard, S. J., A flexible glutamine regulates the catalytic activity of toluene o-xylene monooxygenase. *Biochemistry* **2014,** *53* (22), 3585-3592.
227. Kabsch, W., XDS. *Acta Crystallogr D Biol Crystallogr.* **2010,** *66*, 125-132.
228. Rogers, M. S.; Lipscomb, J. D., Salicylate 5-hydroxylase: intermediates in aromatic hydroxylation by a Rieske monooxygenase. *Biochemistry* **2019,** *58* (52), 5305-5319.
229. Groce, S. L.; Miller-Rodeberg, M. A.; Lipscomb, J. D., Single-turnover kinetics of homoprotocatechuate 2,3-dioxygenase. *Biochemistry* **2004,** *43* (48), 15141-15153.
230. Whittaker, J. W.; Lipscomb, J. D., Transition state analogs for protocatechuate 3,4-dioxygenase. Spectroscopic and kinetic studies of the binding reactions of ketonized substrate analogs. *Journal of Biological Chemistry* **1984,** *259* (7), 4476-86.
231. Bondi, A., van der Waals volumes and radii. *J. Phys. Chem.* **1964,** *68* (3), 441-51.

232. Batsanov, S. S., Van der Waals radii of elements. *Inorg. Mater.* **2001,** *37* (9), 871-885.
233. Kammeyer, C. W.; Whitman, D. R., Quantum mechanical calculation of molecular radii. I. Hydrides of elements of periodic Groups IV through VII. *J. Chem. Phys.* **1972,** *56* (9), 4419-21.
234. Murphy, K. I. Graham's law explained: The difference between effusion and permeation 2007. https://www.getnitrogen.org/pdf/graham.pdf.
235. Mehio, N.; Dai, S.; Jiang, D.-e., Quantum mechanical basis for kinetic diameters of small gaseous molecules. *J. Phys. Chem. A* **2014,** *118* (6), 1150-1154.
236. Liebgott, P. P.; Leroux, F.; Burlat, B.; Dementin, S.; Baffert, C.; Lautier, T.; Fourmond, V.; Ceccaldi, P.; Cavazza, C.; Meynial-Salles, I.; Soucaille, P.; Fontecilla-Camps, J. C.; Guigliarelli, B.; Bertrand, P.; Rousset, M.; Léger, C., Relating diffusion along the substrate tunnel and oxygen sensitivity in hydrogenase. *Nat Chem Biol* **2010,** *6* (1), 63-70.
237. Tyson, C. A.; Lipscomb, J. D.; Gunsalus, I. C., The role of putidaredoxin and $P450_{cam}$ in methylene hydroxylation. *Journal of Biological Chemistry* **1972,** *247* (18), 5777-84.
238. Berger, R. L.; Antonini, E.; Brunori, M.; Wyman, J.; Rossi-Fanelli, A., Observations on the kinetics of the reaction of hemoglobin with oxygen. *J. Biol. Chem.* **1967,** *242* (20), 4841-3.
239. Bowman, J. P.; Sly, L. I.; Nichols, P. D.; Hayward, A. C., Revised taxonomy of the Methanotrophs: Description of *Methylobacter* gen. nov., emendation of *Methylococcus,* validation of *Methylosinus* and *Methylocystis* species, and a proposal that the family *Methylococcaceae* includes only the group I methanotrophs. *Int. J. Syst. Evol. Microbiol.* **1993,** *43* (4), 735-753.
240. Bernard, A. R.; Jessop, T. C.; Kumar, P.; Dickenson, N. E., Deoxycholate-enhanced *Shigella* virulence is regulated by a rare π-helix in the type three secretion system tip protein IpaD. *Biochemistry* **2017,** *56* (49), 6503-6514.
241. Riek, R. P.; Graham, R. M., The elusive π-helix. *Journal of Structural Biology* **2011,** *173* (1), 153-160.
242. Weaver, T. M., The π-helix translates structure into function. *Protein Science* **2000,** *9* (1), 201-206.
243. Matsuo, H.; Walters, K. J.; Teruya, K.; Tanaka, T.; Gassner, G. T.; Lippard, S. J.; Kyogoku, Y.; Wagner, G., Identification by NMR spectroscopy of residues at contact surfaces in large, slowly exchanging macromolecular complexes. *J. Am. Chem. Soc.* **1999,** *121* (42), 9903-9904.
244. Gorman, J.; Chowdhury, A.; Surtees, J. A.; Shimada, J.; Reichman, D. R.; Alani, E.; Greene, E. C., Dynamic basis for one-dimensional DNA scanning by the mismatch repair complex Msh2-Msh6. *Molecular Cell* **2007,** *28* (3), 359-370.
245. Jones, J. C.; Banerjee, R.; Shi, K.; Aihara, H.; Lipscomb, J. D., Structural studies of the *Methylosinus trichosporium* OB3b soluble methane monooxygenase hydroxylase and regulatory component complex reveal a transient substrate tunnel. *Biochemistry* **2020,** *59* (32), 2946-2961.
246. Mitic, N.; Schwartz, J. K.; Brazeau, B. J.; Lipscomb, J. D.; Solomon, E. I., CD and MCD studies of the effects of component B variant binding on the biferrous active site of methane monooxygenase. *Biochemistry* **2008,** *47* (32), 8386-97.
247. Arntson, K. E.; Pomerantz, W. C. K., Protein-observed fluorine NMR: A bioorthogonal approach for small molecule discovery. *Journal of Medicinal Chemistry* **2016,** *59* (11), 5158-5171.
248. Leone, M.; Rodriguez-Mias, R. A.; Pellecchia, M., Selective incorporation of ^{19}F-labeled Trp side chains for NMR-spectroscopy-based ligand–protein interaction studies. *ChemBioChem* **2003,** *4* (7), 649-650.
249. Mishra, N. K.; Urick, A. K.; Ember, S. W. J.; Schonbrunn, E.; Pomerantz, W. C., Fluorinated aromatic amino acids are sensitive ^{19}F NMR probes for bromodomain-ligand interactions. *ACS Chem. Biol.* **2014,** *9* (12), 2755-2760.
250. Knowles, F. C., Conversion of the reactive sulfhydryl groups of proteins to the S-trifluoroethyl derivatives: Application to human hemoglobin. *Analytical Biochemistry* **1981,** *110* (1), 19-26.

251. Heil, J. R.; Lynch, M. D. J.; Cheng, J.; Matysiakiewicz, O.; D'Alessio, M.; Charles, T. C., The completed PacBio single-molecule real-time sequence of *Methylosinus trichosporium* strain OB3b reveals the presence of a third large plasmid. *Genome Announcements* **2017,** *5* (49), e01349-17.
252. Tiwari, M. K.; Lee, J. K.; Moon, H. J.; Zhao, H., Further biochemical studies on aminopyrrolnitrin oxygenase (PrnD). *Bioorg Med Chem Lett* **2011,** *21* (10), 2873-6.
253. Gee, C. T.; Arntson, K. E.; Urick, A. K.; Mishra, N. K.; Hawk, L. M. L.; Wisniewski, A. J.; Pomerantz, W. C. K., Protein-observed ^{19}F-NMR for fragment screening, affinity quantification and druggability assessment. *Nat. Protoc.* **2016,** *11* (8), 1414-1427.
254. Crowley, P. B.; Kyne, C.; Monteith, W. B., Simple and inexpensive incorporation of ^{19}F-tryptophan for protein NMR spectroscopy. *Chemical Communications* **2012,** *48* (86), 10681-10683.
255. Rashid, S.; Lee, B. L.; Wajda, B.; Spyracopoulos, L., Side-chain dynamics of the trifluoroacetone cysteine derivative characterized by ^{19}F NMR relaxation and molecular dynamics simulations. *The Journal of Physical Chemistry B* **2019,** *123* (17), 3665-3671.
256. Brauer, M.; Sykes, B. D., ^{19}F nuclear magnetic resonance studies of selectively fluorinated derivatives of G- and F-actin. *Biochemistry* **1986,** *25* (8), 2187-91.
257. Cer, R. Z.; Mudunuri, U.; Stephens, R.; Lebeda, F. J., BotDB. 2009.
258. Cer, R. Z.; Mudunuri, U.; Stephens, R.; Lebeda, F. J., IC_{50}-to-Ki: a web-based tool for converting IC50 to Ki values for inhibitors of enzyme activity and ligand binding. *Nucleic Acids Res* **2009,** *37* (Web Server issue), W441-445.
259. Divakaran, A.; Kirberger, S. E.; Pomerantz, W. C. K., SAR by (protein-observed) ^{19}F NMR. *Accounts of Chemical Research* **2019,** *52* (12), 3407-3418.
260. Ruben, E. A.; Gandhi, P. S.; Chen, Z.; Koester, S. K.; DeKoster, G. T.; Frieden, C.; Di Cera, E., ^{19}F NMR reveals the conformational properties of free thrombin and its zymogen precursor prethrombin-2. *J Biol Chem* **2020,** *295* (24), 8227-8235.
261. Welte, H.; Zhou, T.; Mihajlenko, X.; Mayans, O.; Kovermann, M., What does fluorine do to a protein? Thermodynamic, and highly-resolved structural insights into fluorine-labelled variants of the cold shock protein. *Scientific Reports* **2020,** *10* (1), 2640.
262. Chrisman, I. M.; Nemetchek, M. D.; de Vera, I. M. S.; Shang, J.; Heidari, Z.; Long, Y.; Reyes-Caballero, H.; Galindo-Murillo, R.; Cheatham, T. E.; Blayo, A.-L.; Shin, Y.; Fuhrmann, J.; Griffin, P. R.; Kamenecka, T. M.; Kojetin, D. J.; Hughes, T. S., Defining a conformational ensemble that directs activation of PPARγ. *Nature Communications* **2018,** *9* (1), 1794.
263. Horovitz, A.; Levitzki, A., An accurate method for determination of receptor-ligand and enzyme-inhibitor dissociation constants from displacement curves. *Proc Natl Acad Sci U S A* **1987,** *84* (19), 6654-8.
264. Kogan, F.; Hariharan, H.; Reddy, R., Chemical exchange saturation transfer (CEST) imaging: Description of technique and potential clinical applications. *Current Radiology Reports* **2013,** *1* (2), 102-114.
265. Zhou, J.; Zijl, P. C. M. v., Chemical exchange saturation transfer imaging and spectroscopy. *Progress in Nuclear Magnetic Resonance Spectroscopy* **2006,** *48* (2), 109-136.
266. Dalvit, C.; Invernizzi, C.; Vulpetti, A., Fluorine as a hydrogen-bond acceptor: Experimental evidence and computational calculations. *Chemistry – A European Journal* **2014,** *20* (35), 11058-11068.
267. Ycas, P. D.; Wagner, N.; Olsen, N. M.; Fu, R.; Pomerantz, W. C. K., 2-Fluorotyrosine is a valuable but understudied amino acid for protein-observed ^{19}F NMR. *J. Biomol. NMR* **2020,** *74* (1), 61-69.
268. Srinivas, V.; Banerjee, R.; Lebrette, H.; Jones, J. C.; Aurelius, O.; Kim, I.-S.; Pham, C. C.; Gul, S.; Sutherlin, K. D.; Bhowmick, A.; John, J.; Bozkurt, E.; Fransson, T.; Aller, P.; Butryn, A.; Bogacz, I.; Simon, P.; Keable, S.; Britz, A.; Tono, K.; Kim, K. S.; Park, S.-Y.; Lee, S. J.; Park, J.; Alonso-Mori, R.; Fuller, F. D.; Batyuk, A.; Brewster, A. S.; Bergmann, U.;

Sauter, N. K.; Orville, A. M.; Yachandra, V. K.; Yano, J.; Lipscomb, J. D.; Kern, J.; Högbom, M., High resolution XFEL structure of the soluble methane monooxygenase hydroxylase complex with its regulatory component at ambient temperature in two oxidation states. *J. Am. Chem. Soc.* **2020,** *142* (33), 14249-14266.
269. Sligar, S. G.; Gunsalus, I. C., A thermodynamic model of regulation: Modulation of redox equilibria in camphor monooxygenase. *Proc. Natl. Acad. Sci. USA.* **1976,** *73*, 1078-1082.
270. Cooke, R.; Crowder, M. S.; Thomas, D. D., Orientation of spin labels attached to cross-bridges in contracting muscle fibres. *Nature* **1982,** *300* (5894), 776-778.
271. Stroik, D. R.; Yuen, S. L.; Janicek, K. A.; Schaaf, T. M.; Li, J.; Ceholski, D. K.; Hajjar, R. J.; Cornea, R. L.; Thomas, D. D., Targeting protein-protein interactions for therapeutic discovery via FRET-based high-throughput screening in living cells. *Sci. Rep.* **2018,** *8* (1), 12560.